Nonlinear Optics in a-Si:H-on-Insulator and InGaP-on-Insulator Waveguide Circuits

Niet-lineaire optica in golfgeleidercircuits
geïmplementeerd in a-Si:H-op-isolator en InGaP-op-isolator

Utsav Deepak Dave

Promotoren: prof. dr. ir. G. Roelkens, prof. dr. ir. B. Kuyken
Proefschrift ingediend tot het behalen van de graad van
Doctor in de ingenieurswetenschappen: fotonica

UNIVERSITEIT
GENT

Vakgroep Informatietechnologie
Voorzitter: prof. dr. ir. B. Dhoedt
Faculteit Ingenieurswetenschappen en Architectuur
Academiejaar 2016 - 2017

ISBN 978-90-8578-974-1
NUR 965, 926
Wettelijk depot: D/2017/10.500/9

GHENT UNIVERSITY

Universiteit Gent
Faculteit Ingenieurswetenschappen en Architectuur
Vakgroep Informatietechnologie

Promotoren:
Prof. Dr. Ir. Günther Roelkens
Prof. Dr. Ir. Bart Kuyken

Examencommissie:

Prof. Dr. Ir. Patrick De Baets (Voorzitter)	Universiteit Gent, EESA
Prof. Dr. Ir. Günther Roelkens (Promoter)	Universiteit Gent, INTEC
Prof. Dr. Ir. Bart Kuyken (Promoter)	Universiteit Gent, INTEC
Prof. Dr. Ir. Fabrice Raineri	Université Paris Diderot, CNRS-LPN
Prof. Dr. Ir. Simon-Pierre Gorza	Université libre de Bruxelles
Prof. Dr. Ir. Kristiaan Neyts	Universiteit Gent, ELIS
Prof. Dr. Ir. Dries Van Thourhout	Universiteit Gent, INTEC
Prof. Dr. Ir. Roel Baets	Universiteit Gent, INTEC

Universiteit Gent
Faculteit Ingenieurswetenschappen en Architectuur
Vakgroep Informatietechnologie
Technologiepark-Zwijnaarde 15 iGent,
9052 Gent, België

Tel.: +32 (0) 9264 3316
Fax.: +32 (0) 9264 3593

Dit werk werd ondersteund door ERC grants MIRACLE en InSpectra.

Proefschrift tot het behalen van de graad van
Doctor in de ingenieurswetenschappen: fotonica
Academiejaar 2016-2017

Acknowledgements

Never consider yourself to be the cause of the results of your activities. - Krishna.

Even though I never really got the meaning of this quote, what I *do* know is that without the help and guidance of a really long list of people, this thesis wouldn't have been possible. So I would like to take this opportunity to express my deep gratitude to them all. When I first came to Ghent in 2012 - still just a master student - I didn't know if I even wanted to do a PhD. I only had the vague idea that after I wanted to do something that would be interesting. Thankfully, Roel and Wim who were my master thesis supervisors gave me the confidence that this was something I could be somewhat good at (which still remains to be seen). It was only after I talked with Roel after the barbecue of the Erasmus summer school in Brussels that I realized that a PhD was in fact what I wanted to do. By this time it was already July of 2013 and thankfully, a PhD in the topic of my choice - nonlinear optics - was still open in Ghent - the city of my choice. Long story short, I joined the PhD under the supervision of Günther. At that time Bart was still 'just' a PhD student. Now of course, he is officially my co-supervisor, *and* a professor - no big deal. And although I don't deserve any credit for that meteoric rise, I'm going to take some anyway, being his first official PhD student. All joking aside, I couldn't have asked for better supervisors. Always ready to provide help as and when needed but also not breathing down my neck if I was trying to solve something on my own. As Mance Rayder said, *"The freedom to make my own mistakes is all I ever wanted"*. So thank you both for that opportunity.

At this point, I must also mention François for effectively being my other, other supervisor, at least during the first half of my PhD. Starting with the very first alignment session at the horizontal setup in the midIR room back in good old days of the Technicum, I've learnt a lot from you, and that includes not just the technical stuff. So thanks for all that. And finally, I must also mention Fabrice, without whose help I would still be trying (and probably failing) to fabricate my first working structures. But even over and above that collaboration, you made the numerous visits I made to LPN enjoyable and productive even through all the countless delays one typically experiences in doing fabrication on a tight schedule. I guess here I should apologize for always bringing bad luck and causing the Ebeam to

break down every other time that I came there - hopefully, that will stop now that I'm gone and the productivity of LPN will once again rise.

I would also like to thank our collaborators at Thales - Alfredo and Sylvain not just for generously providing the III-V material I used throughout the PhD but also for providing crucial feedback and help whenever it was needed. A special thank you also to Simon-Pierre at ULB where I spent so many weeks, chasing supercontinuum measurements and conducting the student labs for the nonlinear course. I've always liked your style of working and have learnt a lot even in the relatively short time I spent at ULB.

I would also like to thank all the people of the mid-IR group with whom I've shared labspace over the past few years - Chen, Aditya, Nannicha, Muneeb, Anton, Sanja and Ruijun. It was always a pleasure working with you guys, even in that cramped space back in Technicum, and also in our brand new (and still equally cramped) space in iGent. I'll also include a note of thanks to the 'nonlinear team' here - Pijush, Haolan, Stéphane, Artur and Koen for all our interesting discussions (the dipoles are coupled guys - duh!). Thanks also to both the master thesis students Sarah and Vincent, for being good at your jobs so that I didn't have to do much 'supervising'. Especially Sarah, since at that time I was still a first year student who knew about as much as you did - which was of course next to nothing. And finally, thanks to Liesbet, Steven and Muneeb for keeping the CR running as well as you guys did. And Sulakshana and Sarah, thanks for the help within our little 'GaAs-minigroup'.

A special thanks to all the people at LPN who made my visits feel more like mini-vacations than actual work - Guillaume, Dorian, Alex, Avishek, Nhung, Rama, Ivens and Ray. You all made me feel welcome there. Thanks for teaching me a little bit of French (most of which I've already forgotten, of course). Guillaume - thank you for driving me even back and forth to the campus even though my hotels were generally a somewhat out of the way for you. And Dorian, thanks for all the random conversations while waiting around in the cleanroom.

My office-mates, beginning with Bart, Pieter, Yannick and Herbert and then eventually, Koen, Kasper Stéphane and Camiel, thanks for a nice day-to-day working environment. Same goes for Bendix, who although was officially in the adjoining office, was also the one with closest desk to mine and with whom probably I've 'invested' the most time in tea/coffee breaks, as well as Muneeb, Anton and Sarvagya.

Now if I begin thanking all the people who made my life in general in Ghent enjoyable, I'm afraid it's going to take too long, and they all know it anyway. I would just briefly express a note of appreciation to all the colleagues at PRG who made the sometimes long and tedious days designing or processing etc. bearable. I'll especially fondly remember all the De Brug lunch sessions where one never quite

knew in which weird and sometimes disturbing direction the conversation was going to go (I'm looking at you Frédéric, Sarvagya and Alfonso). I would be remiss if I didn't especially thank the 'Indian gang' in Ghent who made it feel more like home than I ever imagined Belgium would feel like. Ananth-Kamal, Sullu-Kullu, Sarvagya, Aditya-Kirti, Manan-Nammi, Gaurav-Nikki, Ashwyn, Ark, and Bendix (our honorary Indian) thanks for all the Diwali, Holi, new years and other celebrations we did. I will remember all the random stuff like the Indian Dhaba enterprise. My travel buds - Vijay, Anandram, Prasanna, Esrom etc. - thanks for braving everything from the bitter colds of Norway to the ruins of Greece with me.

And finally, thanks to my family for always being there through it all.

Ghent, October 2012-January 2017
Utsav D. Dave

Table of Contents

List of Figures

List of Tables

List of Acronyms

3

3PA	Three-photon Absorption

A

AlGaAs	Aluminium Gallium Arsenide
ASE	Amplified spontaneous emission
a-Si	Amorphous silicon
a-Si:H	Hydrogenated amorphous silicon

B

BCB	Benzocyclobutene

C

CE	Conversion efficiency
CMOS	Complementary metal-oxide-semiconductor
c-Si	Crystalline silicon
CW	Continuous wave

D

DC	Direct current

DI	Deionized water
DFG	Difference-frequency generation
DW	Dispersive wave

E

EDFA	Erbium-doped fiber amplifier

F

FCA	Free-carrier absorption
FCD	Free-carrier dispersion
FDTD	Finite-difference time-domain
FWHM	Full-width half-maximum
FWM	Four-wave mixing

G

GB	Gigabyte
GaP	Gallium Phosphide
GaAs	Gallium Arsenide
GNLSE	Generalized Nonlinear Schrödinger equation
GVD	Group velocity dispersion

H

HSQ	Hydrogen silsesquioxane

I

InGaP	Indium Gallium Phosphide
InP	Indium Phosphide
ICP	Inductively coupled plasma

IPA	Isopropyl alcohol
IR	Infrared

K

KDP	Potassium dihydrogen phosphate, KH_2PO_4

L

LOC	Lab-on-a-chip
LN	Lithium niobate, $LiNbO_3$

M

MIR	Mid-infrared
MI	Modulation instability
MIBK	Methyl isobutyl ketone
MO	Microscope objective

N

NA	Numerical aperture
NLSE	Nonlinear Schrödinger equation

O

OPO	Optical parametric oscillator
OSA	Optical spectrum analyzer

P

PCF	Photonic crystal fiber

PECVD	Plasma-enhanced chemical vapour deposition
PMMA	Polymethyl methacrylate

Q

QPM	Quasi-pshase matching

R

RIE	Reactive ion etching

S

SC	Supercontinuum
SC1	Standard clean
SEM	Scanning electron microscope
SHG	Second-harmonic generation
SFG	Sum-frequency generation
SiN	Silicon Nitride
SOI	Silicon-on-insulator
SPM	Self-phase modulation

T

TE	Transverse electric
THG	Third-harmonic generation
TM	Transverse magnetic
TPA	Two-photon Absorption

Z

XPM	Cross-phase modulation
XAM	Cross-amplitude modulation

Z

ZDW	Zero-dispersion wavelength

NEDERLANDSE SAMENVATTING –SUMMARY IN DUTCH–

Doelstellingen en motivatie

GEÏNTEGREERDE fotonische platformen zoals het silicium-op-isolator (Engels: silicon-on-insulator, SOI) platform zijn gedurende het laatste decennium heel matuur geworden. De verschillende individuele componenten op zo een platform zoals golfgeleiders met laag verlies, mode conversiestructuren, interferometers, resonatoren, koppelaars, ... met heel goede specificaties zijn al aangetoond. Actieve componenten zoals heterogeen geïntegreerde lasers en monolithisch geïntegreerde modulatoren en detectoren zijn ook ontwikkeld. Naast deze componten is er ook nood aan niet-lineaire componenten. In verschillende toepassingen zoals golflengteconversie, modulatie, sensoren, spectroscopie ... wordt de niet-lineaire respons van een materiaal uitgebuit. In termen van derde orde niet-lineariteit is silicium een heel goed materiaal omdat het een grote niet-lineaire index heeft. Daarenboven laat het hoge lineaire brekingsindexcontrast op het SOI platform ons toe om het licht in golfgeleiders met een heel kleine doorsnede op te sluiten [1]. Zo is het mogelijk om heel hoge lichtintensiteiten te verkrijgen bij matige vermogens. Verder laat het platform ook toe om de dispersie van de golfgeleiders te controleren in het ontwerp. Dit is heel belangrijk: de propagatieconstanten van de golven die deelnemen aan het niet-lineaire proces kunnen op mekaar worden afgestemd. Dit laat toe om het niet-lineaire proces efficiënt te maken. Spijtig genoeg zijn voor sommige functionaliteiten ook tweede orde niet-lineariteiten nodig en heeft silicium geen tweede orde niet-lineaire respons. Dit komt omdat silicium een centro-symmetrische kristalstructuur heeft. Een ander probleem met silicium is dat het een relatief kleine bandkloof heeft. Dit heeft als gevolg dat twee-foton-absorptie optreedt in de telecommunicatieband. Deze vorm van absorptie is inherent niet-lineair en daarenboven genereert het proces ook nog eens vrije ladingsdragers. Deze ladingsdragers absorberen op hun beurt nog meer licht en veroorzaken zo nog meer verlies. Het gebruik van met waterstof gepassiveerd amorf silicium in de plaats van kristallijn silicium is daarom onderzocht als een manier om de niet-lineaire verliezen te onderdrukken. Ook werd er werk verricht om het platform uit te breiden naar het mid-infrarode (MIR) golflengte gebied. Dit kan belangrijk zijn voor toepassingen met betrekking tot spectroscopie. Deze aanpak helpt evenwel niet om het gebrek aan een tweede-orde niet-lineariteit

in kristallijn silicium op te lossen.

Samengevat is silicium een ideale kandidaat voor een waaier aan toepassingen, inclusief de niet-lineaire maar kan het niet gebruikt worden in een aantal specifieke, doch belangrijke toepassingen. Zo is silicium een heel slecht winstmateriaal omdat het een indirecte bandkloof heeft. Hierdoor hebben verschillende onderzoekers in de wereld gezocht naar manieren om andere materialen te integreren op het SOI platform. Zodoende kan extra functionaliteit alsnog worden toegevoegd aan het platform en kunnen de enorme voordelen van het platform, zoals de schaalbaarheid van de goedkope CMOS compatibele fabricageprocessen behouden blijven. Dit heeft er voor gezorgd dat de zogenaamde hybride integratie van SOI en III-V materialen een actief onderzoeksgebied is geworden. Deze III-V materialen zijn niet alleen een excellent winstmedium, ze bezitten ook een sterke twee-orde en derde-orde niet-lineariteit. De sterkte van deze niet-lineariteit is gelijkaardig of zelfs groter dan deze van lithiumniobaat (voor de tweede orde processen) en silicium (voor de derde orde processen). Het integreren van III-V materialen is dus niet enkel interessant voor het genereren van licht, maar ook voor niet-lineaire toepassingen zoals supercontinuumgeneratie, vier-bundelmenging, frequentieverdubbeling ... Zo komen we tot de kern van het doctoraat. Het doel is om een platform te ontwikkelen dat zowel een sterke tweede- en derde-orde niet-lineariteit bezit. Verder willen we deze niet-lineariteiten karakteriseren en een aantal niet-lineaire functionaliteiten aantonen. Finaal willen we deze functies integreren met bestaande platformen zoals SOI en het siliciumnitride (SiN) platform.

Resultaten

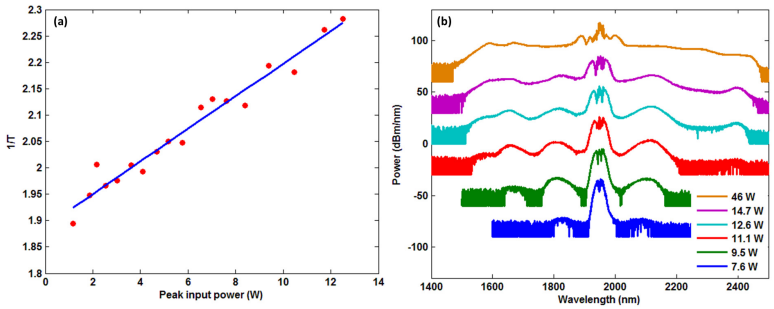

Figuur 1 (a) Een lineaire fit van de inverse van de transmissie als functie van het piekvermogen van de pulsen. De uitgangsspectra van de golfgeleider tonen hoe het supercontinuum evolueert als functie van het piekvermogen. Het supercontinuum beslaat zowel de telecom als de mid-ir band.

Zoals hierboven aangehaald, is met waterstof gepassiveerd amorf silicium al onderzocht als niet-lineair materiaal omdat het minder niet-lineaire verliezen vertoont in de telecommunicatieband. In dit werk wordt supercontinuumgeneratie

met een mid-infrarode gepulste picoseconde bron [2] aangetoond in golfgeleiders gebaseerd op amorf silicium. Figuur 1(a) toont een lineaire trend voor de inverse van de transmissie van de golfgeleider als in functie van ingangsvermogen voor de gepulste bron bij 1950 nm golflengte. Uit deze grafiek wordt de twee-foton-absorptiecoëfficiënt afgeleid. Deze bedraagt 2.3 cm/GW en is daarmee veel kleiner dan de coëfficiënt in kristallijn silicium. Hierdoor is het mogelijk om efficiënt een supercontinuum te genereren in een voor dispersie geoptimaliseerde golfgeleider. Het spectrum van het supercontinuum liep van 1450 nm tot 2450 nm zodat het zowel de telecom band als de mid-infrarode band besloeg. Het spectrum wordt getoond in figuur 1(b). Deze resultaten worden besproken in hoofdstuk 2.

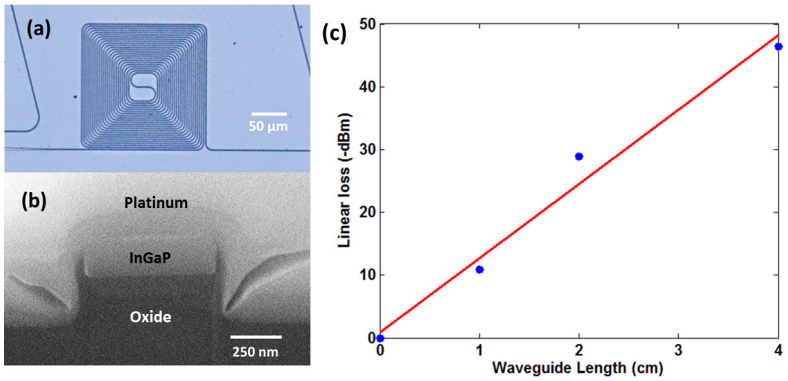

Figuur 2 (a) Een 1 cm lange golfgeleider opgerold in een spiraal (b) Een dwarsdoorsnede van de InGaP golfgeleider. Het platina is gedeponeerd om de doorsnede te maken. (c) Het lineaire verlies was 12 dB/cm.

Het III-V materiaal dat prominent gebruikt wordt in dit doctoraat is het ternaire Indium Gallium Phosifide (InGaP). In een eerste stap is de bonding van dunne membranen van dit materiaal op silicium substraten ontwikkeld. Bouwende op bestaande technieken worden optische componenten zoals golfgeleiders en resonatoren gefabriceerd aan de hand van elektronenstraallithografie en plasma etsstappen. Doordat de InGaP laag optisch geïsoleerd is van het substraat door een glaslaag ziet het licht een heel groot brekingsindexcontrast. Dit heeft als gevolg dat het licht kan worden opgesloten in golfgeleiders met een heel kleine doorsnede. In het doctoraat werden de gefabriceerde componenten gekarakteriseerd [3]. Er werd zowel gekeken naar de lineaire eigenschappen als de tweede-orde en de derde-orde niet-lineariteiten. Fig. 2(a) toont een 1 cm lange golfgeleider opgerold in een spiraal die maar een oppervlakte van 0.03 mm^2 beslaat. Fig. 2(b) toont een doorsnede van dezelfde golfgeleider. Fig. 2(c) toont de transmissie van de golfgeleiders als een functie van de lengte. Deze meting liet ons toe om het verlies te meten. Deze was 12 dB/cm voor de gefabriceerde golfgeleiders.

De derde-orde niet-lineaire eigenschappen zijn samengevat in Fig. 3. Door de

grote bandkloof van het materiaal is er geen niet-lineaire twee-fotonabsorptie. Er is evenwel drie-fotonabsorptie. Dit is bevestigd door de transmissie van hoog vermogen pulsen in de InGaP golfgeleiders te bestuderen (zie ook figuur 3 (a) en (b)). Omdat het drie-fotonabsorptieproces een zwakker effect is dan het twee-foton absorptieproces is de niet-lineaire absorptie in het materiaal veel zwakker dan in kristallijn silicium. Bovendien werden vier-bundelmenging experimenten uitgevoerd om de niet-lineaire parameter van de golfgeleiders te bepalen (zie ook Fig. 3 (c) en (d)). Er werd een waarde van 475 $W^{-1}m^{-1}$ gemeten. De grootte van deze parameter is lichtjes groter dan de waarde van standaard SOI golfgeleiders en dus zeker groot genoeg voor niet-lineaire optische experimenten, zeker wanneer we ook de lage niet-lineaire absorptie van de golfgeleiders in rekening brengen. Deze resultaten zijn beschreven in hoofdstuk 3.

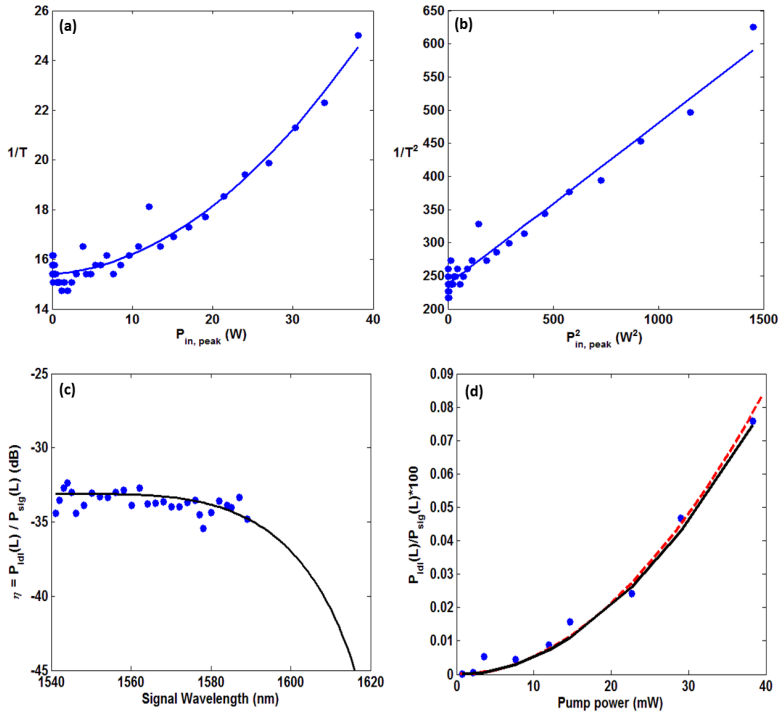

Figuur 3 (a) De inverse van de transmissie als functie van het piekvermogen van de gepulste laser bij 1550 nm. De trend is niet-lineair, (b) terwijl het kwadraat van de inverse een lineaire trend vertoont. Dit betekent dat het absorptieproces een vijfde-orde proces is: het gaat hier om drie-foton absorptie (c) De efficiëntie van het vier-bundelmengingsproces als functie van de pomp-signaal detuning. (d) Een kwadratische fit van de efficiëntie als functie van het pompvermogen laat toe om de niet-linaire parameter γ te bepalen: 475 $W^{-1}m^{-1}$.

Er werd ook aangetoond dat door de golfgeleiders te pompen met sub-picoseconde pulsen supercontinuumgeneratie mogelijk was [4]. Het uitgangsspectrum is te zien op Fig. 4 (a). De coherentie van het gegenereerde supercontinuum is ook opge-

meten (zie Fig. 4(b)). De resultaten alsook de vergelijking met de theorie en de simulaties worden beschreven in hoofdstuk 4.

In hoofdstuk 3 wordt de frequentieverdubbeling in InGaP golfgeleiders en ringresonatoren besproken. Op Fig. 5(a) is het uitgangsfacet te zien van een InGaP golfgeleider. Hier kan men het frequentieverdubbelde licht zien van een CW laser bij 1540 nm. De *phase matching* in het niet-lineaire proces wordt bekomen doordat de effectieve index van een hogere orde transversale magnetische (TM) mode gelijk is aan de index van de fundamentele tranversale elektrische (TE) mode bij het pompgolflengte. it blijkt uit de kwadratische afhankelijkheid van de tweede harmonische vermogen als fubnctie van het pompvermogen (zie Fig. 5(b)). Fig 5 (c) toont een foto van de ring resonator waarin quasi-*phase matched* frequentieverdubbeling plaats vindt.

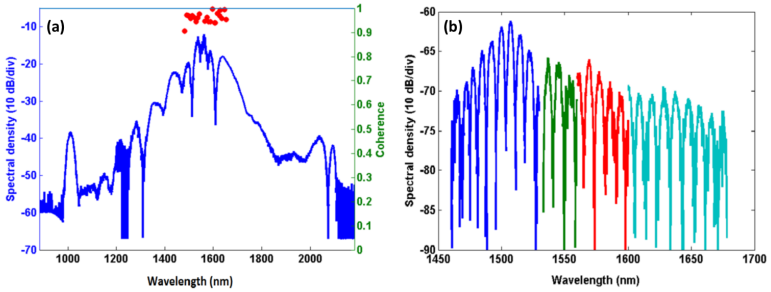

Figuur 4 (a) Het uitgangsspectrum van de golfgeleider als deze gepompt wordt door een gepulste laser bij 1550 nm. De pulsen waren 170 fs lang en hadden op de chip een piekvermogen van 10 W. (b) De coherentie is gemeten via de franjes veroorzaakt door de interferentie van twee opeenvolgende pulsen.

De extra processtappen die nodig zijn om de InGaP golfgeleiders te integreren met een CMOS compatibel platform worden besproken in hoofdstuk 5. Vierbundelmenging in InGaP microschijfresonatoren geïntegreerd op het SOI platform is gedemonstreerd alsook InGaP componenten geïntegreerd op het SiN platform (zie ook figuur Fig. 6 (a)-(d)). Dit laat toe om sterke niet-lineare optische functionaliteiten te integreren op een CMOS compatibel platform met alle voordelen van dien.

Conclusie en Perspectieven

Het werk dat gedaan is in het kader van dit doctoraat is een eerste stap in de richting van een volledig geïntegreerd niet-lineair platform dat de voordelen van een groot brekingsindexcontrast, lage niet-lineaire verliezen, sterke tweede-orde en derde-orde niet-lineariteit combineert. *Phase matching* is aangetoond voor verscheidene

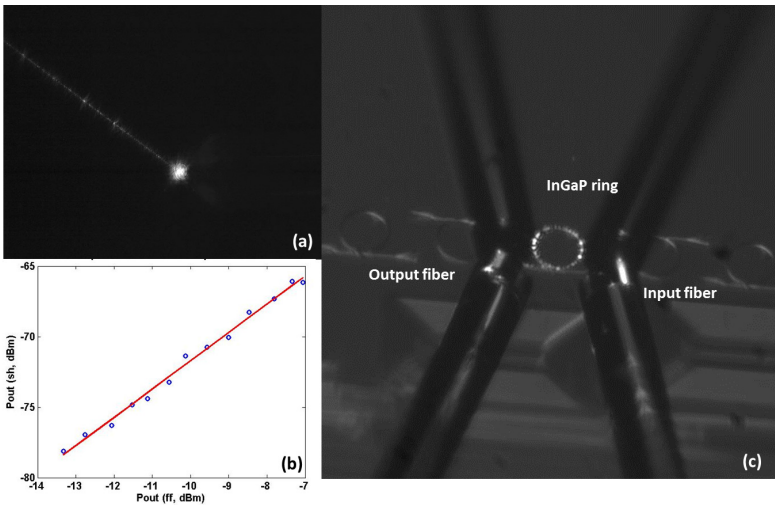

Figuur 5 a) Frequentieverdubbeld licht aan het uitgangsfacet van een golfgeleider (b) De richtingscoëfficiënt van een lineaire fit van het vermogen van het frequentieverdubbelde licht als functie van het ingangsvermogen in een dubbel logaritmische schaal is 2. (c) Frequentieverdubbeld licht gegenereerd in een microresonator.

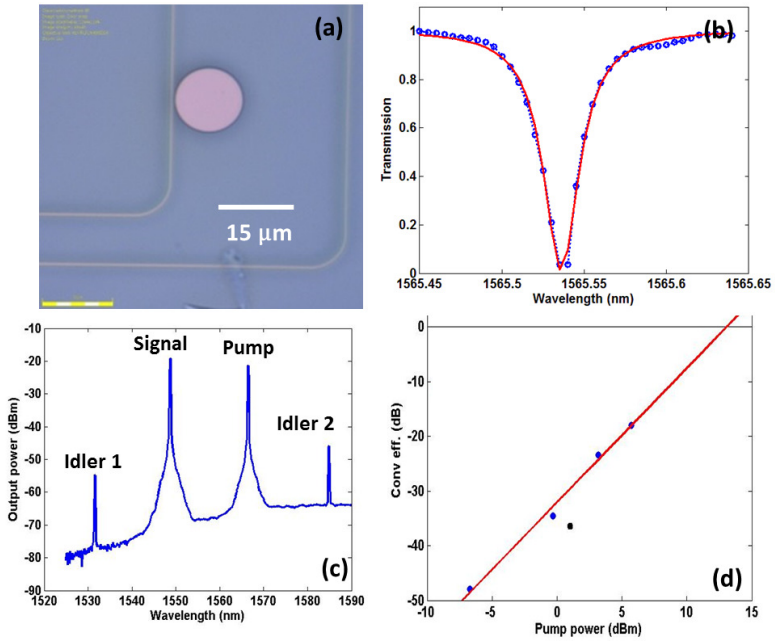

Figuur 6 Een InGaP microschrijfresonator met een diameter van 15 μm geïntegreerd op het SOI platform. (b) De resonantie bij 1565 nm heeft een Q factor van 60000. (c) Vier-bundelmenging in SOI-gekoppelde InGaP microschijfresonatoren. (d) De vier-bundelmengingefficiëntie als functie van het pompvermogen.

processen zoals vier-bundelmenging en frequentieverdubbeling. Een laag vermogen coherent supercontinuum werd gegeneerd door de voordelen van het platform uit te buiten. Verder zijn ook de eerste stappen gedaan om deze componenten te integreren met mature CMOS compatibele platformen zoals het SOI en SiN platform. Het is aangetoond dat de finale geïntegreerde component de vereiste performantie heeft.

Als we de InGaP membraangolfgeleiders in de toekomst willen gebruiken in *real-life* toepassingen moet het verlies omlaag. Aan de fabricagekant is er nog ruimte voor optimalisatie. De *yield* in het farbicage is beperkt, zeker voor de structuren die geïntegreerd zijn op het SOI of SiN platform. In tegenstelling tot het SOI platform laat het SiN platform ons toe om ook golflengtes met een kortere golflengte dan 1.1 μm te gebuiken. Dit is belangrijk omdat het frequentieverdubbelde licht anders wordt geabsorbeerd. In de toekomst moet gekeken worden naar betere technieken om dit niet-lineare proces te *phase matchen*. De huidige techniek is beperkt in efficïentie. Als dit lukt, zouden belangrijke toepassingen zoals het stabiliseren van een frequentiekam door het meten van zijn carrier-offset frequentie mogelijk worden. Men zou ook kunnen denken aan andere III-V materialen en deze integreren voor specifieke eigenschappen. Zo is GaP [5] al gebruikt door verschillende groepen en is het eenvoudig om op basis van hun methodologie het materiaal te incorperen in het geïntegreerde platform. Dit is bijvoorbeeld recent gedaan door gebruik te maken van AlGaAs [6]. We kunnen besluiten dat dit doctoraat kan gebruikt worden als een basis voor toekomstig werk dat nog meer focust op de toepassing.

Referenties

[1] B Kuyken, F Leo, S Clemmen, U Dave, R Van Laer, T Ideguchi, H Zhao, X Liu, J Safioui, S Coen, et al. *Nonlinear optical interactions in silicon waveguides* Nanophotonics, 2016.

[2] Utsav D Dave, Sarah Uvin, Bart Kuyken, Shankar Selvaraja, Francois Leo, and Gunther Roelkens *Telecom to mid-infrared spanning supercontinuum generation in hydrogenated amorphous silicon waveguides using a Thulium doped fiber laser pump source* Optics express, 21(26):32032–32039, 2013.

[3] Utsav D Dave, Bart Kuyken, François Leo, Simon-Pierre Gorza, Sylvain Combrie, Alfredo De Rossi, Fabrice Raineri, and Gunther Roelkens *Nonlinear properties of dispersion engineered InGaP photonic wire waveguides in the telecommunication wavelength range* Optics express, 23(4):4650–4657, 2015.

[4] Utsav D Dave, Charles Ciret, Simon-Pierre Gorza, Sylvain Combrie, Alfredo De Rossi, Fabrice Raineri, Gunther Roelkens, and Bart Kuyken *Dispersive-wave-based octave-spanning supercontinuum generation in InGaP membrane waveguides on a silicon substrate* Optics letters, 40(15):3584–3587, 2015.

[5] David P Lake, Matthew Mitchell, Harishankar Jayakumar, Laís Fujii dos Santos, Davor Curic, and Paul E Barclay *Efficient telecom to visible wavelength conversion in doubly resonant gallium phosphide microdisks* Applied Physics Letters, 108(3):031109, 2016.

[6] Minhao Pu, Luisa Ottaviano, Elizaveta Semenova, and Kresten Yvind *Efficient frequency comb generation in AlGaAs-on-insulator* Optica, 3(8):823–826, 2016.

ENGLISH SUMMARY

Goals and motivation

INTEGRATED photonic systems such as silicon-on-insulator (SOI) have, within the last decade, began maturing as numerous individual components such as low-loss waveguides, mode converters, interferometers, resonators, couplers etc. with very good performance have been demonstrated. Active components such as lasers and modulators have also been developed. In many applications such as wavelength conversion, modulation, sensing, spectroscopy etc. the nonlinear response of materials to incident electromagnetic radiation is exploited. With regards to the third-order nonlinearity, silicon is a good material because it offers a strong nonlinearity. Furthermore its large refractive index contrast enables large light intensities to be achieved, which is obviously desirable for nonlinear optics [1]. Another important feature is that the platform allows for the design of the dispersion properties, which is important for achieving phase matching. Hence, it allows for efficient nonlinear interactions. However, several nonlinear functionalities exploit a second-order nonlinear response which is lacking in silicon due to its centrosymmetric crystal structure. Another problem with silicon is that due its relatively small bandgap, two-photon absorption (TPA) is very strong in the wavelength range of several of these applications. TPA by itself is nonlinear, furthermore it leads to the generation of free carriers that also heavily absorb the incident light leading to even more losses. Using amorphous instead of crystalline silicon has been investigated as a possible means of overcoming this problem of nonlinear loss, and some work was done as part of this PhD to extend the amorphous silicon platform into the mid-infrared (MIR) regime, which is important for applications like spectroscopy. However, this does not overcome the problem of the absence of the second-order nonlinearity in silicon. Thus, while silicon has been a material of choice for many applications including nonlinear ones, for many others, SOI is not necessarily the ideal platform. The primary example of this is that it is a poor laser material due to its indirect bandgap structure. This has spurred many in the integrated photonics community to develop methodologies to incorporate other materials that are more suitable for such tasks into the SOI platform. This allows one to keep the advantages that initially motivated the adoption of SOI in the first place namely the compatibility with complementary metal-oxide-semiconductor (CMOS) manufacturing techniques developed in the electronics industry, which brings with it massive economies of scale and thus the

potential for low-cost, mass-market applications. As a result, for many years, hybrid integration of the SOI platform with III-V materials has been an active area of research and development. III-V materials along with being good for lasing are also known to possess both second- and third-order nonlinearities. The strength of these nonlinear responses is also comparable to or better than other most commonly used nonlinear materials such as Lithium Niobate (for second order) and silicon (for third order nonlinear applications). Thus, it is very attractive to use these materials in conjunction with a platform like SOI not just for the addition of active functionalities such as lasers, but also for nonlinear ones such as supercontinuum generation, four-wave mixing, second harmonic generation etc. This forms the basis of the motivation for the work in this PhD. The goal is to develop a versatile platform that exhibits both second and third-order nonlinearities and to characterize them for implementing specific functionalities like those mentioned above. Demonstration of these functions integrated with existing platforms such as SOI and silicon nitride (SiN) whose existing library of well-developed components could then be leveraged for applications defines the final goal of this work.

Results

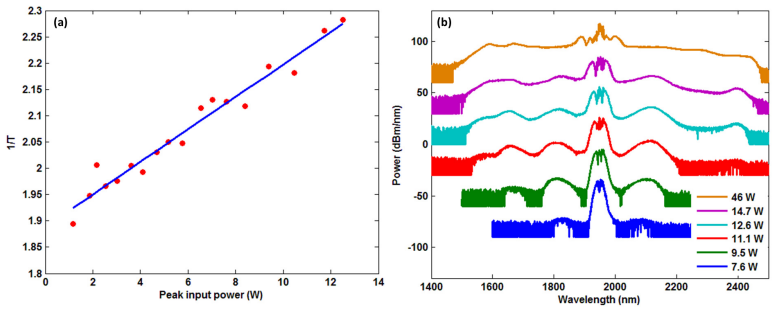

Figure 7 (a) The linear fit to the plot of the inverse transmission as a function of the increasing input power gives a small TPA coefficient. (b) The buildup of the supercontinuum pumped by a Thulium doped picosecond fiber laser source connects the telecom and MIR wavelength regimes.

As mentioned above, for the purpose of overcoming the nonlinear losses in crystalline silicon, amorphous silicon has previously been investigated. In this work, supercontinuum generation in amorphous silicon pumped by a picosecond fiber laser was demonstrated [2]. In Fig. 7(a), the linear trend of the inverse transmission with the increasing input peak power of the pulsed laser source centered at 1950 nm gives a TPA coefficient of 2.3 cm/GW which is much lower than the reported values for crystalline silicon. This, along with proper dispersion engineering of the waveguide enabled the generation of a supercontinuum spectrum that spans the wavelength range 1450-2450 nm thus connecting the telecommunications and mid-infrared wavelength regimes, as shown in Fig. 7(b). These results

are discussed in Chapter 2.

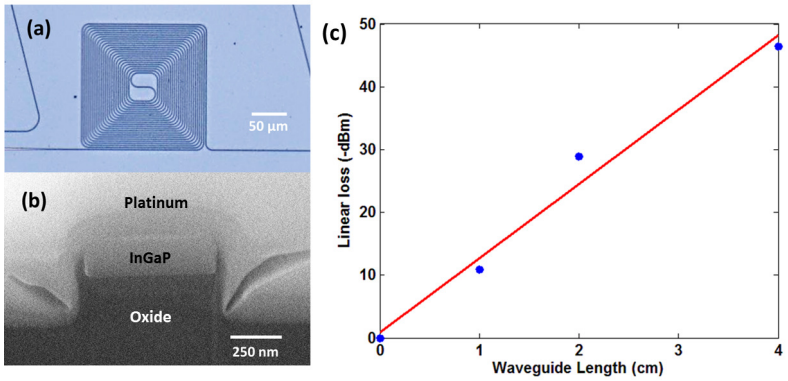

Figure 8 (a) A 1 cm long waveguide, fabricated in the form of a compact spiral, enabled by the large index contrast. (b) The cross-section of the InGaP waveguide. The Platinum is deposited during the milling process while making the cross-section for taking the SEM image. (c) The linear loss was measured by the cut-back method to be 12 dB/cm.

The primary III-V material used in this PhD is the ternary material Indium Gallium Phosphide (InGaP). First, the process flow for bonding thin membranes of this material on top of silicon substrates was developed. Existing techniques for electron beam lithography and dry etching were then used to fabricate various devices in this membrane such as waveguides and resonators. The InGaP material is optically isolated from the substrate by a silica cladding, thus ensuring that the advantageous high index contrast is maintained, just like in SOI. These fabricated devices were then used for the characterization of the linear as well as second- and third-order nonlinear properties of this material [3]. Fig. 8(a) shows an image of a fabricated 1 cm long waveguide wound up in a tight spiral in an area of just 0.03 mm^2 demonstrating that the high index platform indeed makes it possible for highly compact devices and Fig. 8(b) shows the SEM cross-section of one such fabricated InGaP waveguide. The linear loss of the fabricated waveguides was measured to be 12 dB/cm as shown in Fig. 8(c). The third-order nonlinear properties are summarized in Fig. 9. Due to its large bandgap, the nonlinear loss for this material in the wavelength range around 1550 nm arises from three- instead of two-photon absorption. Measurements of the inverse transmission of a high power pulsed laser through an InGaP waveguide prove this point, as shown in Fig. 9(a) and (b). Thus, the InGaP material suffers from far lower nonlinear losses compared to silicon because three-photon absorption (3PA) is a much weaker process compared to TPA. Finally, four-wave mixing in these waveguides was demonstrated and the value of the nonlinear parameter γ was extracted to be 475 $W^{-1}m^{-1}$ from those measurements, as shown in Fig. 9(c) and (d). This value of γ is slightly larger than in SOI and is thus large enough for several nonlinear applications. Thus, with a strong nonlinear response and the much-lowered nonlinear losses, this platform is shown to be quite attractive for various nonlinear applications. These results are

described in Chapter 3.

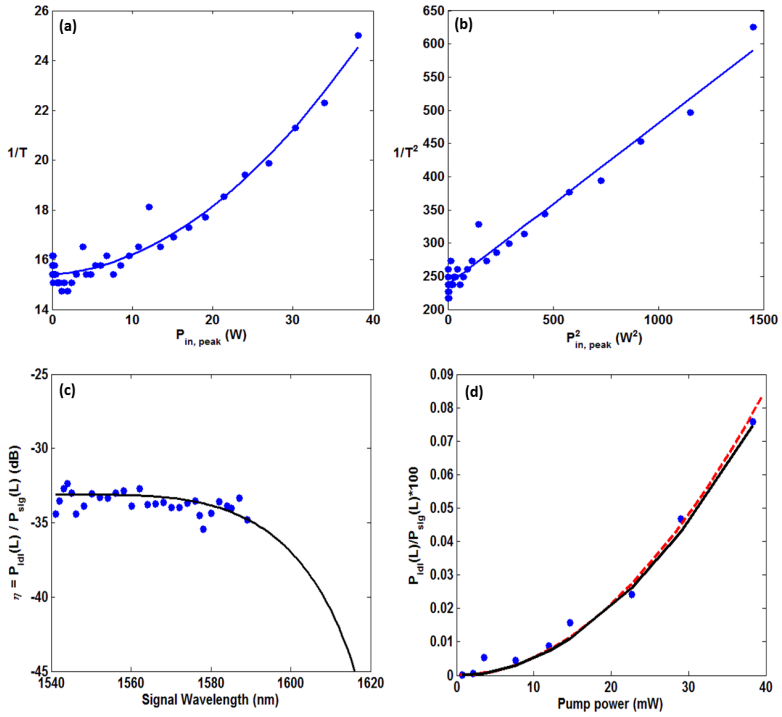

Figure 9 (a) The inverse transmission as a function of the input peak power of a pulsed laser at 1550 nm shows a nonlinear trend while, (b) the square of the inverse transmission shows a linear trend with the input peak power squared showing that the nonlinear loss is the fifth-order process of three-photon absorption. (c) The four-wave mixing efficiency as a function of pump-signal wavelength detuning shows a bandwidth exceeding 48 nm. (d) The quadratic fit of the four-wave mixing efficiency as a function of pump power is used to extract a value of the nonlinear parameter γ to be 475 $W^{-1}m^{-1}$.

Supercontinuum generation pumped by a femtosecond laser via soliton fission and dispersive wave generation was also demonstrated in these waveguides [4], as shown in Fig. 10(a). Coherence of the generated supercontinuum was also measured and is shown in Fig. 10(b). In Chapter 4, these results are described in detail and compared to theory and simulations. They show the importance of having a good understanding of both the nonlinear and linear dispersive properties of the platform for such applications. Second harmonic generation in InGaP membrane waveguides and ring resonators is also discussed in Chapter 4. Figure 11(a) shows the output facet of an InGaP waveguide where the second harmonic of a 1540 nm continuous wave pump is visible. Phasematching for the second harmonic generation process is achieved by using a higher order transverse magnetic (TM) mode at the second harmonic wavelength whose effective index matches with that of the fundament transverse electric (TE) mode of the 1540 nm pump,

which is proved by the quadratic dependence of the second harmonic power on the pump power as shown in Fig. 11(b). Figure 11(c) shows the image of a ring resonator where quasi-phasematched second-harmonic generation is achieved by properly designing the resonant modes at the fundamental and second harmonic wavelengths.

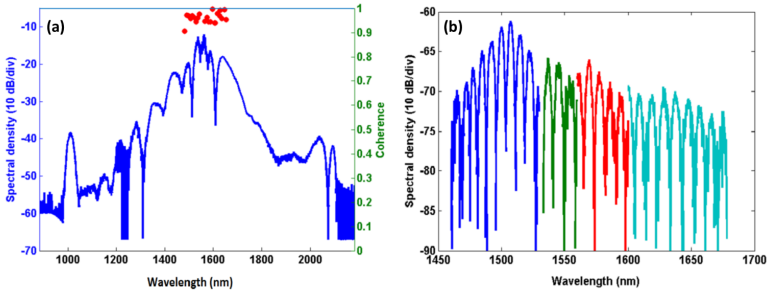

Figure 10 (a) The supercontinuum spectrum pumped by a pulsed laser centered at 1550 nm with a FWHM of 170 fs and an on-chip peak power of 10 W and the coherence measurement across a 200 nm spectral range. (b) The coherence is measured by looking at the fringe visibility of interference between supercontinua generated by two successive pump pulses.

Finally, in Chapter 5, the additional processing steps needed for the integration of these InGaP membrane devices with CMOS-fabricated chips are detailed. Four-wave mixing in InGaP microdisk resonators integrated on top of an SOI chip and coupled to waveguides therein is demonstrated, as shown in Fig. 12 (a)-(d). Similarly, InGaP devices integrated with a SiN chip are also demonstrated. This paves the way towards achieving integrated nonlinear functionalities of both second- and third-order while taking full advantage of the advanced state of the art of photonic circuits fabricated in CMOS foundries.

Conclusions and Perspectives

The work presented in this PhD takes a step towards achieving an integrated nonlinear platform that combines the advantages of a large index contrast, low nonlinear losses and large second-order and third-order nonlinearities. With dispersion engineering and other techniques, phasematching was demonstrated for various processes such as four-wave mixing and second harmonic generation. Combining these advantages, it was also shown that important nonlinear applications such as coherent supercontinuum generation can be implemented with ultra-low energy requirements on the pump, in a robust way and in a compact form factor. This paves the way towards efficient generation and stabilization of on-chip frequency combs. The initial steps needed for the integration of these devices with CMOS-manufactured platforms such as the SOI and SiN platform were also carried out and it was shown that the final integrated nonlinear devices can still deliver the

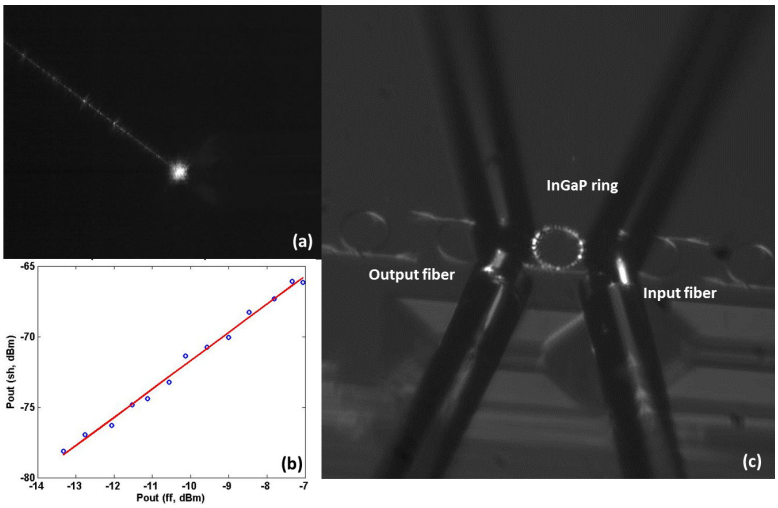

Figure 11 (a) Second harmonic light observed at the output facet of an InGaP waveguide pumped by a CW laser at 1540 nm, (b) The slope of the linear fit of the second harmonic power in dB scale as a function of the fundamental power is 2, showing phasematched operation. (c) Second harmonic power seen in a ring resonator with the CW pump at 1540 nm.

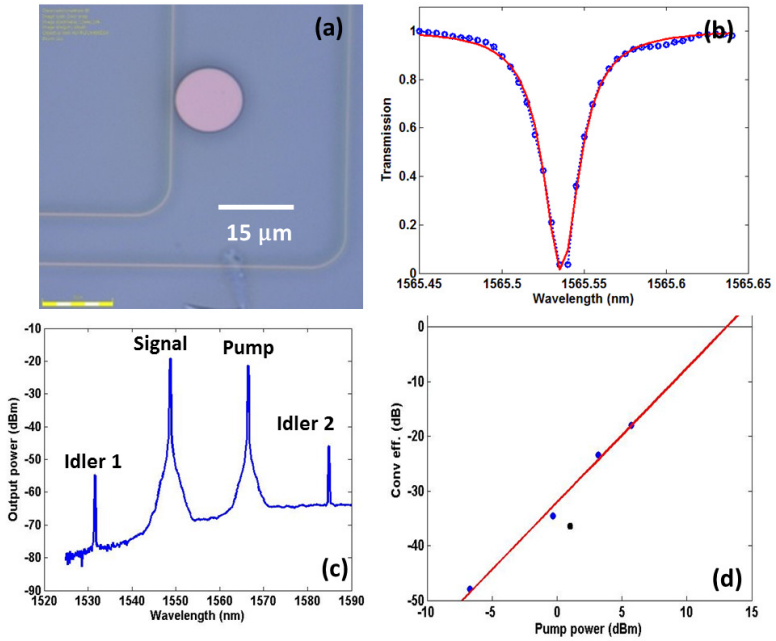

Figure 12 (a) An InGaP microdisk resonator of diameter 15 μm integrated on top of a SOI chip with the silicon waveguide evanescently coupled to it. (b) The resonance at 1565 nm with a loaded quality factor of about 60,000. (c) Four-wave mixing in SOI-coupled InGaP microdisk resonator. (d) The four-wave mixing conversion efficiency as a function of pump power.

expected performance.
Moving forward, more work needs to be done to improve the linear losses of the InGaP membrane waveguides if they are to be used in real-world applications such as wavelength conversion for telecommunications purposes. Other problems that still need solving on the fabrication side are improving the yield of the entire process flow and improving the alignment accuracy of fabricated InGaP devices to the SOI or SiN chip underneath. In particular, the SiN platform is interesting because the large bandgap III-V materials allow access to wavelengths below 1.1 μm, which is not possible in SOI because of silicon's small bandgap. For the second-order nonlinear applications, more phasematching techniques need to be explored and demonstrated to fully exploit the large $\chi^{(2)}$ nonlinearity. For example, for the application of carrier-offset stabilization of frequency combs mentioned above, achieving efficient second harmonic generation would be essential. Further down the road, other III-V materials more suitable for specific applications should also be included in the process flow so that a varied library of materials is available according to the needs of the application. Materials such as GaP [5] have already been used by various groups in different applications, and it would be straightforward to modify the methodologies developed in this work to incorporate these materials into the integrated framework as well, like done already for AlGaAs as reported in [6]. Hence, based off of the work presented in this PhD, there are several avenues down which future work can proceed in order to expand into more applications.

References

[1] B Kuyken, F Leo, S Clemmen, U Dave, R Van Laer, T Ideguchi, H Zhao, X Liu, J Safioui, S Coen, et al. *Nonlinear optical interactions in silicon waveguides* Nanophotonics, 2016.

[2] Utsav D Dave, Sarah Uvin, Bart Kuyken, Shankar Selvaraja, Francois Leo, and Gunther Roelkens *Telecom to mid-infrared spanning supercontinuum generation in hydrogenated amorphous silicon waveguides using a Thulium doped fiber laser pump source* Optics express, 21(26):32032–32039, 2013.

[3] Utsav D Dave, Bart Kuyken, François Leo, Simon-Pierre Gorza, Sylvain Combrie, Alfredo De Rossi, Fabrice Raineri, and Gunther Roelkens *Nonlinear properties of dispersion engineered InGaP photonic wire waveguides in the telecommunication wavelength range* Optics express, 23(4):4650–4657, 2015.

[4] Utsav D Dave, Charles Ciret, Simon-Pierre Gorza, Sylvain Combrie, Alfredo De Rossi, Fabrice Raineri, Gunther Roelkens, and Bart Kuyken *Dispersive-wave-based octave-spanning supercontinuum generation in InGaP membrane waveguides on a silicon substrate* Optics letters, 40(15):3584–3587, 2015.

[5] David P Lake, Matthew Mitchell, Harishankar Jayakumar, Laís Fujii dos Santos, Davor Curic, and Paul E Barclay *Efficient telecom to visible wavelength conversion in doubly resonant gallium phosphide microdisks* Applied Physics Letters, 108(3):031109, 2016.

[6] Minhao Pu, Luisa Ottaviano, Elizaveta Semenova, and Kresten Yvind *Efficient frequency comb generation in AlGaAs-on-insulator* Optica, 3(8):823–826, 2016.

1
INTRODUCTION

"The amount of amplification [by stimulated emission of radiation] which can be produced by such methods is very small under ordinary circumstances and does not appear to be able to compete with other methods. The method may have certain special applications." - Joseph Weber, 1953.

1.1 A brief historical overview of nonlinear optics

One way to look at the influence of any particular field of study is to take a look at the number of Nobel prizes given out in that field over the years. Table 1.1 below shows just a selection of the Nobel prizes awarded to work in the field of optics. As can be seen, there has been a considerable uptick in frequency of those awards in the decades since 1960, with prizes being awarded at a rate of about once per decade, and increasing even more since the end of the last millennium. The single most significant reason for this increase in the pace of breakthroughs is the invention of the laser, for which work the Nobel Prize in Physics was awarded to Townes, Basov and Prokhorov in 1964. Building on a theoretical prediction by Einstein in 1917 of the phenomenon of stimulated emission, as well as on their own earlier work on masers [1], these researchers proposed the basic principles required for building a laser in the early fifties [2, 3]. The first working laser was then demonstrated in 1961 by T. H. Maiman [4]. With this, researchers had for the first time access to a powerful source of coherent radiation which greatly expanded the tool kit for researchers in many different fields leading to many breakthroughs. As a result, various applications and associated technologies have since then garnered their own Nobel prizes such as those awarded 1971 and 1999 for the development of laser based spectroscopy and the study of chemical reactions on femtosecond timescales respectively and most recently in 2014 for the development of efficient light emitting diodes in the blue region of the visible spectrum.

Although optical nonlinearities had previously been observed, including very important nonlinear effects such as the DC Kerr effect [5] and the Pockels effects [6], it was only with the invention of the laser that light intensities large enough for observing nonlinear optical interactions with relative ease became accessible to researchers for the first time. As a result, within a decade or so of the demonstration of the first laser, observations of many fundamentally important nonlinear effects such as second- and third-harmonic generation (SHG and THG) [7, 8], stimulated Raman scattering [9], self-phase modulation [10], supercontinuum generation [11], soliton propagation [12] etc. had all been reported. Maiman's first laser gave an irregularly pulsed output, but within a few years, well-controlled pulsed lasers were developed with the Q-switched laser coming first in 1962 [13] and then the modelocked laser in 1964 [14]. These approaches made possible sources capable of generating output pulses whose peak powers were on the order of thousands to even millions of Watts, which also provided another major boost to nonlinear optical research. Another important advancement was the rise of waveguiding platforms; specifically, the development of low-loss optical fibers. It allowed a substantially increased light-matter interaction by not only providing

Table 1.1: Physics Nobel Prizes related to optics

Year	Names and Prize share	Prize Motivation Statement
1930	C. V. Raman	"for his work on the scattering of light and for the discovery of the effect named after him"
1964	C. H. Townes, N. G. Basov, and A. M. Prokhorov	"for fundamental work in the field of quantum electronics, which has led to the construction of oscillators and amplifiers based on the maser-laser principle"
1981	A. L. Schawlow and N. Bloembergen (1/2)	"for their contribution to the development of laser spectroscopy"
1999	A. H. Zewail (*Chemistry*)	"for his studies of the transition states of chemical reactions using femtosecond spectroscopy"
2000	Z. I. Alferov and H. Kroemer (1/2)	"for developing semiconductor heterostructures used in high-speed- and opto-electronics"
2005	T. W. Hansch and J. L. Hall (1/2)	"for their contributions to the development of laser-based precision spectroscopy, including the optical frequency comb technique
2009	C. K. Kao (1/2)	"for groundbreaking achievements concerning the transmission of light in fibers for optical communication"
2014	I. Akasaki, H. Amano and S. Nakamura	"for the invention of efficient blue light-emitting diodes which has enabled bright and energy-saving white light sources"

tight confinement for the laser light (thereby increasing the light intensity) but also by allowing the accumulation of the nonlinear response over very long interaction lengths, in contrast to bulk nonlinear optics where significant light-matter interaction could only take place near the focal point of a focused laser. In the last couple of decades, integrated optical circuits have come up which further this trend and are covered in the following sections.

1.2 Integrated photonic platforms

The concurrent development of low loss optical fibers and semiconductor lasers in the 1970s (for which Nobel Prizes were awarded in 2009 and 2000 respectively, see Table 1.1 above), led to the field of communications entering a new era. Old copper links were rapidly replaced by fiber-optic cables that were capable of much higher data rates. By the end of the eighties, fiber optic cables were already in widespread use in commercial communication networks spanning thousands of kilometers and connecting people across continents and oceans. These developments along with the simultaneous explosion of computing power following Moore's Law [15] have enabled an extraordinary boom in the information market. It is hard to overstate just how monumental the changes ushered in by these technologies are to the global economy. An indication is given by the moniker *'Information Age'* gener-

ally given to the current epoch of civilization, arguably putting it on the same scale in terms of societal impact as the Industrial Age. Within just the last decade, the massive expansion of internet-based services, especially video streaming services like Youtube and Netflix, has driven the need for the development of ever faster optical communication links. As indicated in Fig. 1.1, due to the rapid increase in the number of devices connected to the internet, by 2020, the total global internet traffic is projected to have reached about 95 times the level of 2005, probably surpassing the zettabyte (which is 1 trillion GB) level sometime this year [16]. On the chip level, in order to keep up with Moore's law and enable this growth, the semiconductor industry has sought to integrate ever smaller and thus faster-switching transistors into the same chip area, thereby increasing the integration density and eventually the computational power. The fabrication techniques developed to accomplish this have advanced to a stage that today billions of transistors can be integrated into a single square cm of chip area. As a result of this, the information capacity of electrical interconnects even for on-chip communications is becoming increasingly insufficient [17, 18]. This has spurred the development of integrated *photonic* platforms seeking to replace the old electrical interconnects with optical ones, similar to how optical fibers replaced the old copper links for long-distance communications and now, increasingly, server interconnects [19]. Mimicking the electronic integrated circuit, these photonic platforms seek to integrate on a small chip all the optical components that would be needed for applications and that one would normally find on an optical table in a laboratory setting. The electronics industry has, over the past few decades, invested billions of dollars towards establishing the manufacturing base for the fabrication of electronic chips using the complementary metal-oxide semiconductor (CMOS) technology. In order to take advantage of this massive industrial infrastructure, the photonics community has devoted a lot of research effort towards developing the silicon-on-insulator (SOI) platform for photonics applications [20]. This is because, just as silicon is the workhorse material for electronics, fortunately, it is also a very good material for photonic applications, as will be discussed in section 1.3. The application potential for a platform that integrates both electronics and photonics in the same platform is enormous, and SOI is a great candidate for achieving this. The typical photonic SOI chip consists of a 220 nm thick light-guiding layer of silicon in which the components of the photonic circuit are fabricated using the CMOS process. Below the light guiding layer is a 2 μm thick silicon dioxide cladding layer (which is also a very good electrical insulator and why it was used in electronics in the first place, explaining the name of the platform). The bottom substrate is silicon. Depending on the needs of the application, various modifications can be made to this layer structure. For example, in order to integrate lasers, detectors etc. onto the same chip, materials besides silicon are needed. In such cases, a variety of techniques are used to integrate these materials with the CMOS-fabricated SOI chips as is

explained in the next section.

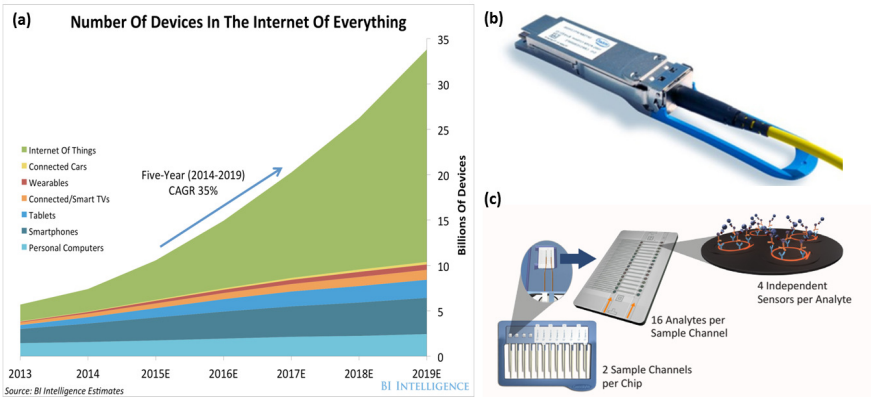

Figure 1.1 (a) Growth in the total number of devices connected to the internet, with the biggest growth in the next few years expected to come from the so-called internet-of-things [16]. (b) Intel's Silicon Photonics offers an optical transceiver at 100 Gbps (image from [21]). (c) The biosensing technology by Genalyte uses functionalized SOI ring resonators and can detect several analytes within just a few minutes (image from [22]).

Such CMOS-compatible photonic platforms offer a way to achieve the increased data rates required for future on-chip interconnects. However, since antiquity, light has been used for more purposes than just communications, such as sensing, diagnostic purposes etc. Hence, these photonic platforms also have the potential to offer advantages for many other application areas such as sensing, machine learning, quantum information, etc. [23–27]. Because CMOS fabrication promises low-cost, high quality and large throughput manufacturing of such chips, there is naturally a lot of interest in exploiting these platforms for all possible applications. While commercial SOI based products for telecommunications purposes are already being provided by established electronics giants such as Intel [21] (see Fig. 1.1(b)) as well as newer ones such as Luxtera [28] and Inphi [29], other applications are also emerging concurrently. Thus we see companies such as Genalyte [22] commercializing SOI ring resonator based biosensors for medical purposes aiming towards the realization of lab-on-chip (LOC) products (see Fig. 1.1(c)). Such LOC systems hold the promise to revolutionize the medical field in every way by providing cheaper, better and faster diagnostic tools and enabling 'personalized' medicine [30, 31].

SOI is not the only integrated photonics platform that has been investigated for such applications. Silicon nitride (SiN) is another material sometimes used instead of silicon, because unlike silicon it has a transparency window that extends

into the visible spectrum, thus allowing for applications that work at those wavelengths. In the SiN platform, the silicon layer is substituted by a deposited silicon nitride layer and the advantage is that the process is still CMOS-compatible. Thus, SiN retains the advantage of scalability for potential low-cost applications [32]. Another prominent material used in commercial photonic platforms is the III-V material Indium Phosphide, championed by companies such as Infinera [33] and Aurrion [34] for telecommunications applications. In conclusion, integrated photonic platforms that provide unique, low-cost solutions for a diverse range of applications are maturing into useful products in the real world even as researchers continue to improve them and induct even more applications into the realm of integrated photonic platforms.

1.3 The silicon-on-insulator platform

Silicon, the material at the heart of the SOI technology, has advantageous optical properties that make it a good choice for implementing several of the functionalities needed in photonic integrated circuits. In the infrared spectral region, it is transparent for wavelengths longer than 1.1 μm which makes it suited for telecommunications applications since fiber optic telecommunications use wavelength bands around 1.31 μm and 1.55 μm. The platform is also transparent in the mid-infrared regime (up to 8 μm for silicon but only up to 3.8 μm for SOI as a whole because of absorption in the silicon dioxide cladding [35]). This is an important wavelength range for sensing and spectroscopic applications since many important molecules have their characteristic rotational-vibrational absorption bands in this wavelength range, and so a lot of work has recently been done in developing integrated platforms for it [36]. However, at present the wavelength range where most of the advancements in photonic integrated circuits have taken place is the aforementioned telecommunications wavelength range because of the enormous market potential. Several basic photonic components needed for such telecommunications applications such as optical fiber couplers, power splitters, mode converters, wavelength multiplexers and demultiplexers, interferometers, resonators etc. have all been demonstrated. Propagation losses below 1 dB/cm have been demonstrated in SOI waveguides fabricated with state-of-the-art lithography techniques used in CMOS foundries [37]. As such, there exists now a rich and ever-expanding library of high-quality components that one could choose from while designing a photonic circuit for any given application.

Another important property of silicon is that it has a large refractive index contrast with its cladding. This large index contrast is important because it allows for tight waveguide bends without incurring radiation loss, thus making it possible to

achieve very compact designs and thus a high density of devices on-chip. Finally, integration of these photonic circuits with electronics could allow for very compact solutions to real world problems; which is something many companies and research groups worldwide are working towards.

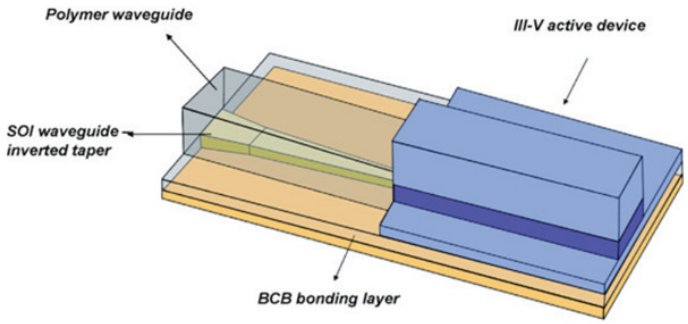

Figure 1.2 A III-V active device integrated on top of an SOI circuit by means of an adhesive bonding layer and optically connected to it using tapers (image from [38]).

Silicon does have certain drawbacks however. The most important one is its indirect bandgap. Hence, in order to incorporate a laser in to the photonic circuit, one has to instead rely on other materials that are more suitable as gain media. This is why several researchers have worked towards heterogeneously integrating active materials such as III-V materials with CMOS-fabricated SOI chips. These III-V materials provide the optical gain medium in which lasers are fabricated. By dividing the job such that all the 'passive' photonic circuit operations such as routing of the light are performed in the SOI chip while the 'active' functionalities such as lasing action are provided by the III-V materials, one can overcome this problem [38]. In one such approach, the III-V material is 'bonded' on top of the SOI chip by means of an intermediate adhesive layer. The silicon and III-V layers are optically connected by means of tapers or other coupling mechanisms allowing light to flow back and forth, as shown in Fig. 1.2. The III-V layer is then post-processed to fabricate the laser and it can be pumped either optically or electrically to provide gain for the lasing action. In this way, lasers can be incorporated in the SOI platform even though silicon itself lacks that functionality. Other active functionalities such as on-chip modulation of the light can also be done by employing III-V materials [39]; or directly in silicon itself by injecting/depleting charge carriers from it which modifies its dispersion properties, thus allowing for modulation of the light [40, 41]. Similarly, the problem of on-chip detection of light can be tackled by germanium detectors. Germanium can be epitaxially grown on silicon, making it possible to have integrated photodetectors with high functionality

and performance [42]. In this way, the possible functionalities of silicon photonic platforms can be greatly extended by using various techniques to integrate other suitable materials, which we will again encounter in the next section in the context of on-chip nonlinear optics.

1.4 On-chip nonlinear optics

As mentioned before, until the development of lasers, nonlinear optics remained largely outside the reach of researchers. This is because under most circumstances, when electromagnetic radiation interacts with a transparent medium, nothing really happens apart from a decrease in its propagation speed. If there are multiple frequencies present in the same medium, they do not interact with or influence one another. This is the principle of superposition. However, when the intensity is strong enough, the nonlinear nature of materials manifests itself. The exact nature of the nonlinearity and how to treat it mathematically depends on the detailed microscopic structure of the material as has been described in several excellent textbooks on the subject [43–45]. In short, the nonlinear response is considered as a small perturbation to the linear polarization induced by the light. Ironically, the first ever demonstration of nonlinear interaction using the ruby laser was so weak that it rendered the second harmonic light generated from the nonlinear crystal as nothing but a barely-visible smudge in the photographic image, causing it to be removed during the publication process in the journal *Physical Review Letters* [7]. This gives an indication of just how weak the optical nonlinearities are in general and why the development of lasers providing intense, coherent radiation was so vital to the development of the field. But this also means that treating the nonlinearity as a perturbation is a valid approach in most cases [43]. Having said that, it is important to realize that despite their weak nature, nonlinear processes can still produce a strong effect under the right conditions. For example, when there is phasematching between the fundamental and its harmonics in optical harmonic generation, significant conversion of the pump power can be achieved in practice [46]. Integrated photonic platforms like those discussed in the previous section provide advantages for achieving large light intensities as well as in arranging the proper phasematching conditions and thus allow for efficient nonlinear processes. These advantages are discussed below along with a short overview of integrated nonlinear optics.

In order to compare the advantages and disadvantages of specific nonlinear platforms, one needs to do it on a case by case basis for each type of nonlinear process because of the large number of considerations that go into deciding whether the nonlinear processes will be efficient. However, a few general notes can still be

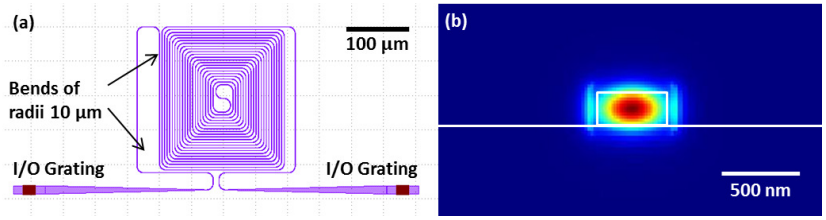

Figure 1.3 (a) A 1 cm long SOI waveguide tightly wound in the form of a spiral occupying an on-chip area of about 0.03 mm^2. The 10 μm bends are made possible by the large index contrast. (b) The mode profile of a typical sub-wavelength SOI waveguide with dimensions 450 nm $\times$ 220 nm showing strong confinement of 1550 nm light due to its large index contrast.

made as discussed below.

1.4.1 Index contrast

As mentioned above, the large index contrast of the SOI platform enables tight bends without radiation loss, allowing for a dense, compact design of photonic circuits, as shown schematically in Fig. 1.3(a). This is obviously desirable for on-chip platforms where chip real estate is valuable. To get an idea of the numbers involved, at 1550 nm - the wavelength used in communications - the refractive index of the oxide cladding is about 1.45 while that of silicon is 3.46. This can be contrasted with the case in standard single mode optical fibers where the index difference between the core and cladding is about 0.005. This gives rise to the large difference between the effective modal areas which are 0.2 μm^2 and 85 μm^2 respectively, representing a 400-fold decrease for the SOI platform in comparison to the fiber. Thus, because of the large index contrast, light can be confined to subwavelength dimensions. This is demonstrated in Fig. 1.3(b) where the mode profile of transverse electric polarized light of 1550 nm wavelength in a typical SOI waveguide of cross-section 450 nm x 220 nm is shown. Thus, in comparison to fibers, for the same power level, much larger intensity levels can be achieved in SOI waveguides which is obviously advantageous for stronger nonlinear interactions. This is one of the advantages of using such high index-contrast integrated platforms.

1.4.2 Waveguide loss

The interaction length between light and the nonlinear medium is important for nonlinear processes because the nonlinear response needs to be built up over contributions from many atoms/molecules given the extremely weak nature of optical

nonlinearities. For example, in Raman scattering (for which the Nobel prize in Physics of 1930 was awarded, see Table 1.1), approximately only 1 out of every million pump photons is converted to the new 'Stokes' frequency [43]. Hence, loss in the waveguide plays an important role the stronger the losses the shorter the waveguide length will be beyond which the nonlinear process becomes too weak because a significant portion of the light was lost. In this case, standard optical fibers with a loss of about 0.2 dB/km offer a much longer interaction length than standard silicon waveguides with losses on the order of 1 dB/cm - a 4 order of magnitude difference, which is obviously significant. For certain nonlinear processes we will encounter in this work, the effective interaction length is defined as $L_{eff} = \frac{1-exp(-\alpha_{lin}L)}{\alpha_{lin}}$ where α_{lin} is the loss coefficient in m^{-1} and L is the physical waveguide length. Thus, a fiber length of 1 km turns in to an interaction length of about 0.98 km, while for SOI, a waveguide length of only 1 cm turns into a an effective length of 0.89 cm. It is clear that the relatively large loss in the SOI platform dramatically shortens the effective interactions length for nonlinear interactions. Fortunately, other factors more than make up for this deficit, as is shown in the next subsection.

1.4.3 Material nonlinearity

The nonlinear response is modeled mathematically by writing the polarization induced by the electric field of the incident radiation as a power series in the field [43]:

$$\begin{aligned} \boldsymbol{P}(t) &= \boldsymbol{P_{lin}}(t) + \boldsymbol{P_{nl}}(t) \\ &= \epsilon_0 \big[\chi^{(1)}\boldsymbol{E}(t) + \chi^{(2)}\boldsymbol{E}(t)\boldsymbol{E}(t) + \chi^{(3)}\boldsymbol{E}(t)\boldsymbol{E}(t)\boldsymbol{E}(t) + ...\big] \end{aligned} \tag{1.1}$$

In the above equation, $\boldsymbol{P}(t)$ is the total induced polarization, ϵ_0 is the permittivity of free space, E(t) is the incident electric field, and $\chi^{(n)}$ is the nth-order susceptibility which is described as a *n*+1 rank tensor. The first term on the right hand side corresponds to the linear susceptibility responsible for the linear refractive index while all the other terms represent the different orders of the nonlinear response of the material. Thus, $\chi^{(2)}$ represents the second-order nonlinearities responsible for all second-order nonlinear interactions, $\chi^{(3)}$ the third-order nonlinearities and so on. The existence, sign and magnitude of these tensor elements depends on various symmetry considerations and the detailed microscopic structure of the medium. They determine the strength of the induced nonlinear response of the medium. Hence, individual tensor components can be compared across different materials when comparing the nonlinearity between different platforms. For example, for the third-order nonlinear process of intensity dependent refractive index,

the relevant susceptibility tensor is $\chi^{(3)}$. In this process, the refractive index felt by light in the medium is no longer independent of its intensity. The Kerr index n_2 determines the amount of index change due to the presence of the light:

$$n = n_0 + n_2 I; \;\; n_2 = \frac{3\chi^{(3)}}{4n_0^2\epsilon_0 c} \tag{1.2}$$

Here, n_0 is the linear refractive index, n_2 is the Kerr index, I is the intensity of light and c is the speed of light in vacuum. At 1550 nm, the Kerr index for silica is $2.7 \times 10^{-20} m^2/W$, while that of silicon is reported to be in the range 4-14 $\times 10^{-18} m^2/W$ i.e. more than two orders of magnitude larger [47]. The combined effects of the nonlinear Kerr index and effective interaction area due to waveguide confinement are generally taken together in the nonlinear parameter γ, defined as:

$$\gamma = \frac{2\pi n_2}{\lambda_0 \, A_{eff}} + i\frac{\alpha_{tpa}}{2 \, A_{eff}} \tag{1.3}$$

Here, A_{eff} is the effective interaction area for the nonlinear process and is roughly equivalent to the modal area mentioned above if the waveguide core material is the nonlinear material (as is usually the case). The second (imaginary) part of the nonlinear parameter describes the nonlinear absorption process of two-photon absorption, which will be discussed in the next section. The real part of γ is what determined the gain available for third-order nonlinear processes such as four-wave mixing, self-phase modulation etc., all of which are investigated in this work. The Re(γ) values across various platforms can thus be compared to get an idea about the combined effect of the effective interaction area as well as the strength of the material nonlinearity. Table 1.2 below shows the typical values for Re(γ) for a few popular on-chip or fiber-based platforms:

Table 1.2: Comparison of Re(γ) values for various platforms

Platform	**Re(γ) [$W^{-1}m^{-1}$]**	**Reference**
Standard optical fiber	0.001	[47]
Highly nonlinear fiber	2	[47]
Silicon-on-insulator	100-1180	[47]
Chalcogenide fiber	10-145	[48, 49]
SiN platform	1	[50]
III-V-on-insulator	475-600	[51, 52]

As can be seen, there is a great range of values available in different platforms. SOI and other integrated platforms form the high end of this range because of the strong confinement as well as large material nonlinearity, resulting in Re(γ) values more than 5 orders of magnitude larger than standard optical fibers. As a result,

SOI and other such integrated platforms can compete with and even significantly outperform fiber based platforms in terms of nonlinear processes even though, in general, they suffer from a larger loss as mentioned in the previous subsection. Thus, nonlinear processes that take kilometers of interaction length in fibers can be accomplished in such platforms in mm to cm long waveguides. Also, because the high index contrast enables tight bends in these waveguides, these waveguides can be fitted inside a very small area on the chip, as shown in Fig. 1.3(a). Thus, extremely compact designs for nonlinear applications are made possible in integrated platforms like SOI because of the compounded advantages of a large index contrast as well as large nonlinearity.

1.4.4 Phase matching and dispersion engineering

The final general consideration that is important for achieving efficient nonlinear processes is the condition known as phase matching. Phase matching is found to be an important condition that needs to be satisfied in a wide variety of nonlinear processes across all platforms. Stated in the most general way, this condition is nothing but the requirement that any newly generated frequencies be in phase with the already existing light at that frequency. It is easy to see that if this condition is not satisfied, then destructive interference will occur between the light generated during the nonlinear process and the already existing light at that frequency (which was either previously generated during the nonlinear process at some prior time or was externally supplied). Hence, the intensity at that frequency will decrease. One can look at this phenomenon as the nonlinear process going in reverse when the phase lag has reached , converting back the new frequency to the old ones. However, if there is phase matching (i.e., the phase lag remains zero), then the newly generated light coherently adds up with the existing light at that frequency, increasing in intensity. In the quantum view, phase matching can be seen as a form of the law of conservation of momentum (while energy conservation is ensured by realizing that the sum of the 'generating frequencies' is equal to the sum of the 'generated frequencies') [43].

Dispersion refers to the change in the refractive index of the medium as a function of frequency. Since the phase evolution of any frequency in a medium is determined by the refractive index felt by that frequency, phase matching conditions generally reduce to conditions on the refractive index (or its derivatives) at those frequencies. Thus, for the numerous processes that require phase matching, it is important to have control over the dispersion properties of the nonlinear platform. As we saw in the previous section, the refractive index experienced by light also depends on its intensity. Thus, both the linear (dispersive) and nonlinear properties can have a role to play in achieving phase matching, especially when talking about

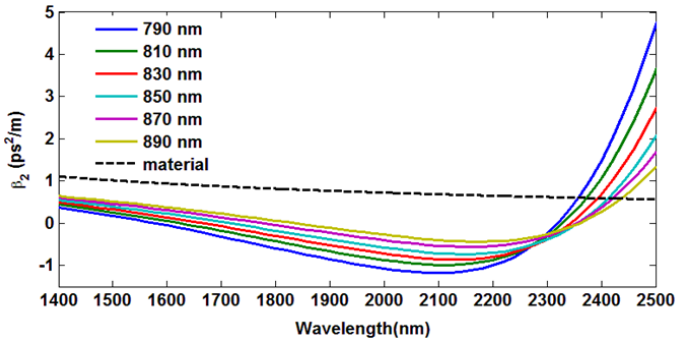

Figure 1.4 The geometric modification of dispersive properties is demonstrated by variation of waveguide width in the amorphous silicon platform. The parameter β_2 is the second order derivative of the propagation constant β with respect to frequency: $\beta_2 = d^2\beta/d\omega^2$. The material dispersion (black dashed line) is markedly different from the waveguide dispersion (solid colored lines) even changing in sign over a certain wavelength range. Waveguides with different widths (in legend) also exhibit different dispersive properties.

third-order processes. One can thus take advantage of the nonlinear contribution to dispersion to achieve phase matching. This concept is exploited for the experiments discussed in Chapters 2 and 4. However, in most cases, the dominant contribution to dispersion comes from the linear properties of the platform, and clever ways of finding phasematching have to be found for most nonlinear processes. In bulk nonlinear optics for example, one common method of achieving phase matching is to use the birefringent nature of the nonlinear medium to match the refractive index at the fundamental and its nonlinearly generated harmonic frequencies. In waveguiding platforms such as fibers and SOI, dispersion is a function both of the material properties as well as its geometry. The confining nature of these platforms imposes certain conditions on the propagation of light, which results in the light feeling an 'effective' index instead of purely the material refractive index. And as one changes the geometric properties, this effective index will also change. As a result, the geometry of the waveguiding platform has an impact on its dispersive properties, as shown in Fig. 1.4. Hence, one can design the platform to have the overall dispersive properties that are favorable for a particular nonlinear process (and even suppress unwanted nonlinear processes). This phenomenon is exploited in many publications as well as throughout this work for achieving phase matched operation of nonlinear processes, as demonstrated in chapters 3 and 4.

In conclusion, integrated photonic platforms offer several advantages for the implementation of nonlinear functionalities because of the general reasons mentioned above. Integration of course allows one to have both the linear and nonlinear optical elements on the same chip and this greatly improves the scope of applications

where these functionalities may be used. For example, III-V lasers integrated on top of an SOI chip could be used as the pump source for performing nonlinear operations to generate new frequencies which could then be routed to the desired optical port using filters and waveguides in the SOI photonic circuit and eventually detected by on-chip Ge photodiodes. In this way, one can integrate an experimental setup that would normally take up an entire optical table onto a single chip the size of a coin. Thus, nonlinear optical interactions are a valuable addition to the design toolkit of integrated photonic circuits.

Exploiting these advantages, several groups around the world have demonstrated a wide variety of on-chip nonlinear functionalities [46]. As mentioned above, the third-order nonlinearity in silicon and similar integrated platforms is found to be strong. As a result, a lot of attention has been paid to applications based on third-order nonlinear processes. One such application is supercontinuum generation (SCG) wherein a broadband spectrum (i.e. a 'continuum' of frequencies) is generated. It has applications in spectroscopy, optical coherence tomography, wavelength division multiplexing for telecommunications etc. and is also one of the main subjects of investigation in this work, and will be discussed in chapters 2 and 4. SCG has been demonstrated by a number of groups in the SOI platform using both crystalline [53–59] and amorphous [60–62] forms of silicon. SCG has also been demonstrated in other platforms such as SiN [50, 63–65], chalcogenide fibers and planar waveguides [48, 49], AlGaAs- and InGaP-on-insulator waveguides [52, 66] etc. In several of these demonstrations the supercontinuum spectra extend into the mid-infrared regime [56, 57, 60–62, 65, 66], which is important for spectroscopy as mentioned before. Additionally, it has also been shown both theoretically and experimentally in some of these demonstrations that the supercontinuum can be generated coherently; which means that the phase profile across the generated spectrum is not random which in turn implies that the spectrum is not actually continuous but consists of equidistant lines at specific frequencies. Because of this property, such supercontinua are also referred to as 'frequency combs'. Another important consideration is that several of these demonstrations have achieved octave-spanning spectra. This means that the frequencies within the spectrum span at least one octave i.e. one of the frequencies is at least the double of another frequency present within the bandwidth of the spectrum. Both of these features are important for applications concerning frequency comb generation and its frequency stabilization. In fact, the Nobel Prize for Physics in 2005 was awarded partly in connection to the work done for developing the techniques for the stabilization of such frequency combs (see Table 1.1). Thus, it can be seen that these demonstrations are important for a wide range of applications. Other third-order nonlinear processes such as four-wave mixing and self-phase modulation have also been shown in these platforms and are discussed in Chapter

3. Similarly, third-harmonic generation has been demonstrated in the SOI platform [67]. Second-order nonlinearities have also been demonstrated in several of the aforementioned platforms. Specifically, second-harmonic generation has been shown in the AlN [46], GaAs [68], GaP [69] and other such platforms that possess strong second-order nonlinearities. All these demonstrations cumulatively show that these nonlinear integrated platforms can indeed be used in wavelength ranges extending from the visible to mid-infrared.

Of course, the diversity of both nonlinear optical processes as well as nonlinear platforms is much greater than just those listed in Table 1.2 or mentioned above. For instance, photonic crystals which work on the photonic analog of the bandgap effect [70] have been investigated since the 1970s, both in fibers [70, 71] and more recently in integrated platforms [72]. Other novel approaches include integrating unique materials such as graphene and other 2D materials [73–76], plasmonics [77–80], metamaterials [80–83] etc. into these platforms to exploit their exotic properties for nonlinear applications. Thus, there is a rich variety of materials and techniques available for whichever nonlinear application one is looking to implement on a chip.

1.5 The need for looking beyond silicon

As mentioned before, silicon has a lot of desirable properties that make it a good choice for implementing photonic circuits. We have also seen that in terms of third-order nonlinearity, silicon has also been heavily investigated and some impressive results have been reported, mainly by taking advantage of the large Re(γ) value of SOI. However, going back to Eq. 1.3, it should be realized that the imaginary part of γ poses a problem. Just like in the case of the linear refractive index whose imaginary part is responsible for absorption loss the imaginary part of γ is responsible for third-order nonlinear loss processes. That is, there also exists an intensity dependent loss which is called two-photon absorption (TPA). The name comes from the fact that in contrast to linear absorption where a single photon of light gets absorbed, in this case, two photons simultaneously get absorbed. In case of silicon for example, light of wavelength larger than 1.1 μm cannot be directly absorbed since the photons do not have enough energy to promote electrons from the valence band to the conduction band. However, two-photons together might have enough energy to do so, and this is exactly what happens, as shown in Fig. 1.5(a). Being a third-order nonlinear process, this loss is intensity dependent and so will increase with increasing intensity. Thus, while the available nonlinear gain increases with intensity, so does the nonlinear loss. Additionally, there is another source of nonlinear loss that must be considered. Once electrons

are promoted to the conduction band, they are free to absorb light on their own. In fact, this 'free-carrier' absorption (FCA) is proportional to the square of the intensity, unlike TPA, which is only linearly proportional to the intensity. Thus, as the intensity is increased, eventually FCA becomes the dominant loss term and completely overwhelms any nonlinear gain. Thus, to avoid these loss mechanisms, either these carriers must not stay very long in the waveguide or one must work with frequencies corresponding to photon energies less than half the bandgap of silicon to avoid their generation by TPA in the first place. Both these approaches have been used for achieving efficient third-order nonlinear interactions in silicon. The former approach has been employed in [84, 85] while the latter one in [86]. However, the former approach needs extra fabrication steps, which is not always desirable, and the latter one necessitates working at wavelengths longer than 2.2 μm, which is not always possible. Hence, nonlinear losses in silicon pose a problem for the efficient implementation of third-order processes. Another approach is to use amorphous silicon instead of crystalline silicon, which is used in most applications. Depending on the fabrication methodology, amorphous silicon can have a bandgap that is large enough to suppress TPA for the telecommunications wavelengths [87, 88]. This would certainly alleviate the problem of the nonlinear loss.

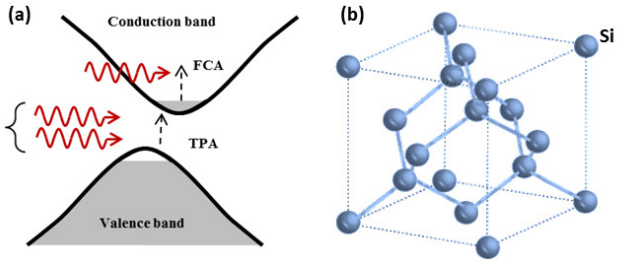

Figure 1.5 (a) Two-photon absorption causes electrons to be promoted to the conduction band, where they cause more loss via free-carrier absorption. (b) The crystal structure of Si is centrosymmetric, meaning that there can be no second-order nonlinearity.

The other major problem with silicon is its lack of second-order nonlinearity. All materials possess third order (and all other odd numbered) nonlinearities, but only materials whose crystal structure does not have inversion symmetry exhibit second (and the other even numbered) nonlinearities. The reason for this can be seen from Eq. 1.1 easily. Considering only even-numbered nonlinearities, if one flips the sign of the electric field, the sign of the induced polarization doesn't change because it is proportional to the electric field raised to an even power. However, since the material possesses inversion symmetry, by definition, when flipping the sign of the electric field, the sign of the polarization must also flip. Thus, we end

up with $\chi^{(2)} = -\chi^{(2)}$ and so the second order (and all even ordered susceptibility terms) must be identically zero. Silicon belongs to a class of crystals that do possess inversion symmetry as shown in Fig. 1.5(b) and hence does not exhibit these even ordered nonlinearities, which as we have seen in the last section are important for several applications.

Both these reasons - the fact that silicon suffers from large nonlinear losses in the important telecommunications wavelength range and that it has no second-order nonlinearity - mean that it is deficient for several nonlinear applications. Thus, as good as it has been demonstrated to be for nonlinear applications, there is a real need to look beyond silicon. This is the main reason for the work taken up in this PhD, which is outlined in the next section.

1.6 An overview of the work presented in this thesis

The approach of using amorphous silicon was further investigated as part of this work. By taking advantage of the reduced nonlinear loss and with proper dispersion engineering, SCG in amorphous silicon waveguides was demonstrated and is discussed in Chapter 2. However, there was still a need to incorporate second-order nonlinearities into the SOI platform, ideally, without needing to sacrifice any of its advantages.

It so happens that several III-V materials like $In_{0.5}Ga_{0.5}P$ and $Al_xGa_{1-x}As$ (with $x > 0.17$) also possess the same advantageous nonlinear properties as silicon, namely, large refractive index as well as a strong third-order nonlinearity. But additionally, they also have bandgaps large enough to avoid TPA in the telecommunications wavelength range. Thus, the penalty of large nonlinear losses can be avoided in this wavelength range. On top of this, since these materials also do not have inversion symmetry, they possess a second-order nonlinearity (which is known to be large enough for practical applications [68, 69]). Thus, III-V materials are ideally placed to eliminate the main problems in doing nonlinear optics with silicon. As we have seen previously, in order to incorporate active functionality into the SOI platform, methodologies have already been developed to integrate III-V materials into the platform. Hence, it should be possible to leverage these techniques for nonlinear applications as well. This is the main motivation for this work.

The III-V nonlinear material used in this work is InGaP. As mentioned above, it has all the properties needed to implement efficient second- and third-order nonlinear processes. Chapter 3 describes the process flow for the fabrication of devices in a thin membrane of InGaP bonded on top of a silicon substrate. This fabrica-

tion ensures that the InGaP membrane is clad either by a low index adhesive or silica in order to maintain a large index contrast. Using the optimized processing flow, simple components such as gratings, waveguides and ring resonators were fabricated which were then used to characterize the linear and nonlinear properties of the platform, as is also discussed in Chapter 3. It is demonstrated that the platform is indeed suitable for the implementation of both second- and third-order nonlinear applications. This point is further exemplified by the demonstration of an octave-spanning, coherence-preserving supercontinuum in these InGaP waveguides which is discussed in Chapter 4. Following that, in Chapter 5, the processing steps required for the integration of the InGaP nonlinear devices with SOI and SiN photonic circuits is discussed and some preliminary results are shown. Finally, Chapter 6 provides a brief overview of the future scope for this work and other perspectives related to this work in the overall context of integrated nonlinear optics.

1.7 List of Publications

1.7.1 List of International Journal Publications

[1] A. Rahim, E.M.P. Ryckeboer, A. Subramanian, S. Clemmen, B. Kuyken, A. Raza, A. Hermans, M. Muneeb, S. Dhoore, Y. Li, **Utsav D. Dave**, P. Bienstman, N. Le Thomas, G. Roelkens, D. Van Thourhout, Helin, Philiplle, Severi, Simone, Rottenberg, Xavier, R. Baets, *Expanding the Silicon Photonics Portfolio with Silicon Nitride Photonic Integrated Circuits*, (invited), Journal of Lightwave Technology, 99, 1 (2016).

[2] B. Kuyken, F. Leo, S. Clemmen, **Utsav D. Dave**, R. Van Laer, T. Ideguchi, H. Zhao, X. Liu, J. Safioui, S. Coen, S.P. Gorza, S. Selvaraja, S. Massar, R.M. Osgood Jr, P. Verheyen, J. Van Campenhout, R. Baets, W.M.J. Green, G. Roelkens, *Nonlinear optical interactions in silicon waveguides*, Journal of nanophotonics (invited), (2016).

[3] G. Roelkens, A. Abbasi, P. Cardile, **Utsav D. Dave**, A. De Groote, Y. De Koninck, S. Dhoore, X. Fu, A. Gassenq, N. Hattasan, Q. Huang, S. Kumari, S. Keyvaninia, B. Kuyken, L. Li, P. Mechet, M. Muneeb, D. Sanchez, H. Shao, T. Spuesens, A. Subramanian, S. Uvin, M. Tassaert, K. Van Gasse, J. Verbist, R. Wang, Z. Wang, J. Van Campenhout, X. Yin, J. Bauwelinck, G. Morthier, R. Baets, D. Van Thourhout, *III-V-on-silicon photonic devices for optical communication and sensing, Photonics* (invited), 2(3), 969-1004 (2015).

[4] **Utsav D. Dave**, C. Ciret, S.-P. Gorza, S. Combrie, A. De Rossi, F. Raineri, G.

Roelkens, B. Kuyken, *Dispersive wave based octave spanning super continuum generation in InGaP membrane waveguides on a silicon substrate*, Optics Letters, 40(15), 3584 (2015).

[5] A. Subramanian, E.M.P. Ryckeboer, A. Dhakal, F. Peyskens, A. Malik, B. Kuyken, H. Zhao, S. Pathak, A. Ruocco, A. De Groote, P.C. Wuytens, D. Martens, F. Leo, W. Xie, **Utsav D. Dave**, M. Muneeb, Pol Van Dorpe, Joris Van Campenhout, W. Bogaerts, P. Bienstman, N. Le Thomas, D. Van Thourhout, Zeger Hens, G. Roelkens, R. Baets, *Silicon and silicon nitride photonic circuits for spectroscopic sensing on-a-chip*, Photonics Research (invited), 5(3), B47 (2015).

[6] **Utsav D. Dave**, B. Kuyken, F. Leo, S.P. Gorza, S. Combrie, A. De Rossi, F. Raineri, G. Roelkens, *Nonlinear properties of dispersion engineered InGaP photonic wire waveguides in the telecommunication wavelength range*, Optics Express, 23(4), 4650 (2015).

[7] F. Leo, S-P. Gorza, J.Safioui, P. Kockaert, S. Coen, **Utsav D. Dave**, B. Kuyken, G. Roelkens, *Dispersive wave emission and supercontinuum generation in a silicon wire waveguide pumped around the 1550 nm telecommunication wavelength*, Optics letters, 39(12), 3623 (2014).

[8] G. Roelkens, **Utsav D. Dave**, A. Gassenq, N. Hattasan, C. Hu, B. Kuyken, F. Leo, A. Malik, M. Muneeb, E.M.P. Ryckeboer, D. Sanchez, S. Uvin, R. Wang, Z. Hens, R. Baets, Y. Shimura, F. Gencarelli, B. Vincent, R. Loo, J. Van Campenhout, L. Cerutti, J.B. Rodriguez, E. Tournie, X. Chen, M. Nedeljkovic, *Silicon-based photonic integration beyond the telecommunication wavelength range*, IEEE Journal of Selected Topics in Quantum Electronics (invited), 20(4), 8201511 (2014).

[9] F. Leo, **Utsav D. Dave**, S. Keyvaninia, B. Kuyken, G. Roelkens, *Measurement and tuning of the chromatic dispersion of a silicon photonic wire around the half band gap spectral region*, Optics Letters, 39(3), 711-714 (2014).

[10] **Utsav D. Dave**, S. Uvin, B. Kuyken, S. Selvaraja, F. Leo, G. Roelkens, *Telecom to mid-infrared spanning supercontinuum generation in hydrogenated amorphous silicon waveguides using a Thulium doped fiber laser pump source*, Optics Express, 21(26), 32032-32039 (2013).

[11] G. Roelkens, **Utsav D. Dave**, A. Gassenq, N. Hattasan, C. Hu, B. Kuyken, F. Leo, A. Malik, M. Muneeb, E.M.P. Ryckeboer, S. Uvin, Z. Hens, R. Baets, *Silicon-based heterogeneous photonic integrated circuits for the mid-infrared*, Optical Materials Express (invited), 3(9), 1523-1536 (2013).

1.7.2 List of International Conference Publications

[1] G. Roelkens, **Utsav D. Dave**, S. Keyvaninia, F. Leo, S. Uvin, K. Van Gasse, Z. Wang, S. Latkowski, E. Bente, B. Kuyken, *Frequency comb generation in III-V-on-silicon photonic integrated circuits*, Advanced Photonics Congress - IPR (invited), Canada, IM2A.5 (2016).

[2] G. Roelkens, A. Abbasi, S. Keyvaninia, S. Uvin, K. Van Gasse, Z. Wang, **Utsav D. Dave**, B. Kuyken, G. Morthier, D. Van Thourhout, *III-V-on-silicon photonic integrated circuits for communication and sensing applications*, 28th IEEE Photonics Conference (IPC 2015) (invited), United States, 593-594 (2015).

[3] **Utsav D. Dave**, B. Kuyken, Sylvain Combrie, Alfredo De Rossi, Fabrice Raineri, G. Roelkens, *Octave spanning supercontinuum generation in InGaP waveguides on a silicon substrate at 1550 nm*, Integrated Photonics Research, Silicon and Nano Photonics (IPR 2015), United States, IM4B.5 (2015).

[4] G. Roelkens, **Utsav D. Dave**, A. Gassenq, N. Hattasan, C. Hu, B. Kuyken, F. Leo, A. Malik, M. Muneeb, E.M.P. Ryckeboer, D. Sanchez, S. Uvin, R. Wang, Z. Hens, R. Baets, Y. Shimura, F. Gencarelli, B. Vincent, R. Loo, J. Van Campenhout, L. Cerutti, J.B. Rodriguez, E. Tournie, X. Chen, M. Nedeljkovic, G. Mashanovich, L. shen, N. Healy, A. Peacock, X. Liu, R. Osgood, W.M.J. Green, *Long-wavelength silicon photonic integrated circuits*, 11th International Conference on Group IV Photonics (GFP) (invited), France, 23-24 (2014).

[5] F. Leo, S.P. Gorza, J. Safioui, P. Kockaert, S. Coen, **Utsav D. Dave**, B. Kuyken, G. Roelkens, *Femtosecond supercontinuum generation in a silicon wire waveguide at telecom wavelengths*, CLEO-QELS, United States, JTu4A.16 (2014).

[6] G. Roelkens, **Utsav D. Dave**, A. Gassenq, N. Hattasan, C. Hu, B. Kuyken, F. Leo, A. Malik, M. Muneeb, E.M.P. Ryckeboer, S. Uvin, Z. Hens, R. Baets, Y. Shimura, F. Gencarelli, B. Vincent, R. Loo, J. Van Campenhout, L. Cerutti, J. Rodriguez, E. Tournie, X. Chen, M. Nedeljkovic, G.Z. Mashanovich, L. Shen, N. Healy, A.C. Peacock, X. Liu, R. M. Osgood, W. Green, *Mid-IR heterogeneous silicon photonics*, Photonics West 2014 (invited), 899316, (2013).

[7] S. Uvin, **Utsav D. Dave**, B. Kuyken, S. Selvaraja, F. Leo, G. Roelkens, *Mid-infrared to telecom-band stable supercontinuum generation in hydrogenated amorphous silicon waveguides*, IEEE Photonics Conference 2013 (IPC), United States,

WB2.3 (2013).

References

[1] James P Gordon, Herbert J Zeiger, and Charles H Townes *Molecular Microwave Oscillator and New Hyperfine Structure in the Microwave Spectrum of NH3* Physical Review, 95(1):282, 1954.

[2] Joseph Weber *Amplification of microwave radiation by substances not in thermal equilibrium* Transactions of the IRE Professional Group on Electron Devices, (3):1–4, 1953.

[3] NG Basov and AM Prokhorov *Application of molecular beams for radiospectroscopic investigation of molecular rotational spectra* Zh. Eksp. Teor. Fiz., 27(4):431–438, 1954.

[4] T. H. Maiman *Stimulated Optical Radiation in Ruby* Nature, 187(4736):493–494, 1960.

[5] John Kerr *XL. A new relation between electricity and light: Dielectrified media birefringent* The London, Edinburgh, and Dublin Philosophical Magazine and Journal of Science, 50(332):337–348, 1875.

[6] F. Pockels *On the Effect of an Electrostatic Field on the. Behavior of Piezoelectric Crystals* Abh. Gott., 39:1–7, 1894.

[7] PA Franken, Alan E Hill, CW Peters, and G Weinreich *Generation of optical harmonics* Physical Review Letters, 7(4):118, 1961.

[8] RW Terhune, PD Maker, and CM Savage *Optical harmonic generation in calcite* Physical Review Letters, 8(10):404, 1962.

[9] EJ Woodbury and WK Ng *Ruby laser operation in near IR*, 1962.

[10] RR Alfano and SL Shapiro *Observation of self-phase modulation and small-scale filaments in crystals and glasses* Physical Review Letters, 24(11):592, 1970.

[11] R. R. Alfano and S. L. Shapiro *Emission in the Region 4000 to 7000* Å *Via Four-Photon Coupling in Glass* Phys. Rev. Lett., 24:584–587, Mar 1970.

[12] Akira Hasegawa and Frederick Tappert *Transmission of stationary nonlinear optical pulses in dispersive dielectric fibers. I. Anomalous dispersion* Applied Physics Letters, 23(3):142–144, 1973.

[13] RW Hellwarth *Advances in quantum electronics*, 1961.

[14] LE Hargrove, Richard L Fork, and MA Pollack *Locking of He-Ne laser modes induced by synchronous intracavity modulation* Applied Physics Letters, 5(1):4–5, 1964.

[15] Gordon E Moore *Cramming more components onto integrated circuits, Reprinted from Electronics, volume 38, number 8, April 19, 1965, pp. 114 ff.* IEEE Solid-State Circuits Newsletter, 3(20):33–35, 2006.

[16] *Cisco white paper* http://www.cisco.com/c/en/us/solutions/collateral/service-provider/visual-networking-index-vni/complete-white-paper-c11-481360.html.

[17] David AB Miller *Rationale and challenges for optical interconnects to electronic chips* Proceedings of the IEEE, 88(6):728–749, 2000.

[18] David AB Miller *Low-Energy Optoelectronics for Interconnects* In Frontiers in Optics, pages FTu4E–1. Optical Society of America, 2013.

[19] Alan F Benner, Michael Ignatowski, Jeffrey A Kash, Daniel M Kuchta, and Mark B Ritter *Exploitation of optical interconnects in future server architectures* IBM Journal of Research and Development, 49(4.5):755–775, 2005.

[20] Graham T Reed *Silicon Photonics: the state of the art* John Wiley & Sons, 2008.

[21] *Intel website* http://www.intel.com/content/www/us/en/architecture-and-technology/silicon-photonics/silicon-photonics-overview.html.

[22] *Genalyte website* http://www.genalyte.com/.

[23] Katrien De Vos, Irene Bartolozzi, Etienne Schacht, Peter Bienstman, and Roel Baets *Silicon-on-Insulator microring resonator for sensitive and label-free biosensing* Optics express, 15(12):7610–7615, 2007.

[24] Z Li, Y Chen, X Li, TI Kamins, K Nauka, and R Stanley Williams *Sequence-specific label-free DNA sensors based on silicon nanowires* Nano Letters, 4(2):245–247, 2004.

[25] Michiel Hermans and Thomas Van Vaerenbergh *Towards Trainable Media: Using Waves for Neural Network-Style Training* arXiv preprint arXiv:1510.03776, 2015.

[26] Joshua W Silverstone, Damien Bonneau, Kazuya Ohira, Nob Suzuki, Haruhiko Yoshida, Norio Iizuka, Mizunori Ezaki, Chandra M Natarajan, Michael G Tanner, Robert H Hadfield, et al. *On-chip quantum interference between silicon photon-pair sources* Nature Photonics, 8(2):104–108, 2014.

[27] Alberto Politi, Jonathan CF Matthews, and Jeremy L O'brien *Shors quantum factoring algorithm on a photonic chip* Science, 325(5945):1221–1221, 2009.

[28] *Luxtera website* http://12.162.78.22:8080/luxtera/technology.

[29] *Inphi website* https://www.inphi.com/.

[30] M-Carmen Estevez, Mar Alvarez, and Laura M Lechuga *Integrated optical devices for lab-on-a-chip biosensing applications* Laser & Photonics Reviews, 6(4):463–487, 2012.

[31] Adrián Fernández Gavela, Daniel Grajales García, Jhonattan C Ramirez, and Laura M Lechuga *Last Advances in Silicon-Based Optical Biosensors* Sensors, 16(3):285, 2016.

[32] A. Rahim, E. Ryckeboer, A. Subramanian, S. Clemmen, b. kuyken, A. Dhakal, A. Raza, A. Hermans, M. Muneeb, S. Dhoore, Y. Li, U. Dave, P. Bienstman, N. LeThomas, G. Roelkens, D. Van Thourhout, X. Rottenberg, P. Helin, S. Severi, and R. Baets *Expanding the Silicon Photonics Portfolio with Silicon Nitride Photonic Integrated Circuits* Journal of Lightwave Technology, PP(99):1–1, 2016.

[33] *Infinera website* https://www.infinera.com/.

[34] *Aurrion website* http://forums.juniper.net/t5/The-New-Network/Welcome-Aurrion-to-Juniper-Networks/ba-p/295183.

[35] Richard Soref *Mid-infrared photonics in silicon and germanium* Nature Photonics, 4(8):495–497, 2010.

[36] Ananth Z Subramanian, Eva Ryckeboer, Ashim Dhakal, Frédéric Peyskens, Aditya Malik, Bart Kuyken, Haolan Zhao, Shibnath Pathak, Alfonso Ruocco, Andreas De Groote, et al. *Silicon and silicon nitride photonic circuits for spectroscopic sensing on-a-chip [Invited]* Photonics Research, 3(5):B47–B59, 2015.

[37] Guoliang Li, Jin Yao, Hiren Thacker, Attila Mekis, Xuezhe Zheng, Ivan Shubin, Ying Luo, Jin-Hyoung Lee, Kannan Raj, John E Cunningham, et al. *Ultralow-loss, high-density SOI optical waveguide routing for macrochip interconnects* Optics express, 20(11):12035–12039, 2012.

[38] Günther Roelkens, Liu Liu, Di Liang, Richard Jones, Alexander Fang, Brian Koch, and John Bowers *III-V/silicon photonics for on-chip and intra-chip optical interconnects* Laser & Photonics Reviews, 4(6):751–779, 2010.

[39] Qiangsheng Huang, Yingchen Wu, Keqi Ma, Jianhao Zhang, Weiqiang Xie, Xin Fu, Yaocheng Shi, Kaixuan Chen, Jian-Jun He, Dries Van Thourhout, et al. *Low driving voltage band-filling-based III-V-on-silicon electroabsorption modulator* Applied Physics Letters, 108(14):141104, 2016.

[40] Jun Li, Guoliang Li, Xuezhe Zheng, Kannan Raj, Ashok V Krishnamoorthy, and James F Buckwalter *A 25-Gb/s monolithic optical transmitter with micro-ring modulator in 130-nm SoI CMOS* IEEE Photonics Technology Letters, 25(19):1901–1903, 2013.

[41] Graham T Reed, G Mashanovich, FY Gardes, and DJ Thomson *Silicon optical modulators* Nature photonics, 4(8):518–526, 2010.

[42] Jurgen Michel, Jifeng Liu, and Lionel C Kimerling *High-performance Ge-on-Si photodetectors* Nature Photonics, 4(8):527–534, 2010.

[43] Robert W Boyd *Nonlinear optics* Academic press, 2003.

[44] Govind P Agrawal *Nonlinear fiber optics* Academic press, 2007.

[45] Geoffrey New *Introduction to nonlinear optics* Cambridge University Press, 2011.

[46] Xiang Guo, Chang-Ling Zou, and Hong X Tang *Second-harmonic generation in aluminum nitride microrings with 2500%/W conversion efficiency* Optica, 3(10):1126–1131, 2016.

[47] C Koos, L Jacome, C Poulton, J Leuthold, and W Freude *Nonlinear silicon-on-insulator waveguides for all-optical signal processing* Optics Express, 15(10):5976–5990, 2007.

[48] Michael RE Lamont, Barry Luther-Davies, Duk-Yong Choi, Steve Madden, and Benjamin J Eggleton *Supercontinuum generation in dispersion engineered highly nonlinear (γ= 10/W/m) As2S3 chalcogenide planar waveguide* Optics Express, 16(19):14938–14944, 2008.

[49] Dong-Il Yeom, Eric C Mägi, Michael RE Lamont, Michaël AF Roelens, Libin Fu, and Benjamin J Eggleton *Low-threshold supercontinuum generation in highly nonlinear chalcogenide nanowires* Optics letters, 33(7):660–662, 2008.

[50] Haolan Zhao, Bart Kuyken, Stéphane Clemmen, François Leo, Ananth Subramanian, Ashim Dhakal, Philippe Helin, Simone Severi, Edouard Brainis, Gunther Roelkens, et al. *Visible-to-near-infrared octave spanning supercontinuum generation in a silicon nitride waveguide* Optics letters, 40(10):2177–2180, 2015.

[51] Utsav D Dave, Bart Kuyken, François Leo, Simon-Pierre Gorza, Sylvain Combrie, Alfredo De Rossi, Fabrice Raineri, and Gunther Roelkens *Nonlinear properties of dispersion engineered InGaP photonic wire waveguides in the telecommunication wavelength range* Optics express, 23(4):4650–4657, 2015.

[52] Minhao Pu, Luisa Ottaviano, Elizaveta Semenova, and Kresten Yvind *Efficient frequency comb generation in AlGaAs-on-insulator* Optica, 3(8):823–826, 2016.

[53] I-Wei Hsieh, Xiaogang Chen, Xiaoping Liu, Jerry I Dadap, Nicolae C Panoiu, Cheng-Yun Chou, Fengnian Xia, William M Green, Yurii A Vlasov, and Richard M Osgood *Supercontinuum generation in silicon photonic wires* Optics express, 15(23):15242–15249, 2007.

[54] Lianghong Yin, Qiang Lin, and Govind P Agrawal *Soliton fission and supercontinuum generation in silicon waveguides* Optics letters, 32(4):391–393, 2007.

[55] François Leo, Simon-Pierre Gorza, Jassem Safioui, Pascal Kockaert, Stéphane Coen, Utsav Dave, Bart Kuyken, and Gunther Roelkens *Dispersive wave emission and supercontinuum generation in a silicon wire waveguide pumped around the 1550 nm telecommunication wavelength* Optics letters, 39(12):3623–3626, 2014.

[56] Bart Kuyken, Xiaoping Liu, Richard M Osgood, Roel Baets, Günther Roelkens, and William MJ Green *Mid-infrared to telecom-band supercontinuum generation in highly nonlinear silicon-on-insulator wire waveguides* Optics Express, 19(21):20172–20181, 2011.

[57] Bart Kuyken, Takuro Ideguchi, Simon Holzner, Ming Yan, Theodor W Hänsch, Joris Van Campenhout, Peter Verheyen, Stéphane Coen, Francois Leo, Roel Baets, et al. *An octave-spanning mid-infrared frequency comb generated in a silicon nanophotonic wire waveguide* Nature communications, 6, 2015.

[58] Takahiro Goto, Atushi Ishizawa, Rai Kou, Tai Tsuchizawa, Nobuyuki Matsuda, Kenichi Hitachi, Tadashi Nishikawa, Koji Yamada, HIdeki Gotoh, et al. *Octave spanning frequency comb generation in a dispersion-controlled short silicon-wire waveguide with a fiber laser oscillator* In CLEO: Science and Innovations, pages SW4G–1. Optical Society of America, 2015.

[59] Lin Zhang, Qiang Lin, Yang Yue, Yan Yan, Raymond G Beausoleil, Anu Agarwal, Lionel C Kimerling, Jurgen Michel, and Alan E Willner *On-chip octave-spanning supercontinuum in nanostructured silicon waveguides using ultralow pulse energy* IEEE Journal of Selected Topics in Quantum Electronics, 18(6):1799–1806, 2012.

[60] Utsav D Dave, Sarah Uvin, Bart Kuyken, Shankar Selvaraja, Francois Leo, and Gunther Roelkens *Telecom to mid-infrared spanning supercontinuum generation in hydrogenated amorphous silicon waveguides using a Thulium doped fiber laser pump source* Optics express, 21(26):32032–32039, 2013.

[61] Hongcheng Sun, Ke-Yao Wang, Reza Salem, Peter Fendel, and Amy C Foster *Coherent Mid-IR Supercontinuum Generation in a Hydrogenated Amorphous Silicon Waveguide* In CLEO: Science and Innovations, pages SM1P–6. Optical Society of America, 2015.

[62] L Shen, N Healy, L Xu, HY Cheng, TD Day, JHV Price, JV Badding, and AC Peacock *Four-wave mixing and octave-spanning supercontinuum generation in a small core hydrogenated amorphous silicon fiber pumped in the mid-infrared* Optics letters, 39(19):5721–5724, 2014.

[63] AS Mayer, A Klenner, AR Johnson, K Luke, MRE Lamont, Y Okawachi, M Lipson, AL Gaeta, and U Keller *Frequency comb offset detection using supercontinuum generation in silicon nitride waveguides* Optics express, 23(12):15440–15451, 2015.

[64] Ting Wang, Doris KT Ng, Siu-Kit Ng, Yeow-Teck Toh, AKL Chee, George FR Chen, Qian Wang, and Dawn TH Tan *Supercontinuum generation in bandgap engineered, back-end CMOS compatible silicon rich nitride waveguides* Laser & Photonics Reviews, 9(5):498–506, 2015.

[65] Davide Grassani, Adrien Billat, Martin Hubert Peter Pfeiffer, Hairun Guo, Thibault North, Tobias J Kippenberg, and Camille-Sophie Brès *Mid-infrared supercontinuum generation in a SiN waveguide pumped at 1.55 micron* In Frontiers in Optics, pages FTu5D–3. Optical Society of America, 2016.

[66] Utsav D Dave, Charles Ciret, Simon-Pierre Gorza, Sylvain Combrie, Alfredo De Rossi, Fabrice Raineri, Gunther Roelkens, and Bart Kuyken *Dispersive-wave-based octave-spanning supercontinuum generation in InGaP membrane waveguides on a silicon substrate* Optics letters, 40(15):3584–3587, 2015.

[67] Bill Corcoran, Christelle Monat, Christian Grillet, David J Moss, Benjamin J Eggleton, TP White, Liam O'Faolain, and Thomas F Krauss *Green light emission in silicon through slow-light enhanced third-harmonic generation in photonic-crystal waveguides* Nature photonics, 3(4):206–210, 2009.

[68] Paulina S Kuo, Jorge Bravo-Abad, and Glenn S Solomon *Second-harmonic generation using-quasi-phasematching in a GaAs whispering-gallery-mode microcavity* Nature communications, 5, 2014.

[69] David P Lake, Matthew Mitchell, Harishankar Jayakumar, Laís Fujii dos Santos, Davor Curic, and Paul E Barclay *Efficient telecom to visible wavelength conversion in doubly resonant gallium phosphide microdisks* Applied Physics Letters, 108(3):031109, 2016.

[70] John D Joannopoulos, Steven G Johnson, Joshua N Winn, and Robert D Meade *Photonic crystals: molding the flow of light* Princeton university press, 2011.

[71] NGR Broderick, TM Monro, PJ Bennett, and DJ Richardson *Nonlinearity in holey optical fibers: measurement and future opportunities* Optics Letters, 24(20):1395–1397, 1999.

[72] John M Dudley and J Roy Taylor *Ten years of nonlinear optics in photonic crystal fibre* Nature Photonics, 3(2):85–90, 2009.

[73] Marin Soljačić, Chiyan Luo, John D Joannopoulos, and Shanhui Fan *Nonlinear photonic crystal microdevices for optical integration* Optics letters, 28(8):637–639, 2003.

[74] Chenran Ye, Sikandar Khan, Zhuo Ran Li, Ergun Simsek, and Volker J Sorger *λ-size ITO and graphene-based electro-optic modulators on SOI* IEEE Journal of Selected Topics in Quantum Electronics, 20(4):40–49, 2014.

[75] Koen Alexander, Yingtao Hu, Marianna Pantouvaki, Steven Brems, Inge Asselberghs, Simon-Pierre Gorza, Cedric Huyghebaert, Joris Van Campenhout, Bart Kuyken, and Dries Van Thourhout *Electrically controllable saturable absorption in hybrid graphene-silicon waveguides* In CLEO: Science and Innovations, pages STh4H–7. Optical Society of America, 2015.

[76] Christine Donnelly and Dawn TH Tan *Ultra-large nonlinear parameter in graphene-silicon waveguide structures* Optics express, 22(19):22820–22830, 2014.

[77] Ivan D Rukhlenko, Malin Premaratne, and Govind P Agrawal *Nonlinear propagation in silicon-based plasmonic waveguides from the standpoint of applications* Optics express, 19(1):206–217, 2011.

[78] Frédéric Peyskens, Ashim Dhakal, Pol Van Dorpe, Nicolas Le Thomas, and Roel Baets *Surface enhanced Raman spectroscopy using a single mode nanophotonic-plasmonic platform* ACS Photonics, 3(1):102–108, 2015.

[79] Wenshan Cai, Alok P Vasudev, and Mark L Brongersma *Electrically controlled nonlinear generation of light with plasmonics* Science, 333(6050):1720–1723, 2011.

[80] Gregory A Wurtz, Robert Pollard, Willam Hendren, GP Wiederrecht, DJ Gosztola, VA Podolskiy, and Anatoly V Zayats *Designed ultrafast optical nonlinearity in a plasmonic nanorod metamaterial enhanced by nonlocality* Nature nanotechnology, 6(2):107–111, 2011.

[81] Bo Peng, Sahin Kaya Ozdemir, Fuchuan Lei, Faraz Monifi, Mariagiovanna Gianfreda, Gui Lu Long, Shanhui Fan, Franco Nori, Carl M Bender, and Lan Yang *Nonreciprocal light transmission in parity-time-symmetric whispering-gallery microcavities* arXiv preprint arXiv:1308.4564, 2013.

[82] Haim Suchowski, Kevin OBrien, Zi Jing Wong, Alessandro Salandrino, Xiaobo Yin, and Xiang Zhang *Phase mismatch–free nonlinear propagation in optical zero-index materials* Science, 342(6163):1223–1226, 2013.

[83] Alec Rose and David R Smith *Overcoming phase mismatch in nonlinear metamaterials [Invited]* Optical Materials Express, 1(7):1232–1243, 2011.

[84] Andrzej Gajda, Lars Zimmermann, Mahmoud Jazayerifar, Georg Winzer, Hui Tian, Robert Elschner, Thomas Richter, Colja Schubert, Bernd Tillack, and Klaus Petermann *Highly efficient CW parametric conversion at 1550 nm in SOI waveguides by reverse biased pin junction* Optics express, 20(12):13100–13107, 2012.

[85] Amy C Turner-Foster, Mark A Foster, Jacob S Levy, Carl B Poitras, Reza Salem, Alexander L Gaeta, and Michal Lipson *Ultrashort free-carrier lifetime in low-loss silicon nanowaveguides* Optics express, 18(4):3582–3591, 2010.

[86] Bart Kuyken, Xiaoping Liu, Günther Roelkens, Roel Baets, Richard M Osgood Jr, and William MJ Green *50 dB parametric on-chip gain in silicon photonic wires* Optics letters, 36(22):4401–4403, 2011.

[87] Bart Kuyken, Hua Ji, Stéphane Clemmen, SK Selvaraja, Hao Hu, Minhao Pu, Michael Galili, Palle Jeppesen, Geert Morthier, Serge Massar, et al. *Nonlinear properties of and nonlinear processing in hydrogenated amorphous silicon waveguides* Optics express, 19(26):B146–B153, 2011.

[88] C Grillet, L Carletti, C Monat, P Grosse, B Ben Bakir, S Menezo, JM Fedeli, and DJ Moss *Amorphous silicon nanowires combining high nonlinearity, FOM and optical stability* Optics express, 20(20):22609–22615, 2012.

2

HYDROGENATED AMORPHOUS SILICON AS A NONLINEAR PLATFORM

"Perfect is the enemy of good enough." - French/Italian Proverb

2.1 Amorphous silicon as a CMOS-compatible nonlinear optical material

As discussed in the previous chapter, performing nonlinear operations in an integrated platform offers various advantages over bulk nonlinear optics. Also, because of its CMOS compatibility, the SOI platform offers the possibility for the production of these integrated chips at a very low cost, which is thus very attractive for specific applications. In terms of nonlinear properties, a large index contrast, low linear losses and large third order nonlinearity are the advantages of crystalline silicon (c-Si). However, c-Si suffers from large nonlinear losses arising from two-photon and free-carrier absorption. When photons with energy larger than half the bandgap energy of c-Si are present, two of them can be simultaneously absorbed thus promoting electrons from the valence to the conduction band. These free electrons can further cause losses by absorbing more photons, referred to as free carrier absorption as shown in Fig. 2.1 below.

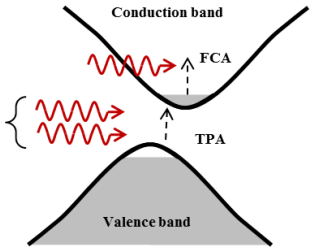

Figure 2.1 The nonlinear loss mechanisms in c-Si: two-photon absorption and free-carrier absorption.

In general, the total loss in a waveguide arising from all sources can be written as [1]:

$$\frac{dI}{dz} = -(\alpha_{lin} + \alpha_{tpa} I + ... + \sigma_{fca} N_c) I \tag{2.1}$$

$$\frac{dN_c}{dt} = \frac{\alpha_{tpa}}{2h\nu_0} I^2 - \frac{N_c}{\tau_{recomb}} \tag{2.2}$$

Here, α_{lin} and α_{tpa} correspond to the linear and two-photon absorption loss coefficients, σ_{fca} is the absorption cross section for free carriers and N_c is free-carrier density. Higher order multi-photon absorption terms could also be included in the above equation if needed. Clearly, the two-photon absorption loss increases with the incident intensity and thus at high enough intensities, it dominates over the linear loss. The second equation gives the free carrier concentration where two-photon absorption is the source term for the carriers. Here, ν_0 is the frequency of the light and τ_{recomb} is the recombination lifetime of the carriers. It should be

noted that due to the Kramers-Kronig relations, the presence of carrier-induced loss also has a dispersive effect which can be important in certain situations [2, 3].

From these equations, it is clear that with increasing light intensity in the c-Si nonlinear waveguide, the loss arising from both the two-photon as well as the free-carrier absorption increases. Specifically, from Eq. 2.2, it can be seen that FCA scales with the square of the intensity, while the nonlinear gain for nonlinear processes such as four-wave mixing scales linearly with the intensity. Thus, at large intensities, the intensity dependent loss overwhelms the nonlinear gain, limiting the efficiency of any nonlinear functionality one may want to implement. One way to circumvent this problem is to work at frequencies with photon energies smaller than the half bandgap value of silicon, i.e. at wavelengths of 2.2 μm or longer. However this is not always possible for all applications - for example, applications in the telecom domain may require one to work at wavelengths around 1550 nm. Another problem of working at these longer wavelengths compared to the telecommunications wavelength range is the scarcity of sources, detectors etc. Another approach is to apply a voltage over the waveguide and sweep out the carriers that are generated, limiting the losses from the free-carrier term. This approach has been successfully applied by researchers for applications such as four-wave mixing in SOI waveguides in the telecom wavelength regime [4–6]. However, the presence of TPA means that net gain can still only barely be achieved. This approach also adds to the complexity of the fabrication process, and suffers from distortions at high-speed signals (depending on the lifetime of the carriers). Another approach is to use ultrashort pulses with pulse widths of up to a few hundred femtoseconds for nonlinear applications. Since FCA and FCD are proportional to the integral of the square of the intensity, these effects for such pulses can, in many cases, be neglected because of the short pulse duration, even considering their large instantaneous power. This approach has been exploited for some applications such as supercontinuum generation in the telecommunications wavelength range [7, 8]. However, this approach is obviously limited by the constraint on the pulse duration. One approach which keeps the advantages of the SOI platform of CMOS-manufacturability, a relatively simple fabrication process, large index contrast, loss linear losses and large third-order nonlinearity but avoids the disadvantages of the nonlinear losses is to use hydrogenated amorphous silicon instead of crystalline silicon. Hydrogenated amorphous silicon (a-Si:H) has been shown - depending on the fabrication process - to have a larger bandgap compared to c-Si [9, 10]. Thus, one can work at shorter wavelengths while either avoiding or at the very least significantly lowering TPA and FCA losses compared to the losses at the same wavelengths in c-Si. This has enabled several nonlinear functionalities such as all-optical control or signal processing [11, 12]. To that end, the use of the a-Si platform for generating a broad supercontinuum with a spectrum extending from the telecommunications wavelength range to the mid-infrared is described in this chapter.

2.2 Introduction to supercontinuum generation

Supercontinuum generation (SCG) - an all-encompassing term for the various manifestations of using nonlinear processes to generate a broadband source with a large power spectral density - has been the subject of intense study for several years now [13–19], both because of its interesting properties as well as its potential for application in various domains including spectroscopy, optical coherence tomography, wavelength division multiplexing etc. [20–25]. In particular, because broadband spectra that are spatially and/or temporally coherent can be controllably generated, it is of particular interest for spectroscopic applications. Specific implementations of SCG can be classified according to many considerations - the nonlinear platform used for the SCG, the pump wavelength and pulse duration, the spectral coverage of the supercontinuum, the spatial and temporal coherence properties, the underlying nonlinear dynamics etc. From the point of view of spectroscopic applications, the most important considerations would be the wavelengths covered by, as well as the power spectral density of the supercontinuum spectrum and its coherence properties. Initially, SCG was practiced mainly in the fiber community and especially the photonic crystal fiber community because of some inherent advantages such as low losses (enabling a long interaction length) and accurate control over dispersion properties of the fiber which, as we will see, are critical for achieving a broad spectrum. In recent years, with the maturing of integrated photonic platforms like SOI, these have also been investigated for SCG. There have been several demonstrations in the SOI platform [8, 19, 26–33], the SiN platform [17, 34–36], the chalcogenide platform [37–40] etc. which cover several different wavelength ranges in the visible and infrared.

As mentioned above, for pump wavelengths below the half bandgap value of silicon of 2.2 μm, the SOI platform suffers from large nonlinear losses as a result of TPA and FCA and thus efficient SCG is difficult, especially in the case where the pump pulse duration is in the order of picoseconds. Thus, SCG below the half bandgap value is only possible with pump pulse durations significantly smaller than 1ps [8, 27]. For example, in [8] a 550 nm wide spectrum was generated by pumping SOI waveguides with 150 fs pulses centered at 1550 nm while in [29] and [30], octave spanning spectra are generated in extensively dispersion engineered SOI waveguides by pumping them with similar femtosecond-scale pulses centered at 1550 and 1800 nm respectively. The pulse energy in these cases is in the range of 5 to 50 pJ. However, it is not always possible to have convenient access to such short pulses, mainly because the most common sources for them are mode-locked sources which are not necessarily available in the wavelength range of interest. Optical parametric oscillator (OPO) setups that can translate the output of these mode-locked lasers to the wavelength range of interest are also available, but are so bulky that they tend to occupy entire optical tables. In recent years, thulium-doped fiber laser sources with picosecond pulse durations and pump wavelengths slightly below 2 μm have become commercially available [41]. Using these convenient sources would allow for SCG in the mid-infrared wavelength

range. The mid-infrared - which spans the 2-20 μm wavelength range - is interesting from an application point of view because of various reasons. Chief among them is the fact that the rotational-vibrational absorption bands of several important molecules like water, CO_2 etc. fall in this region, which makes it an important wavelength range for spectroscopy and sensing. However, there has been a shortage of cheap, integrated solutions for sources, detectors etc. in this wavelength range. Thus, it is attractive to use compact and cheap sources like the Thulium doped fiber modelocked laser in conjunction with an integrated nonlinear optical platform like a-Si:H to perform SCG since it allows for an extension of the source spectrum into the mid-infrared. This opens up the possibility of having cheap, reliable sources in that wavelength range.

Another reason why pumping at 1.95 μm is advantageous is because it should allow for a further reduction of the nonlinear losses. While pumping at 1.55 μm might be preferable under most circumstances because of the easy availability of sources, detectors etc., previous experiments conducted at 1550 nm [42] have shown that the hydrogenated amorphous silicon suffers from degradation effects when exposed to the high pump powers needed for SCG. In this earlier work, the degradation was attributed to the Staebler-Wronski effect where breakage of Si-Si bonds occurs due to the recombination of electron-hole pairs created by TPA. Thus, pumping at longer wavelengths is expected to reduce the number of carriers generated by TPA and help alleviate the material degradation issues. And since the bandgap of a-Si is larger than that of c-Si, one doesn't need to move the pump wavelength all the way above 2.2 μm where, as mentioned above, compact and cheap sources are scarce. Instead, one can make the happy compromise between source availability and material needs and pump at 1.95 μm while still managing to generate a useful supercontinuum. It should be noted that the tendency for the material to degrade when exposed to high intensities is known to be a function of the deposition technique, and other groups have shown that it is possible to deposit degradation-free material [9, 43]. Thus, it is possible that even this compromise may not be strictly necessary in all implementations of SCG [7]. Nevertheless, with the mid-infrared being an important wavelength range for spectroscopic applications means that for several applications, pumping around 2 μm might just be the best option.

2.2.1 Mechanism for supercontinuum generation

As mentioned above, various implementations of SCG are categorized according to the pump pulse duration, the underlying physical dynamics and the coherence of the supercontinuum spectrum. It turns out that in general, a parameter called the soliton number gives a strong indication of exactly which physical processes will contribute to the supercontinuum generation, as well as what the coherence properties of the resulting supercontinuum will be [15]. The square of the soliton number is proportional to the nonlinearity, peak power and the pulse width and inversely proportional to the magnitude of the group-velocity dispersion. For small soliton

numbers, the route to SCG is through a process called soliton fission and the theory behind that will be discussed in detail in chapter 4. Here, we are concerned with the SCG mechanisms for large soliton numbers because the laser employed here is of picosecond duration. Since the soliton number is directly proportional to the pulse duration, for the picosecond pump pulse duration, the soliton number is in general too large for the soliton fission process. Instead, the mechanism leading to the generation of the supercontinuum in the picosecond regime begins with self-phase modulation of the pump pulse leading to spectral broadening and then the subsequent amplification of the background noise which results in the generation of modulation instability (MI) sidebands on either side of the pump. Both of these processes create new frequency components, thus extending the spectral coverage. With increasing pump powers, the MI sidebands may merge together with the original pump pulse creating a continuous spectrum. As we will see in the subsequent discussion in this section, if the nonlinear medium is appropriately designed to have the correct dispersion properties, then it's even possible for multiple sidebands to exist which experience nonlinear gain thus giving rise to several MI sidebands, which arise from noise with increasing pump power. Additionally, four-wave mixing between the different spectral components can also occur. In some cases, Raman scattering may also play a role in the dynamics that lead to the formation of the supercontinuum, especially if there is a strong Raman gain that lies in the same spectral region as the MI sidebands. Since the spectral positions of the MI sidebands depend on both the dispersion and nonlinear properties of the medium, there is a clear need for careful management of both if one wants to generate the broadest possible supercontinuum. As a result, with a proper design of the cross-section of the a-Si:H waveguide, it ought to be possible to generate a supercontinuum with a large spectral bandwidth. In this chapter, it will be shown that it is indeed possible to efficiently generate a broad supercontinuum using a-Si:H waveguides when pumped by a Thulium-doped pulsed fiber laser source at 1.95 μm.

In order to get insight into all the physical dynamics underlying supercontinuum generation, it is instructive to start with the simple model of four waves propagating down a waveguide. The properties of the waveguide can be characterized by its linear properties of effective and group indices, effective area of interaction, linear loss, group velocity (and higher order) dispersion terms, as well as its nonlinear properties (nonlinear Kerr index and any nonlinear loss terms such as TPA and FCA). These four waves will interact with one another through the nonlinear response of the waveguide material. Thus, we end up with four coupled equations that we can then solve analytically if possible or numerically.

We can start by looking at how the third order nonlinear response of a material is written [44]:

$$P_{NL,i} = \sum_{j,k,l} \chi^{(3)}_{ijkl} E_j E_k E_l \tag{2.3}$$

Here, $P_{NL,i}$ describes the i-component of the nonlinear polarization arising due to the third order response of the material to incident radiation described by the electric fields E_i. $\boldsymbol{P_{NL}}$ acts as the source term in the general wave equation:

$$\nabla^2 \boldsymbol{E} - \frac{1}{c^2}\frac{\partial^2 \boldsymbol{E}}{\partial t^2} = \mu_0 \frac{\partial^2 \boldsymbol{P}}{\partial t^2} \tag{2.4}$$

where

$$\boldsymbol{P} = \boldsymbol{P}_L + \boldsymbol{P}_{NL} \tag{2.5}$$

This gives a complete description of the third order effects that can occur in the material. In general, we can write the incoming field at a frequency ω_n as:

$$\boldsymbol{E}(\omega_n) = \frac{\left[\boldsymbol{E}\, e^{i(\omega_n t - k_n z)} + \boldsymbol{E}^*\, e^{-i(\omega_n t - k_n z)}\right]}{2} \tag{2.6}$$

By substituting Eq. 2.6 back into Eq. 2.3, we can look at the general case when four different fields are interacting inside the nonlinear material. The degenerate cases where two or more of the fields are at the same frequency can be understood from the general properties. Substituting, we have:

$$\begin{aligned}
\boldsymbol{P} =& \frac{3}{4}\chi^{(3)}|\boldsymbol{E}(\omega_4)|^2\boldsymbol{E}(\omega_4) \\
& \frac{6}{4}\chi^{(3)}\left(|\boldsymbol{E}(\omega_1)|^2 + |\boldsymbol{E}(\omega_2)|^2 + |\boldsymbol{E}(\omega_3)|^2\right)\boldsymbol{E}(\omega_4) \\
& \frac{6}{4}\chi^{(3)}\boldsymbol{E}(\omega_1)\boldsymbol{E}(\omega_2)\boldsymbol{E}(\omega_3)exp(j\theta_1) + ... \\
\theta_1 =& (\omega_1 + \omega_2 - \omega_3 - \omega_4)t + (k_1 + k_2 - k_3 - k_4)z
\end{aligned} \tag{2.7}$$

All the terms in the above equation are grouped according to the different physical processes that they denote. The first term represents a process called self-phase modulation (SPM) where, as the name implies, the presence of the electric field influences its own phase through the instantaneous Kerr response of the material. Similarly, the second group of terms describes the influence of the other fields on the refractive index experienced by the first one and is thus called cross-phase modulation (XPM). Note that for all these terms, the imaginary part of the susceptibility describes the corresponding absorption processes of two-photon absorption (TPA), cross-amplitude modulation (XAM) etc. The final group of terms represents the processes of four-wave mixing (FWM) where a fourth field is generated at a frequency that is some linear combination of the frequencies of the incident fields (and thus also includes the term corresponding to third-harmonic and third order sum-frequency generation). It can be seen that the efficiency of this process is dependent on a phase term, which is defined by the phase mismatch terms θ_1 etc. Thus, it can already be seen that phase-matching between the various frequencies in the medium is an important consideration for effective wavelength conversion

to take place.

Substituting Eq. 2.7 into the general wave equation for each frequency component, we end up with four coupled equations that describe the evolution of each of the frequencies due to the various nonlinear interactions.

$$\begin{aligned}
\frac{dA_1}{dz} &= iRe(\gamma)\Big[\big(|A_1|^2 + 2|A_2|^2 + 2|A_3|^2 + 2|A_4|^2\big)A_1 + 2A_2^* A_3 A_4 e^{i\Delta k_{lin} z}\Big] \\
\frac{dA_2}{dz} &= iRe(\gamma)\Big[\big(|A_2|^2 + 2|A_3|^2 + 2|A_4|^2 + 2|A_1|^2\big)A_2 + 2A_1^* A_3 A_4 e^{i\Delta k_{lin} z}\Big] \\
\frac{dA_3}{dz} &= iRe(\gamma)\Big[\big(|A_3|^2 + 2|A_4|^2 + 2|A_1|^2 + 2|A_2|^2\big)A_3 + 2A_1 A_2 A_4^* e^{-i\Delta k_{lin} z}\Big] \\
\frac{dA_4}{dz} &= iRe(\gamma)\Big[\big(|A_4|^2 + 2|A_1|^2 + 2|A_2|^2 + 2|A_3|^2\big)A_4 + 2A_1 A_2 A_3^* e^{-i\Delta k_{lin} z}\Big]
\end{aligned} \tag{2.8}$$

Here, the linear phase mismatch is defined as $\Delta k_{lin} = k_3 + k_4 - k_1 - k_2$ and γ is the nonlinear parameter defined as follows (also see [44–48] for useful discussions on the appropriate definition for the effective area):

$$\gamma = \frac{2\pi n_2}{\lambda_0 A_{eff}} + i\frac{\alpha_{tpa}}{2A_{eff}} \tag{2.9}$$

If we now take a look at what happens when two of the waves (A_1 and A_2) are much stronger compared to the others - referred to as the undepleted pump approximation - the situation can be greatly simplified. Hence, we can set A_3 and A_4 to zero in Eqs. 2.8 and obtain the following expressions for the pump waves:

$$\begin{aligned}
A_1(z) &= \sqrt{P_1} exp\big[i\gamma(P_1 + 2P_2)z\big] \\
A_2(z) &= \sqrt{P_2} exp\big[i\gamma(2P_1 + P_2)z\big]
\end{aligned} \tag{2.10}$$

Clearly, the amplitude of the pumps is uninfluenced in this process and they merely serve to alter the phase acquired by each other though SPM and XPM. The evolution of the other two waves - known as the signal and idler waves - can now be written as:

$$\begin{aligned}
\frac{dA_3(z)}{dz} &= 2i\gamma\Big[(P_1 + P_2)A_3(z) + \sqrt{P_1 P_2} exp\big[-i(\Delta k - 3\gamma(P_1 + P_2))z\big]A_4^*(z)\Big] \\
\frac{dA_4^*(z)}{dz} &= -2i\gamma\Big[(P_1 + P_2)A_4^*(z) + \sqrt{P_1 P_2} exp\big[i(\Delta k - 3\gamma(P_1 + P_2))z\big]A_3(z)\Big]
\end{aligned} \tag{2.11}$$

After some algebraic manipulations, we end up with the equation for evolution of the signal and idler waves along the waveguide:

$$\begin{aligned} B_3(z) &= \left(a_3 e^{gz} + b_3 e^{-gz}\right) e^{(-i\kappa z/2)} \\ B_4^*(z) &= \left(a_4 e^{gz} + b_4 e^{-gz}\right) e^{(i\kappa z/2)} \end{aligned} \tag{2.12}$$

Here, the total phase-mismatch is written as follows:

$$\kappa = \Delta k + \gamma(P_1 + P_2) \tag{2.13}$$

The gain g is defined as $g = \sqrt{(2\gamma\sqrt{P_1\,P_2})^2 - (\kappa/2)^2}$ and the amplitudes $B_m (m = 3, 4)$ are related to the signal and idler amplitudes A_m by the transformation $B_m = A_m\, exp[-2i\gamma\,(P_1 + P_2)z]$.

As can be seen from the above equation, the gain experienced by the signal and idler waves depends on two factors: the linear phase mismatch, denoted by Δk as well as a contribution by the nonlinear interactions, which is proportional to the power as well as the nonlinear parameter γ. Thus, we can see that proper dispersion control is required to make sure that the overall phase-mismatch, including the nonlinear contributions, is zero for efficient conversion.

It is instructive to look at the dependence of the nonlinear gain as a function of the total dispersion of the waveguide. For this, we assume that there is only one pump wave. For this case, the gain becomes $g = \sqrt{(\gamma\,P_0)^2 - (\kappa/2)^2}$ and the phase-mismatch becomes $\kappa = \Delta\,k + 2\gamma P_0$. The linear phase-mismatch can be written in terms of the dispersion by writing the propagation constant β of the signal and idler waves as a Taylor expansion around the pump frequency:

$$\beta(\omega) = \beta(\omega_0) + \sum_{i=1}^{\infty} \frac{d^i\beta}{d\omega^i}(\omega_0)\frac{(\omega - \omega_0)^i}{i!} \tag{2.14}$$

Here, $\beta(\omega)$ corresponds to the propagation constant at the frequency ω and ω_0 and ω are the pump and signal (or idler) frequencies. Ideally, one would know all the dispersion terms in the expansion, but for now we limit ourselves to the fourth order:

$$\beta(\omega) = \beta(\omega_0) + \beta_1(\omega_0)\Delta\omega + \frac{\beta_2(\omega_0)}{2!}\Delta\omega^2 + \frac{\beta_3(\omega_0)}{3!}\Delta\omega^3 + \frac{\beta_4(\omega_0)}{4!}\Delta\omega^4 \tag{2.15}$$

Here, β_i is the i^{th} order derivative of the propagation constant. β_1 and β_2 are commonly encountered in many areas of optics. β_1 is reciprocal of the group velocity and β_2 is the group velocity dispersion (GVD) and is related to the dispersion parameter *D* commonly used in fiber optic systems by the relation $D = -2\pi c\beta_2/\lambda^2$. Note that the *D* and β_2 have opposite signs. Depending on whether β_2 is positive or negative, the dispersion is termed to respectively be in the normal or anomalous regime. Using this expansion for each of the participating frequencies, we can write the linear phase mismatch as follows:

$$\begin{aligned}\Delta k &= (n_3\omega_3 + n_4\omega_4 - 2n_0\omega_0)/c \\ &= 2\beta(\omega_0) \\ &+ \beta_1(\omega_0)\big[(\omega_3-\omega_0)+(\omega_4-\omega_0)\big] + \frac{\beta_2(\omega_0)}{2}\big[(\omega_3-\omega_0)^2+(\omega_4-\omega_0)^2\big] \\ &+ \frac{\beta_3(\omega_0)}{6}\big[(\omega_3-\omega_0)^3+(\omega_4-\omega_0)^3\big] + \frac{\beta_4(\omega_0)}{24}\big[(\omega_3-\omega_0)^4+(\omega_4-\omega_0)^4\big] \\ &- 2\beta(\omega_0)\end{aligned} \tag{2.16}$$

Since $\omega_3 - \omega_0 = -(\omega_4 - \omega_0)$ due to the requirement of energy conservation, only the even orders of the expansion survive. Thus, we can re-write Eq. 2.13 it as follows:

$$\kappa = \beta_2(\omega_0)\Delta\omega^2 + \frac{\beta_4(\omega_0)}{12}\Delta\omega^4 + 2\gamma P \tag{2.17}$$

Using the above equation, we can immediately see the effect of the interplay between dispersion and nonlinearity on κ. Fig. 2.2 below shows how the different signs of β_2 and β_4 affect the phase matching (under the assumption of a positive n_2 and thus positive γ).

Clearly, both the sign and magnitude of both β_2 and β_4, along with the magnitude of the nonlinear phase mismatch - which equals $2\gamma P$ - influence the regions where gain is achieved. For example, in the case where both β_2 and β_4 are negative, one can only have a single phase matching point (M1) close to the pump frequency as shown in Fig. 2.2(a). While in the case of negative β_2 but positive β_4, there can be two phase matching bands (M1 and M2), one close and one far away from the pump, as shown in Fig. 2.2(b). In fact, if the nonlinear contribution is strong enough, the two sidebands are no longer distinct and merge into a single large spectral band where there is gain. In this way, one can control the wavelength regions where there is phase matching and consequently, nonlinear gain for the signal and idler waves. It should be noted that even though the preceding discussion was for the case where the signal and idler waves are present in the waveguide, the same arguments clearly also apply even when there are no signal or idler waves present [49].

In such a case, the nonlinear gain would amplify the ever-present noise around the phase matching points where there is the maximum gain. Thus, if a sufficiently intense pump is launched down a waveguide, the resulting large nonlinear gain would cause signal and idler frequencies to arise out of the noise. This situation is sometimes encountered in fiber communication networks where a large power maybe required for reliably transmitting data over hundreds or even thousands of kilometers of fiber length [50]. In that case, the nonlinear gain amplifies the noise in the system and gives rise to additional frequencies around the pump. Thus, the

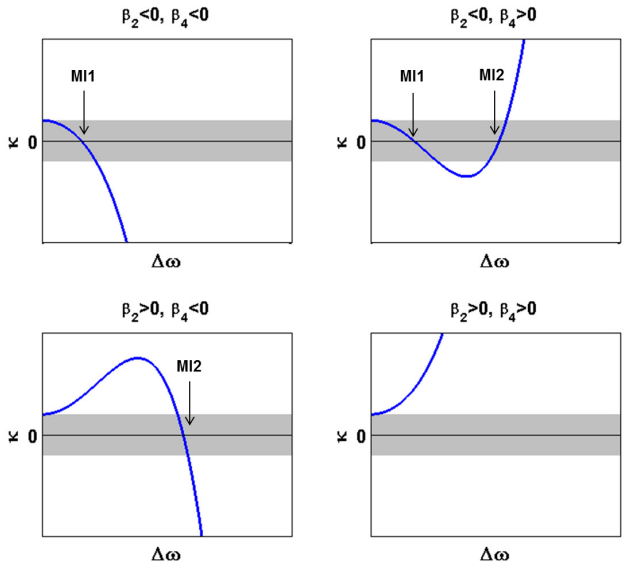

Figure 2.2 The total dispersion including the nonlinear contribution is shown as a function of the frequency detuning from the pump. The role of second and fourth order dispersion terms in phase matching can be clearly discerned. The shaded area is the region where the nonlinear gain is available, i.e. $-2\gamma P > \kappa > 2\gamma P$. (a) When both β_2 and β_4 are negative, then there is only one modulation instability sideband close to the pump frequency, labelled as MI1. (b) When β_2 is negative but β_4 is positive, there is one sideband close and another one far away from the pump frequency, labelled as MI1 and MI2 respectively. (c) When β_2 is positive and β_4 is negative, only the sideband far away from the pump frequency exists. (d) No phase matching is possible when both β_2 and β_4 are positive.

strong CW pump can break up into a periodic pulse train the frequency of which is determined by the phase matching points. This is termed as sideband or modulation instability and is in fact a phenomenon that is ubiquitously encountered in many kinds of nonlinear systems. In this thesis, the term modulation instability (MI) will be used. As is clear from Eq. 2.12, as long as g is real, there will be some gain available in the sidebands. We can thus we can derive the gain bandwidth and arrive at the condition $0 > \Delta k > -4\gamma P$ with the maximum occurring when the linear and nonlinear contributions exactly cancel each other: $\Delta k = -2\gamma P$. For the sidebands closest to the pump where only the β_2 term is important, the gain is maximum at a pump frequency detuning given by $\Omega_{MI} = \sqrt{2\gamma P/|\beta_2|}$. As shown in Fig. 2.2, the MI sideband close to the pump is possible only when the second order dispersion is negative, while there are two possible sidebands when the fourth order dispersion is additionally positive. These phase matching points will be called MI1 and MI2 respectively in this thesis. The existence of these multiple MI sidebands will be leveraged for broadband supercontinuum generation.

2.2.2 Waveguide design

As discussed above, it is critical to have the correct dispersion properties for generating a broadband supercontinuum. The linear phase-mismatch between the waves interacting in a waveguide is composed of two contributions: the 'bulk' dispersion arising from the material and the geometrical dispersion arising from the properties of the waveguide. Both contributions can be of significant importance depending on the circumstances. Geometrical dispersion arises from the confining nature of the waveguide. This can be intuitively understood by realizing that the relative dimensions of the waveguide as experienced by different wavelengths are different. As a result, there is a dispersive nature associated with purely the geometric properties of the waveguide. Thus, even in wavelength regimes where the material dispersion is pretty flat - such as wavelengths far away from the material bandgap - the geometric contribution can still result in significant dispersion. Also, since in many cases, one is working close to the bandgap, the material dispersion can become quite strong and thus there needs to be a way to compensate for it. The total dispersion can thus be tailored to have the desired value by selecting an appropriate cross-section of the waveguide. It should be noted that a method for dispersion measurement as well as dispersion tuning by post-processing the fabricated waveguides to remove the bottom oxide cladding by wet etching in buffered hydrogen fluoride solution has been presented in [51]. Typically, the waveguide height is fixed by other considerations - for example in the SOI chips fabricated at *imec* [52, 53], the height is fixed at either 220 nm or 400 nm - and hence, one can only alter the waveguide width to achieve the desired dispersion at any given wavelength. In silicon, in the wavelength regimes of interest in this work, the material contribution to GVD is generally normal. Thankfully, in these large index contrast (and thus strongly confining) waveguides, the geometric dispersion contribution can be strong enough to overcome the normal material dispersion such that the total dispersion is anomalous in certain wavelength regions. Figure 2.3 below shows an example of the contributions of the waveguide geometry and material to the total second and fourth order dispersion for different waveguide widths. It is clear that by adjusting the waveguide width, one can access the anomalous dispersion regime, which, as was discussed above, is essential for achieving phase matching in sidebands both near and far away from the pump wavelength. The fourth order dispersion is similarly modified allowing for the MI2 sideband.

2.3 Experimental supercontinuum generation

In order to prove that hydrogenated amorphous silicon is a viable nonlinear platform, supercontinuum generation in the short-wave infrared was demonstrated. The pump wavelength was chosen to be 1.95 μm because of the reasons of convenience and relevance to spectroscopic applications as outlined above. The pump source was a thulium-doped modelocked fiber laser from AdValue Photonics [41] with a full width at half maximum of 1.24 ps and a repetition rate of 26 MHz. The

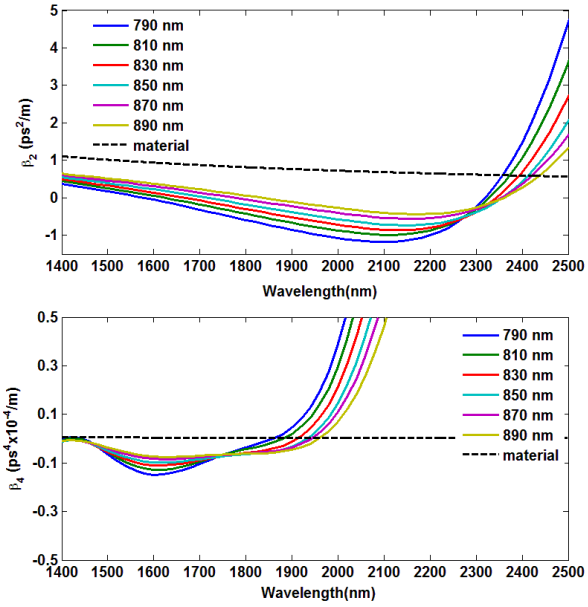

Figure 2.3 The influence of the geometric properties of the waveguide on the overall dispersion at any given wavelength can be quite pronounced. (a) For certain waveguide widths, the group velocity dispersion can become anomalous in a certain wavelength range even when the material contribution is normal. (b) The fourth order dispersion can similarly become stronger due to the waveguide contributions, thus making it possible to position the MI2 sideband reasonably close to the MI1 sideband.

a-Si:H chips with the waveguides for SCG were fabricated at imec.

2.3.1 Linear loss properties

In order to evaluate the potential of using the a-Si:H material platform for nonlinear applications, the linear and nonlinear losses need to be evaluated. Figure 2.4(a) below shows the linear losses as measured by the cut-back method at a wavelength of 1950 nm [54]. The different lengths were actually different waveguides fabricated simultaneously and are located next to each other on the chip. Hence, the loss is assumed to be identical for all of them and thus the cut-back method is suitable.

As one can see, the linear loss of 2.2 dB/cm is comparable to the SOI platform and is low enough to allow for relatively long interaction lengths. This can be quantified by calculating the effective length L_{eff} of these waveguides which is

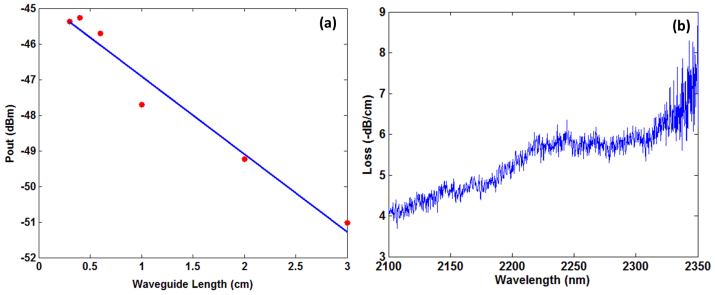

Figure 2.4 (a) Linear loss measurement of the a-Si:H waveguides by the cutback method at the pump wavelength of 1950 nm. The slope of the linear fit gives the loss as 2.2 dB/cm. (b) Losses at longer wavelengths measured with the same technique.

given by

$$L_{eff} = \frac{1 - e^{(-\alpha_{lin} L)}}{\alpha_{lin}}$$

where L is the physical length of the waveguide and α is the loss parameter in m^{-1}. In the present case, the measured loss of 2.2 dB/cm means that a waveguide with a physical length of 1 cm reduces to an effective length of 7.85 mm. It is a handy metric to use for comparison with other characteristic length scales such as the nonlinear and the dispersion length. Figure 2.4(b) shows the linear loss at longer wavelengths showing a dramatic increase in the linear losses at longer wavelengths. Because these wavelengths are less well confined in the waveguides and thus are more strongly affected by both the sidewall scattering losses as well as any radiation leakage through the substrate the losses are higher. This can be a limiting factor in some applications.

2.3.2 Nonlinear loss properties

Two-photon absorption occurring in the waveguide can be quantified by measuring the transmission through the waveguide as a function of input power. Since the effects of TPA are only expected at high powers, the modelocked laser was used for this experiment. Figure 2.5(a) below shows that the peak output power from the waveguide has a sub-linear trend with respect to input peak power, thus showing that the waveguide experiences stronger losses at higher input powers. The relationship between the input and output powers can be discerned more clearly by plotting the inverse transmission as a function of the input power, which is shown in Fig. 2.5(b). As can be seen, the two have a linear relation, which proves that TPA and not any other higher-order absorption terms are responsible for the losses. If we limit Eq. 2.1 to only the TPA term, then we can integrate it to derive the expression for the inverse transmission as a function of the input power [55].

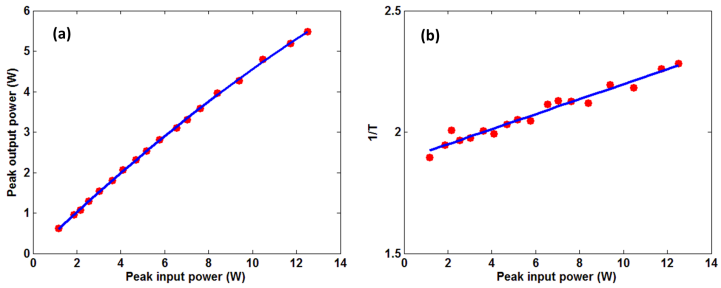

Figure 2.5 (a) Output peak power is a sub-linear function of the input peak power, showing the existence of nonlinear losses.

$$I(L,t) = \frac{e^{-\alpha_{lin}L} I(0,t)}{(1+\alpha_{tpa} I(0,t) L_{eff})}$$
$$T_{NL}^{-1} = \frac{I(0,t)}{I(L,t)} = \frac{1+\alpha_{tpa} I(0,t) L_{eff}}{e^{-\alpha_{lin}L}} \tag{2.18}$$

Thus, from the slope of the linear fit in Fig. 2.5(b), we can extract the TPA coefficient for the waveguide as 4.9±0.3x10^{-13} mW^{-1}. This compares well with other values reported in literature [56], and as expected, it is significantly lower than the TPA coefficient at 1.55 μm which is 7x10^{-12} mW^{-1}. Hence, we can expect the nonlinear figure of merit which we will discuss in the next section to be far better than at 1.55 μm.

2.3.3 Self-phase modulation

To characterize the real part of the nonlinear parameter, self-phase modulation of a laser pulse was measured as a function of input power. As explained in sec. 2.2.1, self-phase modulation takes place because the instantaneous Kerr response of the material modifies its own refractive index. This modification is given by $\Delta n_{Kerr}(t) = n_2 I(t)$ where n_2 is the Kerr index of the material and I is the intensity. Thus, the additional phase acquired is given by $\phi_{NL}(z,t) = k_0 z \Delta n_{Kerr}(t) = \omega_0 n_2 I(t) z/c = \gamma P z$. Now consider what happens when a pulse of light is incident on the nonlinear medium. Since the index change - and hence the additional phase acquired by the light - is proportional to the intensity which is a function of time (as shown in Fig. 2.6(a)), the total phase acquired by the light including the nonlinear phase ϕ_{NL} will now be a function of time, resulting in a change in the frequency spectrum of the pulse - i.e. the pulse modifies its own spectrum because of the intensity dependence of the refractive index. This spectral modification is expressed as a change in the instantaneous frequency, which is related to the nonlinear phase as $\delta\omega(t) = -d\phi_{NL}(t)/dt$. Thus it can be seen that the rising and falling edges of the pulse will experience a red and

blue shift respectively as shown schematically in Fig. 2.6(b). The longer the pulse travels through the nonlinear medium, the more spectral shift it will accumulate. Similarly, for the same length of the nonlinear medium, increasing the input power will mean an increased spectral shift for the pulse at the output end. Hence, we can quantify the nonlinear response of the medium by measuring the output pulse spectrum as a function of the input power.

Figure 2.7(a) shows the result of the measurement through the same waveguide that was used for the nonlinear transmission experiment of sec. 2.3.2. It can be observed that with increasing input power not only does the output spectrum broaden, but it also displays the lobed structure characteristic to SPM [44, 57]. These lobes in the spectrum are a result of the time-dependent phase introduced across the pulse and the exact amount that is accumulated depends on both the power and the length of the waveguide. It should be noted that the small, rapid oscillations in the spectra are not a result of SPM but because the input pulse itself does not have a clean spectral profile, which is related to the internal dynamics of the pulsed laser itself. Nevertheless, it is clear that the increasing input power introduces the characteristic lobed structure of SPM.

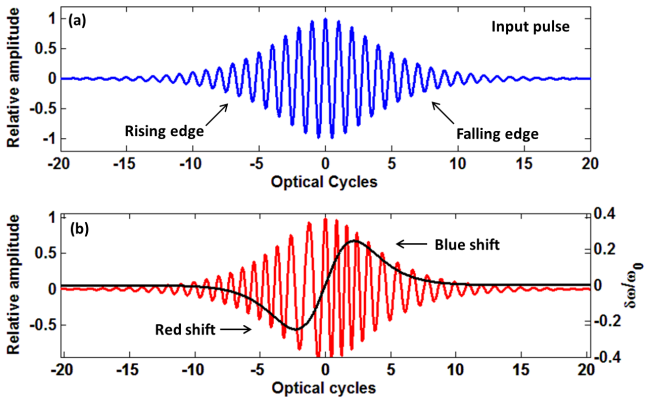

Figure 2.6 (a) The initial pulse (blue line) shown with no phase modulation, whose leading and trailing edges induce a phase shift proportional to the instantaneous intensity. (b) The output pulse (red line) after propagation through some length of the nonlinear medium shows frequency chirp. The black line shows the relative instantaneous frequency shift induced by the pulse at the rising and the falling edges respectively.

In order to extract the nonlinear parameter γ from this measurement, the effects of not only SPM, but also GVD and higher order dispersion terms as well as nonlinear losses need to be properly taken into account as all these processes will have an effect on the output pulse spectrum. For this purpose, the generalized nonlinear Schrödinger equation (NLSE) was numerically integrated:

$$\frac{\partial E}{\partial z} = \sum_{k\geq 2} i^k \frac{\beta_k}{k!} \frac{\partial^k E}{\partial t^k} - \frac{\alpha_{lin}}{2} E + \left(1 + \frac{i}{\omega_0}\frac{\partial}{\partial t}\right)\left(iRe(\gamma)|E|^2 - \frac{\alpha_{tpa}}{2A_{eff}}|E|^2\right)E - \frac{\sigma}{2}(1+i\mu)N_c E \tag{2.19}$$

The derivation of the exact form of the NLSE is left for Chapter 4 where it will be discussed in more detail. Here, E is the amplitude, normalized such that $|E|^2$ represents the total power. The first term on the right hand side of the equation corresponds to the dispersive effects of the waveguide, the second terms accounts for the linear loss, next two terms are for SPM and TPA respectively while the last term accounts for FCA and FCD. The results of the numerical integration of Eq. 2.19 for the experimental conditions of Fig. 2.7(a) - with only the value of γ being a free parameter - are shown in Fig. 2.7(b). It can be seen that there is a reasonably good match with the experimental spectra. Specifically, the extra lobes introduced to the spectra as a result of SPM can be clearly identified. Thus, the value for the nonlinear parameter γ was extracted to be 100 $W^{-1}m^{-1}$. With this, the nonlinear figure of merit (FOM) for these waveguide can be calculated as $FOM_{NL} = Re(\gamma)/\left[4\pi Im(\gamma)\right] = 3.5$ which is quite impressive compared to other nonlinear platforms [58–60]. With the Re(γ) value, one can also calculate the characteristic nonlinear length, which is defined as the length over which the nonlinear phase ϕ_{NL} is 1 radian: $L_{NL} = (\gamma P)^{-1}$. Thus, we see that for peak input powers of up to 78 W, $L_{NL} > L_{eff}$.

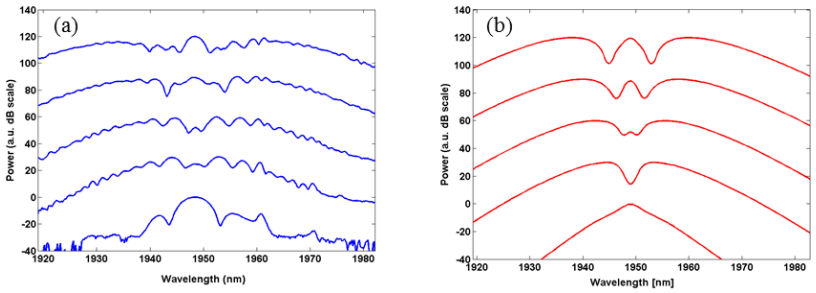

Figure 2.7 (a) The experimental output spectra for coupled peak powers of 1.9 W, 6.1 W, 7.6 W, 9.5 W and 11.1 W showing SPM-mediated broadening and the characteristic lobed spectral profile. (b) The simulated spectra using the NLSE to extract the nonlinear parameter.

2.3.4 Supercontinuum generation

With the results and understanding of the previous two sections, all the important and relevant parameters of the a-Si:H waveguide for supercontinuum generation

have been characterized. Figure 2.8 below shows the build-up of the supercontinuum spectrum in this waveguide with increasing input pump powers.

Several features of this build-up should be noted that relate to the previous sections. First, as the input pump peak power increases beyond 6 W, clear SPM-related spectral broadening is observed, as expected from the discussion in the previous section. Secondly, above a pump peak power of 7.5 W, two sidebands are visible at 1820 nm and 2100 nm, emerging from the background noise on either side of the pump. We know from sec. 2.2.1 that this is the first modulation instability sideband (labelled as MI1 in Fig. 2.8) due to the anomalous dispersion of the waveguide at the pump wavelength. As the pump power approaches 10 W, the second pair of MI sidebands (labelled as MI2 in Fig. 2.8) is seen emerging farther away around 1650 nm and 2100 nm. As the pump power is further increased to about 11 W, the MI sidebands begin merging into a continuous spectrum. Upon further increase of the pump power, the spectrum broadens further until at 46 W peak power its -40 dB bandwidth extends from 1470 nm to 2470 nm, thus connecting the telecom and short-wave infrared range. It can be observed that on the longer wavelength side, the MI sidebands are less pronounced. This is a result of the increased linear losses in that wavelength range as was shown in Fig. 2.4(b).

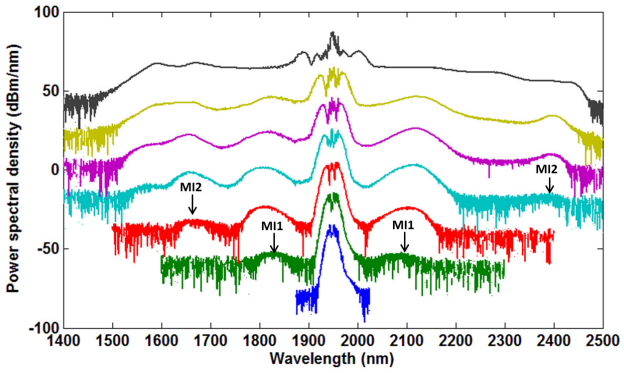

Figure 2.8 The buildup of the supercontinuum with increasing input pump peak powers of (from bottom up) 6.1 W, 7.6 W, 9.5 W, 11.1 W 12.6 W, 14.7 W and 46 W. Successive plots are shifted up by 20 dB for visual clarity. The rise of modulation instability sidebands MI1 and MI2 is shown.

Clearly, both the dispersive and nonlinear properties of a-Si:H are important in realizing this large bandwidth. Since the value of γ is known from the SPM measurement, we can extract the values of the second and fourth order dispersion of the a-Si:H waveguide from the positions of the MI1 and MI2 bands respectively as $\beta_2 = 0.4\, ps^2/m$ and $\beta_4 = 1.3 \times 10^{-3}\, ps^4/m$. The value of β_2 compares well with the simulated value for the waveguide shown in Fig. 2.3, however, the β_4 value is much larger than expected. This discrepancy can be explained by realizing that

the higher order dispersion terms are very sensitive to exact parameters of the simulation, both for the material as well as geometric. The simulations of Fig. 2.3 were performed for a waveguide cross-section as measured in the scanning electron microscope and the material dispersion of c-Si since this data was unavailable for a-Si:H. Obviously, using the actual material dispersion of a-Si:H would give a better simulation of the dispersive properties of the waveguides. However, it was observed in [51] that even for the case of SOI waveguides where the material dispersion of c-Si is very well known, extracting the correct β_4 value from simulations is unlikely because even small errors in the knowledge of the geometry is enough to significantly affect the calculations. Hence, values for dispersion terms of orders higher than β_2 need to be measured experimentally [51].

The figure of merit for this a-Si:H shows that it is definitely an attractive candidate for nonlinear applications such as SCG. However, as we have seen in the discussions of sec. 2.2.1, the dispersive properties remain a vital component in such applications. Thus, it is instructive to be able to examine the roles that the dispersive and nonlinear properties each play in this specific case of SCG. For example, it might be argued that the main advantage of the platform comes from its dispersive properties. Specifically, it is the emergence of the MI2 sidebands that makes it possible to achieve the broadband SCG. While this is true, the nonlinear properties also have an important role to play. This can be proven by trying to generate a supercontinuum in a similar waveguide structure on the SOI platform, and thus be able to directly compare the a-Si:H and c-Si materials. Their similarity in terms of material dispersion should mean that one should be able to set up a c-Si waveguide with similarly placed MI1 and MI2 sidebands. In that case, one can directly compare the efficiency of SCG on both platforms purely in terms of their respective nonlinearities. Exactly such an experiment was performed and the results of the supercontinuum buildup in such a c-Si waveguide are shown in Fig. 2.9. The cross section dimensions of this waveguide were nominally the same as the one used for SCG in the amorphous case.

We can see that similar to the case of the a-Si:H waveguide, MI1 and MI2 sidebands emerge with increasing pump powers, but the spectral coverage at the same input powers is much smaller in this case. This is because the nonlinear losses arising from TPA are quite significant in c-Si since the pump wavelength of 1.95 μm is below its half-bandgap value. Clearly, the high figure-of-merit of the material is vital for SCG and other nonlinear applications.

Compared to other integrated nonlinear platforms, the present demonstration of SCG is certainly not the broadest, both in terms of the absolute bandwidth and in terms of the number of octaves it spans. However, the present demonstration of SCG does highlight the possibility of using this material platform for useful applications in important spectral windows such as the MIR wavelength range. This could thus enable low-cost, robust solutions for such applications because of the CMOS-compatibility of the a-Si:H platform. Table 2.1 shows a comparison of the

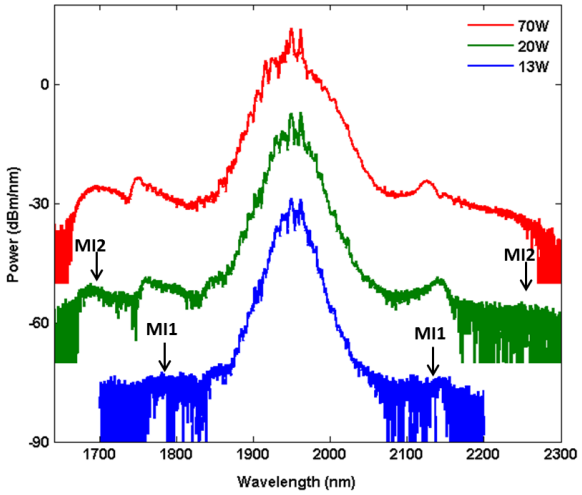

Figure 2.9 Supercontinuum generation experiment in a c-Si waveguide with the same dimensions for a-Si:H. The dispersive properties are clearly similar as shown by the positions of the MI1 and MI2 sidebands. However, the SCG is not as efficient, showing the importance of a high figure of merit platform.

different results in various on-chip nonlinear platforms in terms of the SC bandwidth and various pump characteristics such as the pulse width, center wavelength, average and peak powers. The present work is shown in the first row of the table (published in [31]).

Table 2.1: Comparison of present work to supercontinuum generation in literature

Ref.	Material platform	Bandwidth (in octaves at -30 dB)	Pulse energy (pJ)	Pulse width (fs)	Average power (mW)	Peak power (W)	Pump Wavelength (nm)
[31]	a-Si:H	0.65	21	1240	0.54	16.5	1950
[7]	a-Si:H	0.53	6.4	1600	0.064	5	1550
[37]	Chalcogenide waveguide	0.7	60	610	0.5	68	1550
[61]	Silicon Nitride	1.6	160	200	13	800	1335
[62]	Lithium Niobate	1 (-40 dB level)	7000	97	500	72000	2000

A final consideration is the material stability in the presence of high powers that was alluded to in section 2.2. Since it was hypothesized in [63] that the mate-

rial degradation observed when high power pulses are coupled into the waveguide occurs due to TPA, the reduced TPA absorption coefficient at the pump wavelength of this experiment should allow for a better material stability. Indeed, it was found that no material degradation occurs at this pump wavelength even when the coupled-in peak powers are more than an order of magnitude higher than those required to degrade it at 1.55 μm. Figure 10 shows that a broad supercontinuum is continuously observed for a time period of several hours, which is a timescale about 40 times longer than the timescales over which the degradation was observed at 1.55μm. Clearly, the lowered TPA at this pump wavelength significantly alleviates the problem of material degradation.

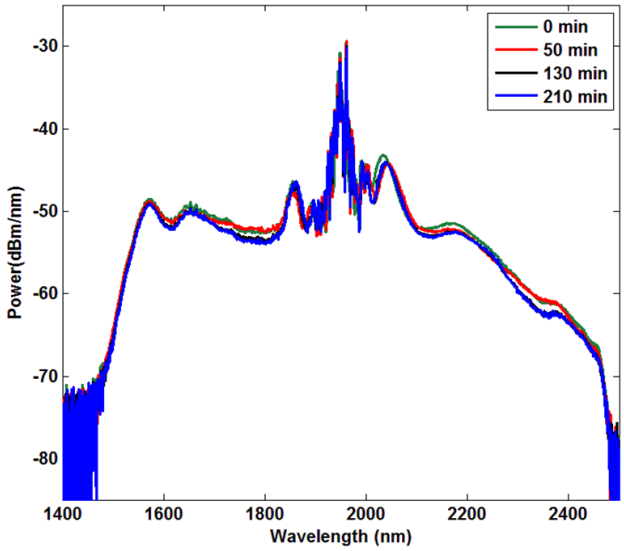

Figure 2.10 Stability of the generated supercontinuum over several hours showing no significant material degradation due to the high pump powers coupled into the waveguide.

2.4 Conclusions

Hydrogenated amorphous silicon was shown to be an interesting material for nonlinear applications. Its inherent advantages over crystalline silicon in terms of reduced nonlinear losses were highlighted. Specifically, supercontinuum generation spanning the telecom to mid-infrared wavelength range was demonstrated with a fiber-based pump source. It was also shown that unlike the experiments at telecom wavelengths, material stability to high pump powers is not a problem in this wavelength range. Thus, it is an interesting platform for spectroscopy and sensing, not in least because it is an integrated platform with a high figure of merit that can be

mass manufactured in a CMOS foundry.

References

[1] JS Aitchison, DC Hutchings, JU Kang, GI Stegeman, and AIEEEJ Villeneuve *The nonlinear optical properties of AlGaAs at the half band gap* IEEE journal of quantum electronics, 33(3):341–348, 1997.

[2] Juthika Basak, Ling Liao, Ansheng Liu, Doron Rubin, Yoel Chetrit, Hat Nguyen, Dean Samara-Rubio, Rami Cohen, Nahum Izhaky, and Mario Paniccia *Developments in gigascale silicon optical modulators using free carrier dispersion mechanisms* Advances in Optical Technologies, 2008, 2008.

[3] Tsung-Yang Liow, Kah-Wee Ang, Qing Fang, Jun-Feng Song, Yong-Zhong Xiong, Ming-Bin Yu, Guo-Qiang Lo, and Dim-Lee Kwong *Silicon modulators and germanium photodetectors on SOI: monolithic integration, compatibility, and performance optimization* IEEE Journal of Selected Topics in Quantum Electronics, 16(1):307–315, 2010.

[4] K Yamada, H Fukuda, T Tsuchizawa, T Watanabe, T Shoji, and S Itabashi *All-optical efficient wavelength conversion using silicon photonic wire waveguide* IEEE Photonics Technology Letters, 18(9):1046–1048, 2006.

[5] Andrzej Gajda, Lars Zimmermann, Mahmoud Jazayerifar, Georg Winzer, Hui Tian, Robert Elschner, Thomas Richter, Colja Schubert, Bernd Tillack, and Klaus Petermann *Highly efficient CW parametric conversion at 1550 nm in SOI waveguides by reverse biased pin junction* Optics express, 20(12):13100–13107, 2012.

[6] Junrong Ong, Ranjeet Kumar, and Shayan Mookherjea *Efficient continuous-wave four-wave mixing in SOI waveguides with active carrier removal* In CLEO: Science and Innovations, pages CTh1F–6. Optical Society of America, 2013.

[7] Jassem Safioui, François Leo, Bart Kuyken, Simon-Pierre Gorza, Shankar Kumar Selvaraja, Roel Baets, Philippe Emplit, Gunther Roelkens, and Serge Massar *Supercontinuum generation in hydrogenated amorphous silicon waveguides at telecommunication wavelengths* Optics express, 22(3):3089–3097, 2014.

[8] François Leo, Simon-Pierre Gorza, Jassem Safioui, Pascal Kockaert, Stéphane Coen, Utsav Dave, Bart Kuyken, and Gunther Roelkens *Dispersive wave emission and supercontinuum generation in a silicon wire waveguide pumped around the 1550 nm telecommunication wavelength* Optics letters, 39(12):3623–3626, 2014.

[9] C Grillet, L Carletti, C Monat, P Grosse, B Ben Bakir, S Menezo, JM Fedeli, and DJ Moss *Amorphous silicon nanowires combining high nonlinearity, FOM and optical stability* Optics express, 20(20):22609–22615, 2012.

[10] Stephen K OLeary, SR Johnson, and PK Lim *The relationship between the distribution of electronic states and the optical absorption spectrum of an amorphous semiconductor: An empirical analysis* Journal of applied physics, 82(7):3334–3340, 1997.

[11] N Vukovic, N Healy, FH Suhailin, P Mehta, TD Day, JV Badding, and AC Peacock *Ultrafast optical control using the Kerr nonlinearity in hydrogenated amorphous silicon microcylindrical resonators* Scientific reports, 3:2885, 2013.

[12] Xin Gai, Duk-Yong Choi, and Barry Luther-Davies *Negligible nonlinear absorption in hydrogenated amorphous silicon at 1.55 μm for ultra-fast nonlinear signal processing* Optics express, 22(8):9948–9958, 2014.

[13] R. R. Alfano and S. L. Shapiro *Emission in the Region 4000 to 7000 Å Via Four-Photon Coupling in Glass* Phys. Rev. Lett., 24:584–587, Mar 1970.

[14] PB Corkum, Claude Rolland, and T Srinivasan-Rao *Supercontinuum generation in gases* Physical review letters, 57(18):2268, 1986.

[15] John M Dudley, Goëry Genty, and Stéphane Coen *Supercontinuum generation in photonic crystal fiber* Reviews of modern physics, 78(4):1135, 2006.

[16] EJR Kelleher, M Erkintalo, and JC Travers *Fission of solitons in continuous-wave supercontinuum* Optics letters, 37(24):5217–5219, 2012.

[17] AS Mayer, A Klenner, AR Johnson, K Luke, MRE Lamont, Y Okawachi, M Lipson, AL Gaeta, and U Keller *Frequency comb offset detection using supercontinuum generation in silicon nitride waveguides* Optics express, 23(12):15440–15451, 2015.

[18] Alireza Marandi, Charles W Rudy, Victor G Plotnichenko, Evgeny M Dianov, Konstantin L Vodopyanov, and Robert L Byer *Mid-infrared supercontinuum generation in tapered chalcogenide fiber for producing octave-spanning frequency comb around 3 μm* Optics express, 20(22):24218–24225, 2012.

[19] Bart Kuyken, Takuro Ideguchi, Simon Holzner, Ming Yan, Theodor W Hänsch, Joris Van Campenhout, Peter Verheyen, Stéphane Coen, Francois Leo, Roel Baets, et al. *An octave-spanning mid-infrared frequency comb generated in a silicon nanophotonic wire waveguide* Nature communications, 6, 2015.

[20] ST Sanders *Wavelength-agile fiber laser using group-velocity dispersion of pulsed super-continua and application to broadband absorption spectroscopy* Applied Physics B, 75(6-7):799–802, 2002.

[21] Yuan Liu, Matthew D King, Haohua Tu, Youbo Zhao, and Stephen A Boppart *Broadband nonlinear vibrational spectroscopy by shaping a coherent fiber supercontinuum* Optics express, 21(7):8269–8275, 2013.

[22] CF Kaminski, RS Watt, AD Elder, JH Frank, and J Hult *Supercontinuum radiation for applications in chemical sensing and microscopy* Applied Physics B, 92(3):367–378, 2008.

[23] I Hartl, XD Li, C Chudoba, RK Ghanta, TH Ko, JG Fujimoto, JK Ranka, and RS Windeler *Ultrahigh-resolution optical coherence tomography using continuum generation in an air–silica microstructure optical fiber* Optics letters, 26(9):608–610, 2001.

[24] T Morioka, H Takara, S Kawanishi, O Kamatani, K Takiguchi, K Uchiyama, M Saruwatari, H Takahashi, M Yamada, T Kanamori, et al. *1 Tbit/s (100 Gbit/s$\times$ 10 channel) OTDM/WDM transmission using a single supercontinuum WDM source* Electronics Letters, 32(10):906–907, 1996.

[25] Teppei Nakasyotani, Hiroyuki Toda, Toshiaki Kuri, and Ken-ichi Kitayama *Wavelength-division-multiplexed millimeter-waveband radio-on-fiber system using a supercontinuum light source* Journal of lightwave technology, 24(1):404, 2006.

[26] I-Wei Hsieh, Xiaogang Chen, Xiaoping Liu, Jerry I Dadap, Nicolae C Panoiu, Cheng-Yun Chou, Fengnian Xia, William M Green, Yurii A Vlasov, and Richard M Osgood *Supercontinuum generation in silicon photonic wires* Optics express, 15(23):15242–15249, 2007.

[27] Lianghong Yin, Qiang Lin, and Govind P Agrawal *Soliton fission and supercontinuum generation in silicon waveguides* Optics letters, 32(4):391–393, 2007.

[28] Bart Kuyken, Xiaoping Liu, Richard M Osgood, Roel Baets, Günther Roelkens, and William MJ Green *Mid-infrared to telecom-band supercontinuum generation in highly nonlinear silicon-on-insulator wire waveguides* Optics Express, 19(21):20172–20181, 2011.

[29] Takahiro Goto, Atushi Ishizawa, Rai Kou, Tai Tsuchizawa, Nobuyuki Matsuda, Kenichi Hitachi, Tadashi Nishikawa, Koji Yamada, HIdeki Gotoh, et al. *Octave spanning frequency comb generation in a dispersion-controlled short silicon-wire waveguide with a fiber laser oscillator* In CLEO: Science and Innovations, pages SW4G–1. Optical Society of America, 2015.

[30] Lin Zhang, Qiang Lin, Yang Yue, Yan Yan, Raymond G Beausoleil, Anu Agarwal, Lionel C Kimerling, Jurgen Michel, and Alan E Willner *On-chip octave-spanning supercontinuum in nanostructured silicon waveguides using ultralow pulse energy* IEEE Journal of Selected Topics in Quantum Electronics, 18(6):1799–1806, 2012.

[31] Utsav D Dave, Sarah Uvin, Bart Kuyken, Shankar Selvaraja, Francois Leo, and Gunther Roelkens *Telecom to mid-infrared spanning supercontinuum generation in hydrogenated amorphous silicon waveguides using a Thulium doped fiber laser pump source* Optics express, 21(26):32032–32039, 2013.

[32] Hongcheng Sun, Ke-Yao Wang, Reza Salem, Peter Fendel, and Amy C Foster *Coherent Mid-IR Supercontinuum Generation in a Hydrogenated Amorphous Silicon Waveguide* In CLEO: Science and Innovations, pages SM1P–6. Optical Society of America, 2015.

[33] L Shen, N Healy, L Xu, HY Cheng, TD Day, JHV Price, JV Badding, and AC Peacock *Four-wave mixing and octave-spanning supercontinuum generation in a small core hydrogenated amorphous silicon fiber pumped in the mid-infrared* Optics letters, 39(19):5721–5724, 2014.

[34] Haolan Zhao, Bart Kuyken, Stéphane Clemmen, François Leo, Ananth Subramanian, Ashim Dhakal, Philippe Helin, Simone Severi, Edouard Brainis, Gunther Roelkens, et al. *Visible-to-near-infrared octave spanning supercontinuum generation in a silicon nitride waveguide* Optics letters, 40(10):2177–2180, 2015.

[35] Ting Wang, Doris KT Ng, Siu-Kit Ng, Yeow-Teck Toh, AKL Chee, George FR Chen, Qian Wang, and Dawn TH Tan *Supercontinuum generation in bandgap engineered, back-end CMOS compatible silicon rich nitride waveguides* Laser & Photonics Reviews, 9(5):498–506, 2015.

[36] Davide Grassani, Adrien Billat, Martin Hubert Peter Pfeiffer, Hairun Guo, Thibault North, Tobias J Kippenberg, and Camille-Sophie Brès *Mid-infrared supercontinuum generation in a SiN waveguide pumped at 1.55 micron* In Frontiers in Optics, pages FTu5D–3. Optical Society of America, 2016.

[37] Michael RE Lamont, Barry Luther-Davies, Duk-Yong Choi, Steve Madden, and Benjamin J Eggleton *Supercontinuum generation in dispersion engineered highly nonlinear (γ= 10/W/m) As2S3 chalcogenide planar waveguide* Optics Express, 16(19):14938–14944, 2008.

[38] Dong-Il Yeom, Eric C Mägi, Michael RE Lamont, Michaël AF Roelens, Libin Fu, and Benjamin J Eggleton *Low-threshold supercontinuum generation in highly nonlinear chalcogenide nanowires* Optics letters, 33(7):660–662, 2008.

[39] Christian Rosenberg Petersen, Uffe Møller, Irnis Kubat, Binbin Zhou, Sune Dupont, Jacob Ramsay, Trevor Benson, Slawomir Sujecki, Nabil Abdel-Moneim, Zhuoqi Tang, et al. *Mid-infrared supercontinuum covering the 1.4–13.3 μm molecular fingerprint region using ultra-high NA chalcogenide step-index fibre* Nature Photonics, 8(11):830–834, 2014.

[40] Ravi Pant, Chunle Xiong, Steve Madden, Barry Luther Davies, and Benjamin J Eggleton *Investigation of all-optical analog-to-digital quantization using a chalcogenide waveguide: A step towards on-chip analog-to-digital conversion* Optics Communications, 283(10):2258–2262, 2010.

[41] *AdValue Photonics:* http://www.advaluephotonics.com/products/2-um-broadband-light-sources/2-0-um-ase-source.

[42] Bart Kuyken, Hua Ji, Stéphane Clemmen, SK Selvaraja, Hao Hu, Minhao Pu, Michael Galili, Palle Jeppesen, Geert Morthier, Serge Massar, et al. *Nonlinear properties of and nonlinear processing in hydrogenated amorphous silicon waveguides* Optics express, 19(26):B146–B153, 2011.

[43] J Matres, GC Ballesteros, Pauline Gautier, JM Fédéli, J Martí, and CJ Oton *High nonlinear figure-of-merit amorphous silicon waveguides* Optics express, 21(4):3932–3940, 2013.

[44] Govind P Agrawal *Nonlinear fiber optics* Academic press, 2007.

[45] Mark A Foster, Kevin D Moll, and Alexander L Gaeta *Optimal waveguide dimensions for nonlinear interactions* Optics Express, 12(13):2880–2887, 2004.

[46] C Koos, L Jacome, C Poulton, J Leuthold, and W Freude *Nonlinear silicon-on-insulator waveguides for all-optical signal processing* Optics Express, 15(10):5976–5990, 2007.

[47] Shahraam Afshar and Tanya M Monro *A full vectorial model for pulse propagation in emerging waveguides with subwavelength structures part I: Kerr nonlinearity* Optics express, 17(4):2298–2318, 2009.

[48] Ivan D Rukhlenko, Malin Premaratne, and Govind P Agrawal *Effective mode area and its optimization in silicon-nanocrystal waveguides* Optics letters, 37(12):2295–2297, 2012.

[49] Xiaoping Liu, Bart Kuyken, Gunther Roelkens, Roel Baets, Richard M Osgood Jr, and William MJ Green *Bridging the mid-infrared-to-telecom gap with silicon nanophotonic spectral translation* Nature Photonics, 6(10):667–671, 2012.

[50] N Kikuchi and S Sasaki *Fibre nonlinearity in dispersion-compensated conventional fibre transmission* Electronics Letters, 32(6):570–572, 1996.

[51] François Leo, Utsav Dave, Shahram Keyvaninia, Bart Kuyken, and Gunther Roelkens *Measurement and tuning of the chromatic dispersion of a silicon photonic wire around the half band gap spectral region* Optics letters, 39(3):711–714, 2014.

[52] *imec:* http://www2.imec.be/be_en/home.html.

[53] *Europractice:* http://www.europractice-ic.com/SiPhotonics_general.php.

[54] Graham T Reed *Silicon Photonics: the state of the art* John Wiley & Sons, 2008.

[55] HK Tsang, RV Penty, IH White, RS Grant, W Sibbett, JBD Soole, HP LeBlanc, NC Andreadakis, R Bhat, and MA Koza *Two-photon absorption and self-phase modulation in InGaAsP/InP multiquantum-well waveguides* Journal of applied physics, 70(7):3992–3994, 1991.

[56] L Shen, N Healy, P Mehta, TD Day, JR Sparks, JV Badding, and AC Peacock *Nonlinear transmission properties of hydrogenated amorphous silicon core fibers towards the mid-infrared regime* Optics express, 21(11):13075–13083, 2013.

[57] RH Stolen and Chinlon Lin *Self-phase-modulation in silica optical fibers* Physical Review A, 17(4):1448, 1978.

[58] Thomas Vallaitis, Siegwart Bogatscher, Luca Alloatti, Pieter Dumon, Roel Baets, Michelle L Scimeca, Ivan Biaggio, François Diederich, Christian Koos, Wolfgang Freude, et al. *Optical properties of highly nonlinear silicon-organic hybrid (SOH) waveguide geometries* Optics express, 17(20):17357–17368, 2009.

[59] Christian Koos, Philipp Vorreau, Thomas Vallaitis, Pieter Dumon, Wim Bogaerts, Roel Baets, Bweh Esembeson, Ivan Biaggio, Tsuyoshi Michinobu, François Diederich, et al. *All-optical high-speed signal processing with silicon–organic hybrid slot waveguides* Nature photonics, 3(4):216–219, 2009.

[60] HK Tsang, CS Wong, TK Liang, IE Day, SW Roberts, A Harpin, J Drake, and M Asghari *Optical dispersion, two-photon absorption and self-phase modulation in silicon waveguides at 1.5 μm wavelength* Applied Physics Letters, 80(3):416–418, 2002.

[61] R Halir, Y Okawachi, JS Levy, MA Foster, M Lipson, and AL Gaeta *Ultrabroadband supercontinuum generation in a CMOS-compatible platform* Optics letters, 37(10):1685–1687, 2012.

[62] CR Phillips, Carsten Langrock, JS Pelc, MM Fejer, J Jiang, Martin E Fermann, and I Hartl *Supercontinuum generation in quasi-phase-matched LiNbO 3 waveguide pumped by a Tm-doped fiber laser system* Optics letters, 36(19):3912–3914, 2011.

[63] DL Staebler and CR Wronski *Reversible conductivity changes in discharge-produced amorphous Si* Applied physics letters, 31(4):292–294, 1977.

3

INDIUM GALLIUM PHOSPHIDE-ON-INSULATOR AS AN INTEGRATED NONLINEAR PLATFORM

"People won't ever remember how many failures you've had, but they will remember how well it worked the last time you tried it." - Charles F. Kettering

3.1 Introduction

We saw for the case of the hydrogenated amorphous silicon platform in chapter 2 that there are several important considerations that need to be taken into account for achieving efficient nonlinear processes. Ideally, one would have a medium where both linear losses arising from scattering and absorption as well as nonlinear losses arising from multiphoton absorption and free-carrier absorption are minimal in the entire wavelength range of interest. Simultaneously, a large index contrast is desirable because the strong confinement leads to an enhanced intensity of the light and thus a stronger light-matter interaction. Another important consideration is of course the ability to tailor the dispersion properties in order to achieve phase matching as we have already encountered in the last chapter. Finally, access to both the second and third order nonlinearities in the same platform would greatly widen the range and kinds of nonlinear functionalities available.

III-V semiconductor materials offer the possibility to fulfill all of the above requirements. III-V materials are already in widespread use for various active functionalities such as lasers [1–3], modulators [4, 5] etc. As such, there exist robust techniques for the growth, processing and integration of these materials with the already well-developed SOI platform. Moreover, many III-V materials such as $Al_xGa_{1-x}As$ [6], GaAs [7], GaP [8], InGaP [9–13] etc. have been investigated in various contexts for the implementation of nonlinear functionalities. Furthermore, it is desirable (and indeed necessary for certain applications such as wavelength-division multiplexing) to work in the telecommunications wavelength range. Certain III-V materials such as Indium Gallium Phosphide - which will be the primary III-V material employed in the work presented in this thesis - have a bandgap larger than 1.6 eV [14] which means that there is no two-photon absorption when working at 1550 nm, which goes a long way towards reducing the nonlinear losses at these wavelengths in comparison to silicon [9]. Also, because the crystal structure of III-V materials lacks centrosymmetry, they possess non-zero even-order nonlinear susceptibilities contrary to the case of bulk silicon and silicon nitride [15–17]. As a result, important second-order nonlinear processes such as sum and difference frequency generation become possible. Finally, integration of III-V materials with CMOS-compatible platforms such as SOI and SiN is eventually needed for fully integrated solutions. Towards that end, since these materials are already in widespread use for achieving active functionalities in these platforms, one can leverage the existing technologies to also use them for nonlinear functionalities. Hence, the use of the III-V material InGaP for integrated nonlinear optical applications is investigated in this thesis.

3.2 Bulk optical properties of InGaP

Indium Gallium Phosphide ($In_xGa_{1-x}P$) is a ternary alloy where the III-sites are occupied by either Indium or Gallium atoms while the V-sites are occupied by Phosphorus atoms. Figure 3.1(a) shows the material refractive index as a function of wavelength as measured by ellipsometry and compared to the values found in literature [18]. As can be seen, in the telecommunication wavelength range, the index is comparable to that of silicon (which is 3.45 at 1550 nm) and hence structures with a similar index contrast are possible. This provides one of the motivations for using this III-V semiconductor material for on-chip nonlinear applications since the large index contrast implies large intensities for stronger nonlinear interactions.

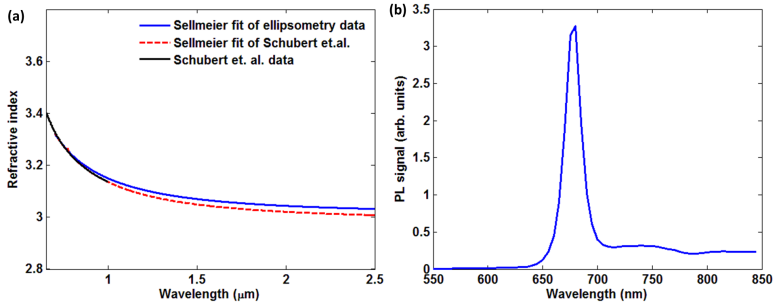

Figure 3.1 (a) Refractive index of the bulk InGaP material as measured by ellipsometry as well as a comparison to values found in literature for $In_{0.49}Ga_{0.51}P$ grown lattice matched on GaAs. (b) The photoluminescence measurement of InGaP shows a peak at 675 nm, indicating a partially ordered crystal structure and a bandgap large enough to avoid TPA around 1500 nm.

Another motivation for using this material is its crystal structure. In general, III-V semiconductors have a zinc blende type crystal symmetry, i.e. they belong to the crystal symmetry group $\bar{4}3m$. For InGaP, the crystal class it belongs to depends on the growth conditions. This is because under certain conditions, when the material is grown on GaAs, it could either be in what is known as the ordered or the disordered state. The ordered state is where the In and Ga atoms are all aligned in alternating planes along the $[\bar{1}, 1, 1]$ or the $[1, \bar{1}, 1]$ directions [15], while the disordered state is the one where the In and Ga atoms are randomly distributed among the III-sites. The disordered state belongs to the usual $\bar{4}3m$ symmetry class. The ordered state on the other hand, has some extra symmetry because of the ordered arrangement of the III atoms and consequently belongs to the $C3v$ or the $3m$ crystal class. The ordered state is known to be stable as the material has been used in red laser diodes which have been shown to stay operational for long periods of time, and can be reliably grown under a wide range of growth parameters. The ordered and the disordered states differ from each other in their bandgap energies with the disordered state exhibiting bandgap energies of up to 0.47 eV higher than the ordered one (depending on the amount of disordering) [14, 19, 20]. Thus the

largest bandgap would be that of the fully disordered state which is known to be 2.005 eV [20] - well above the threshold needed for suppressing TPA at 1550 nm. Since the bandgap decreases for a more ordered material structure, it is important to determine the degree of ordering to be sure of avoiding any TPA in the material at 1550 nm. Figure 3.1(b) shows the photoluminescence spectrum of the InGaP material used in this work. It indicates that the bandgap is large enough to suppress TPA at 1550 nm. It should be noted that the exact bandgap value has a complicated dependence on the degree of ordering, the strain profile etc [21, 22]. Another difference is that since they belong to different crystal symmetry classes, the number of non-zero elements of the second-order nonlinear susceptibility tensor $\chi^{(2)}$ is different [15–17]. However, the dominant $\chi^{(2)}$ contribution in both cases comes from the d_{14} element which is unaffected by the amount of ordering present in the crystal (since it is a feature of the zinc-blende structure itself). The interesting implications of this ordering based change in the $\chi^{(2)}$ tensor will be discussed further later on. For now, it suffices to say that the value of the dominant tensor element d_{14} is approximately 110 pm/V [16]. This is large enough to be of interest for several second-order nonlinear applications such as second-harmonic and difference frequency generation (SHG and DFG). For these processes, d_{eff}/n^2 is the relevant metric and its value for InGaP is more than double the value for $LiNbO_3$, the material of choice for several second-order nonlinear applications. Thus, at least from the point of view of the strength of the available second-order nonlinearity, III-V materials in general and InGaP specifically are very interesting indeed. Similarly, the $\chi^{(3)}$ properties of the material have already been shown to be useful for several on-chip third-order nonlinear applications such as four-wave mixing, self-phase modulation etc. in a photonic crystal platform [9–13]. Thus, the optical properties of the material definitely provide enough motivation for investigating it as a material of choice for integrated nonlinear applications.

3.3 Fabrication of InGaP-on-insulator devices

As mentioned above, a large index contrast is important to have strong confinement of the light, which in turn enables strong light-matter interactions. For example, in the supercontinuum generation experiments discussed in chapters 2 and 4, the strength of the nonlinear interaction is dependent both on the material nonlinearity (characterized by its Kerr index value n_2) as well as the effective area A_{eff}. A stronger index contrast implies a stronger light matter interaction for the same power by decreasing the effective area. Traditionally, many nonlinear functions implemented in popular III-V materials such as AlGaAs establish waveguiding by slightly varying the material composition to define the core and cladding layers [23–27]. This enables convenient growth of these layers and fabrication, and hence is a great approach for proof-of-concept demonstrations. However, this approach does not lend itself to easy integration with other platforms which is important for final applications. Moreover, it also results in a reduced index contrast since the index difference between various III-V material compositions is typi-

cally small. Compared to that, the index contrast between III-V materials and the cladding layer in the SOI platform - silicon dioxide - is much larger. Hence, if instead of another III-V material, one could have a low index material like silica as the cladding layer for the III-V core, then the resulting index contrast would be much higher. For example, at 1550 nm, InGaP has a refractive index difference of about 1.60 and 2.05 with silica and air respectively, which is comparable to that of silicon. The index contrast - defined as $(n_{core}^2 - n_{clad}^2)/2n_{core}^2$ - in SOI is 41% while in case of InGaP it is pretty close at 39%. Thus, one can achieve A_{eff} values approximately as small as those in SOI. This could thus greatly enhance the efficiency of the nonlinear processes and is the motivation for using III-V membranes clad by low index materials to fabricate the devices for implementating nonlinear functionalities. As we shall see, the same approach also allows for easy integration with platforms such as SOI. Also an important feature of this approach is the possibility to modify the dispersion properties according to the needs of a specific application. The high-index contrast nature of this platform naturally lends itself to dispersion engineering because the waveguide contribution to the total dispersion can be significant, similar to what was seen in the previous chapter with the a-Si platform. Another degree of freedom available here while designing for applications is the ability to freely choose the thickness of the III-V membrane in which the nonlinear devices will be fabricated. In platforms such as SOI, the total thickness is restricted by various other considerations. As we shall see in this section, all these advantages naturally come together in the approach followed in this work.

In order to overcome the problem of the lack of a direct bandgap in Si, a lot for work has already been done towards integrating III-V materials with CMOS-fab processed SOI chips by post-processing them to incorporate active elements such as lasers in the SOI platform [1–5]. This can be done either by 'gluing' the III-V layer to the SOI chip thereby bonding them together [28, 29] or by the direct growth of the required material on the SOI itself [30]. Direct growth is difficult to achieve and depends on the specific material used, while the bonding approach is both easier and more versatile in terms of materials, and is the approach followed in this work. The bonding can be done either using an appropriate adhesive agent as the intermediate layer or by means of the so-called direct bonding where the two surfaces to be bonded together are treated such that the intermolecular forces between them cause them to adhere [31]. Direct bonding requires extremely clean surfaces and is procedurally speaking more difficult. Here, the adhesive bonding approach is followed.

Briefly, the procedure begins by taking the desired III-V epitaxial stack and using the polymer Divinylsiloxane-bis-benzocyclobutene (BCB) as the adhesive agent to bond it upside down to the desired substrate as shown in Fig. 3.2. The III-V growth substrate and any other layers not needed for the final devices are then removed with dry or wet etching techniques leaving behind a thin membrane of the desired III-V material bonded on top of the substrate. BCB is a transparent polymer in the wavelength range of interest in this work (which is primarily the

telecommunications wavelength range) and has a refractive index of about 1.55 i.e., only slightly larger than silica. Thus, BCB does not pose a problem in terms of its optical properties, at least when working in this wavelength range. It should be noted for future reference that any nonlinear processes that extend into the mid-infrared (MIR) wavelength regime might be hampered by strong absorption in the BCB, which might be a problem that needs specific attention in the device design to ensure that the BCB layer is nowhere near where the MIR light will be [32]. For those cases, direct bonding might be an option worth considering. After bonding and substrate removal, the devices in the III-V membrane are defined by electron beam (e-beam) lithography and those patterns are subsequently etched by an inductively coupled plasma (ICP), as shown in Fig. 3.2.

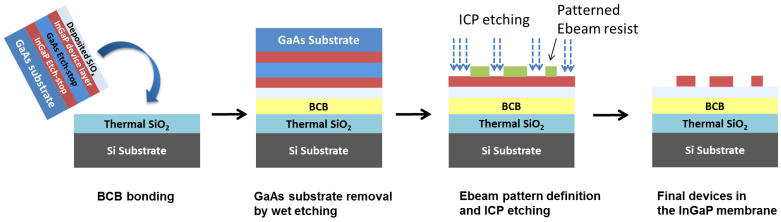

Figure 3.2 Overview of the various steps in the fabrication of InGaP-on-insulator devices. The process begins with BCB bonding of the III-V stack, followed by its substrate removal, E-beam lithography and finally ICP etching of the InGaP membrane to define the devices. The substrate could be a patterned SOI or SiN chip, or, as is shown here, it could just be a 'carrier wafer' which is a silicon substrate and an oxide top cladding.

Obviously, the integration of the devices in the InGaP layer with those in the SOI chip first requires an optimized process for the fabrication of those devices in the bonded membrane. Hence, a step-by-step approach was followed where first the bonding and substrate removal processes of the III-V epitaxial stack to an unpatterned carrier wafer were optimized (see Fig. 3.2). Then, the pattern definition in the bonded InGaP membrane by e-beam lithography and the ICP etching of those patterns was also optimized. The unpatterned carrier wafer (referred to from here onwards as the 'blank substrate') was a silicon substrate wafer with a 3 μm thick thermal oxide layer on top, which acted as part of the cladding for the bonded InGaP layer, thus ensuring a large index contrast for the devices in the InGaP membrane. This approach allowed the optimization of the fabrication of the InGaP structures without worrying about the next step - integration with a CMOS-fab processed chip. Another advantage was that it allowed for the fabrication of simple devices such as gratings, waveguides, ring resonators etc. which are very useful in characterizing the linear and nonlinear properties of the platform. This way, it was possible to test whether or not the overall approach as well as the specific material chosen here are indeed viable for the various intended nonlinear functionalities. Once it is proven that the InGaP devices fabricated in this way are indeed suitable for nonlinear applications, the same process flow can be adapted

to using a patterned SOI or SiN chip as the substrate instead of the blank carrier wafer. In doing so, some additional complications of course arise in terms of aligning the respective patterns in the two device layers to efficiently couple light back and forth, but the overall fabrication flow can be adopted more or less exactly. Thus, as a first step, the fabrication of InGaP devices on a blank carrier wafer was carried out, which is described in this chapter. The details of the extra processing steps required for the integration with both SOI and SiN chips are detailed later in Chapter 5.

3.3.1 Bonding

First, an InGaP layer of appropriate thickness is grown lattice matched to the GaAs substrate. A couple of intermediate etch-stop layers are also incorporated into the stack. They are subsequently used during the substrate removal step, as will be explained later. The typical epitaxial stack is shown in Table 3.1, with only the thicknesses of the individual layers being varied according to the needs of the specific task. The epitaxy was not grown as part of the work of the PhD thesis but was either procured from collaborators at Thales, Paris or LPN, Paris or from the commercial vendor EPILAB, Poland [33]. The top layer is a thin cap layer for protection of the epitaxy. Below that is the InGaP device layer of appropriate thickness in which the nonlinear devices will be eventually fabricated. Beneath the device layer are the two sacrificial layers, which are used as etch stops during substrate removal. Finally, at the bottom is the GaAs substrate whose lattice constant matches that of $In_{0.51}Ga_{0.49}P$ (hereon referred to simply as InGaP).

Table 3.1: The III-V epitaxial layer stack for InGaP-on-insulator devices

Material	Thickness (nm)	Layer function
GaAs	50	Cap Layer
InGaP	250	Device Layer
GaAs	200	Sacrificial Layer
InGaP	200	Etch Stop Layer
GaAs	350 μm	Growth substrate

Immediately upon receiving the epitaxy, a layer of the resist AZ5214E would be spun on top to provide extra protection for ease of handling. This is especially necessary when handling a new wafer without a protective cap layer or when cleaving the wafer into smaller sections. Typically, these cleaved dies used for individual fabrication runs would be $\sim$5$\times$5 mm^2 to 1 cm^2. In case the final devices for whatever reason required a silica layer between the III-V and the BCB/substrate - either to function as buffer layer for optical isolation or merely for improving the adhesion to the BCB - the resist is removed from one of the cleaved sections by rinsing it with Acetone, Isopropyl alcohol (IPA) and deionized (DI) water and silicon oxide (also referred to as just oxide in this thesis) of the required thickness is deposited using plasma enhanced chemical vapour deposition (PECVD). In order

to have a uniform oxide thickness, a piece larger than a few cm is typically cleaved for deposition since some height variation at the edges is usually expected. The required dies are then cleaved from this larger piece while being careful to avoid the edges. If the GaAs cap layer is present it is removed after the resist removal step prior to the deposition by etching the die for 30 s in an oxidizing acid solution of H_3PO_4:H_2O_2:H_2O in volume ratio 3:1:25. This solution selectively etches only the GaAs at a rate of approximately 100 nm/min, thus exposing the InGaP device layer. This surface needs to be as clean as possible since it will form the bottom surface of the InGaP devices and any particles or roughness present will cause losses. The presence of large particles can also ruin the bonding as we shall see. The dies are then kept aside until they are ready to be used for bonding. If needed, the dies can be placed in an ultrasonic bath of Acetone for a few minutes with gentle agitation to remove any particles on the surface. They are then baked on a hotplate set at a temperature of $120\,^{\circ}\mathrm{C}$ for 15 minutes to remove any trace of water.

The preparation of the substrate prior to bonding for both the blank wafer and the CMOS fab-processed SOI or SiN chip begins first with an Acetone-IPA-DI water rinse of the substrate in order to remove any resist layer on top. Just like the III-V die, the substrate also needs to be cleaned thoroughly in order to ensure a successful bonding. For this purpose, the standard clean (SC1) procedure, which involves immersing the substrate in a 5:1:1 solution of ammonia, hydrogen peroxide and DI water for 15 minutes at 70-80 $^{\circ}\mathrm{C}$, can be employed to remove any organic and other particulate contaminants. In case the substrate has a silicon top surface, it also assists in making the silicon surface hydrophilic, which improves the adhesion to BCB since it is hydrophobic. However, in case the substrate is a new wafer of the blank substrate with the thermal oxide on top, this step is typically not necessary. It is then cleaned with O_2 plasma for 15 minutes to both remove any remaining organic contaminants as well as activate the surface for bonding. The substrate is subsequently also baked for 15 minutes on a hotplate at $120\,^{\circ}\mathrm{C}$ to ensure complete water desorption before bonding. Meanwhile, the BCB bonding solution is prepared by mixing the commercially available BCB solution BCB-3022-35 (CYCLOTENE^{TM} 3000 Series from Dow chemicals [34]) with its solvent Mesitylene. The exact ratio of the BCB and the solvent depends on the desired thickness of the final BCB layer. The solution is then spin coated onto the substrate, with the spin rate, again depending on the desired BCB thickness. In this work, a distinction is made between two kinds of bondings that were performed, characterized by the approximate thickness of the spin-coated BCB layer. In the case of the substrate being the blank silicon wafer, a ”thick” bonding was usually preferred where pure BCB-3022-35 solution undiluted by Mesitylene was used (resulting in a thick BCB layer), while for the case of patterned SOI or SiN chip substrates, a diluted BCB:Mesitylene solution was used. The reason for using a thick BCB for the blank substrate was that since there was no coupling of light between different layers (as would be the case for the patterned SOI/SiN substrate), there is no specific restriction on the BCB thickness based on those optical considerations. The thick BCB layer is more tolerant of any remaining particu-

late contaminants and thus increases the chances of a successful bonding. On the other hand, with the patterned chip substrates, the necessity of coupling of light between the silicon/SiN layer and the InGaP layers imposes certain restrictions on the overall thickness of the intermediate layers between them. The exact thickness needed depends on the manner of light coupling, the exact geometry as well as the refractive indices of all the layers. However, as we will see in chapter 5, these thicknesses are in the range of 50-300 nm and thus, large BCB thicknesses are not desirable. In that case, the BCB solution is diluted by Mesitylene and spin coated at a specific rate to produce the desired thickness. It should be realized that the final thickness also depends on the amount of pressure applied to the III-V die while bonding and thus the BCB dilution, spin rate as well as bonding pressure are all factors to be considered while optimizing the process in terms of the final BCB layer thickness.

For the thick bonding, the pure BCB solution is spin-coated at 2000 rpm for 30 s. Fig. 3.3(a) shows the measured thickness profile across a scratch made in the BCB after the bonding (in an area not under the III-V die) showing that the BCB thickness is 1.59 μm. It should be noted that this is not the BCB thickness beneath the III-V layer, which also depends on the pressure applied. A range of BCB thicknesses can be realized by simply varying the spin-rate of the pure BCB solution as shown in Fig. 3.3(b) [34]. Once the substrate is spin coated with the BCB, it is baked at $155\,^{\circ}\mathrm{C}$ on a hotplate for 15 minutes to evaporate the solvent. The III-V dies are then placed with the InGaP surface (or deposited oxide) contacting the BCB (see Fig. 3.2). To make sure that there are no bubbles trapped underneath, the die is lightly pressed with the handling tweezers and dragged around the substrate. Because the bonding is done "manually" by merely placing the III-V die on top of the substrate, this kind of bonding is also referred to as 'manual bonding'. The hotplate is then switched off and the substrate and III-V die are left to slowly cool down to room temperature. The BCB now needs to be fully cured so that it cross-links and polymerizes thus securely bonding the two surfaces together. In case of the thick bonding, this is done in an oven programmed to increase the temperature in steps to $300\,^{\circ}\mathrm{C}$, at which temperature the BCB is cured for 1 hour. Table 3.2 below gives the details of the temperature ramps and the time spent at a particular temperature. The curing is done in a N_2 environment.

Table 3.2: The curing procedure for bonding with thick BCB

Step no.	Duration (hh:mm:ss)	Temperature (°C)	Ramp rate (°C/min)	N_2 environment
1	0:01:00	25	–	1
2	0:25:00	150	5	1
3	0:25:00	150	0	1
4	1:33:45	300	1.6	1
5	1:00:00	300	0	1
6	1:13:20	25	–3.75	1

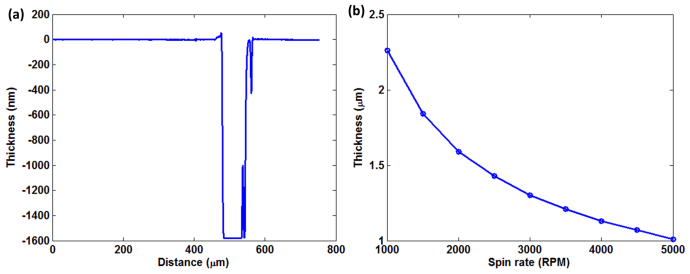

Figure 3.3 (a) The measured BCB thickness across a scratch made in a bonded sample. (b) The spin-coated BCB thickness as a function of the spin rate.

In case of the thin bonding, the BCB:Mesitylene solution is prepared in a volume ratio 4:3 while the substrate is being baked for desorption. After the desorption bake, the substrate is cooled down to room temperature and spin coated with the BCB solution at a rate of 5000 rpm for 30s. The spin-coated chips are then baked at a temperature of $80\,^{\circ}\mathrm{C}$ for 15 minutes before proceeding to bonding. The actual bonding is done in the Suss Microted Bonder [35], which provides control over the various parameters that are important for good, repeatable bondings. The parameters are the pressure in the bonding chamber, the temperature as well as the pressure applied to the III-V/substrate stack while bonding. For the case of thin bonding, since the success of the bonding is very sensitive to these parameters, the level of control provided by the bonder is important. As a result, thin bonding is also sometimes referred to as 'machine bonding'. After the BCB bake, the III-V die is placed on the substrate at the appropriate position and loaded into the bonding machine between two glass plates. The bonder is programmed to evacuate the bonding chamber to a vacuum of 10^{-4} mbar and the temperature is raised to $170\,^{\circ}\mathrm{C}$ and maintained there for 15 minutes to remove all the solvent. Then the temperature is increased to $300\,^{\circ}\mathrm{C}$ and maintained for half an hour. Meanwhile the bonding tool (which applies the preset pressure to the III-V die) is brought in contact with a force calculated to provide a pressure of 500 mbar. Then the temperature is lowered back down to room temperature. This results in a final BCB thickness of about 50 nm. Once the bonding is done, the bonded stack can be taken for removal of the III-V growth substrate.

3.3.2 Substrate removal

The III-V growth substrate removal is done via wet etching. If for some reason, a reduced etching time is needed, grinding can be done beforehand to thin down the substrate. The GaAs substrate is etched by a 1:4:1 volume ratio of HNO_3:H_2O_2:H_2O [36]. The etch process involves two steps both of which occur in the same solution concurrently. In the first step, the peroxide oxidizes the top surface of the GaAs. In the second step the oxidized layer is then removed by the acid. The relative ratio of the oxidizer to the acid can be used to control the etch rate. In fact, several different acids can be employed for the second oxide

removal step [37]. For example a phosphoric acid based etch was also trialed but it was the nitric acid etch that gave the most reliable results with an acceptably fast etch rate. Without any stirring of the solution, the etch rate of the optimized solution is typically 4-5 μm/min and stays more or less constant throughout. The etch rate can be increased to about 6 μm/min by stirring the etch solution at 50 rpm. The etch solution is selective against the etch-stop layer of InGaP. Due to the large selectivity ratio (>100), the etch-stop layer does not need to be very thick, and hence typically, a 200 nm thick etch-stop layer was used. As the substrate is being etched the top surface looks rough and has a grey metallic color. When the etch-stop layer is reached a shiny metallic copper-colored surface can be observed. Hence it is very easy to spot the end of the GaAs substrate removal. The InGaP etch-stop layer is then removed using a pure HCl solution. The etch-stop removal in HCl gives rise to bubbles and the end of bubble formation indicates the end of the etch-stop removal, which takes approximately 30 s. The final sacrificial GaAs layer is removed using the same nitric acid solution as was used for the substrate removal. The phosphoric acid based etch that was used to remove the cap layer can also be used to ensure a smooth top surface. The final layer has a pinkish or greenish hue depending on whether the InGaP device layer thickness was 250 nm or 320 nm. Fig. 3.4 shows the microscope images of the various stages of the substrate removal for the case of the InGaP device layer being 250 nm thick.

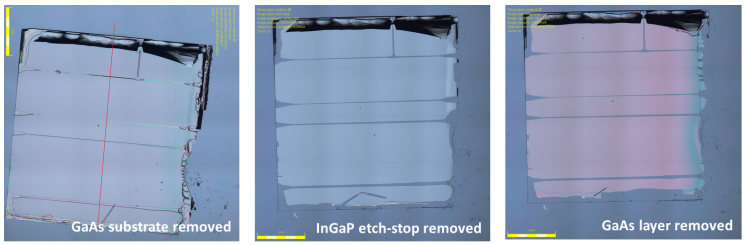

Figure 3.4 Cracks parallel to the cleaved edges are clearly visible after the GaAs substrate is removed. Also observable in these microscope images is the color change associated with each of the successive stages of the substrate removal process.

Several difficulties were encountered during the development of the substrate removal process apart from finding an appropriate etching chemistry. For one, cracks can emerge during any stage of the substrate removal, but are generally observed after there is less than 100 μm of substrate left, and mostly only when a few um of the substrate is left, as shown in Fig. 3.4. They are observed to always be parallel to the edge of the bonded die. The appearance of the cracks can be due to any particle contaminants on either of the surfaces during the bonding. It could also be a result of any residual strain in the epitaxy growth, which is released during substrate removal. However, with careful control of parameters, a strain free growth is possible. If the right stoichiometric ratio of In and Ga atoms can be achieved, it enables the lattice constant of InGaP to be matched to that of GaAs. However, the

growth of the epitaxial stack was not under the scope of this thesis. Still, in order to avoid crack formation it is extremely important to have clean surfaces prior during the bonding. The BCB solution itself may also contain impurities and hence these should be removed by using an appropriate filter.

Another problem associated with the growth is that sometimes a specific section of the epitaxy wafer would contain lots of micron-sized defects and would only be visible after the substrate removal was completed, as shown in Fig. 3.5(a). This can also be avoided with the appropriate optimization of the growth process. Even overetching for several minutes would not get rid of these defects as shown in Fig. 3.5(b). The only solution to this problem was to use a section of the III-V wafer that was free of such defects, which could be done by cleaving a small portion of the wafer close to where the dies to be used for bonding were located and removing its cap layer, and if needed, the device layer, to observe if the surface was defect free or not.

Figure 3.5 (a) Micron-sized defects can be seen in the device layer after the substrate removal has finished. (b) Overetching these defects does nothing to remove them.

Another problem encountered exclusively during the development of the substrate removal process for the thin BCB bonding was that at the point when it is nearly complete and only a few μm of substrate is left, one or multiple corners may debond and that part of the die begins curling back onto itself. This is thought to occur due to etching from the side and the solution reaching underneath the epi from the corners and the residual strain causing the subsequent curling of the epi. The problem is especially exacerbated if the etching solution was being stirred as it promotes the etchants to reach underneath the debonded part. This leads to low yields of the overall bonding-substrate removal process (estimated to be about 30%). The problem was mitigated in the ways outlined below.

The first approach involved applying Crystal Wax to the sides of the bonded epi immediately after the bonding was done and prior to the substrate removal. This wax is impervious to the etching solution and can thus be used to prevent the side etching. The procedure for applying the wax begins with heating the bonded sample up to a temperature of $120\,^{\circ}\mathrm{C}$ on a hotplate, which is the melting temperature of the wax. Thus, when a small piece of the wax is held to the sides of the bonded

die, it will melt and gets deposited on the sidewalls. It is still quite viscous and adhesive and so it doesn't flow away from the sidewalls but rather adheres to them. Once all the sides and corners are satisfactorily coated with the wax, the sample is removed from the hotplate and cooled down. Once it is back to room temperature, the wax will harden and provide protection to the sidewalls. During this procedure, inevitably some of the wax gets onto the top surface and needs to be removed before etching may be performed. Grinding can be performed in a lapping machine for a few minutes to remove any wax on the top side. Once the wax application is finished, the rest of the substrate removal process follows as before. Once the substrate has been removed, the wax can subsequently be removed with Acetone either at room temperature or slightly warmed to a temperature of $50\,^{\circ}\mathrm{C}$. This procedure thus allows for substrate removal without any peeling or curling of the epi. However, it was observed that it often (though not always) lead to the formation of micron-defects sized like the ones mentioned above, which are impossible to remove. Sometimes, the defects would be confined to only the etch-stop layers and their removal would thus get rid of all the defects leading to a large uncracked, defect free and fully bonded InGaP membrane on the substrate, i.e. in nearly ideal condition. Hence, even though this approach solved the one problem of the side etching, it did not significantly improve the yield.

The other approach involved simply sacrificing a part of the die as it began curling back during the final stages of the substrate removal. The curling back of the die usually begins at one corner and if one breaks off that portion by gently tapping it with the tweezers while the rest of the die was still being etched, it would reduce the amount of die that finally became unbonded. This of course required one to bond a III-V die whose area was large enough such that even if a section of the die had to be broken off in this way, the remaining III-V would still cover the relevant areas above the patterned chip. This approach gave higher yields per bonding, but of course, used more of the III-V material to achieve it. Typically, the size of the die needed to ensure full coverage would be larger than the chip design on which the III-V membrane was to be bonded by about 2-3 mm on all sides. With these approaches, bonding of InGaP membranes to patterned chips and then patterning them to couple light between the two layers was successfully achieved, as will be discussed further in chapter 5.

3.3.3 Lithography and etching of InGaP structures

For various nonlinear applications, devices such as gratings, tapers, waveguides, microdisks and microrings needed to be fabricated. Electron beam (e-beam) lithography is the ubiquitous tool for such fabrication needs because not only does it allow for the definition of deep subwavelength, nanometer-scale structures; it also makes rapid prototyping of such devices possible. Thus several design iterations are possible, which is essential while developing new technologies. Hence, e-beam lithography was ideally suited for the purpose of this work. Also, it helps that in the photonics community, there is a large amount of expertise of fabricating

submicron sized features with e-beam lithography for a variety of similar III-V materials in the context of applications such as lasers etc. This applies to not only the lithography but also the etching of these structures. Since, in the cleanroom facilities of the Photonics Research Group of Gent University, e-beam lithography was not available, a collaboration was set up with the group of Fabrice Raineri at LPN, Paris, who do have the required facilities and expertise. There, a process had already been developed for fabricating photonic crystal lasers in InP using e-beam lithography and inductively coupled Plasma (ICP) etching. This same process was leveraged with a few modifications to fabricate the required structures in InGaP since the materials are very similar. It should be noted that although these modifications to the existing lithography and etching process were developed as part of the work of this thesis, it was primarily the work of Fabrice Raineri and his group. Here, a brief overview of the process is given.

For the e-beam lithography, the sample preparation begins with doing oxygen plasma treatment on the sample for 3 minutes followed by baking it in an oven at $150\,^{\circ}\mathrm{C}$ for 15 minutes to remove all the surface moisture. A few nm of oxide is then sputtered onto the surface to improve the adhesion of the resist layer. Then, hydrogen silsesquioxane (HSQ) is spin coated on the sample at 3000 rpm for 60 s resulting in a 280 nm thick layer, followed by baking it at $90\,^{\circ}\mathrm{C}$ on a hotplate for 45 minutes. The sample is then loaded into the e-beam machine for exposure. Care must be taken to properly align the sample's edges with the holder because the e-beam can only handle up to a 1° of angular misalignment of the sample relative to the holder. Thus, it is helpful to have long straight edges or structures on the sample to aid with this pre-alignment. When the sample has been exposed, it is developed in a 1:4 volume solution of AZ400K in DI water for 40 s. During development, bubble formation can be observed and the sample can be gently removed from the solution for an instant to remove the bubbles. Since it is a negative resist, the exposed patterns remain after the development and the structures written in the HSQ resist layer should now be visible under a microscope. Once it is confirmed that the structures have been written properly, the sample is ready to be etched.

The etching is done in the inductively coupled plasma (ICP) etcher. The sample is attached to a silicon carrier wafer with the help of a thermal glue which assists in regulating the heat flow. The silicon carrier is important since it will help in the creation of the oxides that passivate the sidewalls during the etching. The gases used are HBr/O_2/He. HBr provides the reactive species that do the etching. One advantage of using HBr over similar etchants like Cl_2 is that the byproducts formed are more volatile at lower temperatures and need not be removed separately [38, 39]. The oxygen combines with the silicon carrier and aids in the passivation of the sidewalls [40, 41], while the He-species provides the right dilution of the reacting species as well as a physical component to the etch mechanism. The progress of the etching can be followed in real time by observing the reflected signal of a laser as it reflects off of the surface being etched. The interference between the reflected signals from the top and the bottom of the membrane causes a change in the re-

flected signal. Figure 3.6(a) shows an example of this trace. A change in the slope indicates that the etching is finished. From this, the etch rate can be calculated to be 5.8 nm/s. Once the etching is finished, the sample is unmounted from the carrier. If required, the HSQ resist on top of the structures can be removed using reactive ion etching (RIE). As mentioned, several iterations are required to optimize the etching recipe. Each time, the ratio of the gases was slightly varied and the result observed in the SEM. The sidewall roughness is observed and decreased through several iterations in order to get better devices. Figure 3.6(b) shows the SEM image of the optimized InGaP waveguide using the gases in the ratio 10:0.9:90 sccm. As will be described in the next section, there is still room for improvement of the overall processing since the linear losses observed with this were still relatively high.

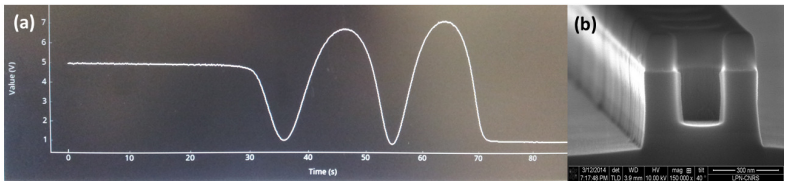

Figure 3.6 (a) The reflected laser signal for following the progress of the etching. The etching begins at about the 30 s mark and finishes at 70 s marked by the change in the laser signal's slope. (b) The SEM image of an InGaP photonic crystal waveguide etched with a 10:0.9:90 sccm gas ratio. The sidewall roughness observed is a quick indication of the etch quality.

If a second etch step is required - as in the case of the shallow etched gratings described in the next section - the same e-beam lithography and ICP etching steps can be repeated with the only modification being that the e-beam resist is a positive tone resist (PMMA) and it is used to define patterns in a silicon nitride hardmask. In this way, the already written structures are protected as only the portions to be etched in the second stage would be exposed in the e-beam and removed at the development stage. The exposed PMMA resist is developed in a 1:3 solution of Methyl isobutyl ketone (MIBK) and IPA in a temperature controlled bath at $20.5\,^{\circ}\mathrm{C}$. Then, the PMMA patterns are transferred to the SiN hardmask by RIE etching (which does not affect the InGaP membrane below). Subsequently, the second ICP etching can be performed. As before, the etching can be followed by observing the reflected laser signal but since this time a full etch is not to be performed, the etching has to be stopped after a time calculated from the etch rate as deduced from Fig. 3.6(a). Then the SiN hardmask is removed using CHF_3/SF_6 gases in RIE. In this way, structures with a two etch steps were fabricated. Figure 3.7 below summarizes the entire fabrication flow.

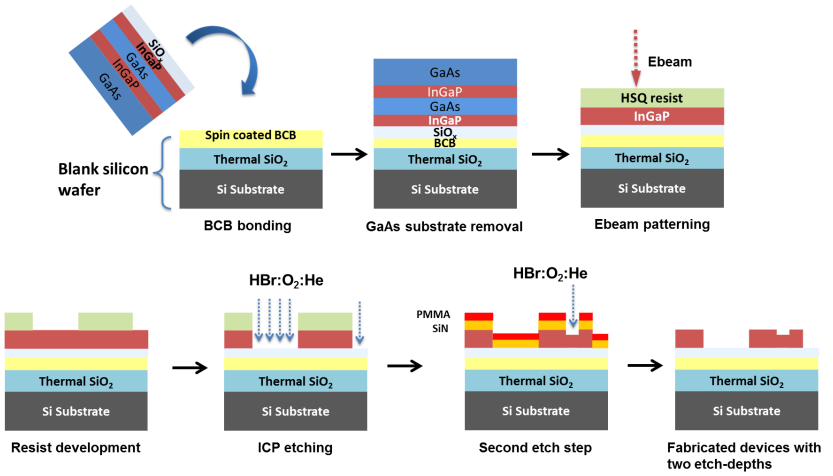

Figure 3.7 A detailed overview of the entire process flow for the fabrication of two etch-step devices in an InGaP membrane bonded to a blank silicon wafer.

3.4 Properties of InGaP waveguides for nonlinear applications

The potential of the InGaP-on-insulator platform as a nonlinear platform is characterized by measuring its linear and nonlinear properties. For this purpose, InGaP waveguides were fabricated in the bonded membranes as outlined in the previous section. To couple light into these waveguides, shallow-etched gratings were designed and fabricated. Both continuous wave and pulsed transmission measurements were performed in order to quantify the linear and nonlinear losses. Finally, four-wave mixing and self-phase modulation measurements were performed in order to determine the Re(γ) value as well as prove the usability of the platform for important nonlinear applications.

3.4.1 Grating coupler design and measurement

As a first step towards characterizing the linear and nonlinear properties of this platform, grating-coupled waveguides of various widths and a height of 250 nm were fabricated. Both fully and partially etched gratings for the transverse electric (TE) polarization were designed and fabricated. Because of the large index contrast between InGaP and the air/oxide cladding, fully etched grating structures are generally not very efficient. The reason for this is that the light experiences a large change in effective index between the unetched and etched portions of the grating, and hence most of the light is coupled out within a few grating periods resulting in a poor mode-overlap with the single-mode fiber, whose mode field diameter is about 10 μm. This is also found to be the case in the SOI platform, which has a

slightly larger index contrast [42, 43]. A smaller index step would thus be beneficial and it is generally achieved by partially etching the grating trenches. This obviously requires two etch steps to be performed which increases the fabrication complexity. However, as explained in the previous section, the second step is not overly difficult since it requires exposure over only the small area of the gratings, which is very fast and also does not need a very precise alignment since the grating is actually defined in the second step. Thus, for most of the work reported in this thesis, these shallow etched gratings were used.

The design process starts with estimating the parameters of the equation for Bragg's Law:

$$\beta_{WG} - G_m = k_z \tag{3.1}$$

$$\frac{2\pi}{\lambda} n_{eff} - \frac{2\pi}{\Lambda} m = \frac{2\pi}{\lambda_0} n_{clad} sin(\theta) \tag{3.2}$$

$$n_{eff} = n_{clad}\, sin(\theta) + m\frac{\lambda_{res}}{\Lambda} \tag{3.3}$$

Here, β_{WG} is the propagation constant of the waveguide mode, G_m is the grating vector and k_z is the projected wave vector in the plane of the grating, n_{eff} and n_{clad} are the effective and the cladding indices respectively, *m* is the grating order, θ is the angle of the incident light, λ_0 is the wavelength of peak grating efficiency and Λ is the grating length. The n_{eff} can be estimated by taking the average of the effective indices of the two slab waveguides corresponding to the unetched and the partially etched thicknesses (or in the case of the fully etched grating, the index of the trench-filler material). The value of the grating order m is generally kept to be 1 for maximum efficiency. Knowing all the other parameters, Λ can thus be extracted. For example, for the shallow etched grating, the average effective index for slab heights of 200 nm and 250 nm was calculated to be 2.257. The slab mode effective index can be easily calculated from the transcendental equation for the fundamental TE mode of an asymmetric slab waveguide. This yields for the period a value of 744 nm for a wavelength of 1550 nm. Compared to the grating period of 630 nm used in 220 nm thick SOI waveguides for the same wavelength, the InGaP period needs to be larger. The larger period is required since the effective index in InGaP is smaller compared to that in silicon. Thus a grating period of 744 nm, a fill factor of roughly 50% and a partial etch depth of 50 nm are thus the starting parameters for full finite-difference time-domain (FDTD) simulations. FDTD is a suitable technique for such simulations because it naturally provides the coupling efficiency for a wide frequency bandwidth in a single simulation run [44, 45]. The parameters that need to be optimized are the period, fill factor, partial-etch depth and coupling fiber angle. The total slab thickness is fixed depending on the specific application considerations and was 250 nm here.

The simulations were performed initially using CrystalWave software from Photon Design [46] and then later using Lumerical FDTD [47]. Fig. 3.8(a) shows

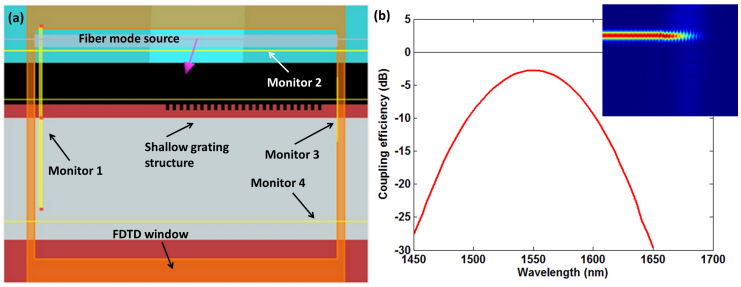

Figure 3.8 (a) The setup for 2D-FDTD simulation of a grating coupler showing the relevant geometry. (b) The simulation gives coupling efficiency over a wide range of wavelengths. Inset: The simulated electromagnetic energy flux (Poynting vector) distribution over the grating structure shown in (a) at the peak grating efficiency wavelength.

the setup for simulation in the Lumerical FDTD software. The simulation in the CrystalWave software was similar. In this 2D simulation, the fiber on the top side is the source that acts as the input to the grating structure. The software simulates the passage of a pulse of light centered at the desired wavelength through this structure. Monitors placed all over the simulation area register the power flux going through them. Once the simulation is complete, these monitors then perform a Fourier transform of the time domain information they registered to give the transmission as a function of frequency. Monitor 2 registers the power flux going through towards the grating and monitor 1 registers the power flux going through the waveguide which is coupled to the grating. The coupling efficiency as a function of wavelength can thus be calculated by taking a ratio of the power flux through the power monitors 1 and 2. If the simulation is setup correctly, the results account for the variation in the coupling efficiency due to the bottom cladding thickness as well. Fig. 3.8(b) inset shows an example of field distribution at the peak coupling efficiency wavelength for one such grating structure. It can be observed that most of the light is coupled to the waveguide on the left while the rest is mostly lost to the substrate or reflected back.

Thus, the output of such a simulation gives the grating coupling efficiency over a wide range of wavelengths, as shown in Fig. 3.8(b). In this way, starting from the values calculated from Eq. 3.3, the various parameters can then be varied to optimize the desired characteristics like the coupling efficiency at any desired wavelength or the 3dB bandwidth of the grating. Designs based on such simulations were fabricated as outlined in the previous section. The best coupling efficiency achieved with a fully etched grating at a wavelength of 1550 nm was only -13 dB. As expected, the fully etched gratings are quite inefficient and hence partially etched gratings were also fabricated. Figure 3.9(a) shows the measured coupling efficiencies of various fabricated partially etched gratings with different periods, all with a fill factor of 0.5 and an etch depth of 70 nm. It can be observed that the grating with period 725 nm has the highest coupling efficiency of -7.5 dB at 1540

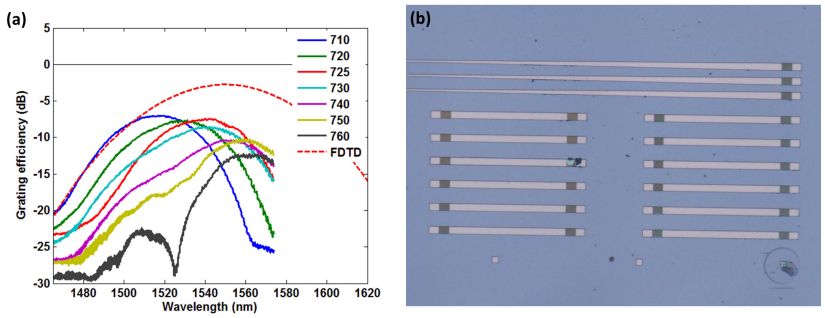

Figure 3.9 (a) The measured coupling efficiencies of various partially etched gratings with different periods (solid lines) and the simulated efficiency for the 725 nm period grating (dashed line). (b) Microscope image of the fabricated test gratings as well as the taper to couple to waveguides.

nm. For comparison, the simulated coupling efficiency for the 725 nm grating as a function of wavelength is also shown in dashed line. The difference in the peak coupling efficiency is only a few nm, while the 3 dB bandwidths vary considerably. The value for the peak efficiency was also higher in the simulation by about 5dB. These differences could arise from a number of factors like deviation of actual grating parameters from the optimized design. For example, a change in the bottom oxide thickness from 3 μm to 3.25 μm causes the simulated peak efficiency to decrease from -3 dB to -7 dB. However, even with these variations, an acceptable coupling efficiency of -7.5dB and a 3dB bandwidth of about 47 nm is obtained for the wavelength range of interest in the telecommunication C-band. Also, the optimized fabrication process flow yields reliable results over several separate fabrication runs. Figure 3.9(b) shows the microscope image of the fabricated gratings at the bottom and, at the top, the gratings coupled via tapers to waveguides. The grating width of 12 μm is tapered down to the required waveguide width (which was typically between 0.5-1 μm) via a 900 μm long taper which is long enough to ensure adiabatic transition and thus minimal conversion loss to the fundamental TE mode of the coupled waveguide.

3.4.2 Linear loss

Once grating couplers with a reasonable efficiency and bandwidth were achieved, loss properties of the waveguides could be characterized. Figure 3.10(a) shows the loss measured as a function of waveguide length at 1540 nm, which is the peak grating efficiency wavelength. From the slope of the linear fit, the linear loss is extracted to be 11.8 dB/cm. Obviously, compared to the SOI platform, the linear loss is about an order of magnitude higher and should be reduced in order to be able to fully exploit the advantageous nonlinear properties of InGaP. This requires further optimization of the fabrication process, and every step along the way needs to be carefully re-optimized to get the best possible quality. For example, in the present case, the large loss is thought to occur due to sidewall roughness of the

waveguides. Thus, to get the smoothest possible sidewall surface, both the e-beam lithography and ICP etching processes should be optimized together. Nevertheless, as we will see demonstrated in the following sections and chapters, despite the relatively large linear loss, the platform is already capable of supporting several nonlinear functionalities with a high efficiency. It should also be noted that in individual fabrication runs linear losses as low as 6 dB/cm were achieved but these have been difficult to repeat. Also, other groups have demonstrated low loss III-V waveguides in similar platforms by developing highly optimized fabrication processes specifically for those materials [48].

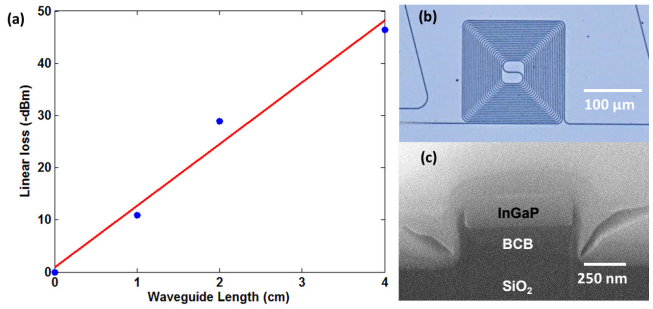

Figure 3.10 (a) Linear loss characterization by the cutback method with waveguide lengths up to 4 cm. (b) The 1 cm long spiral fits easily inside a square space of 180 μm by 180 μm due to the large index contrast of the III-V material. (c) A SEM cross-section image of the waveguide.

Figure 3.10(b) shows the 1 cm long waveguide used in this measurement. It is wound into a tight spiral with bends of 10 μm, thus making it possible to accommodate the full 1 cm long waveguide inside a 180 μm wide square. This is possible because the large index contrast allows for these tight bends without incurring a debilitating loss penalty. This shows another advantage of the high index contrast nature of this InGaP-on-insulator platform: highly compact designs are possible similar to the case of the SOI platform. Figure 3.10(c) shows a SEM image of a waveguide cross-section.

3.4.3 Nonlinear loss

From the photoluminescence measurement shown in Fig. 3.1(b), it is expected that there should be no two-photon absorption loss in InGaP above a wavelength of 1350 nm. Thus, the nonlinear loss consists of the next higher order loss term, which is of course three-photon absorption (3PA). In this situation, the loss in the waveguides is characterized by the following equations:

$$\frac{dI}{dz} = -(\alpha_{lin} + \alpha_{3pa} I^2 + ... + \sigma_{fca} N_c) I \tag{3.4}$$

$$\frac{dN_c}{dt} = \frac{\alpha_{3pa}}{3h\nu_0} I^3 - \frac{N_c}{\tau_{recomb}} \tag{3.5}$$

Here, α_{lin} and α_{3pa} are the linear and three-photon absorption loss terms, σ_{fca} is the free-carrier absorption cross-section, N_c is the carrier concentration, ν_0 is the frequency of light and τ_{recomb} is the recombination lifetime of the carriers. Note that here the source term in the carrier equation corresponds to three-photon absorption since that is the lowest-order mechanism by which electrons can be promoted to the conduction band, as opposed to equation 2.1 where it was the TPA term. And since 3PA is a fifth-order effect, it is expected to be much weaker, and hence its influence is especially small at low to moderate intensities. Hence, as a first approximation, the carrier term can be ignored unless the powers get so high as to cause a significant amount of carriers to be generated.

Following the experiment for the determination of the TPA coefficient of the a-Si:H waveguides in sec. 2.3.2, the 3PA coefficient α_{3pa} of InGaP waveguides can similarly be extracted by measuring the transmission of a pulsed laser with high enough peak powers to induce significant 3PA losses. For this experiment, the source used was a modelocked laser centered at 1540 nm with a *sech*^{2} pulse shape with a width of 2.8 ps (as determined by autocorrelation measurement) and repetition rate of 10 MHz. The measurement was performed on a vertical setup as described in chapter 2 with in- and out-coupling of the pulsed laser through the grating couplers. The laser was kindly provided by collaborators at ULB, Brussels where this experiment was conducted. Figure 3.11 below shows the peak output power from a 1 cm long InGaP waveguide of 650 nm width and 250 nm height as a function of the input peak power and a clear decrease in the transmission at high peak powers is evident.

In order to prove that the decrease in the transmission with increasing pump power is really due to 3PA and not TPA (which would cause a similar looking decrease in the output power with increasing input power), Eq. 3.4 is solved first by keeping only the α_{lin} and α_{tpa} terms and then by only keeping the α_{lin} and α_{3pa} terms to analyze the TPA and 3PA-only cases respectively. The respective solutions are as follows [49]:

$$\frac{1}{T} = \frac{P_{in}}{P_{out}} = \frac{\alpha_{tpa}\, L_{eff}}{A_{3eff}\, e^{(-\alpha_{lin} L)}} P_{in} + \frac{1}{e^{-\alpha_{lin} L}} \tag{3.6}$$

$$\frac{1}{T^2} = \frac{P_{in}^2}{P_{out}^2} = \frac{2\,\alpha_{3pa} L_{3eff}}{A_{5eff}^2\, e^{-2\alpha_{lin} L}} P_{in}^2 + \frac{1}{e^{(-2\alpha_{lin} L)}} \tag{3.7}$$

Here, P_{in} and P_{out} are the input and output peak powers, L_{eff} and L_{3eff} are the respective effective interaction lengths defined as $(1 - e^{-\alpha_{lin} L})/\alpha_{lin}$ and $(1 -$

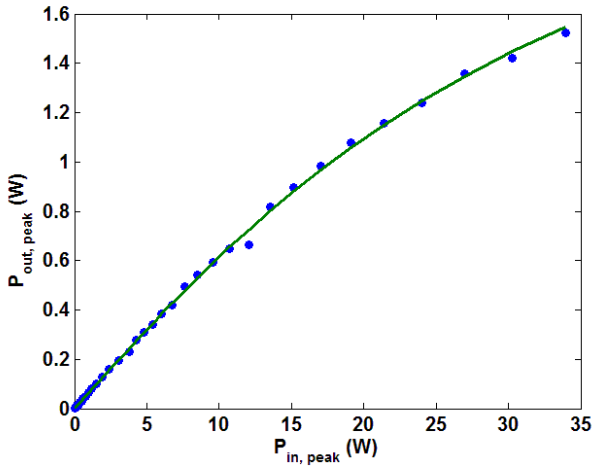

Figure 3.11 The transmission behavior of a 2.8 ps laser pulse as a function of the input peak power (dots) and the fit (solid line) using the theoretical formula of Eq. 3.7 to extract the α_{3pa} value of $2.5 \times 10^{-2} cm^3 GW^{-2}$.

$e^{-2\alpha_{lin}L})/(2\alpha_{lin})$, L is waveguide length and A_{3eff} and A_{5eff} are the effective waveguide areas for third-order and fifth-order processes respectively defined as $(\iint |E|^2 dxdy)^2/(\iint |E|^4 dxdy)$ and $[(\iint |E|^2\, dx\, dy)^3/\iint |E|^6\, dx\, dy]^{1/2}$ [49]. As can be seen from these equations, in case of the TPA dominated waveguide, the reciprocal transmission is a linear function of the input power while in the case of the 3PA dominated waveguide, it is the reciprocal transmission squared that is a linear function of the input power squared. Figure 3.12(a) and (b) show the measured data of Fig. 3.11 replotted in terms of the reciprocal transmission. The clear linear trend of Fig. 3.12(b) shows that the nonlinear loss is indeed 3PA-dominated, as expected from the photoluminescence data in Fig. 3.1(b). The value for the 3PA coefficient can now be extracted using Eq. 3.7. Considering that the nonlinear absorption is strong at the peak of the pulse and weak or negligible at the tails, the time domain nature of the pulse should be taken into account while using Eq. 3.7:

$$T = \int_{-\infty}^{\infty} \frac{(1/2t_0)\, e^{-\alpha L} sech^2(t/t_0)}{\left[1 + (\alpha_{3pa}/\alpha_{lin})\, I_0^2 sech^4(t/t_0)\, (1 - e^{-2\alpha L})\right]^{\frac{1}{2}}}\, dt \qquad (3.8)$$

The solid line in Fig. 3.11 is plotted by fitting this to the data with the 3PA coefficient as the free parameter. In this manner, the value for α_{3pa} is extracted to be 0.025±0.005 cm^3/GW^2. This is comparable to the theoretically calculated value [49] of 0.066 cm^3/GW^2 for similar materials. The theoretical curve of the α_{3pa} value for longer wavelengths is shown in Fig. 3.13. Even though the experimentally determined value is not exactly the same as theory predicts, the general trend is still instructive. As can be seen, the 3PA coefficient peaks at about 1920

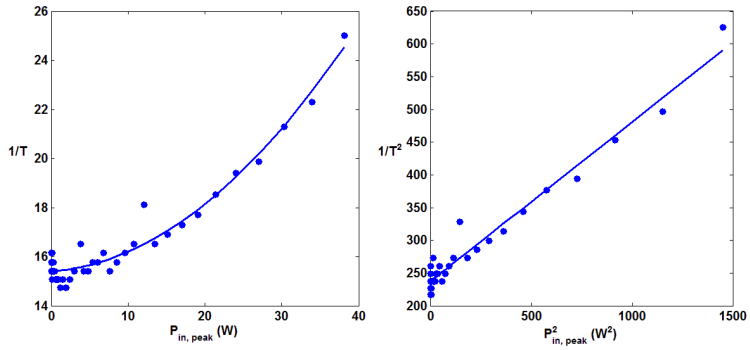

Figure 3.12 (a) The reciprocal transmission is not a linear function of the input peak power as would have been the case if TPA were the lowest order multiphoton absorption according to Eq. 3.6. (b) The reciprocal transmission squared is a linear function of the input peak power squared, which shows that the waveguide is 3PA dominated as described by Eq. 3.7.

nm, which is close to a third of the bandgap and is about 3 times larger. Thus it is important to consider 3PA related losses when especially operating at those longer wavelengths. For wavelengths shorter than 1350 nm, of course, even TPA would be of importance. Thus, for this material the 1.5 μm telecommunications wavelength window is best suited for nonlinear applications since both TPA and 3PA related losses are minimal.

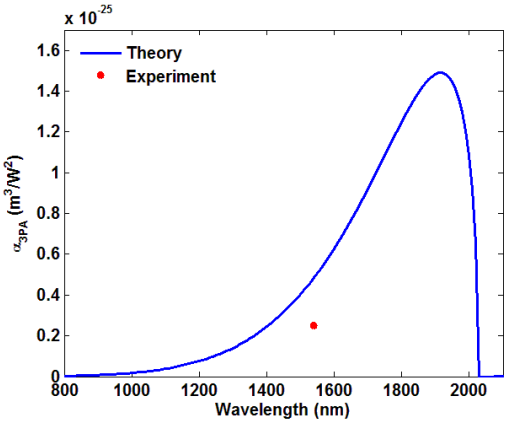

Figure 3.13 Theoretical extension of the 3PA coefficient shows that it is maximal close to a third of the bandgap energy. It shows that operating at longer wavelengths might thus lead to stronger nonlinear losses.

3.4.4 Third order nonlinear gain

The nonlinear parameter γ defined in Eq. 2.9 is still what we are interested in when it comes to the third-order nonlinear processes such as four-wave mixing and self- and cross-phase modulation. As we have seen, there is no TPA, and hence the imaginary part of γ is zero. In this section, the characterization of the real part of γ from a four-wave mixing (FWM) experiment is described. The governing equations (Eq. 2.8) of the FWM experiment have already been described in chapter 2. Here, the FWM experiment is performed in the continuous wave regime as opposed to the pulsed regime. Consequently, the overall efficiency is quite low since the pump power is orders of magnitude smaller than was the case in section 3.4.3. However, the advantage of this approach for the characterization of the nonlinearity is that the various complicating effects that come into play when pulses are involved such as nonlinear losses, self-phase modulation and dispersion related spectral changes (and the associated change in peak power) etc. are absent and we can extract the value of Re(γ) directly from the efficiency of the idler wave generation as a function of the pump or signal power.

The setup for this measurement is shown in Fig. 3.14(a). A CW laser (the pump) is amplified in an Erbium-doped fiber amplifier (EDFA) and the amplified spontaneous emission (ASE) background is filtered out with a narrowband bandpass filter. It is then combined with another CW laser (the signal) using a 50:50 splitter and both are coupled into a 650 nm wide and 2 mm long waveguide via the grating. The waveguide used here is much shorter than the one used for the characterization of the nonlinear loss since the effective interaction length gets saturated due to the high linear losses and hence longer waveguide lengths do not mean any increase in the nonlinear efficiency and in fact, only cause additional losses to the converted signals. The polarization controllers ensure that the polarization of each laser is TE for maximum coupling efficiency. Light from the output grating is sent to an optical spectrum analyzer (OSA), which records the powers of the pump and signal lasers as well as the generated idler wavelength. Figure 3.14(b) shows the output when the coupled in pump (1552 nm) and signal (1551 nm) powers are 38 mW and 1.47 mW respectively. Since the pump power is much larger than the signal or idler powers, we are operating in the undepleted pump regime.

In general, if all three waves are coupled into the waveguide then the direction of the power flow depends on the relative phases of the three waves. Specifically power flow from the pump to the signal and idler waves termed as parametric amplification or the reverse process termed as parametric attenuation occurs if the phase difference $\theta = 2\phi_p - \phi_s - \phi_i = \pi/2$ or $-\pi/2$ respectively [50]. Since in this case, only the pump and the signal are input to the InGaP waveguide, the idler that is generated in the very beginning of the waveguide will have a phase corresponding to that of parametric amplification. In this way as they propagate forward together, the signal and idler waves will be amplified. For this degenerate FWM process, the following equations describe the evolution of the pump, signal

and idler waves along the waveguide [51, 52].

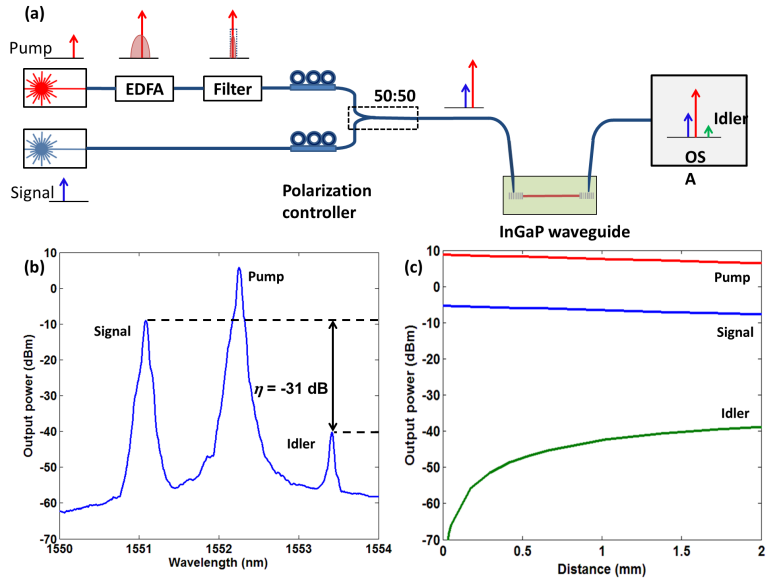

Figure 3.14 (a) The experimental setup for the four-wave mixing experiment for the determination of Re(γ). (b) From the left, the idler, pump and signal powers as measured by OSA for coupled in pump and signal powers of 38 mW and 1.47 mW respectively. (c) The numerically simulated evolution of the pump, signal and idler waves according to Eqs. 3.9-3.11 reproduces the measured idler power for a Re(γ) value of 482 $W^{-1}m^{-1}$. All the powers have been reduced by -7.5 dB to take into account the out-coupling efficiency and facilitate easy comparison with the experimental measurement of Fig. 3.14(b).

$$\frac{dA_s}{dz} = iRe(\gamma)\frac{\omega_s}{\omega_p}\left[\left(|A_s|^2 + 2|A_i|^2 + 2|A_p|^2\right)A_s + A_i^* A_p A_p e^{i\Delta k_{lin} z}\right] - \frac{\alpha_{lin}}{2}A_s \tag{3.9}$$

$$\frac{dA_i}{dz} = iRe(\gamma)\frac{\omega_i}{\omega_p}\left[\left(|A_i|^2 + 2|A_s|^2 + 2|A_p|^2\right)A_i + A_s^* A_p A_p e^{i\Delta k_{lin} z}\right] - \frac{\alpha_{lin}}{2}A_i \tag{3.10}$$

$$\frac{dA_p}{dz} = iRe(\gamma)\left[\left(|A_p|^2 + 2|A_s|^2 + 2|A_i|^2\right)A_p + A_p^* A_s A_i e^{-i\Delta k_{lin} z}\right] - \frac{\alpha_{lin}}{2}A_p \tag{3.11}$$

Here, $A_{s,i,p}$ represents the complex electric field amplitude of the signal, idler and pump waves respectively, z is the position along the waveguide, Δk_{lin} is the linear phase mismatch defined as $\Delta k_{lin} = k_s + k_i - 2k_p \approx \beta_2 \Delta\omega^2$ where $\Delta\omega = \omega_s - \omega_p$

is the pump-signal detuning, and α_{lin} is the linear propagation loss in m^{-1}. Since we are working in the low power continuous wave regime, nonlinear loss terms are negligible and can be ignored. Figure 3.14(c) shows the result of the numerical integration of these coupled equations for the experimental parameters of Fig. 3.14(b). The simulation has Re(γ) as the unknown free parameter and it matches the experimentally observed idler power when setting Re(γ) = 482 $W^{-1}m^{-1}$. The conversion efficiency η is defined as the ratio of the generated idler power to the signal power. To get a better estimate of the Re(γ), the FWM experiment was performed while varying the pump power. Figure 3.15 shows the measured conversion efficiency as a function of the pump power and a comparison with the numerically simulated efficiency which gives a Re(γ) value of 475±50 $W^{-1}m^{-1}$. For comparison, the theoretical conversion efficiency is also included in Figure 3.15. If the undepleted pump approximation is made, theoretically it is given by the following relation [53]:

$$\eta = \frac{P_{idler}(L)}{P_{signal}(L)} = \frac{P_{idler}(L)}{P_{signal}(0)e^{-\alpha_{lin}L}} = \left(\frac{\gamma P_{pump}(0)}{g} sinh(gL)\right)^2 \tag{3.12}$$

$$g = \sqrt{\left(\gamma P_{pump}(0)\right)^2 - \left(\frac{\Delta k_{lin} + 2\gamma P_{pump}(0)}{2}\right)^2} \tag{3.13}$$

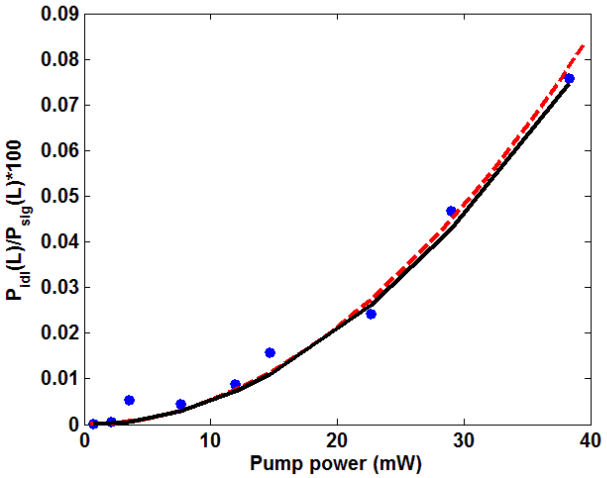

Figure 3.15 The measured (blue dots), numerically simulated (solid black line) and theoretical (red dashed line) conversion efficiency as a function of the coupled in pump power. The simulated and theoretical lines match loosely the experimental data for a Re(γ) value of $475 \pm 50\, W^{-1}m^{-1}$.

Here, g is the parametric gain, $P_{pump}(0)$ is the input pump power and L is the waveguide length. In the regime where the pump-signal detuning $\Delta\omega$ is very small such as in the case of the measurement data shown in Fig. 3.15; the linear phase mismatch $\Delta k_{lin} = \Delta\omega^2\beta_2$ is also very small and thus the effect of the waveguide dispersion is negligible. In that case, η is given by:

$$\eta = \frac{P_{idler}(L)}{P_{signal}(0)e^{-\alpha_{lin}L}} = \left(Re(\gamma)P_{pump}(0)L_{eff}\right)^2 \tag{3.14}$$

Here, L_{eff} is the effective interaction length as defined in Eq. 3.6 and Re(γ) is used in this formula to emphasize that imaginary part of γ is zero in this case. It should be noted that the signal amplification here is very small 0.0034 dB and so the linear loss is the dominant factor in determining the signal output power. Compared to the reported η values for III-V waveguides in literature where the core and cladding layers are both III-V with slightly different compositions, the value measured here is much larger [24–27]. For example, because the Re(γ) values obtained in [27] and [26] are in the range 35-82 $W^{-1}m^{-1}$, the pump power (or effective waveguide length) required to achieve a similar conversion efficiency as in the present case would be about an order of magnitude larger. Shortly after the present work was published, another group used a similar approach as presented here but with the III-V material AlGaAs and achieved even larger conversion efficiency owing to a stronger confinement [54]. This validates the overall approach used here and proves that it can be used with other materials with stronger index contrasts or nonlinearities.

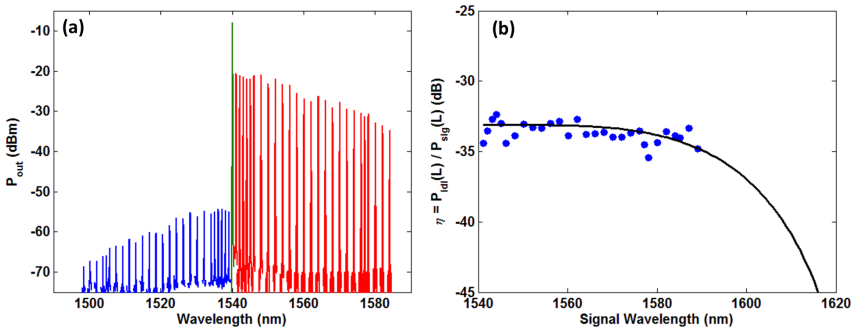

Figure 3.16 (a) The four-wave mixing experiment with several different pump-signal detunings. The pump, signal and idler outputs are shown in green, red and blue respectively. (b) The conversion efficiency for the different detunings (red dots) and the simulated efficiency for Re(γ) = 475 $W^{-1}m^{-1}$ and $|\beta_2| = 0.15ps^2/m$.

It is also instructive to look at the efficiency as a function of the pump-signal detuning. Figure 3.16(a) shows the FWM output from a 1cm long InGaP waveguide (which corresponds to an effective length of 3.4 mm) with 12 mW pump power as the detuning is increased. As the coupling bandwidth of the grating coupler is

limited, the pump-signal detuning can only be increased up to about 40 nm before the generated idler becomes too weak because of higher coupling losses. Of course, at the larger detuning values where Eq. 3.14 may no longer be valid, it is possible that the idler power drops as a result of a reduced conversion efficiency η due to non-negligible role of the phase-mismatch. From Eq. 3.13, it is clear that the detuning required for this drop in the efficiency to be observable depends on the exact value of β_2 (since Δk_{lin} is directly proportional to β_2). If β_2 is small enough, η will remain close to the maximum efficiency even for large detunings. In Fig. 3.16(b), the extracted conversion efficiency as a function of the detuning is shown. As can be seen, there is no significant drop in the efficiency even for the largest detuning, implying that the β_2 value is small. For comparison, the theoretical efficiency calculated using Eq. 3.12 is also shown, where the largest $|\beta_2|$ value that would produce the observed conversion efficiency bandwidth is used. This $|\beta_{2,max}|$ value gives an estimate of the smallest 3dB bandwidth of the conversion efficiency which in this case is 57 nm.

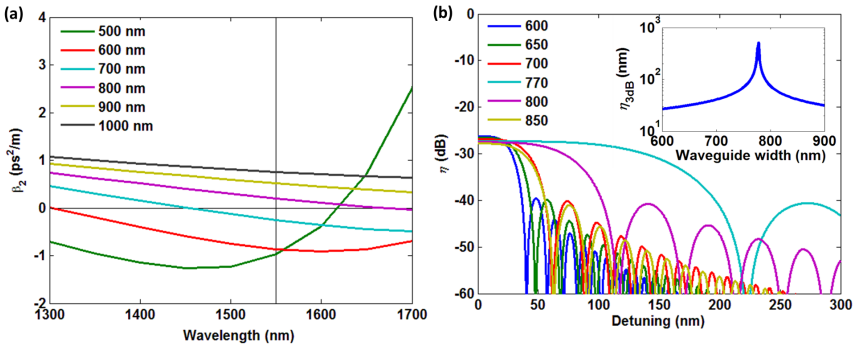

Figure 3.17 (a) The simulated dispersion for InGaP waveguides of various widths (legend, in nm) is shown. (b) The corresponding theoretically calculated FWM conversion efficiency at a pump power of 10 mW and a waveguide length of 1 cm using Eq. 3.12 for various waveguides widths using the experimentally measured Re(γ) value. Inset: 3dB-bandwidths of η as a function of the waveguide width reveals that a bandwidth of several hundred nm is achievable with the right width selection.

This bandwidth can be increased or decreased easily by selecting the appropriate waveguide width to give the required amount of dispersion. A 3 dB-bandwidth of hundreds of nm can be easily achieved by designing the waveguide to have a very small dispersion at the pump wavelength. Figure 3.17(a) shows the simulated dispersion of various waveguides with different widths using the material model from the fit of Fig. 3.1(a). Figure 3.16(b) shows the FWM conversion efficiency for a pump power of 10 mW and a waveguide length of 1 cm calculated using Eq. 3.12 as a function of the pump-signal detuning with the dispersion values corresponding to Fig. 3.17(a) and the experimentally determined value of Re(γ) but rescaled according to the waveguide effective area. As can be seen, by only changing the waveguide width by few tens of nm, the 3 dB-conversion bandwidth

can be significantly modified. There is a small corresponding change in the maximum η of a few dB because the values for the effective area and thus the Re(γ) of the waveguides are slightly different. 3dB-bandwidths of several hundred nm are thus achievable with the right waveguide width as shown in the inset of Fig. 3.17(b). This is just another demonstration of the importance of dispersion engineering for nonlinear applications. Another point that should be noted is that the approach of bonding InGaP membranes allows one to freely choose the height of the waveguide as a parameter, which is not the case in the SOI platform. Thus, if the dispersion properties are more advantageous for a different waveguide height, one could simply bond an InGaP membrane of that thickness.

The Re(γ) measured here is slightly larger than the value reported for the SOI platform which is around 400 $W^{-1}m^{-1}$ [55]. As can be seen from Eq. 3.14, for the same effective interaction length, the generated idler power in the dB scale is linearly proportional to the linear loss of the signal wave. Thus, reducing the losses by 10 dB/cm would give a 10-fold improvement in the generated idler power. With a fully optimized fabrication methodology, such improvements could arguably be expected since other groups have demonstrated such low loss waveguides in a similar platform already [54]. The large linear losses currently experienced mean that it is not possible to improve the conversion efficiency by simply having longer waveguides since the effective interaction length quickly saturates for longer waveguide lengths. For example, at the current loss level, a 2 mm long waveguide reduces to a 1.54 mm long interaction length, while a 1 cm long waveguide, which is physically 5-times longer, only improves the effective interaction length by about a factor of two. Thus, for applications such as wavelength conversion, the only recourse would be to increase the pump power which, as can be seen from Eq. 3.14, provides the same quadratic scaling, but which may not always be desirable.

Nevertheless, even with the current linear loss, and with a Re(γ) value only slightly larger than in SOI, a comparable FWM conversion efficiency in SOI is only obtained in rib waveguides equipped with *p-i-n* diodes that sweep out the carriers thereby reducing the nonlinear losses [56–58]. Without the *p-i-n* diodes mitigating the FCA losses, the efficiency saturates at pump powers somewhat higher than those used here [58], and thus, the efficiency cannot be dramatically improved simply by stronger pumping of the waveguides. This is because, as discussed earlier, for the large intensities involved, it is the nonlinear losses that become the limiting factor. Considering that the nonlinear losses arising from multiphoton absorption (and consequently, from FCA) are much smaller in these InGaP waveguides, it is possible to pump them much harder thus making it possible to implement several nonlinear applications that are either difficult or simply not feasible in the SOI platform without complicated countermeasures such as the incorporation of *p-i-n* diodes. Just such an application - octave spanning supercontinuum generation pumped at telecom wavelengths - is discussed in the next chapter.

3.4.5 Self-phase modulation

As mentioned in the previous chapter, the intensity dependence of the refractive index due to the Kerr effect results in a change in the spectral content (usually a spectral broadening, depending on the sign of n_2 and the initial chirp) of a pulsed laser as it propagates through the nonlinear waveguide. This self-phase modulation (SPM) can be useful in certain applications such as soliton propagation [59], in all-optical regeneration [60], supercontinuum generation especially in the normal dispersion regime [61–63], pulse compression [64, 65] etc., and detrimental in others such as communications [66]. Since the FWM experiment described in the previous section is designed to avoid all interplay with the nonlinear losses, it is interesting to demonstrate a nonlinear process where both the nonlinear gain and loss are present. SPM is one such an application since the peak powers required for large phase shifts of π or more mean that the nonlinear losses can no longer be ignored.

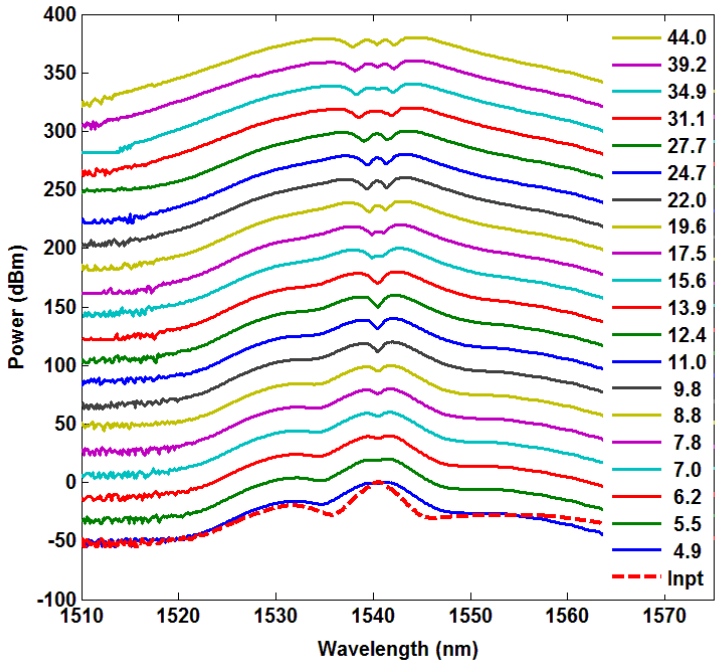

Figure 3.18 The output (solid lines) from the 1 cm long InGaP waveguide show the characteristic SPM initiated dips in the spectra with increasing pump powers. The dotted line shows the input spectrum corresponding to the 4.9 W input peak power and it is identical for all the others except for an increase in the peak power since the input power level was controlled by a variable attenuator.

The setup for measuring SPM was the same one used to characterize the nonlinear losses in sec. 3.4.3. The laser pulse width was 2.8 ps and the repetition rate was 10 MHz. The InGaP waveguide was 1 cm long and had a cross section of 650 nm by 250 nm, light was coupled in and out via gratings. The laser pulses passed through an EDFA, a polarization controller and a variable attenuator before in-coupling through the grating. The variable attenuator is needed so as to allow changing the input power without changing the pulse spectrum which can occur if one instead changes the laser gain. As it is passing through several meters of fiber before the waveguide, certain broadening could occur through SPM in the fiber itself. Hence, to characterize the SPM of the waveguide, it is important to compare it with the input pulse spectrum. Figure 3.18 shows the input and the output spectra for increasing input peak powers. As can be seen, the pulse spectrum both broadens and shows the characteristic spectral dips as the input peak power is increased. The time-bandwidth product of the input pulse is about 0.7 which when compared to the ideal transform limited case of 0.315, shows that the input pulse is not an ideal $sech^2$-pulse as can be seen from spectrum of the dotted line in Fig. 3.18.

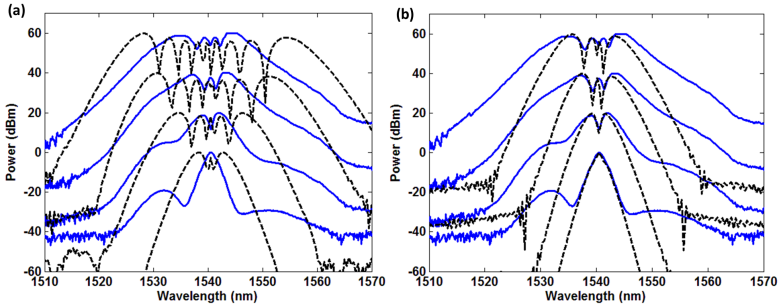

Figure 3.19 (a) The simulated (dotted black lines) and experimental (solid blue lines) for the Re(γ) of 475 $W^{-1}m^{-1}$ for input peak powers of 4.9 W, 9.8 W, 22 W and 44 W respectively from bottom to top. (b) The comparison of the simulated and experimental SPM spectral with a reduced Re(γ) value of 150 $W^{-1}m^{-1}$.

This is not unexpected since the laser passes through several meters of fiber as well as the EDFA before it reaches the InGaP waveguide. Figure 3.19(a) shows the attempt at modelling the behaviour of these pulses in the waveguide by integrating the generalized nonlinear Schrödinger equation (GNLSE) as was done in chapter 2. The only difference is that the TPA term is now replaced by the corresponding 3PA term and the carrier term is given by Eq. 3.5:

$$\frac{\partial E}{\partial z} = -i\frac{\beta_2}{2}\frac{\partial^2 E}{\partial t^2} - \frac{\alpha_{lin}}{2}E + \left(1 + \frac{i}{\omega_0}\frac{\partial}{\partial t}\right)\left(iRe(\gamma)|E|^2 - \frac{\alpha_{3pa}}{3A_{5eff}^2}|E|^4\right)E - \frac{\sigma}{2}(1+i\mu)N_c E \tag{3.15}$$

The simulation was carried out with the known values of the parameters Re(γ), β_2, α_{3pa}, α_{lin} as mentioned above, and the rest were taken from literature [67–69]. Specifically, $\sigma = 7 \times 10^{-21}\, m^2$, $\mu = 5.8$ and the carrier lifetime $\tau_c = 50\, ps$. As can be seen, the simulated spectra do not match the observed experimental ones. In particular, the simulated profiles show that the output spectra ought to have more broadening and many more dips than were actually observed. Even including a (linear) chirp in the input pulse could not account for the large discrepancy between the simulated and experimental spectra. Hence, a more complicated chirp profile might be needed to account for this behavior. Other 'usual suspect' errors such as an overestimation of the input peak power etc. would need to be too large to account for this discrepancy to be reasonably assumed. It is unclear at this point what exactly the reason is for the observed SPM broadening to be smaller than expected. For comparison, Fig. 3.19(b) shows the simulated SPM spectra for a reduced Re(γ) value of 150 $W^{-1}m^{-1}$.

However, one can at the very least estimate the amount of phase shift experienced by the pulse by counting the number of peaks in the output spectrum [51, 70]. In this case, at the highest powers, 4 peaks can be observed, which corresponds to a phase of ϕ_{max} = 3.5π. A better understanding of the dynamics of the interplay between nonlinear gain, loss and the dispersion can be obtained by the use of more ideal pulses, which is what is done in the next chapter for the demonstration of supercontinuum generation by pumping the InGaP waveguides with femtosecond pulses.

3.4.6 Second-order nonlinearity

As mentioned in section 3.2, the d_{14} element of the $\chi^{(2)}$ tensor for InGaP is large enough to be of practical use in applications such as sum- and difference-frequency generation. The fact that it is the d_{14} tensor element that is non-zero (regardless of the amount of ordering present in the crystal) and that it is the dominant tensor element has some implications when it comes to using it for such second-order nonlinear processes. Since it is the $\chi^{(2)}_{xyz}$ tensor element that corresponds to the d_{14} in the shortened representation of the susceptibility tensor [71], it becomes clear that the input field's electric field components need to be along at least any two of the crystal axes in order to invoke this nonlinearity. This will result in a nonlinear polarization along the third crystal axis. Since the growth of InGaP lattice matched to a GaAs substrate is along the [001] direction, the plane of the InGaP membrane layer that is bonded to the substrate will contain the [010] and the [100] crystal directions, as shown in Fig. 3.20. The InGaP membrane facets correspond to the directions the [110] and the [1$\bar{1}$0] directions. Hence, one can immediately see that the electric field of a TE mode (which is of course parallel to the membrane surface) in a waveguide oriented at an angle of 0° will have equal components along two of the crystal axes, while in case of the being waveguide oriented at an angle of 45°, the electric field will be along one of the crystal axes and thus have no second-order response. One can thus easily access the d_{14} tensor element

of the second-order nonlinearity by simply coupling light into the TE modes of waveguides oriented at the correct angle in the InGaP membrane for implementing second-order nonlinear processes. In case of second-harmonic generation for example, light at the fundamental wavelength in a waveguide will generate the second harmonic wavelength with the electrical field oriented along the third crystal axis, which obviously corresponds to the TM mode of the waveguide. Similarly, one could have the input electric fields in some combination of TE and TM modes of the waveguide interacting through the d_{14} tensor element to generate new fields at the sum or difference frequency.

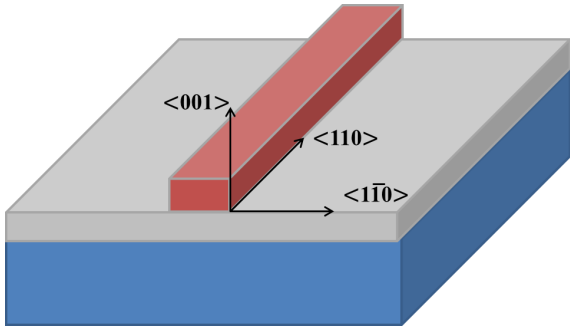

Figure 3.20 Orientation of the InGaP waveguide facets with respect to its crystallographic axes implies that for a waveguide oriented parallel to either of the membrane facets, the TE mode overlaps with two of the crystal axes.

Of course, the efficiency of any such interaction depends on phase matching. Phase matching simply ensures that the phase difference between the nonlinear polarization (whose phase obviously depends on the input fields) and the generated field (whose phase evolves according to the linear dispersive properties of the nonlinear medium) remains zero so that there is coherent addition between the two. For second-order nonlinear processes, there are many techniques that are used for achieving phase matching. One very popular technique exploits the birefringence of anisotropic materials to match the index for fields with different polarizations. This technique has been used especially in bulk nonlinear optics for a long time and has contributed to the popularity of materials such as KH_2PO_4 (KDP) and $LiNbO_3$ (LN) in such applications. While bulk InGaP is isotropic, this functionality can still be exploited by using the birefringence of the high index contrast waveguide structure, in which TM modes have very different propagation properties compared to TE modes. This geometrical birefringence, together with the waveguide dispersion, can be exploited to achieve phase matching by properly designing the waveguide.

For example, in case of SHG, the condition for phase matching is simply that the effective index at the harmonic and the fundamental wavelengths should be equal [71]. Now, in general, the material refractive index at the harmonic wave-

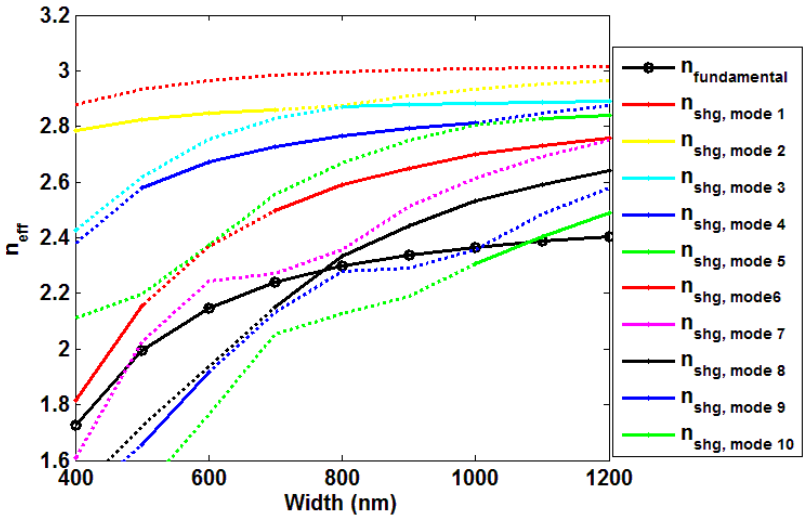

Figure 3.21 The effective index of the fundamental TE mode at 1550 nm (black solid line with black dots) and the first 10 modes at the SH wavelength as a function of the InGaP waveguide width. For the SH modes, the TE modes are plotted in dotted lines and the TM modes are plotted in solid lines.

length is larger than the index at the fundamental wavelength. This is especially true for InGaP when the fundamental wavelength is in the telecommunications wavelength range since the second harmonic wavelengths lie near the band edge where dispersion is quite strong. Now, since at any given wavelength, the effective index of higher-order modes of a waveguide is lower than that of the fundamental mode, it is possible to have a higher-order mode at the second harmonic wavelength whose effective index is equal to that of the fundamental mode at the fundamental wavelength. This is termed as modal phase matching. Figure 3.21 shows how this is possible for SHG at the fundamental wavelength of 1550 nm in InGaP waveguides with a height of 250 nm and various widths. The effective indices of various modes (numbered 1 through 10) at the SH wavelength of 775 nm as well as the effective index of the fundamental mode at 1550 nm are shown. As can be seen, for certain waveguide widths, the effective index for the fundamental mode (which happens to be a TE mode) at 1550 nm is the same as that of one of the higher-order modes at the SH wavelength of 775 nm. Thus, for these widths, that particular higher-order mode at the SH wavelength is perfectly phase matched with the fundamental TE mode at the fundamental wavelength. However, given the previous discussion about the $\chi^{(2)}$ tensor of InGaP, there is another consideration that must be taken into account, which is that the SH mode must be a TM mode because the generated electric field at the SH wavelength will be along the [001] direction. From Fig. 3.21 it can be seen that for a waveguide width of about 770 nm, the fundamental TE mode at 1550 nm will be phase matched with the 8^{th} mode (which is a TM mode) at 775 nm. As can be seen, another possibility

for phase matching is available at a waveguide width of about 1075 nm, where it is the 10^{th} mode (which is also a TM mode) instead which is phase matched. In order to choose between the two, the overlap integral between the two modes needs to be calculated [23]. The higher the overlap, obviously, the greater the non-linear interaction will be between the two modes. Since the fundamental TE mode is symmetric, the SH TM mode should also be symmetric; otherwise the overlap integral will be zero. The respective fundamental TE and SH TM modes that are phase matched for the width of 770 nm are shown in Fig. 3.22. A similar phase matching point can be found for SHG at other wavelengths of course. Thus, in summary, for modal phase matching for second harmonic generation, we need a symmetric higher-order TM mode at the SH wavelength whose index is the same as that of the fundamental TE mode at the fundamental wavelength.

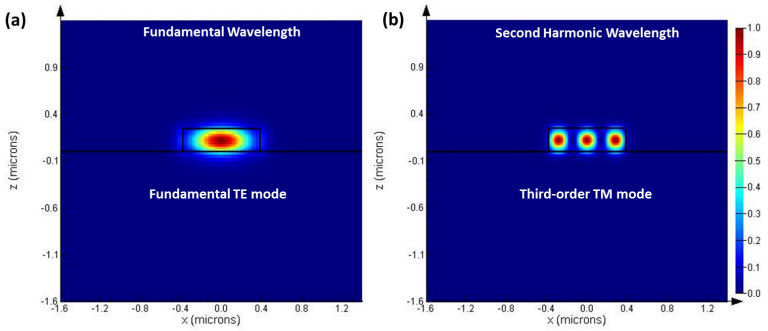

Figure 3.22 (a) The fundamental TE waveguide mode at 1550 nm and (b) the 8^{th} order mode which is a third-order TM mode at the SH wavelength.

To observe second-harmonic generation, 2 mm long InGaP waveguides of various widths and oriented at $0°$, $22.5°$ and $45°$ to the facets were fabricated. The experiment was conducted in a horizontal setup where the cleaved facets of the waveguides were coupled to lensed fibers. The angled waveguides were terminated with a bend such that their end facets were always parallel to the $0°$ waveguide. This was done in order to facilitate the cleaving of the chip on both ends for use in a horizontal measurement setup where the waveguides are coupled to lensed fibers. Figure 3.23 shows the result of one such experiment where a 2 mm long InGaP waveguide of width 800 nm oriented at $45°$ is seen to 'glow' with the generated second-harmonic light when pumped with a CW laser at 1576 nm. Less efficient SHG was observed in the same waveguide oriented at $22.5°$ and no SHG was observed in the $0°$ waveguide. This is contrary to the expectation from the crystallographic orientation as shown in Fig. 3.20. The reason for this discrepancy is not entirely clear at this point. Either the $\chi^{(2)}$ reported in literature is not what we have here and there are other components of the tensor that are non-zero (in this case it would seem to be $\chi^{(2)}_{xyy}$) or the crystallographic orientation of the membrane is along a different direction from what is shown in Fig. 3.20. Nevertheless,

whatever the reason might be, it is clear from this experiment that the second harmonic generation occurs most efficiently in waveguides oriented at 45° angle to the membrane facet with the pump being in the TE mode and the second harmonic output being in the TM mode. And while this information is enough for designing waveguides for such appplications, it is of course important to understand the origin of this discrepancy. This is something that can be tackled in future work. Once the lensed fibers were aligned with the waveguide at the fundamental wavelength, the output lensed fiber was replaced with a multimode fiber because it has a better collection efficiency of the higher-order mode at the second harmonic. Figure 3.24(a) shows collected second harmonic power as a function of pump power. The slope of the linear fit of the collected SH power to the pump power (in dBm) is 2.04, which is of course very close to the expected quadratic scaling of perfectly phase matched SHG.

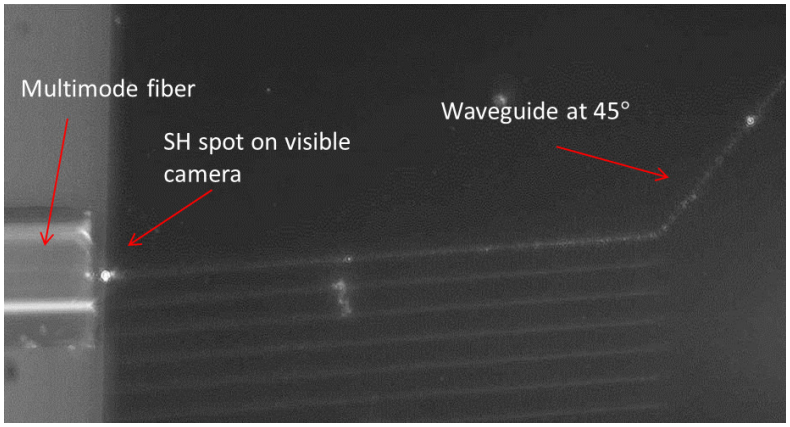

Figure 3.23 The output facet of a 800 nm $\times$ 250 nm InGaP waveguide oriented at 45° shows the glow of generated second harmonic light when pumped by a laser at 1576 nm. The waveguide ends in a bend in order for the waveguide to be cleaved at a zero angle and coupled to a lensed or multimode fiber. The SH light is collected using a multimode fiber.

A couple of different off-chip conversion efficiencies (in units of $\%/W$ and $\%/W/mm^2$) are used in literature, which are defined as follows:

$$\eta_1 = 100\,\frac{P_{SH,out}}{P_{F,in}^2}\% \tag{3.16}$$

$$\eta_2 = 100\,\frac{P_{SH,out}}{(P_{F,in}\,L)^2}\% \tag{3.17}$$

For this particular case, the values of the conversion efficiency are: $\eta_1 = 2.8 \times 10^{-3}\,\%/W$ and $\eta_2 = 6.9 \times 10^{-4}\,\%/W/mm^2$. These values are comparable with the reports in literature of modal phase matching in AlGaAs waveguides

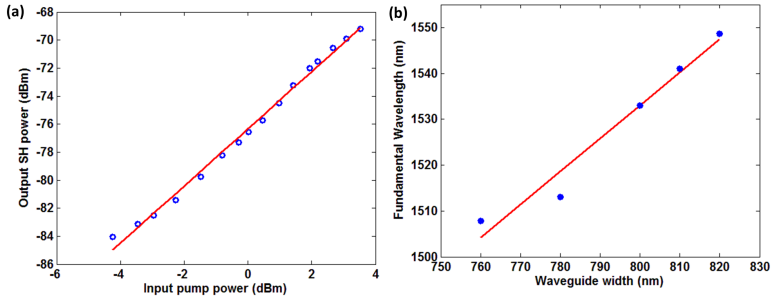

Figure 3.24 (a) Coupled-out SH power as a function of the coupled-in pump power. The slope of the linear fit is 2.04, very close to the expected slope of 2.00 from perfectly phase matched operation. (b) The phase matched fundamental wavelength as a function of the waveguide width (for a slightly smaller waveguide height of 225 nm, different from the case of (a), because of which the phase matching points fall at slightly different wavelengths).

[23]. In other waveguides, coupled-out SH powers as high as -64 dBm and off-chip conversion efficiencies as high as $\eta_1 = 6.6 \times 10^{-3}\,\%/W$ and $\eta_2 = 2.3 \times 10^{-3}\,\%/W/mm^2$ were observed. Figure 3.24(b) shows the wavelengths at which different waveguide widths show modal phase matching, demonstrating that the method can be used to generate SH using a pump across the telecommunications wavelength range. It should be noted that the SH power used in these definitions is the power collected by the multimode fiber and the fundamental power is the coupled-in power to the waveguide. As the out-coupling efficiency and the loss for the higher-order TM mode at the SH wavelength are unknown, the calculation of the internal conversion efficiency is difficult. The coupling efficiency could be estimated by calculating the overlap of the SH mode with those of the multimode fiber. However, in this particular case, such calculations are unreliable because the higher-order modes can couple to other modes in the bend section of the waveguide structure unless the bends are very large (> 100 μm for example). In future designs, such bends could easily be incorporated. Alternatively, the InGaP die itself could be bonded at an angle of 45° so that it is now the 0°-oriented waveguides that exhibit the second-order nonlinearity, removing any need for bends. Another issue is that the loss of the higher-order SH mode has previously been reported to be very high (up to 100 dB/cm) [23] and as such should not be easily neglected in calculations for the internal conversion efficiency. This loss of this higher-order TM can be extracted from the wavelength dependence of the SH conversion efficiency as in [23], or by comparing the generated SH power between waveguides of different lengths.

Until now we have discussed a technique for achieving perfect phase matching. However, perfect phase matching is not always possible and in such cases, another popular technique for achieving efficient nonlinear interactions is quasi-phase matching (QPM). In QPM, in lieu of perfect phase matching, the sign of the $\chi^{(2)}$ tensor element is inverted periodically whenever the phase difference be-

tween the nonlinear polarization and the generated field reaches π, thereby avoiding destructive interference (and thus the power flowing back from the generated to the generating fields). The distance after which the accumulated phase difference equals π and hence the distance after which the $\chi^{(2)}$ inversion needs to take place is called as the 'coherence length'. Obviously, this technique requires a way to invert the sign of the $\chi^{(2)}$ nonlinearity. For III-V material such as InGaP, this tensor inversion is possible but requires significant alterations of the growth process in a technique called orientation patterning [72]. However, there is a way to achieve QPM without having to alter the growth process. Because of the nature of the $\chi^{(2)}$ tensor of III-V materials, turning the material by 90° changes the sign of the $\chi^{(2)}$ [16]. As a result, if a waveguide has a 90° bend, it will experience equal but opposite $\chi^{(2)}$ in the two arms of the bend. Thus, one only needs to have a bend radius such that one 90° bend section is twice the coherence length in order to achieve QPM. Thus, the advantage of this is that it is a very easy way to implement the QPM without having to resort to complicated growth processes. Also, this allows for the freedom to achieve QPM for various different processes simply by changing the bend radius, while in the orientation patterning technique, this is not the case. The inversion period Λ (i.e. one region each of the positive and negative $\chi^{(2)}$, each corresponding to one coherence length) is given by $\Lambda_{QPM} = 2\pi/\Delta k$ where $\Delta k = 2\,k_F - k_{SH}$ is the phase mismatch between the fundamental and SH wavelengths. Thus, $\Lambda_{QPM} = \lambda_F/(2\,\Delta n_{eff})$, where $\Delta n_{eff} = n_{eff,F} - n_{eff,SH}$ and hence the bend radius is given by $R_{bend} = 4/(\Delta k) = \lambda_F/\pi\Delta n_{eff}$. This implies that the index difference between the fundamental and SH fields should be lower than ≈ 0.025 in order to have reasonable bend radii larger than 20 μm. This is the main disadvantage of this technique - the bend radii required for QPM in processes with a large phase mismatch can become too small for efficient operation. Of course, a bend radius which is large enough to avoid losses through radiation leakage and thus appropriate for low-loss operation would depend on the wavelengths involved. For example, the same concept can be extended to quasi-phase matching of sum and difference frequency generation. Again, it is the total phase mismatch Δk that determines the inversion period and thus the bend radius. For example, in the case of generation of mid-infrared frequencies by DFG between two lasers at 1064 nm and 1510 nm (thus generating a difference frequency located at about 3.6 μm), an InGaP rib-waveguide of width 2.8 μm and a height of 220 nm with a rib-height of 110 nm can be quasi-phase matched with a bend radius of about 36 μm.

QPM, while in principle less efficient compared to perfect phase matching, can still be of practical interest, especially considering that the modal overlap can potentially be dramatically improved since now we have the freedom to choose the fundamental modes at all the interacting wavelengths. Using fundamental modes (or at least lower order modes compared to the modal phase matching case) may also improve the loss penalty for the generated wavelengths, thereby further increasing the generation efficiency. It also allows for a larger bandwidth compared to modal phase matching which of course works for a very small range of wave-

lengths with any appreciable efficiency. Hence, it is a promising technique that should be explored in future work.

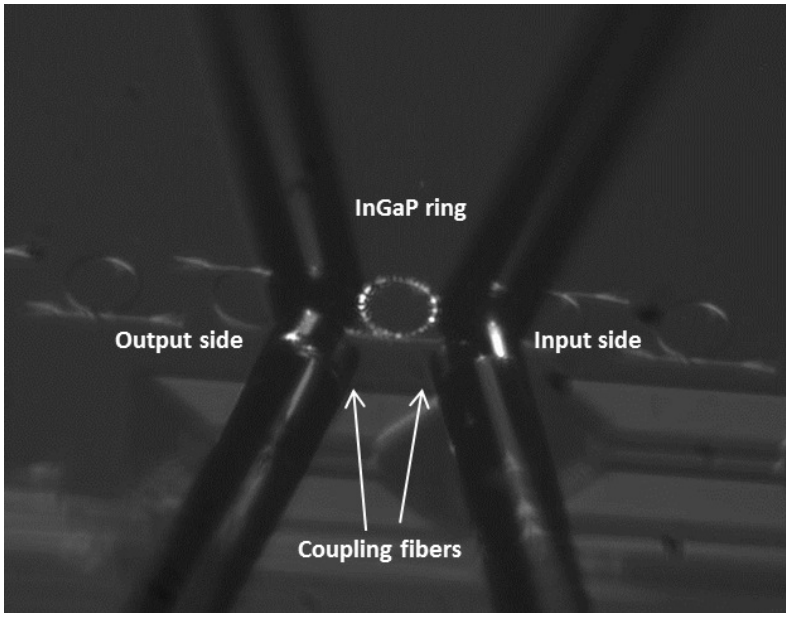

Figure 3.25 InGaP ring resonator with a diameter of 100 μm showing quasi-phase matched second harmonic generation at a pump wavelength of 1526 nm.

Another way to improve the efficiency is to conduct the nonlinear interaction inside a resonant cavity, where the enhancement provided by the cavity greatly increases the nonlinear interaction. As mentioned above, for QPM-SHG with bent waveguides, the index difference between fundamental and SH wavelengths needs to be quite small in order to have reasonable radii. It can be seen from Fig. 3.21 that the bend radius required for QPM-SHG at 1550 nm between the fundamental TE (for the pump wavelength) and TM (for the SH wavelength) modes is in the range of 1 μm, which is too small for low-loss operation. However, combining the modal-phase matching and the QPM techniques can somewhat alleviate this problem (of course at the cost of once again having to use a higher-order SH modes). Basically, if operated close to the modal phase matching point, then the index difference is small enough for large bend radii. Then, if such a waveguide is turned into a ring-resonator, the quasi-phase matching will still occur along the 4 bends of the ring, but now we can take advantage of the intensity enhancement provided by the cavity to boost the conversion efficiency. This approach has been reported before in case of GaAs and GaP microdisks [8].

Figure 3.25 shows the fabricated InGaP ring with a width of 760 nm which is side-

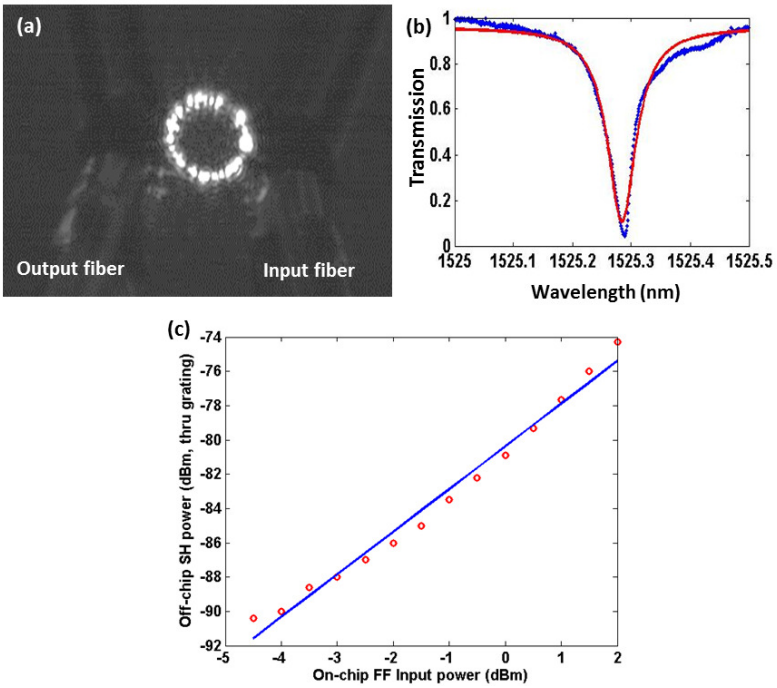

Figure 3.26 (a) The InGaP ring resonator shows the SH light getting coupled out via the bus waveguide on the right hand side. (b) The resonance fit at the fundamental wavelength shows a loaded quality factor of about 26000. (c) The linear fit to the coupled out SH power as a function of the coupled-in fundamental pump power has a slope of 2.49.

coupled to a bus waveguide connected to grating couplers. Light from a CW laser at 1525 nm is coupled into the bus waveguide from the left fiber and one can see the InGaP ring glowing with the generated SH light. The SH light couples to the same bus waveguide and is collected by a (standard single mode) fiber via the same grating. Figure 3.26(a) shows the same ring with the ambient lights switched off to get a better look at the SH light being generated in the ring resonator. Figure 3.26(b) shows the Lorentzian fit for the resonance at the fundamental wavelength of 1525.3 nm from which a loaded quality factor of about 26000 can be extracted. Finally, Fig.3.26(c) shows the dependence of the SH power on the fundamental power. The reason for the slope of the linear fit being larger than 2 is unclear. One possibility is that at the higher powers, the out-coupling of the SH mode is better (due to thermal effects on the ring-bus coupling coefficient) and so the collected SH power also increases with the pump power. Nevertheless, η_1 and η_2 can be extracted from these measurements to be $1.6 \times 10^{-3}\,\%/W$ and $2.55 \times 10^{-2}\,\%/W/mm^2$ (taking the length to be the ring circumference) respectively. Thus, it can be seen that the conversion efficiency is indeed greatly improved. SH power levels comparable to the straight waveguide case can be easily obtained for the same pump powers but

in a far smaller chip-area. Of course, these values are only for the off-chip conversion efficiencies and the out-coupling method is different in both cases (cleaved facet to a multimode fiber in the former and grating coupled to a single mode fiber in the latter case). Also, the efficiency enhancement will depend on whether both the fundamental and the SH modes are in resonance or not. In order to extract the internal conversion efficiency, again, the collection efficiency of the grating needs to be known. These and other issues can be tackled in future works.

3.5 Conclusions

In this chapter, InGaP-on-insulator has been proposed as a platform suitable for various on-chip nonlinear applications. More generally, it was argued that the incorporation of suitable nonlinear III-V materials such as InGaP into integrated platforms provides a path towards the realization of a large array of applications such as those in telecommunications, sensing, spectroscopy etc. This is done by leveraging the maturing technologies of hybrid integration. The integrated photonics approach could provide these applications with cheap, reliable and robust alternatives to current approaches such as those based on bulk or specialized but not easily scalable solutions.

The processing steps required for such an approach with the specific material of InGaP - i.e. bonding, substrate removal as well as the patterning of the bonded InGaP membranes - were developed. The basic characterization of the linear and nonlinear properties was then performed. With this process, a linear loss of 12 dB/cm was measured, which needs to be improved through further optimization of the process flow. Nonlinear losses arising from three-photon absorption were characterized and it was shown that the material is suitable for high power operation in the telecommunications wavelength regime. The third order nonlinear response - characterized by the nonlinear parameter γ - was also measured in a four-wave mixing experiment in the low power continuous wave regime and the value of the nonlinear parameter was determined to be 475 $W^{-1}m^{-1}$. Finally, self-phase modulation was observed in the InGaP waveguides as well.

The second-order nonlinearity of the platform was characterized through second-harmonic generation experiments in both straight waveguides as well as ring resonators. Strategies for achieving efficient nonlinear interactions via modal and quasi-phase matching were discussed and demonstrated.

By extending this work by bonding to patterned silicon or SiN chips, one could compound the advantages of specific III-V materials such as high nonlinearity of both second- and third-order, low loss, and high index contrast with the advantages provided by those technologically mature platforms. Specifically, the well-developed library of filters, modulators, sources, detectors etc. could be leveraged

for fully integrated solutions for the various applications mentioned above. One such application could be the generation and full phase-stabilization of frequency combs to connect the microwave and optical domains. The first step towards such an application is demonstrated in the next chapter. Furthermore characterizations of and demonstrations of the applications using the second-order nonlinear response also need to be carried out to fully realize the vision that motivated this approach - to integrate both second- and third-order nonlinearities onto a CMOS-compatible integrated photonics platform. These issues will be all dealt with in subsequent chapters.

References

[1] John E Bowers *Heterogeneous III-V/Si Photonic Integration* In CLEO: Science and Innovations, pages SM1G–1. Optical Society of America, 2016.

[2] Günther Roelkens, Liu Liu, Di Liang, Richard Jones, Alexander Fang, Brian Koch, and John Bowers *III-V/silicon photonics for on-chip and intra-chip optical interconnects* Laser & Photonics Reviews, 4(6):751–779, 2010.

[3] Helene Duprez, Christophe Jany, Christian Seassal, and Badhise Ben Bakir *Highly tunable heterogeneously integrated III-V on silicon sampled-grating distributed Bragg reflector lasers operating in the O-band* Optics Express, 24(18):20895–20903, 2016.

[4] Qiangsheng Huang, Yingchen Wu, Keqi Ma, Jianhao Zhang, Weiqiang Xie, Xin Fu, Yaocheng Shi, Kaixuan Chen, Jian-Jun He, Dries Van Thourhout, et al. *Low driving voltage band-filling-based III-V-on-silicon electroabsorption modulator* Applied Physics Letters, 108(14):141104, 2016.

[5] Amin Abbasi, Jochem Verbist, Xin Yin, Guang hua Duan, Johan Bauwelinck, Gunther Roelkens, Geert I Morthier, et al. *Above 40 Gb/s Direct Modulation of a Heterogeneously integrated III-V-on-silicon DFB Laser* In Latin America Optics and Photonics Conference, pages LTu2D–3. Optical Society of America, 2016.

[6] Minhao Pu, Luisa Ottaviano, Elizaveta Semenova, and Kresten Yvind *Efficient frequency comb generation in AlGaAs-on-insulator* Optica, 3(8):823–826, 2016.

[7] Todd H Stievater, Rita Mahon, Doewon Park, William S Rabinovich, Marcel W Pruessner, Jacob B Khurgin, and Christopher JK Richardson *Mid-infrared difference-frequency generation in suspended GaAs waveguides* Optics letters, 39(4):945–948, 2014.

[8] David P Lake, Matthew Mitchell, Harishankar Jayakumar, Laís Fujii dos Santos, Davor Curic, and Paul E Barclay *Efficient telecom to visible wavelength conversion in doubly resonant gallium phosphide microdisks* Applied Physics Letters, 108(3):031109, 2016.

[9] Sylvain Combrié, Quynh Vy Tran, Alfredo De Rossi, Chad Husko, and Pierre Colman *High quality GaInP nonlinear photonic crystals with minimized nonlinear absorption* Applied Physics Letters, 95:221108, 2009.

[10] Pierre Colman, Chad Husko, Sylvain Combrié, Isabelle Sagnes, Chee Wei Wong, and Alfredo De Rossi *Temporal solitons and pulse compression in photonic crystal waveguides* Nature Photonics, 4(12):862–868, 2010.

[11] V Eckhouse, I Cestier, G Eisenstein, S Combrié, P Colman, A De Rossi, M Santagiustina, CG Someda, and G Vadalà *Highly efficient four wave mixing in GaInP photonic crystal waveguides* Optics letters, 35(9):1440–1442, 2010.

[12] Chad Husko, Sylvain CombriÚ, Quynh V Tran, Fabrice Raineri, Chee Wei Wong, and Alfredo De Rossi *Non-trivial scaling of self-phase modulation and three-photon absorption in III-V photonic crystal waveguides* Optics express, 17(25):22442–22451, 2009.

[13] Chad A Husko, Alex S Clark, Matthew J Collins, Alfredo De Rossi, Sylvain Combrié, Gaëlle Lehoucq, Isabella H Rey, Thomas F Krauss, Chunle Xiong, and Benjamin J Eggleton *Multi-photon absorption limits to heralded single photon sources* arXiv preprint arXiv:1307.4498, 2013.

[14] P Ernst, C Geng, F Scholz, H Schweizer, Yong Zhang, and A Mascarenhas *Band-gap reduction and valence-band splitting of ordered GaInP2* Applied physics letters, 67(16):2347–2349, 1995.

[15] Yoshiyasu Ueno, Vincent Ricci, and George I Stegeman *Second-order susceptibility of Ga 0.5 In 0.5 P crystals at 1.5 μm and their feasibility for waveguide quasi-phase matching* JOSA B, 14(6):1428–1436, 1997.

[16] Sébastien Sauvage, Yann Bernard, Isabelle Sagnes, Gilles Patriarche, Franck Glas, Guy Le Roux, Marcel Bensoussan, and Juan Ariel Levenson *Normal-incidence (001) second-harmonic generation in ordered Ga 0.5 In 0.5 P* JOSA B, 18(1):81–84, 2001.

[17] B Fluegel, A Mascarenhas, JF Geisz, and JM Olson *Second harmonic generation in ordered Ga 1- x In x P* Physical Review B, 57(12):R6787, 1998.

[18] Hirokazu Kato, Sadao Adachi, Hiroshi Nakanishi, and Kouji Ohtsuka *Optical properties of (AlxGa1-x) 0.5 In0. 5P quaternary alloys* Japanese journal of applied physics, 33(1R):186, 1994.

[19] MA Steiner, L Bhusal, JF Geisz, AG Norman, MJ Romero, WJ Olavarria, Y Zhang, and A Mascarenhas *CuPt ordering in high bandgap GaxIn1-xP alloys on relaxed GaAsP step grades* Journal of Applied Physics, 106(6):63525, 2009.

[20] J Novák, S Hasenöhrl, R Kúdela, M Kucera, MI Alonso, and M Garriga *Effect of strain and ordering on the band-gap energy of InGaP* Materials Science and Engineering: B, 88(2):139–142, 2002.

[21] Eg Eg *Influence of tensile and compressive strain on the band gap energy of ordered InGaP* Applied Physics Letters, 79(17), 2001.

[22] SW Jun, RT Lee, CM Fetzer, JK Shurtleff, GB Stringfellow, CJ Choi, and T-Y Seong *Bi surfactant control of ordering and surface structure in GaInP grown by organometallic vapor phase epitaxy* Journal of Applied Physics, 88(7):4429–4433, 2000.

[23] D Duchesne, KA Rutkowska, M Volatier, F Légaré, S Delprat, M Chaker, D Modotto, A Locatelli, C De Angelis, M Sorel, et al. *Second harmonic generation in AlGaAs photonic wires using low power continuous wave light* Optics express, 19(13):12408–12417, 2011.

[24] Ksenia Dolgaleva, Wing Chau Ng, Li Qian, and J Stewart Aitchison *Compact highly-nonlinear AlGaAs waveguides for efficient wavelength conversion* Optics express, 19(13):12440–12455, 2011.

[25] C Lacava, V Pusino, P Minzioni, M Sorel, and I Cristiani *Nonlinear properties of AlGaAs waveguides in continuous wave operation regime* Optics express, 22(5):5291–5298, 2014.

[26] Paveen Apiratikul, Jeremiah J Wathen, Gyorgy A Porkolab, Bohan Wang, Lei He, Thomas E Murphy, and Christopher JK Richardson *Enhanced continuous-wave four-wave mixing efficiency in nonlinear AlGaAs waveguides* Optics express, 22(22):26814–26824, 2014.

[27] Jeremiah J Wathen, Paveen Apiratikul, Christopher JK Richardson, Gyorgy A Porkolab, Gary M Carter, and Thomas E Murphy *Efficient continuous-wave four-wave mixing in bandgap-engineered AlGaAs waveguides* Optics letters, 39(11):3161–3164, 2014.

[28] Ilse Christiaens, Günther Roelkens, Kurt De Mesel, Dries Van Thourhout, and Roel Baets *Thin-film devices fabricated with benzocyclobutene adhesive wafer bonding* Journal of Lightwave Technology, 23(2):517, 2005.

[29] Shahram Keyvaninia, Muhammad Muneeb, Stevan Stanković, PJ Van Veldhoven, Dries Van Thourhout, and Günther Roelkens *Ultra-thin DVS-BCB adhesive bonding of III-V wafers, dies and multiple dies to a patterned silicon-on-insulator substrate* Optical Materials Express, 3(1):35–46, 2013.

[30] Zhechao Wang, Bin Tian, Marianna Pantouvaki, Weiming Guo, Philippe Absil, Joris Van Campenhout, Clement Merckling, and Dries Van Thourhout *Room-temperature InP distributed feedback laser array directly grown on silicon* Nature Photonics, 9(12):837–842, 2015.

[31] D Liang and JE Bowers *Highly efficient vertical outgassing channels for low-temperature InP-to-silicon direct wafer bonding on the silicon-on-insulator substrate* Journal of Vacuum Science & Technology B, 26(4):1560–1568, 2008.

[32] Gunther Roelkens, Utsav D Dave, Alban Gassenq, Nannicha Hattasan, Chen Hu, Bart Kuyken, Francois Leo, Aditya Malik, Muhammad Muneeb, Eva Ryckeboer, et al. *Silicon-based photonic integration beyond the telecommunication wavelength range* IEEE Journal of Selected Topics in Quantum Electronics, 20(4):394–404, 2014.

[33] *EPI-LAB:* http://ent-epitaxy.com/our-company.

[34] *Cyclotene BCB series:* http://www.dow.com/cyclotene/prod/302235.htm.

[35] *SUSS Wafer Bonder:* https://www.suss.com/en/products-solutions/products/wafer-bonder.html.

[36] CC Li, BL Guan, DX Chuai, X Guo, GD Shen, et al. *Removing GaAs substrate by nitric acid solution* Journal of Vacuum Science & Technology B, 28(3):635–637, 2010.

[37] JR Lothian, JM Kuo, F Ren, and SJ Pearton *Plasma and wet chemical etching of In0. 5Ga0. 5P* Journal of electronic materials, 21(4):441–445, 1992.

[38] S Bouchoule, L Vallier, G Patriarche, T Chevolleau, and C Cardinaud *Effect of Cl2-and HBr-based inductively coupled plasma etching on InP surface composition analyzed using in situ x-ray photoelectron spectroscopy* Journal of Vacuum Science & Technology A, 30(3):031301, 2012.

[39] DC Hays, H Cho, JW Lee, MW Devre, BH Reelfs, D Johnson, JN Sasserath, LC Meyer, E Toussaint, F Ren, et al. *High selectivity inductively coupled plasma etching of GaAs over InGaP* Applied surface science, 156(1):76–84, 2000.

[40] S Bouchoule, S Azouigui, S Guilet, G Patriarche, L Largeau, A Martinez, L Le Gratiet, A Lemaitre, and F Lelarge *Anisotropic and smooth inductively coupled plasma etching of III-V laser waveguides using HBr-O2 chemistry* Journal of The Electrochemical Society, 155(10):H778–H785, 2008.

[41] S Bouchoule, G Patriarche, S Guilet, L Gatilova, L Largeau, P Chabert, et al. *Sidewall passivation assisted by a silicon coverplate during Cl2-H2 and HBr inductively coupled plasma etching of InP for photonic devices* JOURNAL OF VACUUM SCIENCE AND TECHNOLOGY B MICROELECTRONICS AND NANOMETER STRUCTURES, 26(2):666, 2008.

[42] Diedrik Vermeulen, S Selvaraja, Pl Verheyen, G Lepage, W Bogaerts, P Absil, D Van Thourhout, and G Roelkens *High-efficiency fiber-to-chip grating couplers realized using an advanced CMOS-compatible silicon-on-insulator platform* Optics express, 18(17):18278–18283, 2010.

[43] Dirk Taillaert, Peter Bienstman, and Roel Baets *Compact efficient broadband grating coupler for silicon-on-insulator waveguides* Optics letters, 29(23):2749–2751, 2004.

[44] John B. Schneider *Understanding the Finite-Difference Time-Domain Method* www.eecs.wsu.edu/~schneidj/ufdtd, 2010.

[45] Kane S Yee et al. *Numerical solution of initial boundary value problems involving Maxwells equations in isotropic media* IEEE Trans. Antennas Propag, 14(3):302–307, 1966.

[46] *Crystal Wave (Photron Design):* https://www.photond.com/products/crystalwave.htm.

[47] *Lumerical FDTD:* https://www.lumerical.com/tcad-products/fdtd/.

[48] Minhao Pu, Luisa Ottaviano, Elizaveta Semenova, and Kresten Yvind *AlGaAs-On-Insulator Nonlinear Photonics* arXiv preprint arXiv:1509.03620, 2015.

[49] JS Aitchison, DC Hutchings, JU Kang, GI Stegeman, and AIEEEJ Villeneuve *The nonlinear optical properties of AlGaAs at the half band gap* IEEE journal of quantum electronics, 33(3):341–348, 1997.

[50] Jonas Hansryd, Peter A Andrekson, Mathias Westlund, Jie Li, and P-O Hedekvist *Fiber-based optical parametric amplifiers and their applications* IEEE Journal of Selected Topics in Quantum Electronics, 8(3):506–520, 2002.

[51] Govind P Agrawal *Nonlinear fiber optics* Academic press, 2007.

[52] Q Lin, TJ Johnson, R Perahia, CP Michael, and OJ Painter *A proposal for highly tunable optical parametric oscillation in silicon micro-resonators* Optics express, 16(14):10596–10610, 2008.

[53] M Ebnali-Heidari, C Monat, C Grillet, and MK Moravvej-Farshi *A proposal for enhancing four-wave mixing in slow light engineered photonic crystal waveguides and its application to optical regeneration* Optics express, 17(20):18340–18353, 2009.

[54] Minhao Pu, Hao Hu, Luisa Ottaviano, Elizaveta Semenova, Dragana Vukovic, Leif K Oxenlowe, and Krestin Yvind *AlGaAs-on-insulator nanowire with 750 nm FWM bandwidth,-9 dB CW conversion efficiency, and ultrafast operation enabling record Tbaud wavelength conversion* In Optical Fiber Communication Conference, pages Th5A–3. Optical Society of America, 2015.

[55] C Koos, L Jacome, C Poulton, J Leuthold, and W Freude *Nonlinear silicon-on-insulator waveguides for all-optical signal processing* Optics Express, 15(10):5976–5990, 2007.

[56] Junrong Ong, Ranjeet Kumar, and Shayan Mookherjea *Efficient continuous-wave four-wave mixing in SOI waveguides with active carrier removal* In CLEO: Science and Innovations, pages CTh1F–6. Optical Society of America, 2013.

[57] Andrzej Gajda, Lars Zimmermann, Mahmoud Jazayerifar, Georg Winzer, Hui Tian, Robert Elschner, Thomas Richter, Colja Schubert, Bernd Tillack, and Klaus Petermann *Highly efficient CW parametric conversion at 1550 nm in SOI waveguides by reverse biased pin junction* Optics express, 20(12):13100–13107, 2012.

[58] K Yamada, H Fukuda, T Tsuchizawa, T Watanabe, T Shoji, and S Itabashi *All-optical efficient wavelength conversion using silicon photonic wire waveguide* IEEE Photonics Technology Letters, 18(9):1046–1048, 2006.

[59] Akira Hasegawa and Frederick Tappert *Transmission of stationary nonlinear optical pulses in dispersive dielectric fibers. I. Anomalous dispersion* Applied Physics Letters, 23(3):142–144, 1973.

[60] PV Mamyshev *All-optical data regeneration based on self-phase modulation effect* In Optical Communication, 1998. 24th European Conference on, volume 1, pages 475–476. IEEE, 1998.

[61] Akira Hasegawa and Frederick Tappert *Transmission of stationary nonlinear optical pulses in dispersive dielectric fibers. I. Anomalous dispersion* Applied Physics Letters, 23(3):142–144, 1973.

[62] RR Alfano and SL Shapiro *Observation of self-phase modulation and small-scale filaments in crystals and glasses* Physical Review Letters, 24(11):592, 1970.

[63] Fujio Shimizu *Frequency broadening in liquids by a short light pulse* Physical Review Letters, 19(19):1097, 1967.

[64] WJ Tomlinson, RH Stolen, and CV Shank *Compression of optical pulses chirped by self-phase modulation in fibers* JOSA B, 1(2):139–149, 1984.

[65] Linn F Mollenauer, Roger H Stolen, and James P Gordon *Experimental observation of picosecond pulse narrowing and solitons in optical fibers* Physical Review Letters, 45(13):1095, 1980.

[66] Govind Agrawal *Self-phase modulation in optical fiber communications: good or bad?* In CLEO, page JTuB5. Optical Society of America, 2007.

[67] Srini Krishnamurthy, Zhi Gang Yu, Leonel P Gonzalez, and Shekhar Guha *Temperature-and wavelength-dependent two-photon and free-carrier absorption in GaAs, InP, GaInAs, and InAsP* Journal of Applied Physics, 109(3):033102, 2011.

[68] Brian R Bennett, Richard A Soref, and Jesus A Del Alamo *Carrier-induced change in refractive index of InP, GaAs and InGaAsP* IEEE Journal of Quantum Electronics, 26(1):113–122, 1990.

[69] P Thiagarajan, JF Schmerge, Carmen S Menoni, M Marconi, Oscar Eduardo Martinez, Jorge J Rocca, MJ Hafich, HY Lee, and GY Robinson *Picosecond absorption dynamics of photoexcited InGaP epitaxial films* Applied physics letters, 59(1):90–92, 1991.

[70] RH Stolen and Chinlon Lin *Self-phase-modulation in silica optical fibers* Physical Review A, 17(4):1448, 1978.

[71] Robert W Boyd *Nonlinear optics* Academic press, 2003.

[72] CR Phillips, J Jiang, C Mohr, AC Lin, C Langrock, M Snure, D Bliss, M Zhu, I Hartl, JS Harris, et al. *Widely tunable midinfrared difference frequency generation in orientation-patterned GaAs pumped with a femtosecond Tm-fiber system* Optics letters, 37(14):2928–2930, 2012.

4

COHERENT SUPERCONTINUUM GENERATION IN THE INGAP-ON-INSULATOR PLATFORM

I felt electrified when we observed stable interference fringes of high contrast for all the colors that I could record with my handheld camcorder electronic notebook... [this meant that] the white light pulses had to be phase-locked to the driving laser field! - Theodor W. Hänsch, Nobel Lecture, 2005.

Some of the text in this chapter has been adapted from reference [1].

4.1 Introduction

IN the last chapter, InGaP-on-insulator was proposed as an integrated nonlinear platform and shown to exhibit several advantageous properties such as low nonlinear losses and a large value of the third-order nonlinear parameter γ. It was further shown that this strong third order nonlinear response can best be exploited in the telecommunications wavelength range around 1550 nm because the cumulative nonlinear losses from two- and/or three-photon absorption are the lowest there. In this chapter, supercontinuum generation (SCG) using a pump in this wavelength range is demonstrated in this platform showing that these properties can indeed be leveraged for useful practical applications. The underlying dynamics that lead to the formation of the broadband supercontinuum are discussed in detail. The nature of these dynamics is further illustrated by looking at the dependence of the supercontinuum spectral coverage on the dispersion properties in various InGaP-on-insulator waveguides. These insights thus enable designing the InGaP waveguides to tailor the generation of the supercontinuum for specific applications. Furthermore, experimental characterization of the coherence properties of the generated supercontinuum is also carried out and the underlying mechanisms for the observed coherence properties are discussed and compared with other platforms such as the SOI platform and photonic crystal fibers. Compared to the state of the art results in integrated platforms such as SOI or SiN, it is also shown that this particular demonstration of SCG was achieved with ultra-low on-chip pulse energies and results in a wider spectrum that spans more than an octave of frequencies. This octave-spanning characteristic is important for applications such as frequency metrology and spectroscopy. Moreover, because of the strength of the nonlinear interaction as well as the large index contrast, SCG is achieved in waveguides only a couple of millimeters long.

The field of supercontinuum generation began (although not yet named as such) with early reports of the observation of $\chi^{(3)}$ nonlinearity-induced spectral broadening of pulsed sources in a variety of materials [2–4]. Soon afterwards, SCG in borosilicate glass was reported that spanned the entire visible wavelength range [5]. The phenomenon of SCG was interesting because several nonlinear interactions were being observed and utilized for the first time, and also because of its potential in applications such as spectroscopy [6, 7]. As a result, SCG has been intensively studied in all kinds of material systems such as solids [5], liquids [7, 8] and even gases [9]. Initially, SCG was primarily done by exploiting self-phase modulation in these nonlinear materials [4, 8]. However, over the years, more routes to SCG have been discovered and studied in detail as different nonlinear effects became more or less dominant in various platforms depending on a wide variety of experimental parameters. In more recent years, research efforts have focused more on SCG in waveguiding platforms because they enable a much longer

interaction length as compared to bulk materials where significant nonlinear interactions can only happen near the focus or through filamentation of high power lasers [2, 5]. Thereby, the various nonlinear effects previously observed in bulk systems have also been reported in these waveguiding systems with the longer interaction lengths giving the advantage of much lower power requirements. Primary among the waveguiding systems that were first to be explored were ultra-low loss optical fibers that had been concurrently developed for telecommunication purposes. Examples of fiber based systems that were investigated for SCG are single mode silica fibers used in communications [10], photonic crystal fibers (PCFs) [11, 12], chalcogenide fibers [13] etc. The emergence of PCFs near the end of the last millennium provided a fresh impetus to the field because of several inherent advantages for SCG and unprecedented ability to tailor their dispersion properties, as well as the ability to fill the hollow cores with strongly nonlinear materials [12]. Then, as integrated photonic platforms emerged due to a need for faster interconnects and began maturing, SCG has also been investigated in platforms such as amorphous and crystalline silicon-on-insulator platforms [14–20], SiN [21], [22], AlGaAs-on-insulator [23] etc., resulting now in a rich library of materials and platforms where SCG has become well-studied. Thus, there now exists a very good theoretical understanding of the various complicated dynamics that come into play for the generation of the broadband spectra under different experimental circumstances. As a result, properties of the supercontinua can be tailored according to the needs of a particular application. We have already seen how self-phase modulation and the rise of multiple modulation instability sidebands results in supercontinuum generation in the amorphous silicon platform when pumped by picosecond pulses close to the mid-infrared wavelength range. As intimated above, there exist other avenues for SCG which can be chosen according to the desired properties or for practical convenience. In this chapter, SCG in the InGaP-on-insulator platform with pump pulses in the femtosecond regime is discussed.

4.2 Theory

The various routes for achieving SCG were briefly introduced in chapter 2, and SCG in amorphous silicon waveguides spanning the telecom and mid-infrared wavelength regimes was demonstrated. In that case, a thulium doped fiber laser with picosecond pulses was used as the pump to generate the supercontinuum. It was shown that in that context, the route to SCG proceeds through the creation of multiple modulation instability bands via the amplification of the background noise. Since these sidebands are amplified from noise, the supercontinuum spectrum is expected to be different from pulse to pulse [12]. As a result, even though the spectrum is wideband, spectra from individual pulses will not be phase coherent with each other. This is a direct consequence of the nature of the physical mechanism exploited for supercontinuum generation. For applications where such shot-to-shot differences are undesirable, another route to the generation of the su-

percontinuum is needed which preserves the phase coherence between subsequent pulses. Modelocked lasers are one source where the phase coherence is known to be preserved from pulse to pulse. However, the spectral bandwidth of modelocked lasers is generally limited and for many applications, one would want spectra that are much wider. On-chip modelocked lasers have also recently been demonstrated with reasonable peak powers and very good phase properties. Hence, if the pulses from such a modelocked laser could be spectrally broadened without destroying its phase coherence, one could satisfy both the bandwidth as well as coherence requirements. Supercontinuum generation through the fission of a higher order soliton into fundamental solitons and subsequent dispersive wave generation is one mechanism that allows precisely that, as will be explained in this section. This is the mechanism that is exploited for SCG in the InGaP-on-insulator platform.

Solitons, first observed during the study of surface waves in shallow water, have become the subject of study in many nonlinear systems. In a variety of systems that contain nonlinearities, such as hydrodynamics, plasma physics and nonlinear optics, solitons are naturally found as stable wave packets that maintain their own waveforms through a balance of nonlinear and dispersive effects. Apart from this persistence of the waveform over long periods of time, they also exhibit many other interesting properties, such as multiple solitons passing through each other without affecting one another or the splitting of a single large soliton into smaller constituent ones. One of the most well studied manifestations of the soliton phenomenon is in optical fibers. The first investigations of solitons in optics was in single mode fibers used for telecommunications where it was shown that self-phase modulation and anomalous dispersion could compensate each other leading to a stable pulse that propagates down the fiber without any changes in the pulse shape (as would occur if either of the effects were to be present alone) [24–26]. Such (temporal) solitons were initially investigated because of their promise in high-speed telecommunications. Since then, a large amount of research has been done on optical solitons within the community. Spatial solitons have also been studied where the nonlinearity compensates for the diffraction of the beam and creates spatially confined beams that propagate without changing shape, however, these do not concern us here [27].

The existence of solitons can be seen by the derivation of the equation already introduced in previous chapters - the nonlinear Schrödinger equation (NLSE) [28]. We begin with the wave equation:

$$\nabla^2 \boldsymbol{E} - \frac{1}{c^2}\frac{\partial^2 \boldsymbol{E}}{\partial t^2} = \mu_0 \frac{\partial^2 \boldsymbol{P_{lin}}}{\partial t^2} + \mu_0 \frac{\partial^2 \boldsymbol{P_{nl}}}{\partial t^2} \tag{4.1}$$

In the above equation, $\boldsymbol{P_{nl}}$ would, in general, include all the nonlinear contributions. As mentioned above, when it comes to soliton propagation, the third-order nonlinear effect of intensity dependence of the refractive index is what helps counter the dispersive effect of the medium. Hence, in this case we are primarily interested in the third order nonlinear response that was characterized in the pre-

vious chapter. As discussed in the previous chapter, the second order nonlinear response is not important if the InGaP waveguide is oriented parallel to one of the crystal axes (as is the case in the supercontinuum generation experiments described in this chapter) because of the nature of the second-order susceptibility tensor of the material. However, it should be noted that second-order nonlinearities should also be included in systems where both second- and third-order nonlinear effects are strong enough to be relevant. For example, second-order effects in concert with the third-order effects (or even acting alone) have been shown to be enough for supercontinuum generation with ultrashort pulses or for the closely related case of frequency comb generation in microresonators [29, 30]. Here, we proceed with only the third order nonlinear response. As usual, the electric field and the linear and nonlinear polarizations can be decomposed into the slow and fast components:

$$\boldsymbol{V}(\boldsymbol{r},t) = \frac{\hat{\boldsymbol{x}}}{2}\left[V(\boldsymbol{r},t)exp(-i\omega_0 t) + \boldsymbol{c.c.}\right] \tag{4.2}$$

Here, $\boldsymbol{V}$ is $\boldsymbol{E}$, $\boldsymbol{P_{lin}}$ or $\boldsymbol{P_{nl}}$, $\hat{x}$ is the unit vector along the polarization direction of the light and $V(\boldsymbol{r},t)$ is the function defining the envelope of the pulse. Then the Fourier transform is taken to go to the frequency domain where the time derivatives of Eq. 4.1 can be dealt with more easily:

$$\tilde{V}(\boldsymbol{r},\omega-\omega_0) = \int_{-\infty}^{\infty} V(\boldsymbol{r},t)exp[-i(\omega-\omega_0)t]dt \tag{4.3}$$

When these are substituted back into wave equation 4.1, the equation for the electric field envelope reduces to the Helmholtz equation, which needs to be satisfied by the individual frequency components:

$$\nabla^2\tilde{E}(\omega) + \epsilon(\omega)\frac{\omega^2}{c^2}\tilde{E}(\omega) = 0 \tag{4.4}$$

Here, $\epsilon(\omega)$ includes the linear part of the dielectric response as well as the nonlinear part that is proportional to the intensity I through the Kerr index n_2:

$$\epsilon = n^2 = (n_0 + n_2 I)^2 \tag{4.5}$$

Note that in general, $\epsilon(\omega)$ would be complex because the third-order nonlinear modification of the dielectric response also includes the two-photon absorption term. Since it is already known to be zero for InGaP in the wavelength range of interest here that term has been excluded. Also note that sometimes in literature, the Kerr index is defined as the proportionality constant for the square of the electric field instead of the intensity and hence one should be careful to keep the relevant units while doing any comparisons between reported values.

We are interested in the evolution of the wave envelope as it propagates down a waveguide. Since the waveguide will provide transverse confinement and we presume that the field will correspond to one of the modes of the waveguide, the

transverse and longitudinal parts of the electric field envelope can be separated as follows:

$$\tilde{E}(\boldsymbol{r}, \omega - \omega_0) = F(x, y)\tilde{A}(z, \omega - \omega_0)exp(i\beta_0 z) \tag{4.6}$$

Here, $F(x, y)$ is the transverse field profile which represents the guided mode of the waveguide, $A(z, \omega - \omega_0)$ is the envelope function whose evolution along the waveguide is what we are interested in and β_0 is the wave number. Equation 4.6 is normalized such that $|A|^2$ gives the power of the wave. Using Eq. 4.6 in Eq. 4.4, we get the following two equations for the transverse and longitudinal components:

$$\nabla_\perp^2 F(x, y) + [\epsilon(\omega)k_0^2 - \tilde{\beta}^2]F(x, y) = 0 \tag{4.7}$$

$$\frac{\partial^2 \tilde{A}}{\partial z^2}exp(i\beta_0 z) + 2i\beta_0 \frac{\partial \tilde{A}}{\partial z}exp(i\beta_0 z) - \beta_0^2 \tilde{A}exp(i\beta_0 z) + \epsilon(\omega)k_0^2 \tilde{A}exp(i\beta_0 z) = 0 \tag{4.8}$$

Here, the $\nabla_\perp^2$ is the transverse Laplacian which describes the diffraction of the wavefront, k_0 is ω/c and β is the wave number of the guided mode of the waveguide to be obtained by solving Eq. 4.7. Of more interest here is the longitudinal evolution of the envelope, which is given by equation 4.8. Under the slowly varying envelope approximation, the first term of Eq. 4.8 can be dropped to get:

$$2i\beta_0 \frac{\partial \tilde{A}}{\partial z} + (\tilde{\beta}^2 - \beta_0^2)\tilde{A} = 0 \tag{4.9}$$

In this equation, since the difference between β and β_0 is generally quite small, the second term can be approximated as $\beta^2 - \beta_0^2 \approx 2\beta_0(\beta - \beta_0)$to get:

$$\frac{\partial \tilde{A}}{\partial z} - i(\tilde{\beta} - \beta_0)\tilde{A} = 0 \tag{4.10}$$

The value of β at a particular frequency can be approximated by doing a Taylor expansion around ω_0 just like in chapter 2, but this time also including the nonlinear contribution:

$$\tilde{\beta}(\omega) = \beta_0(\omega_0) + \beta_1(\omega_0)(\omega - \omega_0) + \frac{\beta_2(\omega_0)}{2!}(\omega - \omega_0)^2 + ... + \beta_0 n_2 I \tag{4.11}$$

Here β_i is the i^{th} order dispersion term and the final term is the nonlinear contribution due to the intensity *I*. As many higher order dispersion terms as needed could be included in this manner. In fact, that is exactly what will be done in a later discussion in this section, but for now only the second order dispersion is considered. The inverse Fourier transform can now be taken to go back to the time domain with the individual $(\omega - \omega_0)^n$ terms being transformed to $(i\partial/\partial t)^n$ to get:

$$\frac{\partial \tilde{A}}{\partial z} + \beta_1 \frac{\partial \tilde{A}}{\partial t} + \frac{i\beta_2}{2}\frac{\partial^2 \tilde{A}}{\partial t^2} - i\beta_0 n_2 I\tilde{A} = 0 \tag{4.12}$$

Since we are interested in the evolution of the spectral envelope $\tilde{A}$, a co-ordinate transformation of $\tau = t - z/v_g = t - z\beta_1$ can be performed so as to be in the frame of reference that is co-moving with the pulse:

$$\frac{\partial \tilde{A}}{\partial z} + \frac{i\beta_2}{2}\frac{\partial^2 \tilde{A}}{\partial \tau^2} - i\gamma|\tilde{A}|^2\tilde{A} = 0 \tag{4.13}$$

In the above equation the nonlinear parameter γ from the previous chapters has been re-introduced by rearranging the last term of Eq. 4.12. The equation is called the nonlinear Schrödinger equation because of its similarity in structure to the Schrödinger equation. In this basic equation, only the dispersive and nonlinear terms are included, but one can easily extend the same equation to include terms for linear and nonlinear losses as well as other nonlinear processes such as Raman scattering. This needs to be done for matching real experimental conditions where all these effects also play an important role; however, it is still instructive to study just this basic equation to understand soliton propagation and its role in supercontinuum generation. Equation 4.12 is generally solved by numerical methods even though in certain conditions, analytical methods such as the inverse scattering method can also be used [28]. By introducing the some transformations for the spectral envelope A as well as the time and distance co-ordinates, the NLSE can be normalized to be in a more insightful form:

$$\tilde{U} = \frac{\tilde{A}}{\sqrt{P_0}}; L_D = \frac{T_0^2}{|\beta_2|}; L_{NL} = \frac{1}{\gamma P_0}; N^2 = \frac{L_D}{L_{NL}} = \frac{\gamma P_0 T_0^2}{|\beta_2|}; \xi = \frac{z}{L_D}; T = \frac{\tau}{T_0} \tag{4.14}$$

$$i\frac{\partial \tilde{U}}{\partial \xi} = sgn(\beta_2)\frac{\partial^2 \tilde{U}}{\partial T^2} - N^2|\tilde{U}|^2\tilde{U} = 0 \tag{4.15}$$

In Eq. 4.14, P_0 and T_0 are the pulse peak power and width respectively, the value of sgn(β_2) is ± 1 depending on the sign of β_2 being positive or negative and L_D and L_{NL} are the characteristic lengths for the dispersion and nonlinear effects to be prominent. Their ratio defines the parameter *N* which is called the soliton number. As is clear from Eq. 4.15, *N* is the critical parameter determining the properties of the possible solutions to the normalized NLSE. As mentioned before, the NLSE describes the situation where with the right parameter values, it is possible for the nonlinearity and dispersion to cancel each other out and resulting in the pulse shape not changing as it propagates down the waveguide. When the physical parameters are such that *N* = 1, it can be easily verified that a pulse with a *sech* field profile satisfies Eq. 4.13, and is termed as the fundamental soliton:

$$\tilde{A}(\tau, z) = A_0 sech(\tau/\tau_0)e^{i\kappa z}; |A_0|^2 = \frac{-\beta_2}{\gamma\tau^2}; \kappa = \frac{1}{2}\gamma|A_0|^2 \tag{4.16}$$

As can be seen from Eq. 4.16, the signs of the nonlinear parameter γ and the second order dispersion β_2 must be opposite for the existence of a real pulse. Consequently, since n_2 (and hence γ) is positive for most cases, the dispersion has to be

anomalous for the fundamental soliton to exist. Also note that for the fundamental soliton, the peak power and the temporal width are inversely related, implying that to continue satisfying the soliton condition with larger power, a shorter pulse width is needed. Thus, in order to launch a fundamental soliton into a waveguide, the power and temporal width must satisfy the condition $N = 1$. Obviously, fulfilling such a strict criterion may not always be possible or desirable. Fortunately, this condition can be somewhat relaxed since it has been shown that the fundamental soliton is quite stable against small perturbations and that in fact almost any pulse shape close enough to the fundamental soliton will eventually evolve into the soliton. Thus, when a pulse with a pulse width or power slightly differing from the $N = 1$ condition is launched, it will either broaden or compress (thus also changing the peak power in the process) till it satisfies the fundamental soliton condition, after which the soliton propagates without change as prescribed by Eq. 4.15. The final soliton pulse may not have the same energy as before, i.e. the evolution into the soliton sheds away some of the energy of the initial pulse, which we will see later in the context of dispersive wave generation. Nevertheless, this means that these solitons are pretty robust entities. This, along with their other remarkable properties makes them quite attractive for certain applications such as information processing, communication etc. for which they have been indeed intensively studied [30].

As we shall see, soliton evolution dynamics also play an important role in supercontinuum generation. Certain laser systems such as modelocked lasers naturally output *sech*-shaped pulses and hence launching solitons into fibers and other waveguides is not too difficult practically. Apart from the fundamental soliton, Eq. 4.15 also has solutions of higher order when $N > 1$. Unlike the fundamental soliton, these higher order solitons do not retain their shape as they propagate down the waveguide, but rather display a periodic 'breathing' behavior in which their temporal (and consequently the spectral) profile undergoes periodic compression and broadening that repeats after the 'breathing period', given by $\pi L_D/2$. Figure 4.1(a) and (b) show the spectral and temporal evolution of solitons with $N = 1$ and 2 respectively over a waveguide length that corresponds to a couple of breathing periods for the $N = 2$ soliton. The simulation was done by numerically integrating Eq. 4.13 with the physical parameters set to have the required N value. As can be seen, if a soliton with the right power and width to satisfy $N = 1$ is launched, the pulse shape does indeed remain constant along the propagation length. Meanwhile, for the higher order soliton, it can be observed that after a specific propagation length, the spectrum broadens quite significantly and then eventually returns back to its original shape. Thus, the 'breathing' behavior can be observed where the pulse periodically recovers its original waveform. It should be noted that the significant spectral broadening also implies severe pulse compression, which can in fact go down to a few tens of femtoseconds or just a few optical cycles. A number of studies have been published [12] that show that even though the NLSE only deals with the pulse envelope and not the 'carrier frequencies', it is nevertheless valid down to almost the single optical cycle regime, and hence the results predicted by

the NLSE can be trusted even on these extremely short time scale regimes.

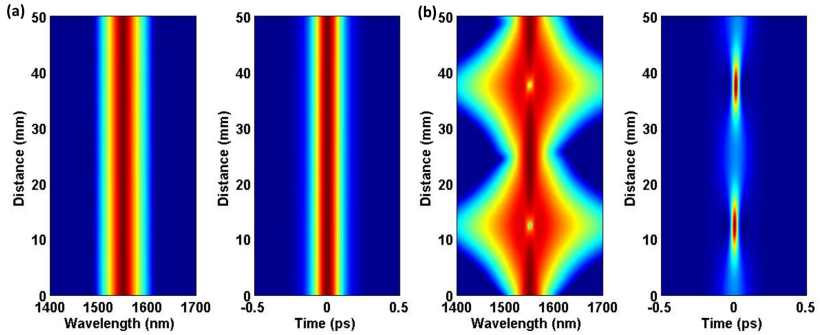

Figure 4.1 The spectral, and temporal evolution of (a) a fundamental soliton and (b) a soliton with N = 2 in a waveguide with properties similar to the InGaP waveguide used here, but where the higher order dispersion and nonlinear absorption effects were artificially set to zero in order to see the pure soliton behavior.

It is immediately clear from this discussion that these higher order solitons could be exploited for supercontinuum generation as the periodic breathing of the higher order soliton seems to provide an easy path to generating a broad spectrum. So if one carefully launched a higher order soliton into a nonlinear waveguide which is carefully selected to have just appropriate length, the wide spectrum generated by this breathing behavior could be accessed. This is indeed exploited for the supercontinuum generation process, as we shall see. At this point, it is reasonable to ask whether in reality these higher order solitons are stable against perturbations or not. The source of perturbations in Eq. 4.13 could for example be the non-zero value of higher order dispersion terms and it is essential to understand if any instability is prohibitive to the spectral broadening process needed for supercontinuum generation. To explore this, it is easy to go back to Eq. 4.13 and add the higher order dispersion terms and see what happens as the soliton propagates down the waveguide. Figure 4.2(a) and (b) show such a comparison between the propagation with and without higher order dispersion terms included in the simulation of the propagation of a soliton with $N = 3$. As can be observed, while the periodic nature of the breathing behavior is indeed disrupted by the presence of the higher order dispersion terms, the temporal pulse compression and the accompanying spectral broadening are still present, although they are somewhat distorted. Thus, it seems that deviation from the ideal soliton behaviour due to higher order dispersion does not necessarily preclude the possibility of supercontinuum generation using this process. Of course, perturbations to the soliton propagation come not just from the existence of the higher order dispersion terms, but also from various other processes such as multiphoton absorption, carrier-induced absorption and dispersion as well as nonlinear scattering processes such as Raman scattering.

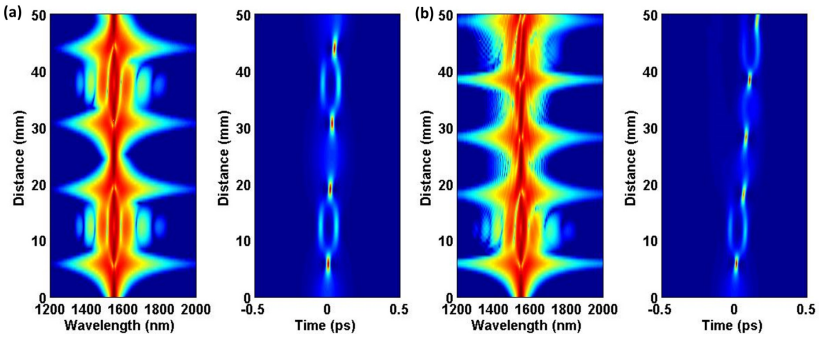

Figure 4.2 The spectral and temporal evolution of a $N = 3$ soliton simulated (a) without and (b) with the higher order dispersion terms included. The perturbation caused by the higher order dispersion terms causes the periodicity of the soliton breathing to be disrupted but the large spectral broadening is still observed.

All of these processes can be systematically included during the derivation of the NLSE. These derivations are outside the scope of the present work and have been described in several excellent textbooks and review papers, and the references therein [12, 28]. Suffice it here to say that we end up with a generalized nonlinear Schrödinger equation (GNLSE) given as follows:

$$\frac{\partial A}{\partial z} = -i\frac{\beta_2}{2}\frac{\partial^2 A}{\partial t^2} + \ldots - \frac{\alpha_{lin}}{2}A + \left(1 + \frac{i}{\omega_0}\frac{\partial}{\partial t}\right)\left(iRe(\gamma)|A|^2 - \frac{\alpha_{3pa}}{3A_{5eff}^2}|A|^4\right)A - \frac{\sigma}{2}(1 + i\mu)N_c A \tag{4.17}$$

Here, the first term on the right hand side represents the group velocity dispersion (with the inclusion of as many higher order dispersion terms as needed being signified by the ellipsis), the second term is the linear loss, the terms inside the brackets are the nonlinear gain and three-photon absorption terms (since there is no two-photon absorption in the wavelength range of interest here) and the final two terms take into account the carrier-induced absorption and dispersion respectively. The term with the time derivative includes the effects of optical shock formation. As in chapter 3, the carrier density N_c is calculated by the following equation:

$$\frac{dN_c}{dt} = \frac{\alpha_{3pa}}{3h\nu_0}\frac{|A|^6}{A_{eff}^3} - \frac{N_c}{\tau_{recomb}} \tag{4.18}$$

Here τ_{recomb} is the recombination lifetime of the carriers. Equations 4.17 and 4.18 can be numerically integrated to simulate the behavior of ultrashort pulses launched into an InGaP waveguide to study the kind of supercontinuum that can be generated.

While quantitative analysis of the supercontinuum generation process via soliton evolution dynamics will be carried out in later sections, a qualitative description is given here. As mentioned above, the soliton number *N* is an important parameter in determining the evolution of the soliton. Notice from Eq. 4.14, that N^2 is directly proportional to γ and the peak power P_0 of the input pulse. Since γ for the InGaP waveguides is quite large, even with modest peak powers the soliton number will be fairly high. For example, for the case of Fig. 4.2, where *N* = 3, the peak power of the input pulse was only 1.25 W. Thus, solitons with much larger *N* values are easily launched into these waveguides. It is known that in the presence of the perturbation of higher order dispersion, these higher order solitons are unstable and split up into several fundamental solitons after a certain propagation distance [12]. This 'soliton fission' process underlies the supercontinuum generation presented in this chapter and is simply an extension of the distortion seen in Fig. 4.2(b). Another important process takes place when the continuum generated by the fission process is wide enough to overlap with the normally-dispersive wavelength regime of the InGaP waveguide. When this happens, the soliton pulse sheds energy in the form of 'dispersive waves' or 'Cherenkov radiation' by analogy to the Cherenkov radiation observed when a charged particle passes through a medium with a velocity larger than the speed of light in that medium [31, 32]. These dispersive waves thus lie in the wavelength range of normal dispersion where solitons are forbidden since anomalous dispersion is required to balance the nonlinearity. Thus, the emission of dispersive waves further increases the total spectral coverage of the generated supercontinuum. The position of and the power contained in these dispersive waves depends on how far away the central frequency of the pump is from the zero-dispersion point. The farther away the pump is, the farther away from the zero-dispersion point (and weaker) the dispersive waves will be. Thus, by properly designing the dispersion properties of the InGaP waveguide, it is possible to maximize the spectral coverage of the supercontinuum through the emission of these dispersive waves. The process of the emission of dispersive waves is a mechanism by which a soliton maintains its soliton nature even though the spectrum overlaps with the normally dispersive regime where it is normally forbidden [31]. It can be viewed as a resonant process where the wave number of the fundamental solitons ejected during the soliton fission stage are equal to (i.e. phase matched with) the wave number at a different frequency and are therefore coupled. The phase matching condition is given by [12]:

$$\beta(\omega_{DW}) - \omega_{DW}\beta_1(\omega_{DW}) = \beta(\omega_{sol}) - \omega_{sol}\beta_1(\omega_{sol}) + \frac{\gamma P_0}{2} \tag{4.19}$$

$$\Omega = \omega_{DW} - \omega_{sol} = \frac{3|\beta_2|}{\beta_3} + \frac{\gamma P_0 \beta_3}{3\beta_2^2} \tag{4.20}$$

Here, β_i is the i^{th}-order derivative of the propagation constant with respect to and Eq. 4.20 is derived from Eq. 4.19 using the Taylor expansion limited to the third-order dispersion. From Eq. 4.20, the wavelength of the dispersive wave can be approximately calculated if the dispersion of the waveguide is well known. In

general, the nonlinear terms in equations 4.19 and 4.20 are small compared to the other terms and can be ignored. It should be noted that the relation 4.20 can also be derived from the equivalent interpretation of the emission of the dispersive waves as a cascaded four-wave mixing process where the phase matching occurs between the soliton and the dispersive wave frequencies [33].

In summary, if one launches a sufficiently powerful pulse (so as to have a high enough N value and thus trigger soliton fission) into an InGaP waveguide with the right dispersion properties (so as to efficiently emit dispersive waves as far away from the pump as possible), then a very wide supercontinuum should be generated. This is what is demonstrated in the following section. As mentioned above, the coherence properties of the generated spectra are also of particular importance for certain applications. It is also shown through simulations and measurements that the soliton fission and dispersive wave emission processes preserve the original phase coherence of the input pump pulses.

4.3 Experimental characterization

As discussed above, the nonlinear and dispersive properties of the waveguide need to be properly managed for supercontinuum generation. Obviously, the stronger the nonlinearity is (as described by the nonlinear parameter γ), the smaller is the pump power required to get the same soliton number. Thus obviously, one wants to have the smallest possible effective area. More interesting is the requirements for the dispersion properties of the waveguide. In order to get the widest possible spectral coverage while pumping near the 1550 nm wavelength, it is necessary for the dispersion at that wavelength to be anomalous. As discussed in the previous chapters, the waveguide contribution to the total dispersion can be exploited to achieve this since the material contribution in this case is normal. However, as mentioned above, dispersive wave generation occurs when the generated wide spectrum after soliton fission overlaps with the normally dispersive wavelength regime of the waveguide. Hence, the pump wavelength should not be too far away from the zero-dispersion wavelength (ZDW) where the dispersion goes from anomalous to the normal dispersion regime. This is also important since the strength of the dispersive wave is directly related to the amount of spectral overlap of the ejected soliton with the normal dispersion regime. So, in order to have sufficient power in the dispersive waves, the pump should not be too far away from the ZDW. Also, since the farther away the pump is from the ZDW, the farther away the dispersive wave will be from the ZDW as well, a tradeoff occurs. The pump should not be too far away from the ZDW to have no or too little overlap with the normally dispersive regime, but it should also not be so close to the ZDW so that the position of the emitted dispersive waves is too close, resulting in minimal bandwidth increase. If this tradeoff is properly achieved, dispersive waves with enough power will be emitted far enough away from the ZDW to significantly enhance the total supercontinuum spectral coverage. Additionally, if ZDWs are present on both sides of

the pump wavelength, then dispersive wave emission on both the red and blue side of the pump could be achieved, which would greatly increase the spectral coverage. This is indeed what was endeavored with the InGaP waveguides as shown in Fig. 4.3. The simulated dispersion profiles show that there exists a ZDW on either side of the 1550 nm spectral region for waveguides of various widths and a height of 250 nm. These widths are comparable to the waveguides investigated in the previous chapter for the characterization of the linear and nonlinear properties, and thus all of the numbers quoted there still hold true here. Consequently, these waveguides have a value of the nonlinear parameter γ large enough to achieve significant nonlinearities but also possess the right dispersion properties as outlined here.

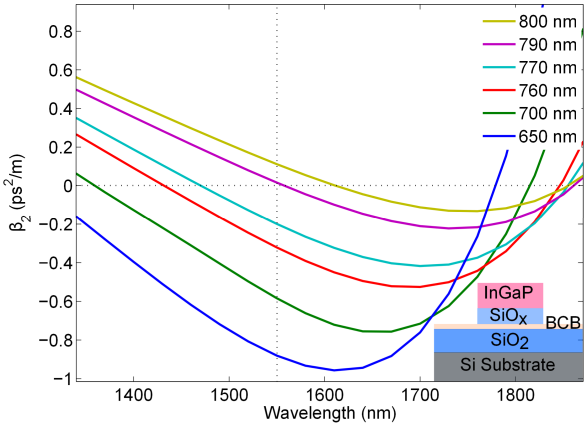

Figure 4.3 Dispersion profiles of various InGaP waveguides used for the supercontinuum generation with zero dispersion wavelengths on both sides of the pump. Inset: Schematic of the waveguide cross-section.

As can be seen, the ZDWs on the red side of the 1550 nm pump lie around 1800 nm while the ZDWs on the blue side vary significantly with the waveguide width. Thus, if the broadened spectrum due to soliton fission can span this wavelength range, dispersive wave emission is expected on either side of the pump wavelength.

4.3.1 Characterization of the supercontinuum

For the experimental demonstration of supercontinuum generation, waveguides of various widths were fabricated according to the procedure described in the previous chapter. These waveguides were then pumped by pulses from an optical parametric oscillator (OPO), which were known to have a sech pulse shape centered at 1550 nm and with a pulse FWHM of 170 fs and a repetition rate of 82 MHz. The pulses were focused on the grating-coupled InGaP waveguides by means of a high numerical aperture (NA) microscope objective (MO). The out-coupling was

done through a lensed fiber focused on the cleaved facet of the waveguide since the output spectrum of the generated supercontinuum is much wider than the grating coupler bandwidth. The lensed fiber output is coupled to an optical spectrum analyzer to measure the supercontinuum spectrum. The objective, chip and lensed fiber are mounted on translation stages in order to properly align them. At the input side, the pump pulses are not coupled to a fiber because the large peak power associated with the femtosecond pulses means that significant nonlinear broadening would occur in standard single mode fibers even for the short fiber lengths of a few tens of cm required to do the coupling to the InGaP waveguides. Thus, the free-space output from the OPO is directly coupled into the waveguides via the MO to avoid any nonlinear effects before the InGaP waveguides. For the output, even with the cleaved facet, the coupling efficiency varies over the spectrum because of it broad nature and care must be taken to realign the lensed fiber while collecting different parts of the spectrum to maximize the collection efficiency, especially for the extreme ends of the spectra. The whole experimental setup is shown in Fig. 4.4.

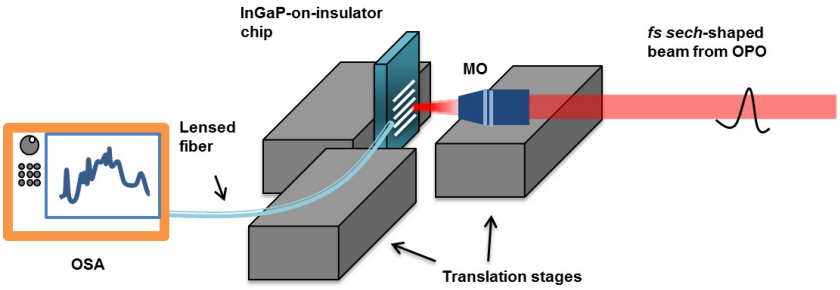

Figure 4.4 The experimental setup for the characterization of supercontinuum generation in InGaP-on-insulator waveguides pumped by a fs-source. The light is coupled to the grating coupled waveguides via a microscope objective and the supercontinuum spectra are coupled out through a lensed fiber to the optical spectrum analyzer.

The resulting supercontinuum spectra for waveguides with different widths are shown in Fig. 4.5 for a waveguide coupled peak power of 10 W. The widest supercontinuum is observed for the 700 nm wide waveguide, where dispersive waves on both sides of the pump at 1005 nm and 2097 nm are observed. Observe that the respective positions of the dispersive waves on either side of the pump wavelength significantly increase the total bandwidth of the supercontinuum. For this particular case, the spectrum spans more than an octave of frequencies at a power level 30 dB below the output maximum power spectral density. As the waveguide's width increases, it can be observed that the blue (red) side dispersive waves move closer to (farther away from) the pump wavelength of 1550 nm, as expected from the ZDW moving closer to (farther away from) the pump in the simulated dispersion profiles shown in Fig. 4.3. Also observe that for the 650 nm waveguide, no dispersive wave is observed on the blue side, implying that the ZDW on that side is too far away for the ejected soliton's spectrum to cross it and thus emit disper-

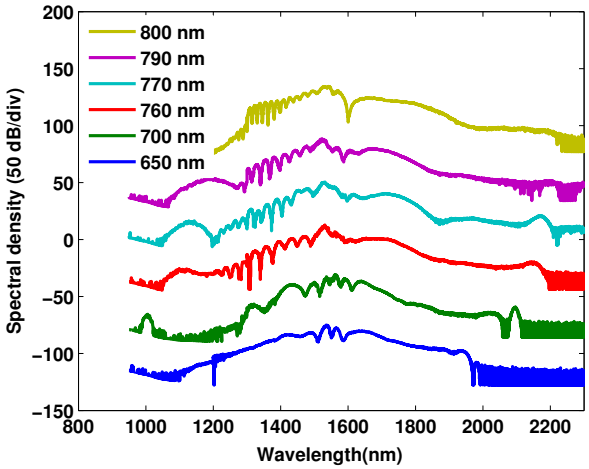

Figure 4.5 The supercontinuum spectra at the output of the InGaP waveguides with varying widths - the spectra are displaced by 40 dB for clarity. The positions of the dispersive waves can be seen to shift with the width as expected. The spectra above and below the 1200 nm wavelength were measured with different optical spectrum analyzers with different noise floors.

sive waves. In this way, the behavior predicted in previous discussions is (at least qualitatively) found to be experimentally realized. It also shows the importance of proper dispersion engineering for maximizing the supercontinuum spectral coverage.

In order to better understand the dynamics of the supercontinuum generation, numerical simulations of the generalized nonlinear Schrödinger equation (GNLSE) shown in Eq. 4.17 (along with 4.18 for taking into account the carriers generated by 3PA) were performed for the 700 nm width. Values for the carrier lifetime τ_c (50 ps), the FCA ($\sigma = 7 \times 10^{-21} m^2$) and the FCD ($\mu$ = 5.8) coefficients were taken from literature or extrapolated from similar materials [34–36]. Fig. 4.6(a) shows the simulated supercontinuum spectrum (dotted line) after 2 mm of propagation length in the waveguide for a hyperbolic secant input pulse with a FWHM of 170-fs and a peak power of 10 W, corresponding to the experimental conditions of Fig. 4.5. It can be seen that it matches reasonably well with the experimentally observed spectrum (solid line) and, in particular, the position of the dispersive waves on either side of the pump. The temporal profile of the simulated spectrum is shown in Fig. 4.6(c). The constituent parts of the total temporal profile - the fundamental solitons as well as the dispersive waves - are labelled in the figure. In particular, the blue and red side dispersive waves are seen respectively on the right and left hand side flanks of the profile. Figures 4.6(b) and (d) show respectively the evolution of the spectrum and the temporal profile as a function of the propagation length along the waveguide. Initially, the pulse goes through a stage

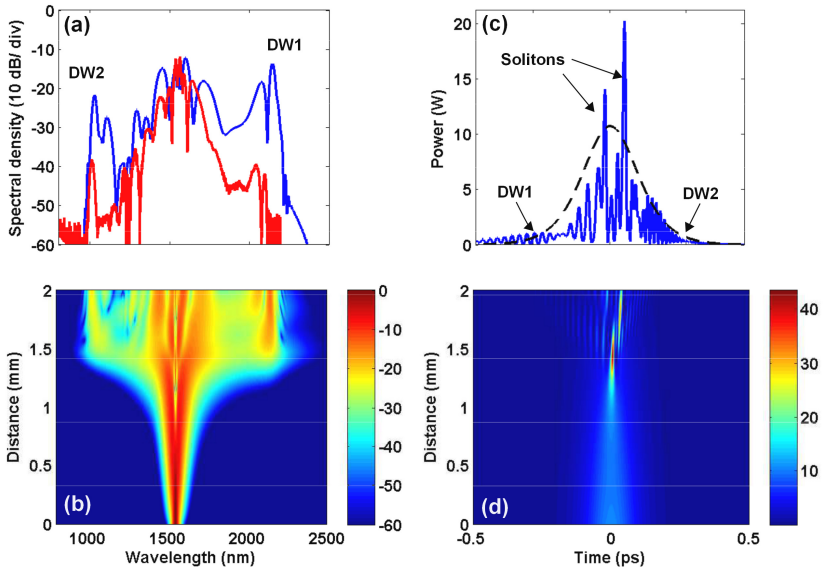

Figure 4.6 (a) The simulated (blue line) and experimental (red line) spectra at the output of the 700 × 250 nm waveguide, with the positions of both the dispersive waves shown. (b) The evolution of the supercontinuum spectrum over the propagation length of 2 mm showing the soliton fission and dispersive wave generation. Color bar is in dB scale. (c) The simulated temporal profile of the supercontinuum (solid line) showing a small number of solitons and the two dispersive waves on the leading and trailing edges. The input temporal profile is shown as the dashed line. (d) Evolution of the temporal profile with distance. Color bar has units of W.

of temporal compression. After about 1.4 mm of waveguide propagation length, the pulse is seen to undergo soliton fission thereby ejecting fundamental solitons. This results in a broadened spectrum which is already beginning to cross over into the normally dispersive regime on both sides of the pump. As a result, dispersive wave generation on both sides of the pump occurs, thereby completing the supercontinuum generation process. In this way, a propagation length of 1.5 mm is enough to generate an octave spanning supercontinuum, demonstrating again that highly compact devices are possible in this nonlinear platform. In contrast to reported supercontinuum generation in crystalline [37] as well as hydrogenated amorphous silicon-on-insulator platforms [38], where the spectra spanned 0.56 and 0.53 octaves respectively, here, a much wider spectrum is achieved under similar experimental conditions. This clearly demonstrates the large impact of the improved nonlinear parameter and lowered nonlinear losses of this platform. Octave spanning supercontinuum has been reported in silicon wire waveguides, but required much larger pulse energies (50 pJ) than in the present case (2 pJ) [19]. Another report of an octave-spanning SCG in the SOI platform with the lowest reported pulse energy of 6.8 pJ [20] required dispersion engineering via the in-

clusion of a nanoslot in the waveguide, which obviously renders the fabrication process quite complicated. Similarly, in case of the SiN platform [21], nonlinear losses are also absent, but a much lower nonlinear parameter is available and thus much larger pulse energies for SCG are required. In contrast, in the present case, the octave-spanning bandwidth is achieved at much lower pulse energies and in a short, straight waveguide with an invariant cross-section requiring no tapering or complicated slot waveguide inclusions. Thus, the advantages of this platform are already evident. The buildup of the supercontinuum with increasing input power is shown in Fig. 4.7. In the experiment, a variable attenuator added before the input MO was used to change the input power, since changing the laser gain could alter the pulse shape. Figure 4.7 shows the comparison of the experimental and simulated buildup of the supercontinuum using the same parameters as those for the simulations shown in Fig. 4.6. One can see that overall, the simulations agree very well with the experimentally observed spectra. Dispersive waves are observed at a coupled peak power of 8.3 W and higher. In the case of this waveguide, the dispersive waves appear on both sides of the pump at the same pump power level, which also corresponds to the experimental observations. This is because, as seen from Fig. 4.6(c), the broadened spectrum after soliton fission is wide enough to span beyond the entire anomalously dispersive range of the waveguide and overlap with the normal dispersive wavelength regimes beyond it.

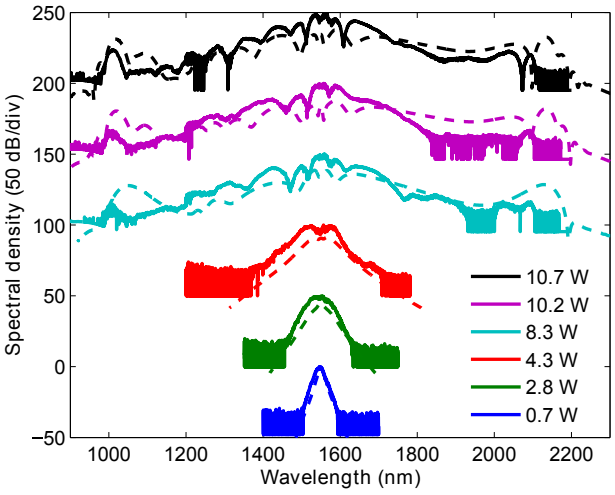

Figure 4.7 The buildup of the supercontinuum in the numerical simulations (dotted lines) matches well with the experimental spectra (solid lines); in particular the peak power at which the dispersive waves become observable.

4.3.2 Coherence characterization

The coherence properties of the supercontinuum generated in these InGaP waveguides were also studied. One approach for characterizing the coherence properties of broadband spectra is to perform a spectral interference experiment between separately generated supercontinua. The interferometric fringes observed can then be directly related to the coherence as a function of wavelength. The coherence can be quantified by the modulus of the first-order coherence function as follows [12, 30]:

$$|g_{12}^{(1)}(\lambda, t_1 - t_2)| = \left| \frac{\langle E_1^*(\lambda, t_1) E_2(\lambda, t_2) \rangle}{\left[\langle |E_1(\lambda, t_1)|^2 \rangle \langle |E_2(\lambda, t_2)|^2 \rangle \right]^{1/2}} \right| \tag{4.21}$$

Here, the angled brackets denote the average over independently generated spectra $E(\lambda, t)$ by several pairs of pulses. By taking $t_1 - t_2 = 0$, the wavelength dependence of the coherence can be measured. Experimentally, the spectral interference pattern produced by the interference of two independent supercontinua generated by two successive pulses of the pump pulse train is measured. The fringe visibility of this pattern is then related to the first-order coherence g_{12} as follows [39]:

$$V(\lambda) = \frac{2\left[I_1(\lambda) I_2(\lambda)\right]^{1/2}}{I_1(\lambda) + I_2(\lambda)} |g_{12}^{(1)}(\lambda)| \tag{4.22}$$

Here, $I_{1,2}$ are the intensities of the individual supercontinua and $V(\lambda)$ is the visibility of the fringes at a given wavelength, defined as $V = (I_{max} - I_{min})/(I_{max} + I_{min})$ where I_{max} and I_{min} are the maxima and minima of the fringes around that wavelength. Thus, given that the power is equally divided between the two arms of the interferometer, $V(\lambda)$ is equal to the first-order coherence at that wavelength. Hence, this method has the advantage that it potentially allows us to quantify the coherence across a broad range of wavelengths within the supercontinuum spectrum in a single measurement. The experimental setup is shown in Fig. 4.8, where the output from the InGaP waveguide is sent to a Michelson interferometer and detected by the OSA. The delay in the left arm of the interferometer is calculated to be such that the supercontinuum from one pulse overlaps with the one from the next pulse of the pump laser. The density of the fringes can be tuned by slightly varying the delay around this value, such that they can be easily observed by the OSA.

In the experiment, the coherence was measured in a 200 nm band around the pump. The low power collected at the waveguide output prevented accurate measurements of the fringe visibility outside this range. Figure 4.9(a) shows the interference fringes recorded in this experiment. Different alignments of the interference setup were needed to both optimize the power collected from the chip from that particular part of the spectrum, as well as equalize the power in each of the arms of the interferometer and are shown as separate colours in Fig 9(a). From Fig. 4.9(b) it can be seen that the coherence is greater than 90% over the range where it was

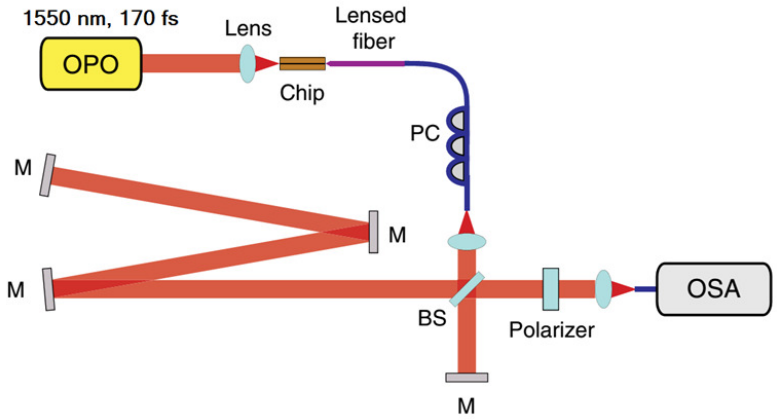

Figure 4.8 The experimental setup for the coherence characterization of the supercontinuum generated in the InGaP waveguides. The delay line corresponds to the travel time between two successive pulses, with slight adjustments made to observe the density of fringes. Figure from ref. [18].

measured. These measurements were limited by the noise floor of the optical spectrum analyzer, meaning the extinction ratio was limited not by the coherence but rather by the experimental constraints. Although the coherence of the spectrum at the dispersive waves' position was not measured because the power there was too low, it has previously been reported in [18] that they can retain a high degree of coherence despite seemingly being spectrally disconnected from the 'main' spectrum. This is because of the resonant nature of the dispersive wave generation, or as viewed in the discrete nonlinear optics picture, because the four-wave mixing process is a phase coherent process. Thus, the phase-coherence between the emitting soliton and its dispersive waves ought to be preserved.

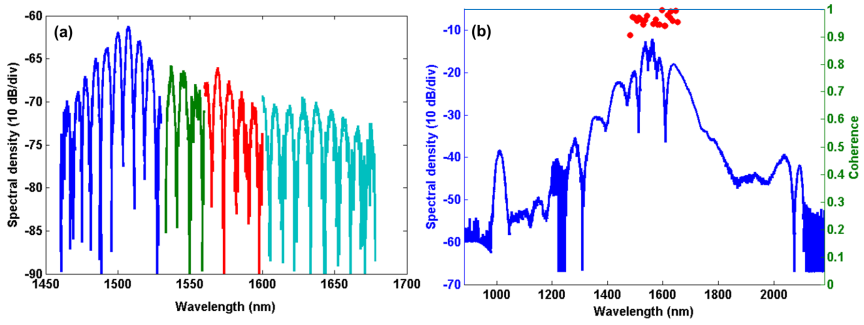

Figure 4.9 (a) The observed interference fringes between two successive pulses of the supercontinuum with different colors representing individual measurements of the spectral fringes. (b) Coherence of the supercontinuum around the pump wavelength.

It should also be noted that unlike the case in crystalline silicon, the soliton number of the input pulse is not very high here - $N \approx 9$. The coherence of the soliton fission process is known to be preserved for small soliton numbers [12], [40]. This is in contrast to the case of crystalline silicon where though the input soliton number was high ($N \approx 20$), the coherence was still preserved but only because two-photon absorption limited the peak powers, and consequently the soliton number in the waveguide. In the present case, the nonlinear losses from three-photon and free-carrier absorption are too low for this effect and hence the input soliton number needs to remain low in order to maintain the coherence.

To stress this point, the effect of increasing pulse widths (and thus increasing soliton number) on the coherence properties of the supercontinuum was simulated, as shown in Fig. 4.10. The first-order coherence is calculated by taking the ensemble average in the formula for g_{12} in Eq. 4.21 over several pairs of the independently simulated spectra of the supercontinuum with random input phase noise as described in literature previously [12, 39]. Other simulation parameters including the peak power, dispersion and nonlinear losses were kept the same as in the current experiment. It is clear that although the bandwidth of the generated supercontinuum is approximately the same for all the pulse widths as shown in Fig. 4.10(a), beyond a pulse width of 170 fs ($N \approx 9$), the coherence degrades dramatically, especially away from the central pump wavelength, as shown in Fig. 4.10(b). Thus, for the case of 70 fs pulse width, the coherence is perfect virtually across the entire spectrum, but is still also octave-spanning. In this way, one can ascertain the needed input pulse properties for applications requiring coherent octave-spanning supercontinuum spectra.

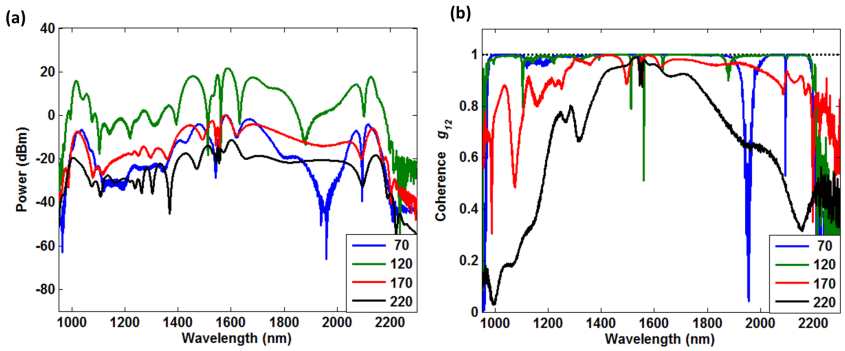

Figure 4.10 (a) The simulated supercontinuum spectra for various input pulse FWHMs ranging from 70 fs to 220 fs corresponding to soliton numbers 4, 6, 9 and 11 respectively are all still octave spanning. (b) The coherence properties of the supercontinuum for the different pulse widths. Degradation of coherence for pulse width larger than 170 fs (soliton numbers $N > 9$) is clear.

Figure 4.11(a) shows the effect of increasing pump power for a pulse width of 170 fs on the spectrum of the supercontinua. Again, it is observed that even though the

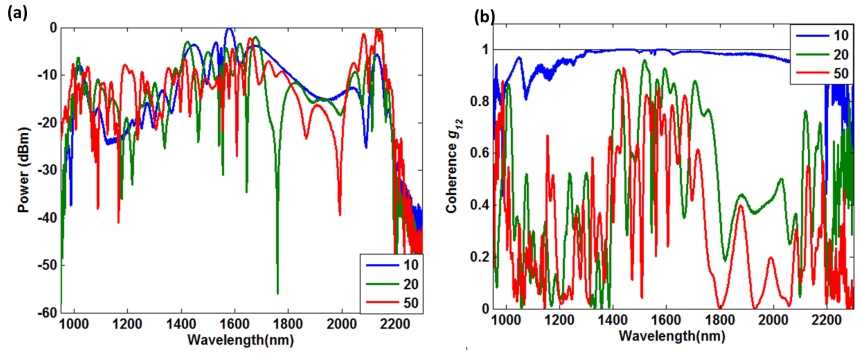

Figure 4.11 (a) The simulated supercontinuum spectra for various input pump powers ranging from 10 W to 50 W corresponding to soliton numbers 9, 13 and 20 respectively are all are very similar in total spectral bandwidth. (b) The coherence properties of the supercontinuum for the different pump powers. Degradation of coherence for powers above 10 W (soliton numbers $N > 9$) is clear.

detailed spectral profile does change, the total spectral bandwidth does not change significantly even when the peak power is increased by about 5 times. The corresponding coherence properties are shown in Fig. 4.11(b). It can be seen that with increasing pump power (and thus increasing soliton number), the coherence again drops quite significantly, even within the experimentally measured bandwidth around the pump wavelength. This clearly shows that unlike the case of SOI waveguides [18], the coherence is not preserved by the soliton-number limiting action of nonlinear absorption which, in that case is two-photon absorption. Instead, due to the absence of strong nonlinear losses, the coherence properties follow a similar trend as observed in photonic crystal fibers where the soliton number has to be kept low for obtaining a high degree of coherence. Fortunately, as demonstrated, due to the large nonlinearity and suitable dispersion properties of these waveguides, octave spanning supercontinuum is obtainable in the telecommunication wavelength range.

4.4 Conclusion

In conclusion, the potential of the proposed InGaP-on-insulator platform for on-chip nonlinear optics is demonstrated by generating an octave spanning supercontinuum pumped at 1550 nm. It was shown that compared to other popular on-chip platforms like silicon-on-insulator, it is possible to generate a wider supercontinuum at significantly lower pulse energies, which is possible due to a larger value of the nonlinear parameter γ as well as significantly lowered nonlinear losses while still pumping at 1550 nm. Wavelengths below 1100 nm are also accessible due to the larger bandgap of the material compared to silicon, thus bridging the near- to mid-infrared wavelength range while still pumping in the telecommunication wavelength range. The advantages of the large index contrast between the InGaP

membrane and the oxide cladding beneath (which enables large intensities to be coupled into the waveguides) as well as dispersion engineering (which enables phase matching) were exploited. Additionally, using this approach, it is also possible to integrate such III-V nonlinear devices with established platforms like SOI or silicon nitride photonic integrated circuits to exploit the already well-developed functionalities there. For example, coupled with the on-chip modelocked lasers that have recently been developed [41], the presented nonlinear waveguide platform could provide a way forward to achieving an entirely on-chip implementation of an octave spanning supercontinuum. Potentially, the large second order nonlinear coefficients of these waveguides could also be exploited on the same platform. This would provide a way to stabilize the carrier envelope offset of the coherent supercontinuum [21, 42]. In view of such applications, the next chapter deals with characterizing the second-order nonlinearity of the platform.

References

[1] Utsav D Dave, Charles Ciret, Simon-Pierre Gorza, Sylvain Combrie, Alfredo De Rossi, Fabrice Raineri, Gunther Roelkens, and Bart Kuyken *Dispersive-wave-based octave-spanning supercontinuum generation in InGaP membrane waveguides on a silicon substrate* Optics letters, 40(15):3584–3587, 2015.

[2] Yoshifumi Ueda and Koichi Shimoda *Observation of Stimulated Raman Emission and Stimulated Rayleigh-Wing Scattering from Self-Trapped Filaments of a Laser Beam* Japanese Journal of Applied Physics, 6(5):628, 1967.

[3] EB Treacy *Compression of picosecond light pulses* Physics Letters A, 28(1):34–35, 1968.

[4] RR Alfano and SL Shapiro *Observation of self-phase modulation and small-scale filaments in crystals and glasses* Physical Review Letters, 24(11):592, 1970.

[5] R. R. Alfano and S. L. Shapiro *Emission in the Region 4000 to 7000 Å Via Four-Photon Coupling in Glass* Phys. Rev. Lett., 24:584–587, Mar 1970.

[6] RR Alfano and SL Shapiro *Picosecond spectroscopy using the inverse Raman effect* Chemical Physics Letters, 8(6):631–633, 1971.

[7] CV Shank, RL Fork, RF Leheny, and Jagdeep Shah *Dynamics of photoexcited GaAs band-edge absorption with subpicosecond resolution* Physical Review Letters, 42(2):112, 1979.

[8] Fujio Shimizu *Frequency broadening in liquids by a short light pulse* Physical Review Letters, 19(19):1097, 1967.

[9] PB Corkum, Claude Rolland, and T Srinivasan-Rao *Supercontinuum generation in gases* Physical review letters, 57(18):2268, 1986.

[10] RH Stolen and Chinlon Lin *Self-phase-modulation in silica optical fibers* Physical Review A, 17(4):1448, 1978.

[11] Jinendra K Ranka, Robert S Windeler, and Andrew J Stentz *Visible continuum generation in air–silica microstructure optical fibers with anomalous dispersion at 800 nm* Optics letters, 25(1):25–27, 2000.

[12] John M Dudley, Goëry Genty, and Stéphane Coen *Supercontinuum generation in photonic crystal fiber* Reviews of modern physics, 78(4):1135, 2006.

[13] Alireza Marandi, Charles W Rudy, Victor G Plotnichenko, Evgeny M Dianov, Konstantin L Vodopyanov, and Robert L Byer *Mid-infrared supercontinuum generation in tapered chalcogenide fiber for producing octave-spanning frequency comb around 3 μm* Optics express, 20(22):24218–24225, 2012.

[14] I-Wei Hsieh, Xiaogang Chen, Xiaoping Liu, Jerry I Dadap, Nicolae C Panoiu, Cheng-Yun Chou, Fengnian Xia, William M Green, Yurii A Vlasov, and Richard M Osgood *Supercontinuum generation in silicon photonic wires* Optics express, 15(23):15242–15249, 2007.

[15] Lianghong Yin, Qiang Lin, and Govind P Agrawal *Soliton fission and supercontinuum generation in silicon waveguides* Optics letters, 32(4):391–393, 2007.

[16] Lianghong Yin and Govind P Agrawal *Impact of two-photon absorption on self-phase modulation in silicon waveguides* Optics letters, 32(14):2031–2033, 2007.

[17] François Leo, Simon-Pierre Gorza, Jassem Safioui, Pascal Kockaert, Stéphane Coen, Utsav Dave, Bart Kuyken, and Gunther Roelkens *Dispersive wave emission and supercontinuum generation in a silicon wire waveguide pumped around the 1550 nm telecommunication wavelength* Optics letters, 39(12):3623–3626, 2014.

[18] François Leo, Simon-Pierre Gorza, Stéphane Coen, Bart Kuyken, and Gunther Roelkens *Coherent supercontinuum generation in a silicon photonic wire in the telecommunication wavelength range* Optics letters, 40(1):123–126, 2015.

[19] Takahiro Goto, Atushi Ishizawa, Rai Kou, Tai Tsuchizawa, Nobuyuki Matsuda, Kenichi Hitachi, Tadashi Nishikawa, Koji Yamada, HIdeki Gotoh, et al. *Octave spanning frequency comb generation in a dispersion-controlled short silicon-wire waveguide with a fiber laser oscillator* In CLEO: Science and Innovations, pages SW4G–1. Optical Society of America, 2015.

[20] Lin Zhang, Qiang Lin, Yang Yue, Yan Yan, Raymond G Beausoleil, Anu Agarwal, Lionel C Kimerling, Jurgen Michel, and Alan E Willner *On-chip octave-spanning supercontinuum in nanostructured silicon waveguides using ultralow pulse energy* IEEE Journal of Selected Topics in Quantum Electronics, 18(6):1799–1806, 2012.

[21] AS Mayer, A Klenner, AR Johnson, K Luke, MRE Lamont, Y Okawachi, M Lipson, AL Gaeta, and U Keller *Frequency comb offset detection using supercontinuum generation in silicon nitride waveguides* Optics express, 23(12):15440–15451, 2015.

[22] Ting Wang, Doris KT Ng, Siu-Kit Ng, Yeow-Teck Toh, AKL Chee, George FR Chen, Qian Wang, and Dawn TH Tan *Supercontinuum generation in bandgap engineered, back-end CMOS compatible silicon rich nitride waveguides* Laser & Photonics Reviews, 9(5):498–506, 2015.

[23] Minhao Pu, Luisa Ottaviano, Elizaveta Semenova, and Kresten Yvind *Efficient frequency comb generation in AlGaAs-on-insulator* Optica, 3(8):823–826, 2016.

[24] Akira Hasegawa and Frederick Tappert *Transmission of stationary nonlinear optical pulses in dispersive dielectric fibers. I. Anomalous dispersion* Applied Physics Letters, 23(3):142–144, 1973.

[25] Linn F Mollenauer, Roger H Stolen, and James P Gordon *Experimental observation of picosecond pulse narrowing and solitons in optical fibers* Physical Review Letters, 45(13):1095, 1980.

[26] AKIRA Hasegawa and Yuji Kodama *Signal transmission by optical solitons in monomode fiber* Proceedings of the IEEE, 69(9):1145–1150, 1981.

[27] George I Stegeman and Mordechai Segev *Optical spatial solitons and their interactions: universality and diversity* Science, 286(5444):1518–1523, 1999.

[28] Govind P Agrawal *Nonlinear fiber optics* Academic press, 2007.

[29] F Leo, T Hansson, I Ricciardi, M De Rosa, S Coen, S Wabnitz, and M Erkintalo *Walk-off-induced modulation instability, temporal pattern formation, and frequency comb generation in cavity-enhanced second-harmonic generation* Physical review letters, 116(3):033901, 2016.

[30] Alexander V Buryak, Paolo Di Trapani, Dmitry V Skryabin, and Stefano Trillo *Optical solitons due to quadratic nonlinearities: from basic physics to futuristic applications* Physics Reports, 370(2):63–235, 2002.

[31] Nail Akhmediev and Magnus Karlsson *Cherenkov radiation emitted by solitons in optical fibers* Physical Review A, 51(3):2602, 1995.

[32] Ilaria Cristiani, Riccardo Tediosi, Luca Tartara, and Vittorio Degiorgio *Dispersive wave generation by solitons in microstructured optical fibers* Optics express, 12(1):124–135, 2004.

[33] M Erkintalo, YQ Xu, SG Murdoch, JM Dudley, and G Genty *Cascaded phase matching and nonlinear symmetry breaking in fiber frequency combs* Physical review letters, 109(22):223904, 2012.

[34] Srini Krishnamurthy, Zhi Gang Yu, Leonel P Gonzalez, and Shekhar Guha *Temperature-and wavelength-dependent two-photon and free-carrier absorption in GaAs, InP, GaInAs, and InAsP* Journal of Applied Physics, 109(3):033102, 2011.

[35] Brian R Bennett, Richard A Soref, and Jesus A Del Alamo *Carrier-induced change in refractive index of InP, GaAs and InGaAsP* IEEE Journal of Quantum Electronics, 26(1):113–122, 1990.

[36] P Thiagarajan, JF Schmerge, Carmen S Menoni, M Marconi, Oscar Eduardo Martinez, Jorge J Rocca, MJ Hafich, HY Lee, and GY Robinson *Picosecond absorption dynamics of photoexcited InGaP epitaxial films* Applied physics letters, 59(1):90–92, 1991.

[37] François Leo, J Safioui, Bart Kuyken, Günther Roelkens, and S-P Gorza *Generation of coherent supercontinuum in a-Si: H waveguides: experiment and modeling based on measured dispersion profile* Optics express, 22(23):28997–29007, 2014.

[38] Jassem Safioui, François Leo, Bart Kuyken, Simon-Pierre Gorza, Shankar Kumar Selvaraja, Roel Baets, Philippe Emplit, Gunther Roelkens, and Serge Massar *Supercontinuum generation in hydrogenated amorphous silicon waveguides at telecommunication wavelengths* Optics express, 22(3):3089–3097, 2014.

[39] John M Dudley and Stéphane Coen *Coherence properties of supercontinuum spectra generated in photonic crystal and tapered optical fibers* Optics letters, 27(13):1180–1182, 2002.

[40] EJR Kelleher, M Erkintalo, and JC Travers *Fission of solitons in continuous-wave supercontinuum* Optics letters, 37(24):5217–5219, 2012.

[41] Sarah Uvin, Shahram Keyvaninia, Francois Lelarge, Guang-Hua Duan, Bart Kuyken, and Gunther Roelkens *Narrow line width frequency comb source based on an injection-locked III–V-on-silicon mode-locked laser* Optics Express, 24(5):5277–5286, 2016.

[42] R Holzwarth, Th Udem, Th W Hänsch, JC Knight, WJ Wadsworth, and P St J Russell *Optical frequency synthesizer for precision spectroscopy* Physical review letters, 85(11):2264, 2000.

5

Integration with CMOS-compatible waveguide platforms

"There are many here among us
Who feel that life is but a joke
But you and I we've been through that
And this is not our fate
So let us not talk falsely now
The hour's getting late." - Bob Dylan, *All Along the Watchtower*.

5.1 Introduction

THE development of the fabrication process for the InGaP-on-insulator platform as well as the characterization of its linear and nonlinear properties was described in chapter 3. Since the CMOS-compatible waveguide platforms SOI and SiN-on-insulator represent the state-of-the-art in terms of the performance of the various functions performed in integrated photonic circuits, it is crucial to develop the technology to integrate the InGaP-on-insulator nonlinear platform with them. Towards that end, the fabrication flow as presented in chapter 3 was modified to include steps for allowing proper optical coupling between the InGaP layer and the silicon or silicon nitride waveguide layer (henceforth called the substrate layer), and these are described in this chapter. As was mentioned in chapter 3, most of the process remains unaltered, with the main modification being the incorporation of additional steps to fabricate markers in the substrate layer. These markers are used while doing the e-beam patterning of the InGaP layer and thus ensuring the proper alignment of the respective devices in the InGaP and substrate layers.
These additional steps to incorporate the markers are described in the following section. For coupling InGaP devices to SOI or SiN waveguide circuits, the design of evanescent coupling of InGaP microdisks to waveguides in the substrate layer as well as the design of InGaP waveguides to substrate waveguides using inverted tapers is described in section 5.3. Using this fabrication flow, microdisks evanescently coupled to SOI and SiN waveguides as well as InGaP waveguide spirals and ring resonators coupled to the SiN platform via inverted tapers were fabricated. The characterization of these evanescently-coupled microdisks for use in experiments such as four-wave mixing and second harmonic generation is described in section 5.4.

5.2 Fabrication flow

The process flow for the fabrication of integrated InGaP membrane devices with SOI/SiN photonic circuits has the same overall bonding, substrate removal and e-beam patterning and ICP etching steps as described in chapter 3. The difference in the fabrication process comes from the fact that a common reference frame is needed in order to write patterns into the InGaP layer aligned with the substrate patterns. This is achieved by having the e-beam recognize markers that are at known positions relative to the patterns of the substrate layer and using them to define a common reference frame while writing patterns into the InGaP layer.
Since the e-beam writing is done with a negative-tone HSQ resist (which has oxide-like properties), a good contrast for markers in the silicon or, especially, the silicon nitride layer is difficult to obtain. This obviously compromises the reliability of the common reference frame. In order to circumvent this problem, gold markers are patterned onto the substrate layer prior to the e-beam writing process. These metallic markers provide a very good contrast with the surrounding mate-

rial and thus a reliable reference frame for the e-beam during the final exposure. The positioning of these gold markers is done using pre-existing markers in the substrate layer (whose position relative to the substrate patterns is known). Thus, the substrate chip must have markers to set the co-ordinates of the common reference frame, and it is these markers that are used to position new gold markers, which will eventually be used while doing the final e-beam writing. Thus it is important to consider these substrate-layer markers while designing the substrate chip. Figure 5.1 shows typical examples of some of the markers present in the substrate layer that were used in this PhD. Since the e-beam recognizes the edge of the marker in order to 'know' its position, these markers are underetched to remove some or all of the buried oxide below the silicon or the silicon nitride layer, and thus improve the visibility of the edge. This is especially true for the silicon nitride case since its contrast with the oxide is particularly low and hence edge-detection without underetching can be quite difficult.

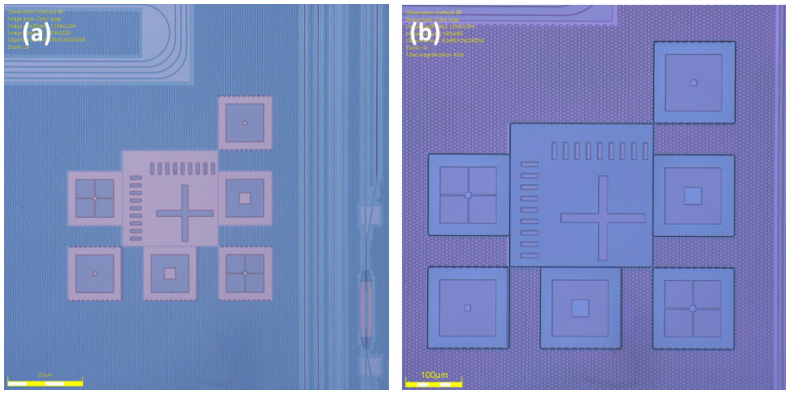

Figure 5.1 (a) A typical group of markers used in this work. The central marker is a Vernier-type marker that is used for alignment during the optical lithography step prior to etching the buried oxide. (b) After the optical lithography, the markers are exposed while the rest of the chip is protected by resist. The dark lines around the markers indicate the edge of the area protected by the resist.

The underetching of the buried oxide is done with buffered hydrofluoric acid. Typically, in order to have a good enough contrast for the markers to be detected by the e-beam, several hundred nanometers of the buried oxide needs to be removed. In case of the silicon nitride substrate, it was found that about 800 nm of height difference between the silicon nitride layer and the remaining buried oxide is enough for easy and reliable marker detection. Similarly, for the case of the SOI substrate, a step size of about 600 nm was found to be more than enough. If the underetching is done without protecting the rest of the chip, there is a danger of small-sized features getting completely underetched and consequently entirely 'lifting off' from the chip. Also, even if nothing gets lifted off, the underetching may prove detrimental to the proper functioning of the different devices that may have been designed for operation without an underetched cladding. Hence, it is a good practice

to protect the rest of the structures in the substrate chip and only underetch the markers. This is done by spinning a resist (in this case TI35E) onto the substrate chip and patterning it with optical lithography to expose only the relevant markers and underetching them. Given that several minutes of underetching is required to remove the several hundred nanometers of buried oxide, a thick resist is required to adequately protect the rest of the chip. This step is not very critical, and any resist that offers enough protection during the BHF treatment can be used. Table 5.1 lists the relevant lithography steps used for this procedure in this work.

Table 5.1: Optical lithography steps followed for the BHF treatment of markers

Step no.	Process step	Parameters
1	Spin resist TI35 E	3000 rpm, 40sec
2	Soft bake	100 C, 3 min
3	Alignment and exposure	50 sec
4	Stand by rest	20 min
5	Reversal bake	125 C, 2 min
6	Flood exposure	185 sec
7	Develop in AZ400k 1: 3 DI	2min 30sec
8	Hard bake (only wet etching)	145 C, 10 min

This 'image reversal' procedure is used to pattern the chip with simple optical lithography and expose the markers. The final resist thickness is typically about 1.6 μm and easily withstands prolonged BHF treatments. After the underetching is completed, the resist is easily removed by rinsing the chip in Acetone/IPA and DI water. Figure 5.1(b) shows the same group of markers after the lithography. The borders of the markers reveal the edge of the patterned resist. Two Vernier-type markers (like the central marker shown in Fig. 5.1(a)) displaced in both the x and y directions from each other, are used for the alignment in step 3 of Table 5.1. While these allow for accurate alignment, they are not strictly necessary, since in this step, a high alignment accuracy is not that critical because we are only aligning large area patterns (for example squares of side 150 μm, corresponding to the bounding box of the markers shown in Fig. 5.1). However, this could be necessary if for some reason, the markers are very small or very close to some critical structures that should not be underetched. Either way, once the underetching is complete, the substrate is ready to go to the next step - bonding.

In chapter 3, it was mentioned that for the case when the substrate was not a patterned chip but just a plain silicon substrate with some top oxide, the BCB layer thickness was generally kept thick in order to improve the yield of the bonding and substrate removal as it is less sensitive to any particulate contaminants. In the case of a patterned chip however, when there is need for light coupling between the InGaP and the substrate layers, the vertical separation between the two layers is an important design parameter. For example, in one of the applications discussed in this chapter, microdisks fabricated in the InGaP layer are evanescently coupled to waveguides in the substrate layer. In order to couple to a specific mode with the high efficiency, the overlap between the corresponding waveguide and disk modes

needs to be controlled properly. Obviously, this is only possible within a certain range of values for the InGaP-substrate separation. As a result, the BCB thickness needs to be well-controlled and lie within a certain range. As a result, thick or manual bonding as described in chapter 3 is not used for the case when the substrate is a patterned SOI or SiN chip. Instead, the bonding is performed in the machine bonder. The procedure for machine bonding was also described in chapter 3. As mentioned in chapter 3, this results in a bonded BCB thickness under the III-V die of about 50 nm. In order to improve the repeatability of the bonding, the bonding procedure is always kept the same, regardless of the actual vertical separation needed for a particular application. In case the vertical separation needed is more than 50 nm (as is frequently the case), the rest of the thickness is made up of deposited oxide on the III-V die or the substrate as needed. Of course, the total thickness needed should be calculated while taking into account that the refractive index of BCB at 1.55 micron is slightly larger than that of oxide. Once the bonding is done, the substrate removal proceeds as described in chapter 3.

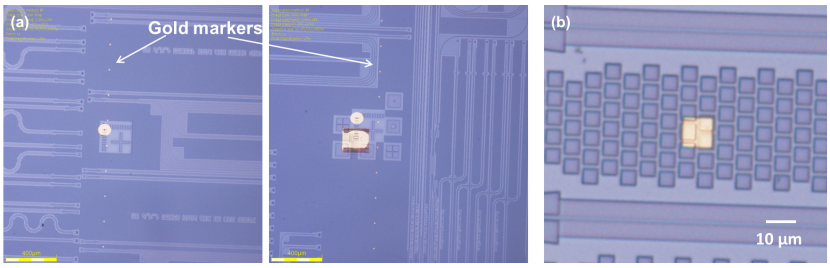

Figure 5.2 (a) Two (vertical) lines of gold markers patterned at two different horizontal positions on the chip using the e-beam patterning. The somewhat large and irregularly shaped areas where the gold has not completely lifted-off are the locations where the underetched markers in the substrate layer were present, and which were used by the e-beam to position itself before writing for the gold markers. This results in that area being exposed to the e-beam and hence the gold does not lift-off in those areas as well. (b) A zoomed-in view of one of the gold markers after lift-off.

After substrate removal, the e-beam patterning for the gold markers is done. If the bonding was done *after* the marker underetching, BCB would have partially filled the underetched portions of the substrate markers. This again lowers the contrast of the markers in the e-beam and so the BCB is first removed in RIE using SF6/CH3 gases. Following that, the e-beam patterning is done using the positive-tone PMMA resist. The underetched markers are detected by the e-beam and using them as reference, new markers are patterned into the PMMA resist. Since the e-beam system needs at least three markers in an L-shaped configuration to position the origin of the common reference frame, two lines of markers are patterned which are offset from each other, as shown in the Figure 5.2(a). The exposed sample is then developed in the MIBK solution as mentioned in chapter 3. Finally, gold is deposited onto the patterned sample and then immersed in trichloroethylene (TCE) for lift-off. The gold is lifted off everywhere except at the patterned markers. In this way, gold markers are patterned onto the substrate layer,

as shown in Fig. 5.2(b).
Following this procedure, the rest of the e-beam patterning using the HSQ resist and InGaP etching in the ICP can be followed as described before in chapter 3. The only difference would be that during the e-beam writing, the new gold markers are used by the e-beam system to define the origin of co-ordinate system for the InGaP patterns. This thus ensures the proper alignment between the two layers. The full fabrication flow including the previously discussed steps is shown in Fig. 5.3.

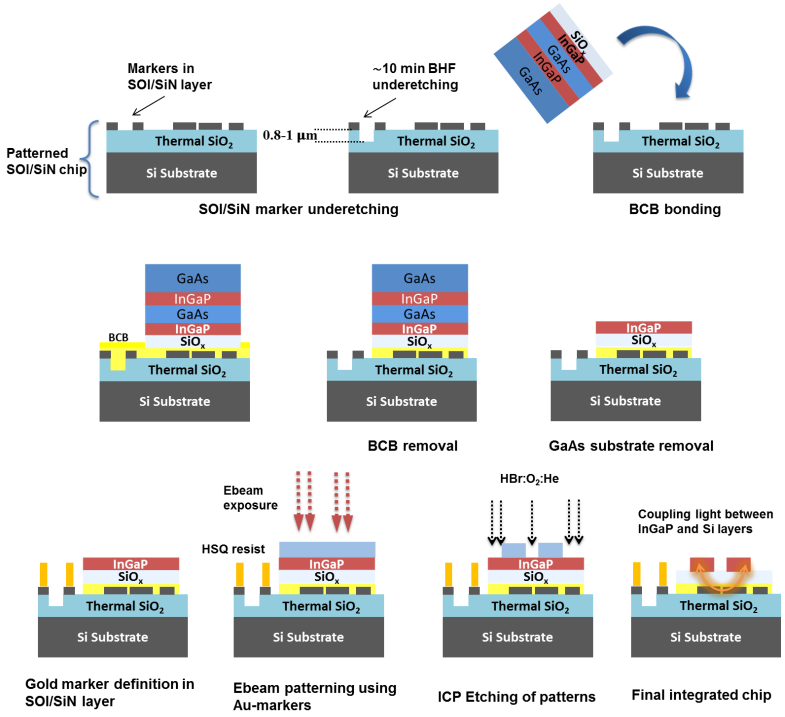

Figure 5.3 The complete process flow for the fabrication of structures in the InGaP layer which are properly aligned for optical coupling to the substrate layer.

5.3 Design of integrated nonlinear devices

In this section, a brief description is given of the design of light-coupling schemes for performing nonlinear functions in the InGaP/SOI or InGaP/SiN integrated platform fabricated as discussed above. For example, for nonlinear applications such as frequency comb generation, and sum and difference frequency generation, optical cavities are often used because of the advantages that they provide for enhanced light-matter interaction. For example, one could be interested in exciting specific modes of a microdisk resonator in the InGaP layer from a SOI or SiN waveg-

uide. This section provides a brief discussion of the results of FDTD simulations of InGaP microdisks coupled to SOI and SiN waveguides. Apart from exciting microdisk modes, a more generic light-coupling scheme would be to use inverted tapers to couple light back and forth between waveguides in the InGaP and substrate layers. This would allow the use of InGaP waveguides, ring resonators etc. for the various nonlinear functions that were demonstrated in the previous chapters, while still being able to couple the light to and from the substrate chip in order to perform any additional functions in those platforms. Thus, it is important to develop such general coupling schemes for the use of this fully integrated nonlinear platform that takes advantage of both the well-developed photonic devices on the SOI and SiN platforms as well as the advantageous nonlinear properties of InGaP.

5.3.1 Evanescently coupled microdisks

The amount of light coupled from a waveguide to a microdisk mode depends on the phase matching (or the effective index difference) as well as the modal overlap between the respective modes. To effectively model this, FDTD simulations were carried out using the Lumerical software. Figure 5.4(a) shows the setup for this simulation. Individual modes can be injected from either the waveguide or the microdisk and the software then calculates the propagation of this mode through the geometrical structure of the setup. Various monitors record the light flux through them during the simulation and this information can be used to calculate the light coupled to the microdisk from the waveguide mode as well as the distribution of that light among the various modes of the microdisk.

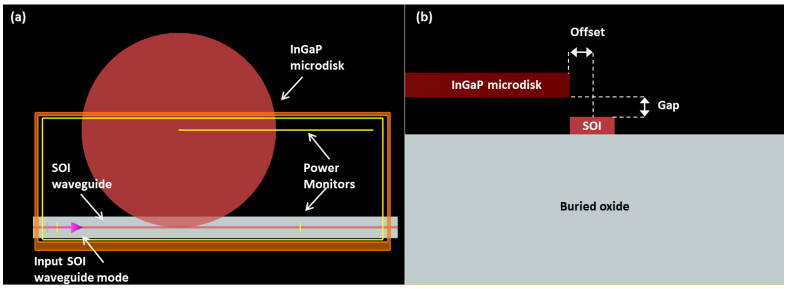

Figure 5.4 (a) The simulation setup in the Lumerical FDTD software for calculating the coupling of waveguide and microdisk modes. The pink arrow indicates the launched mode of the SOI waveguide and the various monitors record the light flux passing through them as this mode propagates through the structure. (b) The cross-sectional view of the simulation environment. The offset and gap parameters for the simulation are shown.

Figure 5.5 shows the results of such simulations for an SOI waveguide of width 500 nm and a InGaP disk of 15 μm diameter and a thickness of 250 nm for different values of the vertical gap and horizontal offset (as defined in Fig. 5.4(b)). The percentage of light from the injected waveguide mode that gets coupled to various disk modes is shown. Using this information, and knowing the expected inter-

nal loss of the fabricated microdisks, one can thus effectively decide the needed coupling strength and accordingly set parameters such as the vertical gap or the horizontal offset between the waveguide and the microdisk. For example, for a critically coupled microdisk, the loss experienced in the disk during one roundtrip has to be matched to the coupling from the waveguide.

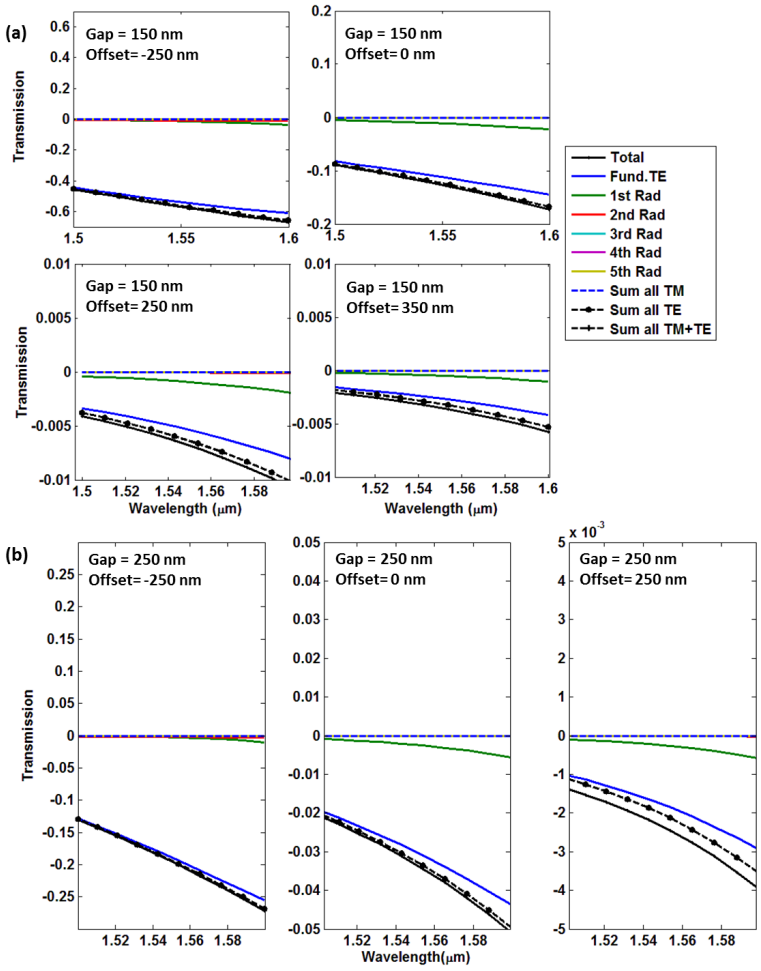

Figure 5.5 The coupling of the fundamental TE mode of a 500 nm $\times$ 220 nm SOI waveguide to various modes of an InGaP microdisk of thickness 250 nm is shown for various gap and offset values. The negative values of the coupling (i.e. transmission) is simply because of the orientation of the power monitors with respect to the co-ordinate frame of reference. The legend lists the various microdisk modes considered (fundamental TE, 1^{st} radial TE mode etc.).

5.3.2 Inverted tapers

Inverted tapers were designed for coupling light to and from SiN waveguides and InGaP waveguides. For applications such as supercontinuum generation described in chapter 4, integration with the SiN platform is interesting considering that the supercontinuum spectrum included wavelengths below 1.1 μm which would be absorbed in case of silicon waveguides. Another application is second harmonic generation from wavelengths in the telecommunication wavelength range as discussed in chapter 3. For both these applications, InGaP waveguides were used. As such, the use of inverted tapers is well-suited for coupling light between waveguides in the SiN and InGaP layers.

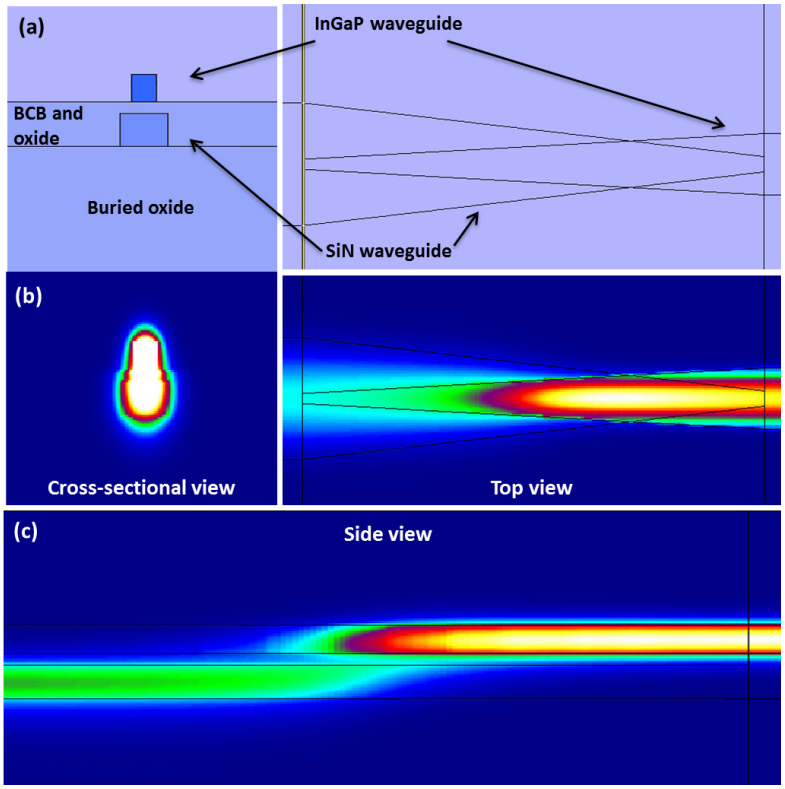

Figure 5.6 (a) The simulation setup for the FIMMPROP software, showing the overlaying SiN and InGaP tapers separated by a vertical gap. (b) The result of the simulation over the course of 100 μm taper length with the wide-end widths of the SiN and InGaP tapers being 1.2 μm and 600 nm and the narrow-end widths of the tapers being 150 nm and 200 nm respectively. The cross-sectional view shows how the light is present in both the tapers in the middle of the coupling region, as expected. (c) The side view shows the light coupling from the SiN taper to the InGaP taper over a length of a few 10's of μm at a wavelength of 1550 nm (TE polarization).

Figure 5.6 shows result of the simulation for the inverted taper design using the

commercial FIMMPROP software. It uses the Eigenmode expansion method to quickly calculate the propagation of individually launched modes in longitudinally varying cross-sections, and as such, it is ideally suited for the design of structures like inverted tapers. In this case, two tapers separated by a vertical gap are designed such that their modes partially overlap. As the bottom taper is decreasing in width, the top one has increasing width. As a result, the confinement of the light in the lower taper is decreasing and its mode expands to overlap with the mode of the top taper, coupling the two. Eventually, all the light is transferred to the top taper as its width increases and completely confines the light. In this specific example, it can be seen that all the light (at 1550 nm wavelength, TE polarization) from a 1200 nm $\times$ 300 nm SiN waveguide can be efficiently coupled to a 600 nm $\times$ 250 nm InGaP waveguide within a 100 μm taper length for a vertical gap of 200 nm between the two waveguides. These results don't change dramatically with waveguide width, and as such, the design is suitable for a wide variety of applications. The tip size for the SiN and InGaP tapers is 150 nm and 200 nm respectively. Simulations using Lumerical MODE software also confirmed these results as shown in Fig. 5.7. In fact, it is clear from Fig. 5.7(a) that even for short taper lengths of a few 10's of μm, more than 98% coupling efficiency can be obtained. However, in practice, there might be some misalignments during the fabrication process, and as such, a longer taper length would be more suitable. This is because obviously, the longer taper designs are more tolerant of misalignments between the SiN and InGaP tapers. Figure 5.7 also shows that for a vertical gap of 200 nm between the layers, and different offset values for the horizontal alignment between the tapers can be tolerated while retaining more than 90% coupling efficiency at 1550 nm wavelength. Thus this is quite a robust method for coupling light between the SiN and InGaP layers. Figure 5.7(b) shows that the taper design is also quite broadband in its operation, with more than 80% coupling for the 100 and 150 μm long tapers in a wavelength range extending from 1400-2200 nm and could thus be useful in applications such as supercontinuum generation.

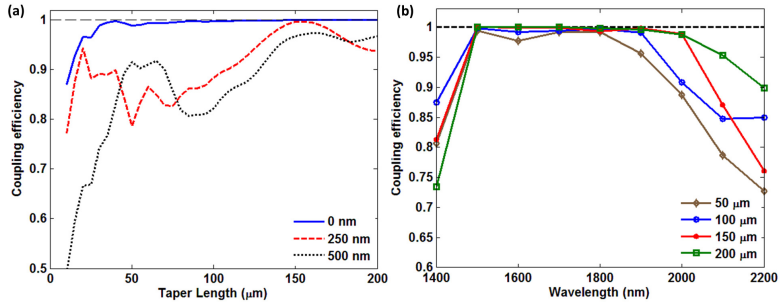

Figure 5.7 (a) The tolerance of the tapers to various misalignment offsets shows that even for 500 nm offset, coupling efficiencies of more than 80% and 90% for the 100 μm and 150 μm long tapers is achieved respectively at a wavelength of 1550 nm (TE polarization). (b) The broadband nature of the inverted tapers for various taper lengths (with zero misalignment).

5.4 Experimental characterization

Using the fabrication flow discussed in section 5.2, InGaP microdisks with diameters ranging from 15 to 10 μm coupled to SOI waveguides of various widths were fabricated, as shown in Fig. 5.8. The zoomed-in image shows one such microdisk coupled to the underlying SOI waveguide.

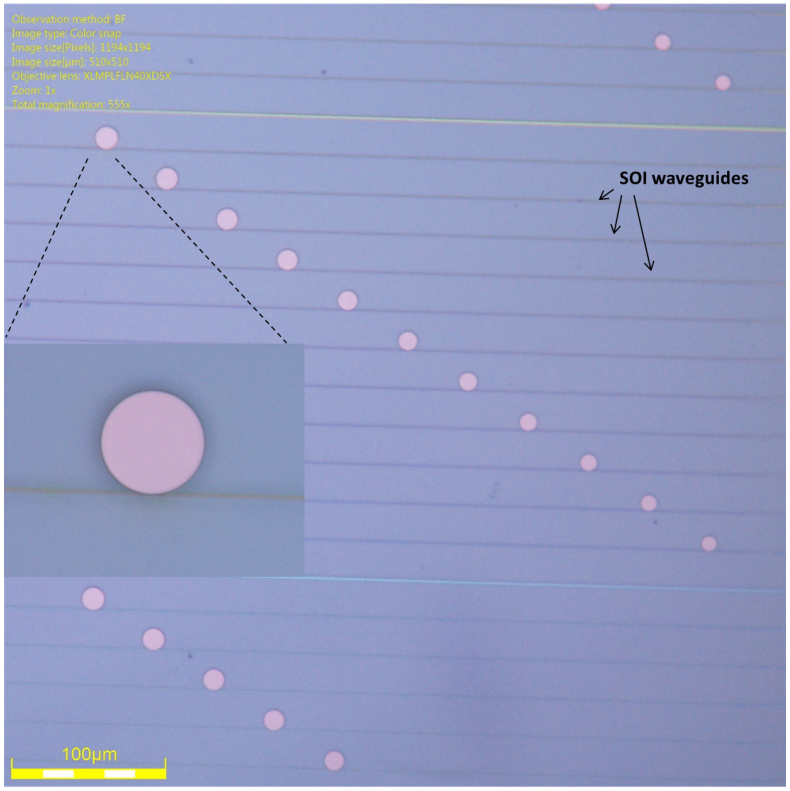

Figure 5.8 Fabricated InGaP microdisks of various diameters coupled to SOI waveguides of various widths. The gap is 250 nm total, of which, about 50 nm is the BCB layer on top of the SOI substrate and the remaining 200 nm is oxide. The zoomed-in image shows a 15 μm microdisk coupled to a 450 nm wide SOI waveguide.

Figure 5.9(a) shows the transmission of a tunable CW laser as a function of the wavelength for a SOI waveguide of cross section 400×220 nm^2 coupled to a InGaP microdisk of radius 7.5 μm and a thickness of 250 nm, separated by a gap of 250 nm and an offset of +200 nm. The gap is made up of a thin ($\approx$ 50 nm) BCB layer on top of the SOI waveguide and 200 nm of oxide. The resonance dips of the microdisk can be seen clearly. Note that for some of the resonances the extinction is more than 15 dB, meaning that they are close to the critical coupling condition. Figure 5.9(b) shows a Lorentzian fit of the resonance

dip at 1549 nm, from which its loaded quality factor is calculated to be about $Q_{loaded} = \lambda_{res}/\delta\lambda_{fwhm} = 26300$. Loaded quality factors of up to 65000 have been observed in other microdisks.

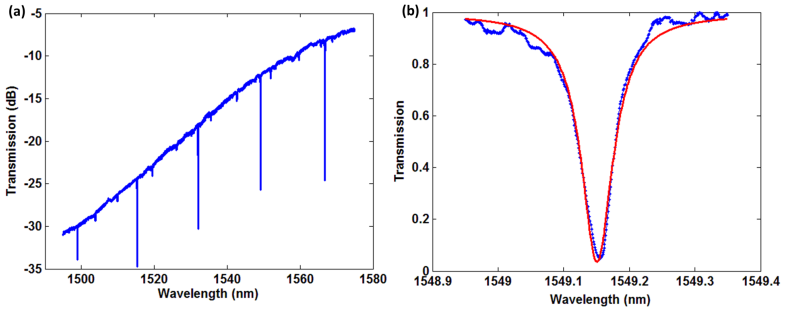

Figure 5.9 (a) Transmission of the SOI waveguide as a function of wavelength shows resonance dips of the coupled InGaP microdisk. The overall change in transmission comes from the grating efficiency of the SOI waveguide, which is designed to couple the TE fiber mode to the fundamental TE mode of the SOI waveguide. The extinction of the resonances can be seen to vary with the resonance wavelength, with extinctions greater than 15 dB for wavelengths close to 1550 nm. The smaller dips indicate resonances where higher-order modes were excited by the SOI waveguide. (b) The normalized transmission of the resonances at 1549 nm (blue dots) fit to a Lorentzian function (solid red line) to extract a loaded quality factor of 26300.

For certain applications, one might need air clad InGaP microdisks. Using the fabrication process as presented here will create microdisks standing on a slab of oxide and BCB. By underetching the fabricated microdisks in BHF for a few minutes, this oxide can be removed selectively without underetching the SOI waveguides beneath because the BCB layer prevents the BHF solution from penetrating beneath it. As such, 'air-clad' microdisks can be fabricated. One specific example of an application where such air-clad microdisks are desired is frequency comb generation in the telecommunications wavelength range. Figure 5.10 shows the calculated dispersion profiles of the fundamental TE and TM modes in InGaP microdisks for various thicknesses in both air-clad and underlying oxide cases. Since an anomalous dispersion at the pump wavelength is desirable for frequency comb applications, it can be seen that exciting the fundamental TM mode of air-clad InGaP microdisks of thicknesses greater than 300 nm is needed. In fact, by performing varying amount of underetching, the entire range of dispersion values between the bottom oxide clad and air clad could be accessed. As such, underetching the fabricated disks can be an important tool for achieving the desired properties for certain applications.

In order to verify that the underetching of the microdisks in BHF indeed does not cause any problems, the fabricated microdisks shown in Fig. 5.8 were underetched in BHF for several minutes. The results of the underetching are shown in Fig. 5.11. As shown in Fig. 5.11(a) no problems are apparent due to the underetching, at least visually. The inset shows the zoomed in image of one of the disks and the underetching of about 1 μm is visible. Figure 5.11(b) shows the corresponding

resonance wavelength shifts of two selected resonances for a particular microdisk after underetching for 2 and 4 minutes. Because the effective index decreases due to the underetching, the resonance wavelength is observed to blue-shift. Some effect is also expected on the quality factor since the total losses (including both the coupling and the scattering loss) will have changed after the underetching. However, the fits reveal that the quality factors do not degrade dramatically, showing that the underetching does not significantly alter the sidewall profile of the fabricated microdisks. Hence, removal of the oxide by BHF treatment is shown to be a useful technique for tailoring the dispersion properties for applications.

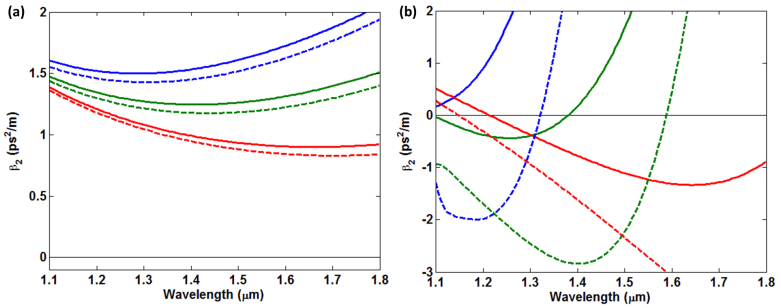

Figure 5.10 (a) Group velocity dispersion of the fundamental TE mode of InGaP microdisks of thickness 250 nm (blue lines), 300 nm (green lines) and 400 nm (red lines). The solid lines are for bottom oxide cladding and the dashed lines are for air-clad disks. The dispersion is normal in the whole wavelength range. (b) The dispersion for the fundamental TM mode. It can be seen that the anomalous dispersion regime is accessible in the telecommunications wavelength range with TM modes of air-clad disks with thicknesses greater than 300 nm.

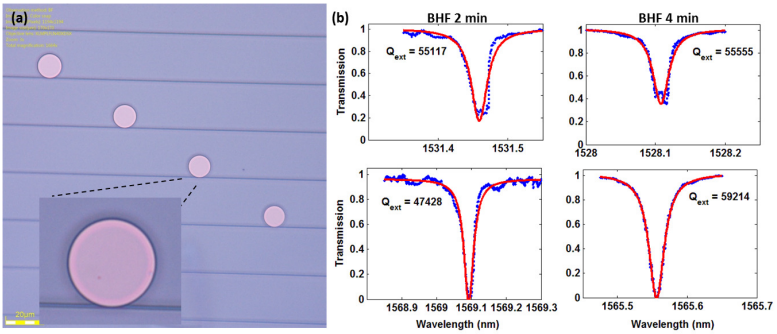

Figure 5.11 (a) No problems (like lifted-off SOI waveguides) are apparent after etching with BHF the bottom oxide cladding of the InGaP microdisks coupled to SOI waveguides. The zoomed-in image shows an underetching extent of about 1 μm as expected after etching for 4 minutes. (b) Two resonances of a particular disk after etching for 2 (left) and 4 (right) minutes. The resonance wavelength blue-shifts as expected, but the quality factor remains similar during the BHF treatment.

5.4.1 Evanescently coupled microdisks

The decent quality factors that were observed for the fabricated microdisks mean that there would be a strong intensity enhancement at the resonant wavelength, which can be helpful in improving the efficiency of nonlinear processes such as four-wave mixing (FWM). Figure 5.12(a) shows the result of a four-wave mixing experiment where both the pump and signal waves were chosen to be on adjacent resonances of a 15 μm diameter InGaP microdisk which was underetched for four minutes (with a loaded Q-factors at the pump, signal and idler wavelengths being about 54100, 47900 and 32500 respectively). The conversion efficiency as a function of pump power is shown in Fig. 5.12(b). As can be seen, compared to the case of straight waveguides discussed in chapter 3, here, one can achieve strong conversion for much lower coupled-in pump powers because of the added effect of the resonant intensity enhancement.

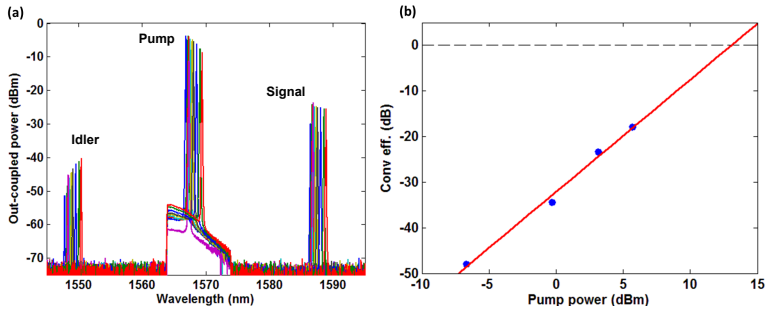

Figure 5.12 (a) The four-wave mixing experiment in InGaP microdisks evanescently coupled to SOI waveguides. The pump and signal are on adjacent resonances of the disk. The different colors represent the tuning of the pump and signal waves into their respective resonances, corresponding to an increase in the generated idler power. (b) The conversion efficiency of the FWM experiment defined as the ratio of the out-coupled idler power (to the SOI waveguide) to the signal wave in-coupled (to the SOI waveguide) power. The slope of the linear fit to the conversion efficiency vs pump power is 2.45.

The idler wave that is generated is also on-resonance (or close to it). In this case, the efficiency of the idler generation depends on more than just the pump power and the value of the nonlinear parameter γ - the effect of the resonances must also be taken into account [1–3]. In this specific case, since the microdisk diameter is rather small - meaning that the free-spectral range (FSR) is rather large - dispersion also plays a significant role. This is because, as in the case of waveguide four-wave mixing, both energy and momentum conservation (which is the same as phase-matching of course) must be satisfied for efficient idler generation. Since the signal, pump and idler waves are on adjacent resonance orders, the momentum conservation is automatically achieved [4]. This can be easily seen from the expression for the mode number m of the resonance: $m = 2\,\pi\,R\,n_{eff}/\lambda_{res} = R\,k_{res}$ where R is the radius of the disk, n_{eff} is the effective index and k_{res} is the propagation constant. Since they are on adjacent resonance orders $m_{s,i} = m_p \pm 1$, which

means that $2\,m_p = m_s + m_i$, which in turn implies that $2\,k_p = k_s + k_i$. However, due to dispersion, the energy conservation will not be respected if all the waves are exactly on-resonance. Thus, the idler wave cannot be exactly on resonance if both the conditions are satisfied. However, as long as the idler wavelength that satisfies the energy conservation is within the resonance linewidth, it will still see some enhancement [5]. Thus, in this particular case, these microdisks are not ideal for achieving large conversion efficiency. Instead, one would rather want microdisks with a smaller FSR (but with the same finesse in order to maintain the same field enhancement, which obviously implies larger quality factors are needed) such that the effects of dispersion can be safely neglected (or compensated for by the nonlinear effects). In the present case, because of the proximity of adjacent waveguides in the SOI chip, microdisks larger than 15 μm in diameter (and thus smaller FSR) could not be fabricated. But new chips with both TE and TM-grating coupled SOI waveguides and with the provision to couple to much larger InGaP microdisks have been designed. Thus, in the future, the same procedure could be easily followed to fabricate appropriate microdisks for such applications.

5.4.1.1 Second harmonic generation

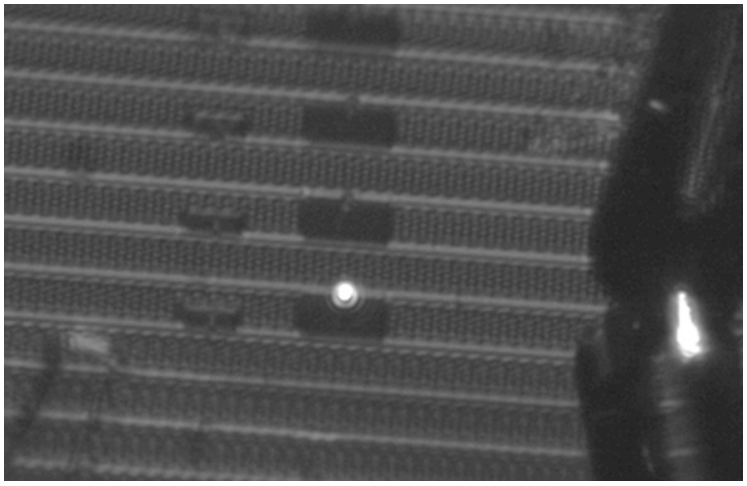

Figure 5.13 Second-harmonic generation observed in an InGaP microdisk coupled to a SiN waveguide that was used to couple the fundamental wavelength of 1525 nm to the microdisk. The visible wavelength camera captures the second-harmonic light at 762.5 nm wavelength.

Similarly, InGaP microdisks coupled to SiN waveguides were fabricated for the purpose of quasi-phasematched second-harmonic generation [6, 7]. Figure 5.13 shows SiN waveguides and InGaP microdisks. The picture is taken with a CMOS camera that is only sensitive to the second harmonic light. We can see that one of the disks is 'aglow' with the second-harmonic light generated inside the disk. Because the coupling efficiency of the fundamental and second-harmonic modes to

the SiN waveguide is quite different, careful design optimization needs to be done to maximize the total out-coupled second-harmonic light, which is something that could be carried out in future works.

5.4.2 Inverted tapers

SiN chips with the relevant markers were also designed and the fabrication procedure presented in section 5.2 was followed to integrate various InGaP devices onto this chip. Figure 5.14(a) shows the design of a SiN chip where the grating-coupled SiN waveguide used for the coupling of light from a fiber is connected to the inverted taper which ends in a bounding box that is free of any SiN structures or tiling (which refers to the practice of having 5 μm sized SiN squares or 'tiles' to fill up any free areas of the chip in the CMOS-fabrication process in order to have a more uniform density of structures across the whole chip). This bounding box can be used to incorporate any InGaP devices of choice. The other side of the bounding box has a similar inverted taper connected to a grating-coupled waveguide for out-coupling. Even though the bounding box is only 200 μm in size, that is large enough to easily incorporate waveguides of 1 cm length (in the form of a tight spiral, made possible by the large index contrast of the InGaP platform), as well as side-coupled microring resonators with large diameters like the ones discussed in the nonlinear experiments of chapter 3. Figures 5.14(b) and (c) shows the fabricated chip with InGaP devices like ring resonators and waveguide spirals coupled to the SiN chip via inverted tapers. These could thus be used for the integration of the nonlinear processes discussed in chapters 3 and 4 into the SiN platform.
Unfortunately, there were some manual errors during the e-beam writing step of this first attempt at the integration of InGaP nonlinear devices with the SiN platform. As a result, the exposure of the waveguides and other devices was incomplete, which resulted in the coupled devices being rendered non-functional. These can of course, be easily avoided in the future fabrication runs. Furthermore, misalignment between the tapers in the SiN and InGaP layers in this first attempt was found to be quite large at about 600 nm (see inset, Fig. 5.15). However, even with these rather significant errors in the e-beam exposure and the misalignment, an average coupling loss of only -2.5 dB across the wavelength range of the grating coupler was found for a test taper of 150 μm length as shown in Fig. 5.15.

5.5 Conclusions

In this chapter, the fabrication process for the integration of the numerous nonlinear devices that were demonstrated throughout this PhD with the CMOS-compatible SOI and SiN waveguide platforms was presented. The fabrication methodology is simple and only involves a few simply additional steps for the incorporation of markers from the process already discussed in chapter 3. The design and characterization of simple devices like evanescently-coupled microdisks was also presented. It was shown that with the presented fabrication process it is indeed

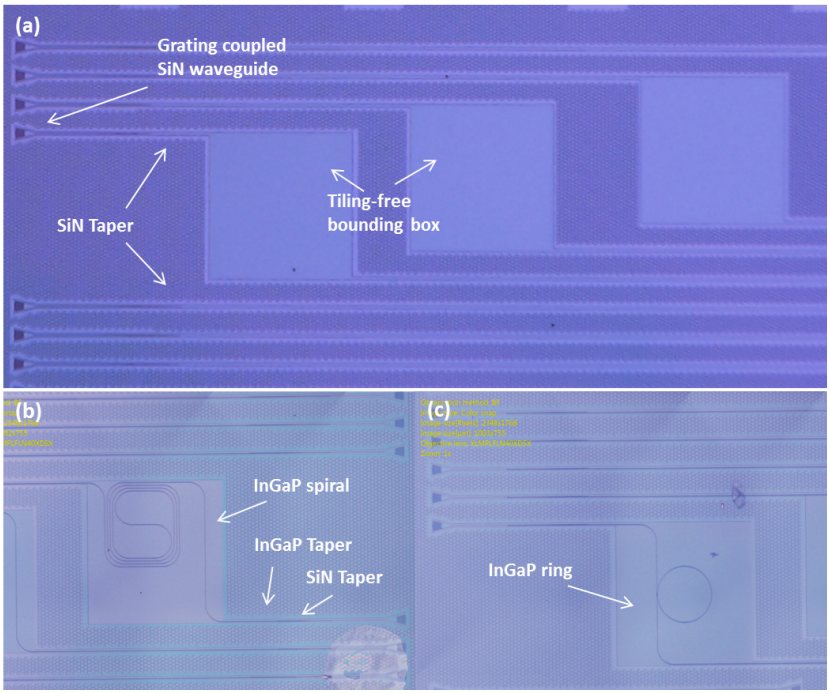

Figure 5.14 (a) The designed SiN chip with grating coupled waveguides connected to the SiN taper which will be used to coupled light to an InGaP taper fabricated on top of it. The InGaP taper can then be connected to a waveguide that leads to any desired device (which is on top of the bounding box). The bounding box has no tiling or any other SiN structures in it so that the InGaP device on top essentially feels the same refractive index environment as it would have in the InGaP-on-insulator platform. As such, the SiN chip can be used as a means of coupling in and out the light from the nonlinear devices in the InGaP-on-insulator platform. The final result of the fabrication process outlined in sec. 5.2 resulting in devices such as (b) an InGaP spiral and, (c) an InGaP ring resonator coupled to the SiN via inverted tapers.

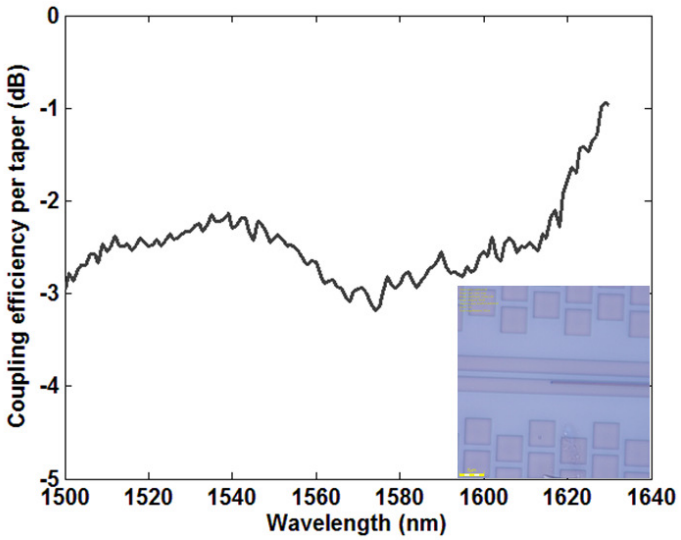

Figure 5.15 The coupling efficiency for the 150 μm long inverted taper in the first attempt at the fabrication of integrated InGaP devices on the SiN platform. With a proper e-beam exposure as well by improving the misalignment between the tapers, a significant improvement should be observed in the coupling efficiency and approach the simulated values as shown in Fig. 5.7. Inset: The fabricated tapers show a misalignment of around 600 nm.

possible to achieve good quality integrated nonlinear devices, which should, with proper device design and optimization, allow for very important and useful nonlinear processes to be implemented efficiently in the SOI and SiN platforms, which may lack such functionality on their own. For more generic devices, inverted tapers were designed and fabricated. In conclusion, the integration of InGaP/SOI and InGaP/SiN nonlinear devices has been demonstrated.
Of course, a lot more work still needs to be done in this arena. For example, in terms of specific applications, the fabrication of larger-diameter microdisks on the SOI chip which has waveguides connected to TM-gratings to specifically excite the anomalously dispersive TM-mode of the disk would allow one to demonstrate frequency-comb generation on this platform. Similarly, the integration of those InGaP waveguides and ring resonators that were investigated in the previous chapters with the SiN platform by the use of inverted tapers would allow for various nonlinear applications such as supercontinuum generation, second-harmonic generation etc. on this platform. And since these applications have already been demonstrated and various strategies already been developed for achieving phasematching etc., the next step is to leverage the functionality of the SOI and SiN platforms to improve these applications or take further steps towards real-world applications. Such future perspectives and some of the potential applications with great promise are briefly discussed in the next chapter.

References

[1] PP Absil, JV Hryniewicz, BE Little, PS Cho, RA Wilson, LG Joneckis, and P-T Ho *Wavelength conversion in GaAs micro-ring resonators* Optics letters, 25(8):554–556, 2000.

[2] M Ferrera, L Razzari, D Duchesne, R Morandotti, Z Yang, M Liscidini, JE Sipe, S Chu, BE Little, and DJ Moss *Low-power continuous-wave nonlinear optics in doped silica glass integrated waveguide structures* Nature photonics, 2(12):737–740, 2008.

[3] Imad H Agha, Yoshitomo Okawachi, Mark A Foster, Jay E Sharping, and Alexander L Gaeta *Four-wave-mixing parametric oscillations in dispersion-compensated high-Q silica microspheres* Physical Review A, 76(4):043837, 2007.

[4] TJ Kippenberg, SM Spillane, and KJ Vahala *Kerr-nonlinearity optical parametric oscillation in an ultrahigh-Q toroid microcavity* Physical review letters, 93(8):083904, 2004.

[5] Amy C Turner, Mark A Foster, Alexander L Gaeta, and Michal Lipson *Ultra-low power parametric frequency conversion in a silicon microring resonator* Optics Express, 16(7):4881–4887, 2008.

[6] David P Lake, Matthew Mitchell, Harishankar Jayakumar, Laís Fujii dos Santos, Davor Curic, and Paul E Barclay *Efficient telecom to visible wavelength conversion in doubly resonant gallium phosphide microdisks* Applied Physics Letters, 108(3):031109, 2016.

[7] Paulina S Kuo, Jorge Bravo-Abad, and Glenn S Solomon *Second-harmonic generation using-quasi-phasematching in a GaAs whispering-gallery-mode microcavity* Nature communications, 5, 2014.

6
CONCLUSIONS AND PERSPECTIVES

"My interest is in the future because I am going to spend the rest of my life there."
- Charles F. Kettering.

6.1 Conclusions from the presented work

In this work, two major problems in implementing nonlinear optical processes in the silicon-on-insulator platform have been tackled. The first of these problems is the large nonlinear losses arising from two-photon and free-carrier absorption in silicon while working at wavelengths below 2.2 μm, and the second is the lack of a bulk second-order nonlinear susceptibility because of its centrosymmetric structure. Two approaches for mitigating the first problem were explored - the use of hydrogenated amorphous silicon-on-insulator and the integration of large-bandgap III-V materials with the CMOS-compatible platforms of SOI and SiN. The second of these two approaches was the major focus of this work because it also tackles the lack of second-order nonlinearity in SOI and SiN waveguide circuits.

In the first approach hydrogenated amorphous silicon was investigated as an alternative to crystalline silicon because it had been previously demonstrated that it possesses a larger bandgap than c-Si which should result in lowered TPA and FCA losses. Since within the last few years convenient fiber-based laser sources around 2 μm - which is below the half-bandgap of crystalline silicon - have become available, the range of wavelengths where nonlinear processes can be practically implemented has expanded to include those wavelengths. As a result, a-Si offers the opportunity for implementing those nonlinear applications that have previously been prohibited by the nonlinear loss suffered by c-Si. To that end, the generation of a 1000 nm wide supercontinuum was demonstrated, as discussed in chapter 2. This particular application was made possible by leveraging the lowered TPA (and consequently, FCA) loss, increased material stability (also due to the lowered TPA) and dispersion engineering (which enabled two distinct modulation instability bands to experience nonlinear gain) of the a-Si waveguides pumped by a thulium-doped fiber laser source centered at 1950 nm. As a result of the all these advantages, the supercontinuum spectrum spans a wide spectrum bridging the telecommunications and the short-wave infrared wavelength ranges from 1470 to 2470 nm. This goes to show that a-Si is indeed an attractive platform for the implementation of integrated nonlinear functionalities, especially since it is compatible with the CMOS fabrication process and is thus conducive to low-cost manufacturing.

The second approach that was explored was to integrate III-V materials, whose bandgaps are known to be larger than twice the photon energy at telecommunications wavelengths, with the CMOS-compatible SOI and SiN platforms. This approach has the benefit that it allows maintaining a large index contrast that is essential in keeping nonlinear interactions efficient and implementing it in a waveguide structure with small footprint. Another advantage is that the III-V materials do not possess a center of inversion, meaning that their second-order nonlinear susceptibility is non-zero. These advantages make III-V materials such as InGaP and AlGaAs very good candidates for on-chip nonlinear optics.

InGaP was the primary material used in the work, but the same approach is easily adaptable to other similar materials such as GaP, AlGaAs etc.

First, taking cue from the techniques developed for integrating lasers onto the SOI platform, the process flow for bonding epitaxially grown InGaP to silicon substrates and subsequently removing the III-V growth substrate was developed and optimized. Then, in collaboration with the group at LPN, Paris, the Ebeam patterning and etching of InGaP was developed.

The devices fabricated in this manner were then characterized for their linear and nonlinear properties. A 12 dB/cm linear loss was measured, which, while being large by the standards of stare-of-the-art SOI fabrication, is still acceptably small for the implementation of several nonlinear functionalities. Thus, the third-order nonlinearity of the fabricated InGaP waveguides was characterized by four-wave mixing experiments. The nonlinear parameter γ was measured to be 475 $\mathrm{W}^{-1}\mathrm{m}^{-1}$, which is large enough for many applications. It was proven that at 1550 nm, these waveguides do not suffer from TPA and that the dominant nonlinear loss comes from the much-weaker three-photon absorption process, which also means that the FCA loss is negligible for the applications investigated in the present work. Finally, the generation of an octave-spanning, coherent supercontinuum in InGaP waveguides pumped at 1550 nm using an ultralow pulse energy of 2 pJ and a 170 fs pulse width was reported, proving that indeed the platform is capable of delivering state-of-the-art performance.

The first step towards the characterization of the second-order nonlinearity of the platform was also taken by the measurement of phasematched second harmonic generation in InGaP waveguides in the 1500 nm wavelength range. In the low-power continuous wave regime with about 1 mW of coupled-in pump power, a decent off-chip conversion efficiency (defined as $100 \times P_{SH,out}/P_{F,in}^2/L^2$) of $\eta_2 = 2.3 \times 10^{-3}\,\%/W/mm^2$ was reported. Similarly, quasi-phasematched second harmonic generation in InGaP ring resonators was also demonstrated with an off-chip conversion efficiency (defined as $100 \times P_{SH,out}/P_{F,in}^2$) of $1.6 \times 10^{-3}\,\%/W$.

Having thus proved that the platform is indeed viable for the implementation of efficient nonlinear applications, steps were taken towards the integration of these InGaP nonlinear devices with SOI and SiN waveguide circuits. The previously developed process flow was adapted to integrate the InGaP devices with patterned chips by additionally patterning gold markers into the SOI or SiN chip before the Ebeam patterning and etching of the InGaP layer. In this way, microdisks evanescently coupled to SOI and SiN waveguides were fabricated and characterized. Finally, coupling of light from the SiN to the InGaP layer with the use of inverted tapers was also demonstrated with good efficiency. In the InGaP microdisks evanescently coupled to SiN and SOI waveguides, second-harmonic

generation was observed and four-wave mixing was measured respectively. For the SOI-coupled microdisks of about 15 μm diameter, a maximum loaded quality factor of about 60000 was measured in critically coupled configuration. It was also shown that these microdisks could be underetched to remove the underlying oxide layer (for dispersion management) without hampering the quality factor. A maximum four-wave mixing efficiency (defined as $P_{idl,out}/P_{sig,in}$) of -18 dB was measured for a coupled-in pump power of 6 dBm in the SOI waveguide. While that is certainly not the highest conversion efficiency reported in the SOI platform, these measurements show that the integrated InGaP devices do exhibit all the expected advantages of a large nonlinearity without debilitating nonlinear losses.

In summary, these results show that indeed the approach of integrating suitable III-V materials such as InGaP with SOI and SiN chips offers a nonlinear platform with full second- and third-order functionality.

6.2 Future perspectives

While the work presented here has demonstrated the feasibility of a-Si:H and InGaP integrated with SOI and SiN platforms for nonlinear applications, there are still many avenues left to explore for both. For example, in literature, coherent supercontinuum generation in the telecommunication wavelength range has subsequently been demonstrated in the a-Si platform [1]. Thus, third-order nonlinear processes at telecommunication wavelengths that can be used for various applications like all-optical switching (as shown in [2]) can be implemented in the a-Si:H platform in the future.

Similarly, the InGaP integrated with SOI and SiN waveguide circuits presents an abundance of opportunities for nonlinear applications. The work presented here was mostly focused on the development of the platform as well as the characterization of its nonlinear properties and demonstrating some basic applications. This has thus set the stage for the realization of many advanced nonlinear applications such as accessing the mid-infrared wavelength range via difference frequency generation, frequency comb generation for spectroscopy and other applications, etc. in this platform because it has now been shown that the corresponding second- and third-order nonlinear interactions are strong enough for such practical purposes. Thus, it would be interesting to implement all those nonlinear applications that have not yet been demonstrated in this platform. Furthermore, integration with SOI or SiN waveguide circuits could provide the additional functionality required for fully integrated solutions that exploit such nonlinear processes and as such, it would be of practical interest to explore them. The mature SOI and SiN platforms could be used for any linear functionality within such applications such as filtering, routing as well as perform operations such as photodetection and modulation.

Before being able to implement such applications however, one obvious step is needed and that is to improve the linear loss of the InGaP waveguides. This can be achieved by further optimization of the Ebeam lithography and etching of the InGaP waveguides. One should also carefully evaluate the contribution to the loss by all possible sources such as from scattering, or loss due to the deposited oxide etc. Getting the loss down to about 1-2 dB/cm would considerably lower the power requirements for the various nonlinear processes discussed in this work as well as dramatically improve their efficiency. For example, as discussed in chapter 3, the 3 dB bandwidth of four-wave mixing conversion efficiency in the low dispersion case is limited by the effective interaction length and thus, the linear loss. Similarly, more of the pump power could be converted to the second harmonic if the phasematched waveguide could be made longer because of lowered linear loss. In the same vein, achieving low-loss (high quality factor) microresonators would improve the second-harmonic conversion efficiency as discussed in chapter 3 and lower the threshold for the onset of the frequency comb generation as discussed in chapter 5.

As for the nonlinear processes that have not yet been demonstrated in this platform, difference frequency generation is an important one. For instance, the mid-infrared wavelength range could be accessed by the generation of the difference frequency between lasers in the telecommunications wavelength range. In order to accomplish this, the quasi-phasematching (QPM) technique using bent waveguides as discussed in chapter 3 could be easily utilized. With the freedom to choose the thickness of the InGaP layer, one can design phase matched operation for a wide range of desired wavelengths. Other phase matching techniques can also be further explored to continue improving the ease and efficiency of either sum or difference frequency generation. These could include the intensity modulation-mediated QPM [3–6], order-disorder QPM [7] etc. Thus, a lot more work still needs to be done in this area.

Another important example is the case of frequency comb generation, where, by leveraging the technology of on-chip modelocked lasers [8] in conjunction with the dispersion engineered InGaP waveguides presented here, a broadband and coherent supercontinuum could be generated just like what was discussed in chapter 4; but in an entirely on-chip configuration. This thus provides a route towards achieving a completely integrated, octave-spanning frequency comb coupled on a SOI or SiN waveguide circuit. Furthermore, since the InGaP platform has also been shown to possess strong second-order nonlinearity, frequency doubling of the long wavelength part of the frequency comb could be performed in the same chip and used for the detection of the carrier-envelope offset. In this way, the f-to-$2f$ [9, 10] technique could be used for the on-chip frequency stabilization of the frequency comb. The nonlinear functions of comb spectral broadening and frequency doubling would be performed in appropriately dispersion engineered InGaP waveguides such as those discussed in chapters 3 and 4 and the filtering

and routing functions would be taken care of by the SOI/SiN photonic circuit, which would be coupled to the InGaP waveguides using the techniques discussed in chapter 5.

Finally, it is interesting to note that other technologies that are on the horizon could also be helpful in further pushing the usefulness of the presently discussed platforms. One such technology is transfer printing [11, 12] where one transfers thin membranes from one substrate to another. As such, one can potentially use one substrate to grow and pattern the devices and subsequently transfer them onto other desired substrates [13]. This allows for a massively scalable way to integrate III-V optoelectronic components with platforms such as SOI. In the present context, the method could be used to transfer membranes pre-patterned with nonlinear devices to the desired SOI or SiN photonic circuits. In this way, one could increase the efficiency of the III-V material usage as well as have the ability to integrate a wide variety of devices designed for different nonlinear processes onto the same photonic circuit even if they required different III-V layer thicknesses or compositions as described in [13].

Thus, there are ample opportunities for further exploration starting from the work and ideas presented in this thesis which could lead to useful contributions to the state-of-the-art in many diverse fields.

References

[1] Jassem Safioui, François Leo, Bart Kuyken, Simon-Pierre Gorza, Shankar Kumar Selvaraja, Roel Baets, Philippe Emplit, Gunther Roelkens, and Serge Massar *Supercontinuum generation in hydrogenated amorphous silicon waveguides at telecommunication wavelengths* Optics express, 22(3):3089–3097, 2014.

[2] N Vukovic, N Healy, FH Suhailin, P Mehta, TD Day, JV Badding, and AC Peacock *Ultrafast optical control using the Kerr nonlinearity in hydrogenated amorphous silicon microcylindrical resonators* Scientific reports, 3:2885, 2013.

[3] Xu Guang Huang and Michael R Wang *A novel quasi-phase-matching frequency doubling technique* Optics communications, 150(1):235–238, 1998.

[4] Po Dong and Andrew G Kirk *Nonlinear frequency conversion in waveguide directional couplers* Physical review letters, 93(13):133901, 2004.

[5] Po Dong, Jeremy Upham, Aju Jugessur, and Andrew G Kirk *Observation of continuous-wave second-harmonic generation in semiconductor waveguide directional couplers* Optics express, 14(6):2256–2262, 2006.

[6] Jeff Chiles, Seyfollah Toroghi, Ashutosh Rao, Marcin Malinowski, Guillermo Fernando Camacho-González, and Sasan Fathpour *Second-harmonic generation in single-mode integrated waveguides through mode-shape modulation* arXiv preprint arXiv:1610.02111, 2016.

[7] Yoshiyasu Ueno, Vincent Ricci, and George I Stegeman *Second-order susceptibility of Ga 0.5 In 0.5 P crystals at 1.5 μm and their feasibility for waveguide quasi-phase matching* JOSA B, 14(6):1428–1436, 1997.

[8] Sarah Uvin, Shahram Keyvaninia, Francois Lelarge, Guang-Hua Duan, Bart Kuyken, and Gunther Roelkens *Narrow line width frequency comb source based on an injection-locked III–V-on-silicon mode-locked laser* Optics Express, 24(5):5277–5286, 2016.

[9] R Holzwarth, Th Udem, Th W Hänsch, JC Knight, WJ Wadsworth, and P St J Russell *Optical frequency synthesizer for precision spectroscopy* Physical review letters, 85(11):2264, 2000.

[10] Th Udem, Ronald Holzwarth, and Theodor W Hänsch *Optical frequency metrology* Nature, 416(6877):233–237, 2002.

[11] E Menard, KJ Lee, D-Y Khang, RG Nuzzo, and JA Rogers *A printable form of silicon for high performance thin film transistors on plastic substrates* Applied Physics Letters, 84(26):5398–5400, 2004.

[12] John Justice, Chris Bower, Matthew Meitl, Marcus B Mooney, Mark A Gubbins, and Brian Corbett *Wafer-scale integration of group III-V lasers on silicon using transfer printing of epitaxial layers* Nature Photonics, 6(9):610–614, 2012.

[13] Andreas De Groote, Paolo Cardile, Ananth Subramanian, Alin M Fecioru, Christopher Bower, Danae Delbeke, Roel Baets, and Günther Roelkens *Transfer-printing-based integration of single-mode waveguide-coupled III-V-on-silicon broadband light emitters* Optics Express, 2016.